Understand and reshape the impact of obesity/type 2 diabetes mellitus and adaptive immunity on bone fracture healing

Inaugural-Dissertation

to obtain the academic degree

Doctor rerum naturalium (Dr. rer. nat.)

submitted to the Department of Biology, Chemistry, Pharmacy

of Freie Universität Berlin

by

M. Sc. Carolin Paschke geb. Rünger

2023

Carolin Paschke

Inaugural-Dissertation

Understand and reshape the impact of obesity/type 2 diabetes mellitus and adaptive immunity on bone fracture healing

Supervision:	PD Dr. rer. nat. Katharina Schmidt-Bleek
Time Peroid:	April 2018 to August 2022
Institution:	Julius Wolff Institute for Biomechanics and Musculoskeletal Regeneration in the Berlin Institute of Health, Berlin, Germany

1st reviewer:	Prof. Dr. rer. nat. Petra Knaus Freie Universität Berlin, Germany Department for Biochemistry
2nd reviewer:	PD Dr. rer nat. Katharina Schmidt-Bleek Berlin Institute of Health, Julius Wolff Institute for Biomechanics and Musculoskeletal Regeneration at Charité - Universitätsmedizin Berlin, Germany
Date of defense:	11.03.2024

Acknowledgements

First, I would like to thank my supervisor Kate, for her guidance and support throughout my dissertation, her endless enthusiasm for science and giving me the freedom to develop as a scientist.

I want to extend my thanks to Petra Knaus for reviewing my doctoral thesis, and would like to express my gratitude to Georg H. Duda for the opportunity to achieve a long-time goal within the Julius Wolff Institute. Additionally, I sincerely appreciate the insightful immunological advice received from Hans-Dieter Volk and for putting my work into relevant perspective.

To all the Biology-of-Bone-healing lab members past and present, thank you for making it such a great place to carry out science. Special thanks to Lisa for the wonderful time in the lab and office. I am also thankful for the help and critical scientific mind of Christian Bucher, Sabine Stumpp for the histological expertise and always offering a helping hand in the lab, Norma Schulz for supporting the working group as backbone, Agnes Ellinghaus and Katja Reiter for being a dream team to work with in the animal facility and for the private chitchats during surgeries, Gabriela Korus for her wisdom in immunohistochemistry, Mario Thiele for his effort in histological assessment and analysis, as well as Oskar Schmidt-Bleek for his valuable support in the micro-CT analysis.

I am eternally grateful for my parents and my whole family, for their belief in me and their support, which made this work possible.

Frieda, my sweet little girl, you are the best thing that happened to me. You show me every day what really is important in life. Last but not least, I thank you, Marco! For your unconditional support and patience with me in the last years. I could not have done it without your motivative words, hands-on attitude and countless lunch packages made for work. You two mean the world to me!

Declaration

The present thesis ”Understand and reshape the impact of obesity/type 2 diabetes mellitus and adaptive immunity on bone fracture healing” has been composed by myself and describes my own work, unless specifically acknowledged in the text. This thesis is submitted to the Department of Biology, Chemistry and Pharmacy of the Freie Universität Berlin to obtain the academic degree Doctor rerum naturalium (Dr. rer. nat.). This work has not been submitted for any other degree.

Berlin, June 2023 Carolin Paschke

List of abbreviations

Abx	antibiotics
ADAM	a disintegrin and metalloprotease
ADAMTS	ADAM with thrombospondin motifs
AF	autofluorescence
ALPL	alkaline phosphatase
AP	alkaline phosphatase
APC	antigen-presenting cell
AT	adipose tissue
AUC	area under curve
B	Bacteroidetes
BM	bone marrow
BMD	bone mineral density
BMI	body mass index
BMP	bone morphogenic proteins
BSA	bovine serum albumin
BV	bone volume
CCL	cysteine-cysteine (CC) chemokine ligand
CCR	CC chemokine receptor
CCRL	CCR-like
CD	cluster of differentiation
cDNA	complementary DNA
CHP	collagen hybridizing peptide
CM	central memory
Col	collagen
CXCL	cysteine-any aminoacid-cysteine (CXC) chemokine ligand
CXCR	CXC chemokine receptor
DA	differental abundance
DAPI	4',6-diamidino-2-phenylindole
DC	dendritic cell
DE	differentially expressed
DIO	diet-induded obesity
DN	double-negative
DNA	deoxyribonucleic acid
EC	endothelial cell
ECM	extracellular matrix
eff	effector

EM	effector memory
ER	endoplasmic reticulum
F	Firmicutes
Fc	flow cytometry
FFA	free fatty acids
Fig.	figure
FoxP3	forkhead box P3
FSC	forward scatter
GATA3	guanine-adenine-thymine-adenine binding protein 3
GT	glucose tolerance
GTT	glucose tolerance test
HCl	hydrochloride
HE	hematoxylin-eosin
HFD	high-fat diet
hi	high
HSC	hematopoietic stem cel
i.p.	intraperitoneal
IFN	interferon
IGF	insulin growth factor
IGFBP	insulin-like growth factor-binding protein
IHC	immunohistochemistry
IL	interleukin
IQR	interquartile range
ITT	insulin tolerance test
kcal	kilocalories
KEGG	Kyoto Encyclopedia of Genes and Genomes
Lox	lysyl oxidase
Loxl	lysyl oxidase-like
M	macrophage
M-CSF	macrophage colony-stimulating factor
MDS	multi-dimensional scaling
mem	memory
micro-CT	micro-computed tomography
MMIp	minimal polar moment of inertia
MMP	matrix metalloproteinase
mRNA	messenger RNA
MSC	mesenchymal stroma cell
N	number
NADP(H)	nicotinamide adenine dinucleotide phosphate
NASH	nonalcoholic steatohepatitis
NF-κB	nuclear factor κ-light-chain-enhancer of activated B cells
NNT	nicotinamide nucleotide transhydrogenase

NOD	nucleotide-binding oligomerization domain
OB	osteoblast
OC	osteoclast
OPG	osteoprotegerin
OTU	operational taxonomic unit
PBS	phosphate-buffered saline
PC	principal component
PCA	principal component analysis
PE	phycoerythrin
PERMANOVA	Permutational multivariate analysis of variance
PFA	paraformaldehyde
Po.tot	total porosity
PPARγ	peroxisome proliferator activated receptor γ
RANK	receptor activator of NF-κB
RANKL	receptor activator of nuclear factor (NF)-κB ligand
RNA	ribonucleic acid
RORγt	regulator retinoid acid-related orphan receptor γt
ROS	reactive oxygen species
rRNA	ribosomal RNA
RUNX	runt-related transcription factor
s.c.	subcutaneous
SA	streptavidin
SCEM	super cryoembedding medium
SCFA	short-chain fatty acid
scRNAseq	single cell RNA sequencing
SD	standard deviation
SMAD	"small" worm phenotype (SMA), mothers against decapentaplegic (MAD)
SNN	shared nearest neighbor
SPF	specific pathogen free
SSC	sideward scatter
T1DM	type 1 diabetes mellitus
T2DM	type 2 diabetes mellitus
Tab.	table
Tb.N	trabecular number
Tb.Sp	trabecular spacing
Tb.Th	trabecular thickness
Tbet	T-box expressed in T cells
TBS	tris-buffered saline
TBST	tris-buffered saline with Triton X-100
TCR	T cell receptor
Th	Thelper
TNF	tumor necrosis factor

Treg	regulatory T cell
t-SNE	t-distributed stochastic neighbor embedding
TV	total volume
VEGF	vascular endothelial growth factor
Wnt	Wingless and Int-1

Abstract

The process of bone fracture healing relies on a tight regulation of cellular and molecular events. However, obesity can disrupt the healing cascade, leading to defective repair. A heightened inflammatory state, primarily regulated by the adaptive immunity, is believed to contribute to the pathophysiology of obesity linked to bone healing defects. Despite the high obesity prevalence, limited research has explored this relationship. Herein, the underlying hypothesis of this work is that increased pro-inflammation associated with obesity may be causative for delayed bone repair. The specific aims were to understand the impact of different degrees of obesity, as encountered in clinical settings, on the modulation of immunity and its effects on bone fracture healing. To investigate this, a high-fat diet (HFD)-induced obesity model was used in conjunction with femoral osteotomy. Based on metabolic measurements, two obese subtypes were included in this study: a group with low glucose intolerance and a group with high glucose intolerance that indicates a possible developing type 2 diabetes mellitus (T2DM).

The findings provided evidence that the early onset of obesity induced by a short-term HFD resulted in a pro-inflammatory state that caused impaired healing of femoral fractures with an altered microarchitecture in both obese groups. Remarkably, obese mice with high glucose intolerance showed signs of adapting to the metabolic conditions in terms of pro-inflammatory responses and bone healing capacity.

Consistently, a long-term HFD resulted in reduced pro-inflammation in both groups. Surprisingly, along with increased weight gain, callus adiposity and bone mineralization, the previously observed healing defects associated with obesity were repealed regarding the mineralization process. However, abnormal extracellular matrix (ECM) remodeling and formation were observed during initial bone fracture healing, with more pronounced effects seen in mice with high glucose intolerance, hinting at a T2DM manifestation. This finding poses a potential risk for the development of fibrosis. Neutralization of potentially detrimental $CD8^+$ T cells during the early healing phase reversed the disturbance in the formation of ECM in the obese group with high glucose intolerance. This finding highlights the critical role of $CD8^+$ T cells in regeneration and offers a potential therapeutic approach to improve bone formation in specific patients.

The microbiome's role in obesity and its connection to adaptive immunity and metabolic inflammation is well established. The analysis of feces and cecal samples revealed that long-term obesity altered the gut microbiome structure, while bacterial diversity remained unchanged. Interestingly, obese mice with high glucose intolerance exhibited a distinct microbial signature associated with metabolic rather than immunological alterations. Importantly, these obesity-related changes were partially reversible through the neutralization of $CD8^+$ T cells.

Overall, this work emphasizes that aberrant bone formation occurs early in the progression of obesity, before the development of obesity-associated T2DM. The activation of the immune system is even enhanced at the onset of obesity, leading to impaired bone formation. Although the skeletal system adapts to the immunological and metabolic imbalance associated with persistent obesity, this still results in an altered ECM. The data increase our comprehension and awareness of obesity progression in clinical contexts, providing potential therapeutic avenues. Addressing obesity becomes crucial to making right and timely decisions for susceptible fracture patients.

Zusammenfassung

Der Heilungsprozess von Knochenbrüchen beruht auf einer strengen Regulierung zellulärer und molekularer Ereignisse. Fettleibigkeit, auch als Adipositas bezeichnet, kann jedoch die Heilungskaskade stören und zu fehlerhaften Reparaturen führen. Es wird angenommen, dass ein erhöhter Entzündungszustand, der vorrangig durch das adaptive Immunsystem reguliert wird, zur Pathophysiologie von Fettleibigkeit und Knochenheilungsdefekten beiträgt. Trotz der hohen Prävalenz von Fettleibigkeit wurde dieser Zusammenhang nur in begrenztem Umfang untersucht. Die dieser Studie zugrunde liegende Hypothese besteht darin, dass die durch Adipositas induzierte Proinflammation für die verzögerte Knochenreparatur verantwortlich ist. Die Ziele bestanden darin, die Auswirkungen unterschiedlicher Schweregrade von Fettleibigkeit, wie sie im klinischen Umfeld auftreten, auf das Immunsystem und die Heilung von Knochenbrüchen zu verstehen. Um dies zu untersuchen, wurde ein Hoch-Fett-Diät (HFD)-Modell zur Induktion von Adipositas in Verbindung mit einer femoralen Osteotomie verwendet. Basierend auf Stoffwechselmessungen wurden zwei adipöse Phänotypen in diese Studie einbezogen: eine Gruppe mit niedriger Glukoseintoleranz und eine Gruppe mit hoher Glukoseintoleranz, die auf einen möglichen sich entwickelnden Typ-2-Diabetes mellitus (T2DM) hinweist.

Die Ergebnisse lieferten Hinweise darauf, dass eine beginnende Fettleibigkeit, hervorgerufen durch eine kurzzeitige HFD, zur systemischen Entzündung führte, die in beiden Gruppen die Knochenheilung beeinträchtigte und die Mikroarchitektur veränderte. Bemerkenswerterweise zeigte die fettleibige Gruppe mit hoher Glukoseintoleranz Anzeichen einer Anpassung an die Stoffwechselstörungen im Hinblick auf Entzündungsreaktionen und Knochenheilungskapazität.

Entsprechend führte eine langfristige HFD in beiden Gruppen zu einer verringerten Proinflammation. Überraschenderweise wurden durch die Zunahme des Gewichts, des Knochenfetts und der Knochenmineralisierung die zuvor beobachteten Heilungsdefekte in Bezug auf den Mineralisierungsprozess aufgehoben. Während der initialen Heilungsphase wurde jedoch eine abnormale Umgestaltung und Bildung extrazellulärer Matrix (ECM) beobachtet, wobei die Auswirkungen bei Mäusen mit hoher Glukoseintoleranz ausgeprägter waren und auf eine T2DM-Manifestation hindeuteten. Dieses Ergebnis stellt ein mögliches Risiko für die Entstehung einer Fibrose dar. Die Neutralisierung potenziell schädlicher $CD8^+$ T-Zellen während der Heilung kehrte die Störung der ECM-Formation in der adipösen Gruppe mit hoher Glukoseintoleranz allerdings um. Dies betont die entscheidende Rolle von $CD8^+$ T-Zellen in der Regeneration und bietet einen potenziellen Therapieansatz zur Verbesserung der Knochenheilung bei bestimmten Patienten.

Die Rolle des Mikrobioms bei Fettleibigkeit und die Verbindung zur adaptiven Immunität und metabolischen Entzündung sind hinlänglich bekannt. Die zusätzliche Analyse von Kot- und Caecumproben ergab, dass die längerfristige Fettleibigkeit die Struktur des Darmmikrobioms veränderte, während die bakterielle Vielfalt unverändert blieb. Interessanterweise zeigten fettleibige Mäuse mit hoher Glukoseintoleranz eine eigene mikrobielle Signatur, die eher mit metabolischen als mit immunologischen Veränderungen in Zusammenhang steht. Wichtig ist, dass die mit Fettleibigkeit verbundenen Veränderungen im Mikrobiom durch die Neutralisierung von $CD8^+$ T-Zellen teilweise reversibel waren.

Insgesamt unterstreicht diese Arbeit, dass eine gestörte Knochenheilung schon früh im Verlauf von Adipositas auftritt, sogar noch vor dem Ausbruch von T2DM. Die Aktivierung des Immunsystems ist zu Beginn von Adipositas verstärkt, was zu einer verschlechterten Knochenbildung führt. Obwohl sich das Skelettsystem an das immunologische und metabolische Ungleichgewicht im Zuge anhaltender Fettleibigkeit anpasst, führt dies dennoch zu einer veränderten ECM. Die Daten erweitern unser Verständnis und Bewusstsein für die Risiken von Adipositas im klinischen Kontext und bieten potenzielle therapeutische Möglichkeiten. Der Umgang mit Adipositas ist von entscheidender Bedeutung, um richtige und rechtzeitige Entscheidungen für gefährdete Fraktur-Patienten zu treffen.

Table of contents

List of figures

List of tables

1 Introduction

1.1 Obesity – a global health priority

1.1.1 Obesity: Epidemiology and link to bone fractures

The pace of the population aging around the world is dramatically increasing [1]. With historically low birth rates and increasing life expectancy, the population is undergoing a significant age shift: It is projected that by 2050, the proportion of individuals aged 60 and over will nearly double, reaching 22 % and 2 billion people in total. This demographic trend poses a challenging clinical situation, especially considering that as of the end of 2014, the elderly already accounted for more than a quarter of the German population, outnumbering children [2]. Today, obesity is becoming increasingly prevalent in the aging population, representing an accompanying epidemic that is growing both nationally and globally. Interestingly, the prevalence of adult obesity has surpassed that of undernutrition, marking a shift in the nutritional landscape [3]. In Germany, more than 50 % of adults are classified overweight (body mass index (BMI) ≥ 25 kg/m^2) with an obesity prevalence (BMI ≥ 30 kg/m^2) of 19 % [4]. Obesity is defined as chronic, relapsing, and multifactorial disorder as consequence of the long-term positive energy balance [5]. Thus, it is discussed to reframe determinants for obesity, as BMI only partially captures the complexity of the metabolic disorder [6]. Therefore, visceral fat in overweight and obese individuals is regarded as novel decisive factor which greatly increases the risk of developing type 2 diabetes mellitus (T2DM) [7]. In Germany, one in five adults is diagnosed with prediabetes [8] and every tenth person with T2DM [9]. The number of T2DM cases has doubled since 1998 and one third of this increase is attributed to demographic aging [9, 10].

The burden of obesity on health extends to multiple organ systems, with obesity-related inflammation exacerbating various pathologies. Of major public health concern is the development of secondary noncommunicable diseases such as cardiovascular and musculoskeletal disorders as well as increasing incidences for premature death [3]. In particular, obesity has been identified as a risk factor for complications in fracture healing. Impairment in bone regeneration is tightly interwoven with gerontology, and in combination with the accelerated obesity rate, results in the need to understand the underlying mechanisms. The incidence of fractures steadily increases in light of the demographic change [11] and consequently, places a burden on the healthcare system. In Germany, the fracture frequency increased by 14 % over the span of 10 years [12]. Delayed or

non-union fracture healing occurs in 5-10 % of all fracture cases causing enduring pain, prolonged immobility and the need for additional surgeries. Obesity-associated T2DM assume a leading role predisposing to this impairment [13]. It has become increasingly evident that excessive inflammation observed in fracture complications and obesity represents a causal link even prior to the diagnosis of T2DM. However, clinical trials often lack the inclusion of obese non-diabetic individuals, despite the high prevalence. Therefore, the study aimed to investigate obesity and prediabetes as precursor conditions, separate from T2DM. The used diet-induced obesity (DIO) study model induces glucose intolerance and insulin resistance *in vivo*, which are commonly associated with obesity and prediabetes, before the development of T2DM [14]. The effects of these compromised metabolic conditions on bone repair and the immune response to injury are poorly examined in the clinic, and thus, underline the importance of this work.

1.1.2 Etiology of hyperinsulinemia and insulin resistance in obesity

The excess of adipose tissue (AT) is considered as primary driver for hyperinsulinemia and insulin resistance, leading to the development of type 2 diabetes mellitus (T2DM) and other metabolic disorders collectively known as metabolic syndrome [15]. Insulin, a proteohormone produced by β-cells of the pancreatic islets of Langerhans, plays a crucial role in regulating the absorption of carbohydrates, proteins, and lipids in insulin-sensitive tissues such as AT, skeletal muscle and liver [16]. Obesity-mediated hyperinsulinemia refers to increased circulating levels of insulin resulting from impaired insulin action in the regulation of cellular glucose uptake. This impairment leads to elevated blood glucose concentrations, a condition known as hyperglycemia [17, 18]. As a response to impaired insulin action and elevated blood glucose levels, pancreatic β-cells are further stimulated to secrete insulin and to prevent from pathological hyperglycemia. Additionally, it is widely accepted that free fatty acids, which are released by adipocytes during lipolysis (the breakdown of stored fats), can trigger insulin production [19].

The abnormal insulin secretion is associated with insulin resistance which indicates that higher-than-normal insulin signaling is required to maintain healthy blood glucose levels [20]. On molecular level, the signal defect from the insulin receptor to downstream factors is characterized as primary cause for resistance [21]. In part, downregulation of the pivotal glucose transporter member 4 (GLUT4), which responds to insulin, further impairs insulin signaling [19]. Mounting evidence demonstrates that also chronic low-grade inflammation caused by obesity confers insulin resistance, although the underlying mechanism is incompletely defined [22]. Oxidative and endoplasmic reticulum (ER) stress, as well as hypoxia and adipocyte dysfunction are additional hypothesized mechanisms that contribute to the development of insulin resistance [23].

Next to impaired insulin action, a deficiency in insulin secretion is another characteristic feature of metabolic dysfunction, especially in T2DM. This β-cell failure occurs when hyperglycemia and FFA persist, leading to an inability of β-cells to compensate for insulin resistance [24].

Long-term obesity, with its metabolic imbalance, regularly leads to a series of complications affecting nearly every tissue in the body including the heart, kidneys, arteries, nerves, and most notably, bone.

1.1.3 Novel definition of prediabetes highlights its medical importance

T2DM is described to develop from obesity and patients with T2DM often undergo a longtime disease progression with preliminary stages of prediabetes. In those phases of development, blood glucose levels are increased, but not yet as high as to manifest T2DM [25]. Nonetheless, prediabetes is already accompanied by developing risk for T2DM and severe secondary diseases such as kidney failure. A 25 year-lasting study by Wagner et al. (2021) [26] accomplished to evaluate disease risk by clustering prediabetes subtypes and thus, helping to prevent further progression of metabolic diseases. By monitoring parameters such as blood glucose and lipid levels, fatty liver status, body fat accumulation and genetic risk factors, it was possible to identify six distinct subtypes of prediabetes (Fig. 1). A low risk for developing T2DM is attributed to three clusters (group 1, 2 and 4). Clusters 1 and 2 primarily consisted of healthy participants, with lean individuals mainly classified into cluster 2. Cluster 4, on the other hand, comprised overweight participants with a fairly healthy metabolic profile. Subtypes 3, 5 and 6 are associated with an elevated risk for T2DM and/or comorbid diseases. People from cluster 3 are characterized by reduced insulin secretion, whereas subtype 5 includes prediabetics that are resistant to insulin and developed a fatty liver. In participants of cluster 6, severe kidney damage emerges even prior to T2DM diagnosis. Consequently, the mortality rate is highly increased in these patients.

In summary, the study emphasizes the multifactorial nature of prediabetes which induces various and severe pathophysiologies. Consequently, early stages before T2DM manifestation gain clinical importance, as the number of individuals with obesity and prediabetes markedly surpasses those with overt T2DM. Hence, the objective of this obesity study was to incorporate different degrees of metabolic alterations to examine their effects on modulating immunity and bone fracture healing before the onset of T2DM.

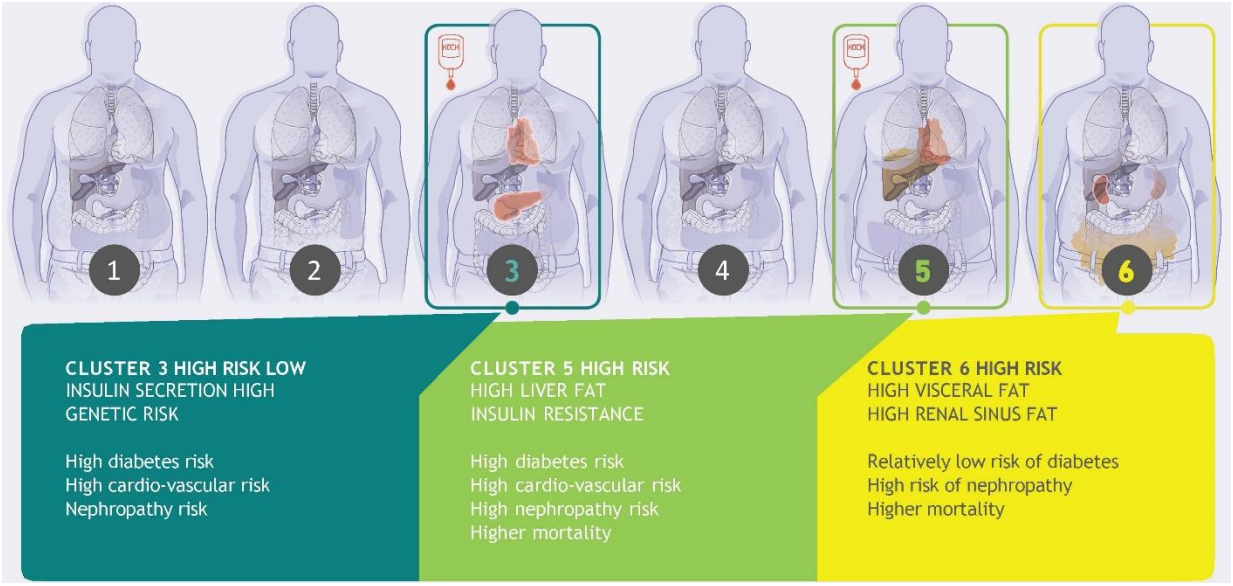

Fig. 1 | Classification of six prediabetes subclusters. Differentiation of subtypes based on disease progression, T2DM risk and the development of complications. Participants of clusters 1, 2 and 4 exhibit a reduced risk of T2DM, while subtypes 3 and 5 are more prone to developing T2DM. Participants in cluster 6 have a low risk of diabetes, but due to an elevated fat mass, they are already diagnosed with damaged kidneys before the onset of T2DM. Figure reproduced with permission of the Institute for Diabetes Research and Metabolic Diseases (IDM) and German Center for Diabetes Research (DZD) [26, 27].

1.2 Obesity and inflammation

Today, obesity is widely accepted to cause chronic mild inflammation, which serves as a key factor in the progression of obesity and related comorbidities. Inflammation is a sequential process aimed at restoring tissue and organ homeostasis to their native condition [28]. Moreover, inflammation is crucial for tissue protection against injury or damage, facilitating the removal or dilution of harmful substances and damaged tissue [29] – a described mechanism involved in bone fracture healing. However, in cases of unmanaged obesity, prolonged pro-inflammatory responses hinder tissue repair. In this regard, excessive AT expansion is believed to lie at the root of chronic inflammation associated with obesity. This expansion leads to the infiltration of immune cells into both AT and the liver, contributing to the development of pro-inflammation and nonalcoholic steatohepatitis (NASH), which is a major risk factor for T2DM-associated complications [30]. Therefore, this study postulates that the heightened inflammation extends to tissues beyond the liver, including the bone, and disrupts homeostasis and regenerative processes.

1.2.1 Crosstalk between adipose tissue and immune cells in obesity

Adipose tissue represents the interface between diet, metabolism and immune system, while AT inflammation is proposed as underlying cause for metabolic complications and comorbidities in obesity [31]. Adipocytes, the primary cellular component of adipose tissue, consist of two subtypes: white and brown adipocytes [32]. White AT (WAT) stores energy reserves as triglycerides, whereas brown AT (BAT) processes excessive fat to provide heat [33]. Particularly, accumulation and imbalanced distribution of WAT mass, especially in the visceral compartment, in obese individuals triggers metabolic dysregulation by increasing glucose intolerance and insulin resistance [34, 35]. According to the portal theory, metabolites secreted from visceral WAT and released into the portal vein, contribute to hepatic fat accumulation and further impair insulin function [36]. Strikingly, AT is an active and dynamic organ with endocrine functions, secreting various adipocytokines such as leptin, resistin, adiponectin, tumor necrosis factor alpha (TNF-α), interferon gamma (IFN-γ), interleukin (IL)-1, IL-6 and IL-8 [37]. Thus, a dysregulated production of AT molecules impacts metabolic and immunological responses. Mild pro-inflammation in obesity is strongly linked to expanded adipocytes, resulting in increased AT and the release of adipocytokines. These changes contribute to severe pathophysiological alterations [38].

1.2.2 Innate immunity and the function in obesity

Next to adipocytes, the AT consists of a stromal vascular structure that harbors fibroblasts, endothelial cells as well as innate and adaptive immune cells [39]. In fact, innate immune cells such as macrophages and neutrophils are required for the initial non-specific defense against invading microorganisms, viruses, parasites and toxins, or for the detection of wounds and trauma [40]. However, in obesity, enlarged adipocytes lead to pathological macrophage infiltration, leading to inflammation. One underlying mechanism is the increased distance between AT vasculature and cells, causing hypoxia and fibrosis [32]. These spatial changes activate tissue-resident and invading macrophages, promoting inflammation through the engulfment of necrotic adipocytes.

The switch of macrophages induced by obesity is a characteristic feature of AT inflammation and is dependent on external stimuli from adipocytes: macrophages can be polarized into either the classical macrophage (M1) or the alternative M2 subtype [41]. The M1 phenotype is associated with pro-inflammatory responses, producing TNF-α, IL-1β and IL-6 [32], thereby contributing to the progression of obesity. In contrast, M2 macrophages dominate in the AT of lean individuals [42] and are primarily involved in tissue remodeling and the resolution of inflammation [43].

Nonetheless, the mechanisms that lead to macrophage infiltration are still not completely understood [44]. Hypoxia is one factor that can trigger this process, but other potential triggers include

lipotoxicity resulting from hypertrophic adipocytes, signaling of reactive oxygen species (ROS), endoplasmic reticulum (ER) stress, or activation of innate toll-like receptors (TLRs) by free fatty acids [45]. These combinatorial signaling events likely exacerbate the production of chemokines by adipocytes or AT leukocytes, leading to the attraction of immune cells. Additionally, co-stimulatory signals may activate resident leukocytes to secrete cytokines and chemokines, further contributing to the inflammatory response.

1.2.3 Adaptive immunity and the role of T lymphocytes in obesity

Initially, the research on obesity and T2DM primarily emphasized M1 macrophages and innate immune functions. However, recent studies have highlighted the pathological involvement of adaptive immunity, specifically T lymphocytes, in contributing to metabolic disturbances [46].

Contrary to innate immune responses, adaptive immune cells recognize antigens with high specificity, allowing for a targeted and strategic immune action. They complement innate immunity by boosting immune responses when the innate system is insufficient to eliminate infections [47]. Conversely, adaptive immune responses are slower after first antigen encounter, but longer lasting. T and B lymphocytes, the two subtypes of adaptive immune cells, originate from the hematopoietic stem cells (HSCs) in the bone marrow (BM). B cells further develop in the bone marrow, while T cells mature in the thymus. Rearrangement of the antigen receptor on B and T cells during development, contributes to the high biological variability, immune repertoire and the formation of an immunological memory, enabling an immediate response upon subsequent encounters with the antigen. Antigen-presenting cells (APCs), such as dendritic cells (DCs), assist in the adaptive immune response by organizing and transferring antigens through the major histocompatibility complex (MHC) for interaction with the antigen receptor on B or T cells. The sequence of events aims to confer a B cell-mediated humoral response by antibodies, whereas T lymphocytes provide cellular immunity.

Defects in either of the two immune systems, can unleash inadequate inflammation and worsen disease conditions. In obesity, T cells infiltrate AT in parallel with macrophages and in this scenario, macrophage activation is affected by T cells [48]. However, the specific antigens in AT that are recognized by T cells have yet to be discovered.

As obesity develops and manifests, the proportions of different T cell phenotypes undergo drastic changes. T cells are classically distinguished based on their membrane antigen-specific T cell receptor, which consists of highly variable αβ- or γδ-chains in complex with the cluster of differentiation 3 (CD3)-chain [49]. The majority of T cells bear the αβ-receptor and co-express CD4 or CD8. Naïve $CD4^+$ and $CD8^+$ T cells undergo maturation in the thymus, where recently developed CD4 or

CD8 single positive T cells are selected based on their antigen recognition capabilities. Upon encountering the respective antigen in the periphery, activated T cells differentiate and undergo clonal expansion. According to a specific cytokine profile, $CD4^+$ T cells are further subdivided into Thelper (Th) subsets. Th1 cells express the master transcription factor Tbet (T-box expressed in T cells) and the cytokine IFN-γ. Th2 cells are identified by the expression of GATA3 (guanine-adenine-thymine-adenine binding protein 3) and the secretion of IL-4 and IL-13. Th17 cells are characterized by the expression of RORγt (regulator retinoid acid-related orphan receptor γt) and the cytokine IL-17. Th9 cells release IL-9 and Th22 cells express the aryl hydrocarbon receptor (AHR) and are the main source for IL-22. Follicular Th cells (Tfh) express the signature transcription factor Bcl-6 and the cytokine IL-21. Induced regulatory T cells (iT_{reg}) are another cellular subset of $CD4^+$ T cells, which develop extrathymically in the periphery expressing CD25 and the transcription factor FoxP3 (factor forkhead box P3). Those Treg cells exert their suppressive function by producing cytokines such as IL-10 and transforming growth factor-β (TGF-β).

Obese human and mouse studies demonstrated an increased infiltration of T cells in AT [50], leading to an altered balance between pro- and anti-inflammatory T cell responses. Obesity promotes the development of pro-inflammatory Th1 and Th17 cells, which are stimulated by IFN-γ, IL-12 and IL-6, and associated with M1 responses. Th1 cells are typically crucial for clearing infections and intracellular pathogens. But in the context of obesity, Th1 cells are implicated in metabolic dysfunction and increased BMI [51]. Th17 cells are widely acknowledged to participate in host defense against fungal and bacterial infections, as well as in the pathologies of autoimmune and metabolic disorders [52-54]. Obesity research showed that Th17 cells contribute to AT infiltration, inflammation and hyperglycemia [52]. Contrary, the frequency of anti-inflammatory Th2 and Treg cells is decreased in obese AT [55], leading to aggravated inflammation. This lack of immunosuppressive mechanisms disrupts immune homeostasis and allows for excessive immune reactions to occur.

Obese individuals are also described to have a predominance of pro-inflammatory $CD8^+$ T cells [56]. Cytotoxic $CD8^+$ T cells typically recognize and remove damaged or dysfunctional cells. However, in obesity, $CD8^+$ T cells are observed to infiltrate AT prior to macrophage infiltration, leading to the initiation and propagation of tissue inflammation *in vivo* [50, 57]. This suggests that $CD8^+$ T cells play an important role in promoting inflammation in AT in the context of obesity.

Unlike conventional αβ T cells, γδ T cells are poorly understood innate-like lymphocytes known for their role in tissue surveillance through the recognition of stress-induced self-antigens or damage-associated molecules [58]. *In vivo* studies have shown an increased presence of γδ T cells in AT, promoting macrophage recruitment and contributing to inflammation [59, 60].

Adaptive immune cells, particularly T cells, have an essential role in launching and maintaining inflammatory responses locally, which can progress to chronic and systemic inflammation. This dysregulated process can affect various tissues, including bone, and can alter cellular programs. Understanding the T cell function is essential for developing new therapeutic approaches to address obesity and its associated disorders.

1.3 Bone fracture repair and its association with obesity

The acute inflammatory phase at the onset of bone fracture healing is essential to initiate regenerative processes, however increased pro-inflammation delays bone repair. Bone tissue itself is a natural composite and protective casing for internal organs, which provides mechanical strength, fracture toughness and load-bearing properties to enable movement [61]. Next to the structural function, bone has an endocrine role, globally supplies minerals (particularly calcium and phosphate), and regulates nutrient homeostasis interlinking with metabolic processes [62].

The dynamic bone tissue undergoes constant remodeling to meet the body's requirements and possesses a unique ability to self-repair. Unlike other tissues and organs, it can transform injured parts back to their original form and function without fibrotic scarring [63]. This mechanism is warranted by the bone's exclusive structure and microenvironment.

1.3.1 Physiology and microenvironment of long bones

Besides flat bones for example formed in scull and pelvis, long bones such as the femur belong to one of the different bone types in the human body (Fig. 2, V). Lamellar and cancellous (trabecular) bone are the dominant structural components of mature bone (Fig. 2, IV) [64]. Peripheral cortical bone is characterized by its lamellar shape and possesses high mechanical strength. In contrast, trabecular bone has low mechanical properties due to its light and porous structure. However, the spongy bone compartment serves multiple functions, including providing space for blood vessels and bone marrow, as well as directing and distributing multidirectional forces during locomotion [64]. The periosteum encloses the outer layer of the bone and contains osteogenic (progenitor) cells and fibrous tissue, playing a pivotal role in tissue expansion and contributing to bone growth and repair [65]. Moreover, osteons, which are cylindrical structures within the cortical part of bone, serve as functional units where nerve fibers and blood vessels integrate in the Haversian system (Fig. 2, III) [66].

Both bone structures provide a niche for specialized cell types, primarily composed of HSCs, mesenchymal stroma cells (MSCs), and the main cell types involved in bone formation and remodel-

ing, including osteoblasts, osteoclasts, and osteocytes [67, 68]. HSCs control the vascularization and formation of immune cell and osteoclasts [68]. Alongside adipocytes and chondrocytes, osteoblasts derive from the mesenchymal lineage and are responsible for tissue homeostasis and defect repair, together with osteocytes that differentiate from osteoblasts.

Osteoblasts are bone-forming cells and develop organic elements of the extracellular matrix (ECM) such as osteocalcin and collagen type I (Col1) (Fig. 2, III) [69]. Stimulation of MSCs by members of the bone morphogenic proteins (BMPs) or Wingless and Int-1 (Wnt) family drives osteoblast development and during early differentiation, runt-related transcription factor 2 (RUNX2) belongs to the signature transcription factor. Osteoblasts localize on the bone surface and can transform into osteocytes or resting bone-lining cells which become reactivated.

Osteocytes reside within the bone matrix in spaces called lacunae (Fig. 2, III) and account for 90-95 % of the cells in the bone [70]. This cellular type is incapable of dividing, but is long-lasting and orchestrates important bone functions as sensors for mechanical loading. Hence, osteocytes regulate osteoblast and osteoclast activity by producing a variety of proteins such as osteocyte-specific sclerostin and dentin matrix protein-1 (DMP-1), as well as cathepsin K, receptor activator of nuclear factor (NF)-κB ligand (RANKL) and osteoprotegerin (OPG). Although osteocytes are crucial in the skeletal system, the mechanisms underlying their formation are still not fully understood.

Contrary to osteoblasts, osteoclasts are large multinucleated bone-resorbing cells of monocyte/macrophage origin (Fig. 2, III) [71]. The lytic function of osteoclasts is predominantly conferred by cathepsin K, a highly potent collagenase, on the bone surface [72]. RANKL, macrophage colony-stimulating factor (M-CSF) and TNF cytokines conduct osteoclast differentiation. However, osteoclast formation is strongly regulated by the RANKL/RANK/OPG axis. Osteoblasts and stromal cell release RANKL, which binds to its corresponding receptor RANK on osteoclasts. On the other hand, OPG, also expressed by osteoblasts and stromal stem cells, prevents the interaction between RANKL and RANK by capturing RANKL. This protective mechanism helps to block excessive bone degradation [73]. Thus, the balance of RANKL and OPG determines bone mass under healthy and disease conditions.

On a micro to nano scale, the bone is composed of extracellular matrix (ECM), which is calcified to provide bone strength and ductility at the same time (Fig. 2, II) [64]. The ECM consists of collagen fibers, which contain triple helical chains that give rise to collagen fibrils (Fig. 2, I). More than 20 different fibrillar and non-fibrillar collagen types have been identified, while Col1 belongs the most abundant protein in bone. The mineral component of the ECM contains hydroxyapatite (HAP) crystals with calcium and phosphate as principal ions linked to collagen [66]. The process is mediated by osteoblasts and is indicated by alkaline phosphatase (ALP) activity, which leads to elevated phosphate levels [74]. When unmineralized, the matrix is referred to as osteoid.

The ECM additionally contains non-collagenous proteins (NCPs), including osteocalcin, osteonectin, osteopontin, bone sialoprotein (BSP), adhesion proteins such as fibronectin and laminin as well as proteoglycans such as decorin (Fig. 2, I) [64]. The regulation and crosstalk between cells are also influenced through cell-matrix interactions or the presence of secreted biomolecules [66]. The ECM commonly serves as a reservoir for cytokines, hormones and growth factors, facilitating their signaling and function.

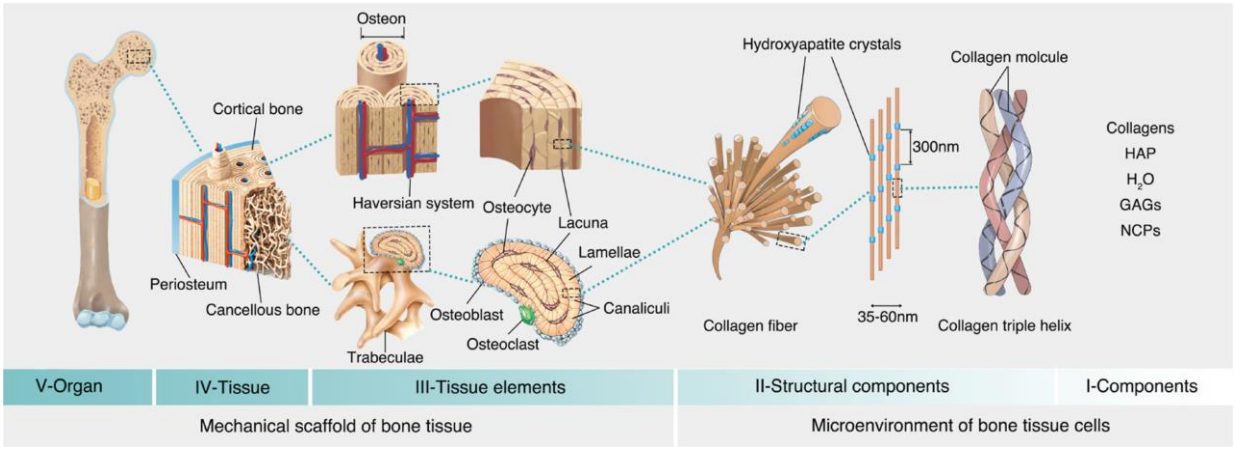

Fig. 2 | Macroscopic-to-microscopic view of the long bone structure. Mechanical and functional properties of long bones (V) are provided by cortical and cancellous (trabecular) tissue (IV). Concentric osteon units lie in the cortical compartment surrounded by lamellae and contain blood vessels and nerve tissue, which are organized as Harvasian canals (III). The bone marrow fills the cavities of cancellous bone. Osteoblasts, osteoclasts and osteocytes account for the predominant bone tissue cells regulating bone homeostasis, formation and degradation. The bone microenvironment and ECM primarily contain collagen fibers that consist of self-assembled collagen triple helices and arrange as collagen fibrils (II). Characteristic for bone ECM is also the abundance of hydroxyapatite (HAP) minerals, proteoglycans with gycosaminoglycan (GAG) side chains, and non-collagenous proteins, as well as water (H_2O) (I). Therefore, the complex structure regulates cellular interaction and contains essential biomolecules. Figure taken from Zhu et al., 2021 [66] and reproduced with permission from KeAi Communications Co., Ltd.

1.3.2 Stages of fracture healing

The preservation of the skeletal system is a prerequisite for the body's protection and support. Consequently, it is crucial to have a system in place that ensures the durability of bones by initiating healing processes after fractures while simultaneously preventing scar formation. Fractures of long bones, which involve damage to trabecular and cortical bone, undergo a process called endochondral ossification to restore the pre-injury structure and function. This process involves the formation of a cartilage template by chondrocytes, which subsequently matures into bone [75]. Whereas defects of the periost and neighboring soft tissue heal through intramembranous ossification, which directly converts mesenchymal tissue into bone [76].

The series of biologic events in bone regeneration follows a specific temporal and spatial sequence coordinating (I) the initial inflammatory response, (II) soft and (III) hard callus formation

as well as (IV) bone remodeling [77]. Upon a bone fracture, ruptured blood vessels around and within the bone lead to hematoma formation, facilitating the infiltration of immune cells and triggering an acute pro-inflammatory response [78]. The coagulation of fibrin generates a provisional matrix, and macrophages are among the first immune cells to invade the fracture site [66]. Together with neutrophils, macrophages remove cell debris and dead cells. Inside the injury, M1 macrophages and other immune cells release inflammatory mediators, such as IL-1, IL-6 and TNF-α, to increase inflammation for the recruitment of immune cells, such as lymphocytes [66, 77]. This stage also promotes neovascularization by endothelial cells, which are attracted through the vascular endothelial growth factor (VEGF) expressed by osteoblasts. The fracture defect is further stabilized by invading fibroblasts and MSCs, which proliferate and differentiate [66]. Platelets of the hematoma produce platelet-derived growth factor (PDGF) and TGF-β1 whereby MSCs, fibroblasts, osteoblasts and endothelial cells infiltrate. Hypoxic conditions further stimulate revascularization by upregulating the transcription factor hypoxia-inducible factor-1 α (HIF-1 α) in osteoblasts and endothelial cells, leading to the release of vascular stimulators such as VEGF and angiopoietin-1 [79].

The increased formation of blood vessels enables the invasion of diverse cells and the replacement of the fibrin clot with granulation tissue [80]. During the resolution of the hypoxic environment, macrophages polarize from the pro-inflammatory M1 to the anti-inflammatory M2 phenotype. Dilution of inflammation is primarily mediated by cytokines such as IL-4, IL-10 and TGF-β. This stage of healing transitions from catabolic to anabolic processes. The phase is dominated by fibroblasts, chondrocytes and osteoblasts as well as osteoprogenitor cells and MSCs [66]. Fibroblasts transform the granulation to fibrous tissue, which provides mechanical strength. The connective tissue primarily consists Col3, which serves as a template for bone deposition [81].

Chondrocytes, derived from MSCs, induce the maturation of the fiber-rich tissue into a soft callus rich in fibrocartilage and hyaline cartilage, resulting in hypertrophy and the formation of a mineralized matrix. As bone healing proceeds, the early soft callus largely contains Col2 and proteoglycans, which are gradually replaced by Col10 [66]. Mature chondrocytes either become apoptotic or differentiate into osteoblast-like cells, which together with osteoblasts deposit Col1 and contribute to ECM mineralization [81]. The established woven bone evolves into hard callus and during the remodeling phase, lamellar bone is organized according to the mechanical load [78].

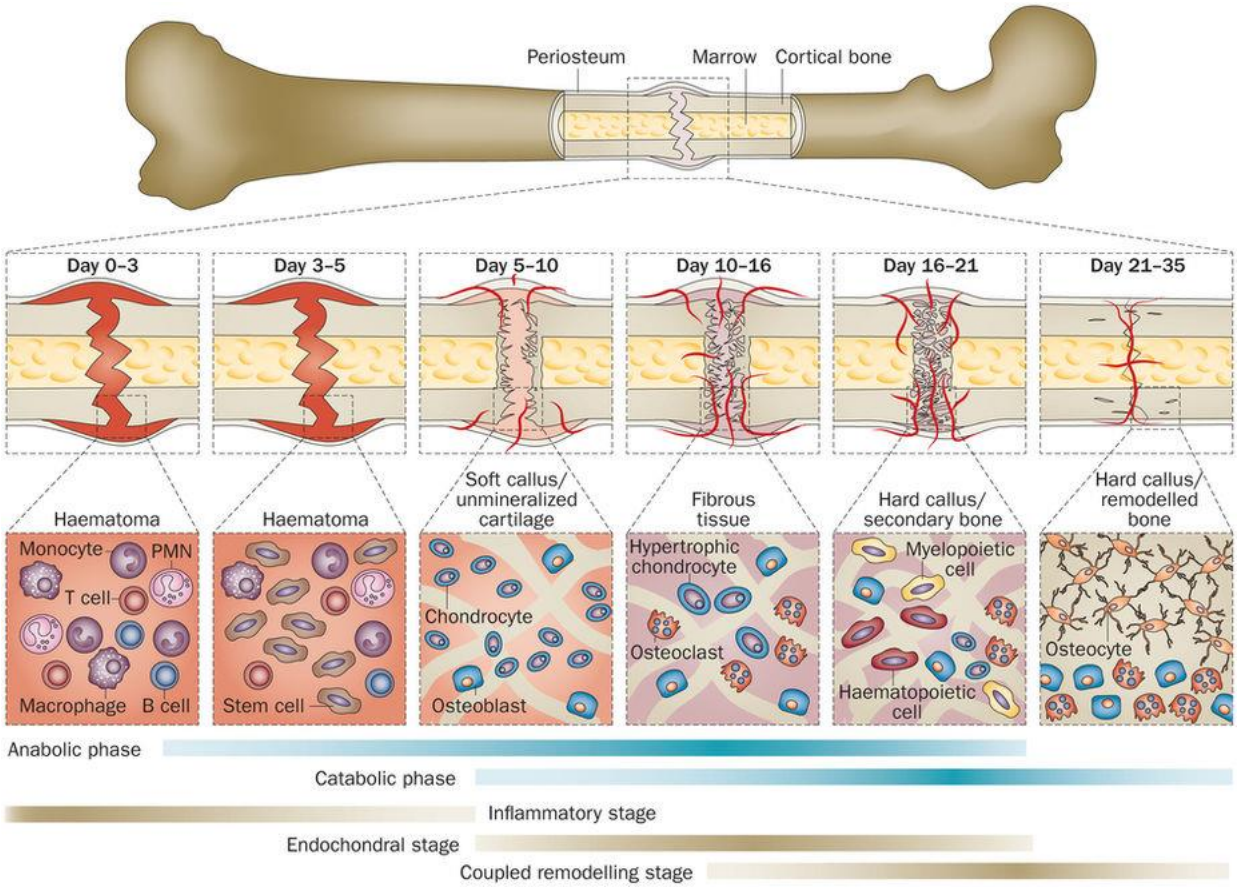

Fig. 3 | Phases of femoral fracture healing. (I) Bone repair is initiated by hematoma formation, starting with a pro-inflammatory phase that is replaced by an anti-inflammatory phase. Polymorphonuclear leukocytes (PMN) such as neutrophils as well as macrophages and lymphocyte reside to the injured area via autocrine and paracrine signaling. Recruitment of platelets and endothelial cells also paves the way for angiogenesis. (II) In the subsequent stage, chondrocytes constitute the fibrocartilage tissue, which stabilizes the bone defect. (III) In the process of endochondral ossification, osteoblasts replace the cartilage with mineralized tissue. (IV) The structure and function of the newly formed bone ultimately undergoes remodeling. Figure taken from Einhorn and Gerstenfeld, 2014 and reproduced with permission from Springer Nature (license number: 5462980989682) [77].

1.3.3 Interdependence of immunity and bone in health and disease

In recent years, bone homeostasis and regeneration has been discovered under the lenses of immunology [82]. The local proximity of immunity and bone marrow, which stores T and B cell precursors next to matured memory lymphocytes, implies a strong interplay between both the skeletal and immune system. The interaction represents an intriguing aspect and it is evident that the two systems are co-regulated by many shared cytokines and signaling molecules. The discovery of the RANKL/RANK axis has resulted in a paradigm shift, as RANKL signaling was initially implicated in immunity, promoting the survival and activation of dendritic cells expressing RANK through the regulation of T cells producing RANKL [83].

Regarding adaptive immunity, T and B cells are present within the early callus during the inflammatory phase [84]. After withdrawal from the fracture site, a second wave of T and B cells infiltrates, which are present at sites of mineralization and in direct contact with osteoblasts and osteoclasts. Thus, the identified interaction suggests a regulatory role of the adaptive immunity in fracture healing.

Although initial and transient inflammation are fundamental for adequate bone repair, prolonged immune reactions are adverse to fracture healing. The aspect of impaired healing preferentially occurring in obese and aged individuals is even more interesting as the clinical courses of bone regeneration in elderly and obesity are highly dependent on the experienced adaptive immunity. In an *in vivo* obesity study, immune-aged mice were generated by subjecting the animals to constant antigen exchange with their non-specific-pathogen free (non-SPF) surrounding, leading to increased numbers of effector T cells in mice fed a high-fat diet (HFD) compared to lean mice [30]. This observation was accompanied by the development of liver pathology resembling NASH. These effects were more pronounced in obese mice under conventional non-SPF conditions, while obese mice housed in the SPF husbandry maintained a more naïve adaptive immune system and exhibited reduced severity of the liver pathology. This finding highlights the crucial role of the experienced adaptive immunity in exacerbating disease conditions, as observed in elderly individuals.

These obesity-associated modifications strongly interlink with the concept of an 'aged' adaptive immune system, commonly referred to as inflamm-aging. This process contributes to increased immunological changes and plays a notable role in the context of fracture healing [85]. The adaptive immune system steadily alters during aging as a result of the lifelong repetitive antigen exposure. Thereby, the inexperienced immunophenotype diminishes in elderly by shifting the naïve T lymphocyte pool with a huge polyclonal repertoire of antigen receptors towards an experienced (memory) T lymphocyte system with a restricted T cell repertoire [86-88]. Increasing evidence now points to effector/memory T cells that are detrimental to bone healing and disturbing the balance between bone resorption and formation [88-90]. Certain subpopulations express tissue-homing receptors enabling them to migrate to inflamed non-immune tissue sites through an activated endothelial layer, even without targeting specific antigens [91]. These cells are characterized by strong hypersensitivity to inflammatory signals, the associated bystander responsiveness and cytokine memory [91, 92]. Moreover, 'aged' effector T cells produce higher amounts of effector cytokines, like TNF-α and IFN-γ, establishing a pro-inflammatory milieu [91] and interfering with osteoblast and osteoclast differentiation [88, 93-95]. A tissue-resident population of memory T cells is also capable of translocating to the bone marrow and remaining in a preactivated inflammatory resting state [96]. Thus, these cells are likely to influence the healing process in close proximity to the fracture gap.

Interestingly, delayed bone fracture healing in a sheep model revealed a prolonged pro-inflammatory reaction characterized by higher levels of $CD8^+$ T cells and an impairment in angiogenic processes [89]. In parallel, clinical studies manifested an association to enhanced levels of terminally differentiated $CD8^+$ effector memory T cells expressing $CD45RA^+$ (termed TEMRA) in blood and fracture hematoma of patients suffering from impaired bone healing [88]. In turn, targeting $CD8^+$ T cells through depletion enhanced bone repair in immune-experienced mice, whereas a transfer of these cells diminished the healing outcome.

One aspect of particular importance is the contribution of T cells to collagen formation by osteoblasts, thus defining the structure of newly formed bone tissue. A study using mice that lack mature lymphocytes ($RAG1^{-/-}$) or T cells ($TCR\beta\delta^{-/-}$) revealed an earlier onset of bone formation [97]. However, the mutant phenotypes underlay severe dysregulation in collagen deposition and osteoblast migration. As recovery of mice without functional B lymphocytes ($JHT^{-/-}$) resembled the wildtype characteristics, the investigations identified a direct link between immune cells and matrix formation that is correlated with T cells rather than B cells.

However, the specific contributions of different T cell subpopulations to the bone regeneration process, such as mobilization and differentiation of MSCs and osteoblasts are largely unknown [88]. Building on the work of El Khassawna et al. (2017) [97], the project will address the influence of the adaptive immunity on the early healing phases to elucidate the interdependency of T cells, osteogenic precursors and matrix formation under compromised conditions.

1.3.4 The impact of obesity on bone health and repair

Bone fracture repair in diabetics is described to be prolonged by 87 % [98], leading to healing complications such as delayed repair or non-unions [99]. The interplay between obesity and bone is multifactorial, including mechanical and biochemical aspects. However, the linked mechanisms are not yet fully understood. Traditionally, obesity is described to not affect or to even increase bone mineral density (BMD), and thus high BMD levels that correlate with high BMI provide protective effects and lower fracture risk [100, 101]. Nonetheless, obesity studies revealed an attenuated risk for particular fractures but an elevated risk for others [102, 103]. In this regard, the increased BMI site-specifically alters the mechanical load and consequently leads to an inefficiently distributed microarchitecture characterized by diminished cortical and increased trabecular bone mass [104].

Another factor contributing to bone quality in obese individuals is the elevated presence of advanced glycation end-products (AGEs) within the skeletal structure [105]. The mechanism underlying this involves Col1, the primary protein component in bone, which provides a structural

framework. The formation of Col1 fibrils is normally stabilized through enzymatic cross-linking. However, in obese and T2DM patients, the presence of excess sugars in the blood leads to additional post-translational modifications, chemically cross-linking collagen fibrils [105, 106]. The accumulation of these AGEs in bone decreases bone biomechanical properties, primarily attributed to increased material stiffness and reduced ductility [105].

Given that angiopathy in obesity-associated T2DM affects the vasculature and results in inadequate blood supply during bone regeneration, it should be recognized as an additional factor that contributes to complications in the healing process [107].

Growing evidence has emerged suggesting that the use of glucose-lowering agents, such as thiazolidinediones (TZDs), may be associated with an increased risk of fractures, regardless of the course of diabetes [108]. Studies have shown that TZDs stimulate peroxisome proliferator-activated receptor gamma (PPARγ) which activates adipogenesis at the expense of osteogenesis [105, 109]. To this regard, obesity additionally shifts differentiation of MSCs in favor of bone marrow adiposity *in vivo* [110, 111]. Factors, such as adiponectin, visfatin, omentin-1 and RANKL, secreted by bone marrow adipose tissue (BMAT) negatively influence hematopoiesis and bone remodeling [111-116]. In addition, the resistance to leptin and irisin observed in obesity can negatively impact bone mass and strength [114, 116, 117].

Of particular importance, however, is the systemic inflammation associated with obesity, which has detrimental effects on bone regeneration by altering the differentiation of osteogenic cells and bone turnover. In obesity, the pro-inflammatory cytokine TNF-α reduces the number of osteoblasts by increasing apoptosis through the upregulation of proapoptotic genes. This results in decreased osteoblast activity, as indicated by reduced levels of osteocalcin, a protein hormone that is exclusively expressed by osteoblasts and plays a role in bone anabolism [118, 119]. Within the bone-pancreas endocrine loop, insulin exerts direct effects on osteoblasts, including promoting their proliferation, reducing apoptosis and stimulating glucose uptake [120]. Nonetheless, the paradox of increased insulin levels in obesity is hindered by cellular insulin resistance and reduced insulin activity, which is predominantly attributed to elevated plasma free fatty acids (FFAs) observed in both obese individuals and rodents [23]. Consequently, chronically increased FFA levels prolong bone resorption mediated by osteoclasts by increasing the RANKL:OPG-ratio and levels of TNF-α and M-CSF [121-123].

Another aspect to consider is the impact of hyperglycemia-induced reactive oxygen species (ROS) production on long-term bone health [124]. It leads to the upregulation of RANKL expression, enhanced osteoclastogenesis and inhibition of antioxidant defenses. These effects are particularly detrimental to long-lived cells such as osteocytes and MSCs.

In conclusion, the unique bone characteristics observed in individuals with obesity and T2DM may contribute to the emergence of a novel syndrome linked to bone disease. Understanding the T cell signaling network and the impact of secretory factors on the bone microenvironment is crucial in the context of metabolic complications. Furthermore, gaining insights into the mechanisms involved in resolving inflammation is essential for mitigating excessive bone resorption.

1.4 Importance of intestinal microbiota in obesity and bone metabolism

Diet and nutritional intake are considered as the main drivers in shaping human health, particularly in the context of obesity. The nutritional value of food is determined by a person's gut microbial community (microbiota) and its corresponding genes (microbiome) [125]. However, another contributing factor is the host immune system that has co-evolved with the microbiota colonizing the body [126]. Hence, the intestinal microbiota plays a crucial role in maintaining a balance between immune activation and tolerance, as well as metabolic regulation – and vice versa. A disrupted interaction, known as dysbiosis, has gained attention in recent years due to its association with various metabolic and immune disorders in both animal models and humans. A study comparing the gut composition of lean, wildtype and obese mice revealed a positive correlation between the abundance ratio of the phyla Firmicutes:Bacteroidetes and the obese groups [127]. Interestingly, induction of a normal diet reversed these compositional changes, underlining the crucial contribution of diet to obesity-associated changes in the gut bacteria. In addition, HFD induces impaired gut permeability and increases the translocation of bacterial components from the gut to other tissues, thereby exacerbating pro-inflammation [128]. More recently, in clinical applications, the beneficial metabolic effects of fecal microbiota transplantation from lean donors to insulin-resistant subjects have highlighted the causal role of gut bacteria in metabolism [129].

Gut microbial flora also affects bone remodeling, bone mass accumulation and bone health by altering the host immune status [130]. Intestinal gut microbiota directly interact with the immune system that regulates the development of bone marrow cells and the cytokine profile. These microorganisms also drive Th17 T cell differentiation in the gut – a T helper cell subset responsible for bone resorption in rheumatoid arthritis. A study demonstrated that germ-free mice exhibited reduced levels of pro-inflammatory cytokines, lower numbers of $CD4^+$ T cells and decreased osteoclast/precursor cells in the bone marrow, resulting in increased trabecular and cortical bone volume [131]. In the context of obesity, Luo et al. (2015) [132] revealed that changes in the microbiota induced by HFD altered the bone marrow niche, leading to increased adiposity, impaired HSC reconstruction and suppressed osteoblastogenesis *in vivo*. Remarkably, the effects were transferred from obese to lean mice by stool transplantation, highlighting the role of intestinal microbiota in regulating bone homeostasis and potentially bone fracture healing.

However, our understanding of the impact of metabolic stress and gut microbiota changes on the bone microenvironment is still limited. Therefore, this study aimed to uncover microbial signatures in obesity that are linked to disease progression and bone properties.

1.5 Immunomodulation as possible novel therapeutic approach in bone regeneration

Growing evidence highlighting the interplay between inflamm-aging and impaired regenerative capacity in bone fracture healing offers valuable insights for developing immunomodulatory strategies tailored to the patient's immune status [133]. Accelerating bone fracture healing through therapeutic treatments could be achieved by modulating immune cells or effector molecules that impair regeneration, or strengthening immune cells that facilitate healing. Cellular therapies aimed at enhancing regulatory T cell functions or promoting the polarization of macrophages towards an M2 phenotype, which exhibit anti-inflammatory and immunosuppressive effects, are particularly intriguing in this regard [133, 134]. Targeting pro-inflammatory $CD8^+$ T cells through depletion has shown improvement in the healing outcomes – but it is not clinically feasible [88]. The role of pro-inflammatory signals, including TNF-α and IL-1, in the impairment of bone fracture healing emphasizes the importance of controlling inflammation through modulation [135]. However, the precise effects of immunotherapeutic strategies on bone regeneration, whether beneficial or potentially detrimental, remain unclear and require further investigation.

Mounting evidence highlights the contribution of immune dysfunction in obesity and reveals areas of overlap to immune modulation as a useful tool to treat impaired bone fracture healing. Overcoming metabolic inflammation and improving islet β-cell function, as well as metabolic control are the major challenges in developing preventive or therapeutic approaches [136]. Treatment of T2DM patients usually starts with metformin and/or sulfonylurea therapy, but patients often show an insufficient response to those oral agents [137]. Specifically targeting T and B cells through antibody therapy has demonstrated clinical efficacy in treating islet autoimmunity associated with T1DM and diet-induced obese mice [138-140]. Given the role of T cell and macrophage infiltration in AT as a cause of obesity and T2DM, targeted immune modulation could be a promising approach for future therapies. Specifically, blockade of IL-1β or its receptor in clinical trials has effectively normalized metabolic control in individuals with T2DM, while therapeutic agents targeting TNF-α have shown limited efficacy in T2DM treatment [137, 141].

The findings indicate that targeting pro-inflammatory signals and reducing tissue-specific T cell responses can improve impaired bone fracture healing and obesity/T2DM. To develop precision interventions, a comprehensive understanding of bone regeneration at the molecular, cellular and tissue levels in the context of metabolic dysfunction is essential.

1.6 Objectives of this work

It is well-established that obesity-associated type 2 diabetes mellitus (T2DM) is considered a risk factor for bone healing complications leading to malunions and nonunions. This poses ongoing challenges in orthopedic practice. However, even in the early stages of metabolic disturbances, such as those observed in obesity, delayed fracture healing can occur. Chronic low-grade inflammation, particularly involving the adaptive immunity, is recognized as a major contributing factor in the development and progression of obesity-related complications, including impaired bone fracture healing. Despite the high obesity prevalence, research on the relationship between obesity, inflammation and bone repair remains largely understudied.

Therefore, the underlying hypothesis of this work is that increased pro-inflammation associated with obesity is causative for delayed bone repair. The specific objectives of this study are twofold: first, to investigate the extent to which obesity modulates the adaptive immune responses and its impact on bone fracture healing, considering both short-term and long-term obesity effects, which reflect the onset and persistence of the condition. The second objective is to assess the potential for reversing the obesity-mediated changes through immunomodulation to improve bone repair. Additionally, given the well-established role of the microbiome in obesity development and its close connection to adaptive immunity and metabolic inflammation, an investigation of the gut microbiome will explore potential pathological changes in bacterial composition in the context of immune-related changes of bone fracture healing.

To investigate these aspects, a mouse model of diet-induced obesity in conjunction with femoral osteotomy is employed. Obese mice are categorized into groups based on their responses in metabolic tests. The study includes the analysis of immune system changes at both cellular and functional levels using flow cytometry and single-cell RNA sequencing, in addition to identifying inflammatory cues through cytokine profiling. The callus formation and composition are evaluated through micro-computed X-ray tomography, histological assessment and RNA sequencing. The microbial composition is additionally assessed through 16S rRNA gene tag sequencing.

By examining the combined effects of immune responses and bone regeneration in diet-induced obesity and their relationship with the gut microbiota, the work addresses a crucial clinical need. The study provides insights for potential immunomodulatory treatment options that can be tailored to the individual's immune, metabolic and microbial profile.

2 Materials and methods

2.1 Materials

2.1.1 Chemicals, proteins and enzymes

Chemical or solution	Company
acetone	Merck KGaA, Darmstadt, Germany
acetic acid, glacial	Carl Roth GmbH + Co. KG, Karlsruhe, Germany
acid fuchsin	Waldeck GmbH & Co. KG, Münster, Germany
Alcian blue 8GX	Merck KGaA, Darmstadt, Germany
ammonia solution (NH_3), 25 %	Merck KGaA, Darmstadt, Germany
Ampuwa	Fresenius Kabi AG, Bad Homburg, Germany
Aquatex	Merck KGaA, Darmstadt, Germany
Brilliant Crocein R	Waldeck GmbH & Co. KG, Münster, Germany
bovine serum albumin (BSA), protease-free	Merck KGaA, Darmstadt, Germany
chloroform	VWR International, LLC, Radnor, USA
citric acid monohydrate	Honeywell International Inc, Morristown, USA
Dako Antibody Diluent	Agilent Technologies, Santa Clara, USA
4′, 6-diamidino-2-phenylindole dihydrochloride (DAPI)	Thermo Fisher Scientific Inc., Waltham, USA
eosin, 2 % (w/v)	Waldeck GmbH & Co. KG, Münster, Germany
ethanol (EtOH)	Carl Roth GmbH + Co. KG, Karlsruhe, Germany, VWR International, LLC, Radnor, USA
FcX blocking solution	Biolegend Inc., San Diego, USA
Fixable Live/Dead staining kit	Thermo Fisher Scientific Inc., Waltham, USA
Fluoromount G	SouthernBiotech Associates, Inc., Birmingham, USA
Papanicolaou's solution 1a Harris' hematoxylin solution	Merck KGaA, Darmstadt, Germany
n-hexane	Carl Roth GmbH + Co. KG, Karlsruhe, Germany
hyaluronidase, H3506	Merck KGaA, Darmstadt, Germany
hydrogen chloride (HCl), 1 N	Carl Roth GmbH + Co. KG, Karlsruhe, Germany
hydrophobic barrier PAP pen	Vector Laboratories, Inc., Newark, USA
ImmPACT Vector Red Substrate Kit, AP	Vector Laboratories, Inc., Newark, USA
Weigert's iron hematoxylin A	Waldeck GmbH & Co. KG, Münster, Germany

continued: ***Chemicals, proteins and enzymes***	
Weigert's iron hematoxylin B	Waldeck GmbH & Co. KG, Münster, Germany
Mayer's hemalum solution	Merck KGaA, Darmstadt, Germany
methyl green counterstain	Vector Laboratories, Inc., Newark, USA
normal goat serum	Vector Laboratories, Inc., Newark, USA
normal horse serum	Vector Laboratories, Inc., Newark, USA
normal rabbit serum	Vector Laboratories, Inc., Newark, USA
nuclease-free water (H_2O)	Qiagen, Venlo, Netherlands
Paraplast Plus	Leica Biosystems, Nussloch, Germany
pepsin, P7012	Merck KGaA, Darmstadt, Germany
phosphotungstic acid	Waldeck GmbH & Co. KG, Münster, Germany
phosphate-buffered saline (PBS) (1x), pH 7.4	Thermo Fisher Scientific Inc., Waltham, USA
PBS (10x), pH 7.2	Waldeck GmbH & Co. KG, Münster, Germany
paraformaldehyde (PFA), 16 %	Electron Microscopy Sciences, Hatfield, USA
red blood cell (RBC) lysis buffer	Biolegend Inc., San Diego, USA
RNase Away	VWR International, LLC, Radnor, USA
RNase Free DNase set	Qiagen, Venlo, Netherlands
RNeasy Mini Kit	Qiagen, Venlo, Netherlands
ROTI Histol, dewaxing agent	Carl Roth GmbH + Co. KG, Karlsruhe, Germany
Safran du Gâtinais	Waldeck GmbH & Co. KG, Münster, Germany
super cryoembedding medium (SCEM)	Section-Lab Co. Ltd., Hiroshima, Japan
SCMM-R2	Section-Lab Co. Ltd., Hiroshima, Japan
sodium azide	Merck KGaA, Darmstadt, Germany
sodium chloride	Merck KGaA, Darmstadt, Germany
sodium citrate dihydrate	Merck KGaA, Darmstadt, Germany
sucrose	commercially available
tissue Tek, OCT compound	Sakura Finetek USA, Inc., Torrance, USA
Transcription Factor Buffer Set	Biolegend Inc., San Diego, USA
Trizma base	Merck KGaA, Darmstadt, Germany
Trizma hydrochloride	Merck KGaA, Darmstadt, Germany
Triton X-100	Merck KGaA, Darmstadt, Germany
TRIzol	Thermo Fisher Scientific Inc., Waltham, USA
trypan blue	Thermo Fisher Scientific Inc., Waltham, USA
Vectamount Permanent Mounting Medium	Vector Laboratories, Inc., Newark, USA
Vectastain ABC-AP Kit	Vector Laboratories, Inc., Newark, USA
Vitro-Cloud	Langenbrinck GmbH, Emmendingen, Germany
xylene	J.T.Baker, Phillipsburg, USA

2.1.2 Buffers and solutions

Compound	Volume or amount
Flow cytometry (FC) buffer	**500 mL**
1xPBS, pH 7.4	500 mL
BSA	5.0 g
sodium azide	0.5 g
1xTris-buffered saline (TBS), pH 8.2	**1 L**
Trizma HCl	6.6 g
Trizma base	0.9 g
NaCl	8.78 g → ad 1 L with distilled H_2O
TBST, pH 8.2	**1L**
1xTBS, pH 8.2	1 L
Triton X-100	0.3 mL
citrate buffer, pH 6.0	**200 mL**
(1) solution A (0.1 M)	1 L
citric acid monohydrate	21.01 g → ad 1 L with distilled H_2O
(2) solution B (0.1 M)	1 L
sodium citrate dihydrate	29.41 g → ad 1 L with distilled H_2O
(3) final citric buffer, pH 6.0	200 mL
solution A	38 mL
solution B	162 mL
chromogen buffer, pH 8.2	**300 mL**
Trizma-HCl	3.96 g
Trizma base	0.54 g → ad 300 mL with distilled H_2O
NaCl	2.63 g
blocking solution with normal serum	**10 mL**
serum	0.5 mL
BSA	0.1 g
1xPBS	ad 10 mL
Brilliant Crocein-acid fuchsin solution	**500 mL**
(1) solution A	100 mL
Brilliant Crocein R	0.1 g
glacial acetic acid	0.5 mL → ad 100 mL with distilled H_2O

continued: ***Buffers and solutions***	
(2) solution B	100 mL
acid fuchsin	0.1 g
glacial acetic acid	0.5 mL → ad 100 mL with distilled H_2O
(3) final solution	500 mL
solution A	400 mL
solution B	100 mL
0.5 % (w/v) pepsin solution	**10 mL**
pepsin	50 mg
0.5 N HCl	ad 10 mL
0.15 % (w/v) hyaluronidase solution	**10 mL**
hyaluronidase	15 mg
1xTBS, pH 8.2	ad 10mL
0.2 % (v/v) eosin solution	**100 mL**
2 % (w/v) ready-to-use solution	10 mL
distilled H_2O	90 mL
glacial acetic acid	2 drops

2.1.3 Laboratory equipment

Product	Company
Basic laboratory material	
cell culture dish, 60 mm Ø	Corning, Inc., Corning, USA
cell strainer, 40 µm	Corning, Inc., Corning, USA
15 mL polypropolyne conical tube	Becton Dickinson Biosciences, Franklin Lakes, USA
50 mL polypropolyne conical tube	Becton Dickinson Biosciences, Franklin Lakes, USA
5 mL polystyrene round-bottom tube	Becton Dickinson Biosciences, Franklin Lakes, USA
syringe discardit II 2 mL	Becton Dickinson Biosciences, Franklin Lakes, USA
0.5 mL tube, protein lobind	Eppendorf SE, Hamburg, Germany
1.0 mL tube, protein lobind	Eppendorf SE, Hamburg, Germany
2.0 mL tube, protein lobind	Eppendorf SE, Hamburg, Germany
2.0 mL tube, DNA lobind	Eppendorf SE, Hamburg, Germany

continued: ***Laboratory equipment***	
Histology equipment	
Cryofilm 2C (16UF)	Section-Lab Co. Ltd., Hiroshima, Japan
microtome blades	Feather Safety Razor Co., Ltd, Osaka, Japan
object slide cover glass	Paul Marienfeld GmbH & Co. KG, Lauda-Königshofen, Germany
object slides, standard	Paul Marienfeld GmbH & Co. KG, Lauda-Königshofen, Germany
object slides, superfrost	Thermo Scientific Fisher, Waltham, MA, USA
Murine osteotomy and *in vivo* treatments	
Accu-Chek Guide glucose meter	Roche Holding AG, Basel, Switzerland
Accu-Chek Guide strips	Roche Holding AG, Basel, Switzerland
Bepanthen (+5 % Dexpanthenol)	Bayer Vital GmbH, Leverkusen, Germany
buprenorphine	RB Pharmaceuticals Ltd, Berkshire, UK
capillary tubes	Sarstedt AG & Co. KG, Nümbrecht, Germany
clindamycin	Ratiopharm GmbH, Ulm, Germany
external fixator MouseExFix	RISystem AG, Landquart, Switzerland
Gigli saw wire, 0.66 mm	RISystem AG, Landquart, Switzerland
glucose solution, 20 % (w/v)	B. Braun Melsungen AG, Melsungen, Germany
heparin tubes	Sarstedt AG & Co. KG, Nümbrecht, Germany
high-fat diet (60 kJ% from fat, 19 kJ% from proteins, 21 kJ% from carbohydrates)	Sniff Spezialitäten GmbH, Soest, Germany
Inject-F Tuberkulinspritze, 1 mL	B. Braun Melsungen AG, Melsungen, Germany
U100 Insulin Actrapid HM	Novo Nordisk, Bagsværd, Danmark
insulin syringe	Becton Dickinson Biosciences, Franklin Lakes, USA
InVivoMAb anti-mouse CD8α, clone 2.43	Bio X Cell, Lebanon, USA
isoflurane	Forene, Abott GmbH & Co. KG, Wiesbaden, Germany
ketamine	Actavis Switzerland AG, Regensdorf-Zürich, Switzerland
medetomidine	Janssen-Cilag GmbH, Neuss, Germany
Sterican cannula	B. Braun Melsungen AG, Melsungen, Germany
surture, Prolene	Ethicon, Norderstedt, Germany
sodium chloride, 0.9 % (w/v)	B. Braun Melsungen AG, Melsungen, Germany
tramadol, 100 mg/mL	Gruenenthal, Brunn am Gebirge, Austria

2.1.4 Antibodies and collagen hybridizing peptide (CHP)

Specificity	Clone	Label	Company
CD3e	145-2C11	BB700	Becton Dickinson Biosciences, Franklin Lakes, USA
CD3e	145-2C11	PE-Cy7	Biolegend Inc., San Diego, USA
CD4	GK1.5	APC/Fire750	Biolegend Inc., San Diego, USA
CD8α	53-6-7	BV785	Biolegend Inc., San Diego, USA
CD11b/Mac-1	M1/70	BV510	Biolegend Inc., San Diego, USA
CD11c	N418	PerCP/Cy5.5	Biolegend Inc., San Diego, USA
CD19	6D5	PE-Cy7	Biolegend Inc., San Diego, USA
CD25	PC61	PE-Dazzle594	Biolegend Inc., San Diego, USA
CD44	IM7	PE-Cy7	Biolegend Inc., San Diego, USA
CD45	30-F11	AF488	Biolegend Inc., San Diego, USA
CD45	30-F11	V500	Becton Dickinson Biosciences, Franklin Lakes, USA
CD62L	MEL-14	APC-R700	Biolegend Inc., San Diego, USA
CD80	16-10A1	BV650	Biolegend Inc., San Diego, USA
CD86	GL-1	BV421	Biolegend Inc., San Diego, USA
CD163	TNKUPJ	PE	Thermo Scientific Fisher, Waltham, MA, USA
CD206	C068C2	PE/Dazzle594	Biolegend Inc., San Diego, USA
CD335	29A1.4	PE-Cy7	Biolegend Inc., San Diego, USA
FoxP3	MF23	AF488	Becton Dickinson Biosciences, Franklin Lakes, USA
GATA3	L50-823	AF647	Becton Dickinson Biosciences, Franklin Lakes, USA
Ly6-G	1A8	APC/Fire750	Biolegend Inc., San Diego, USA
MHC class II	M5/114.15.2	BV785	Biolegend Inc., San Diego, USA
RORγt	Q31-378	PE	Becton Dickinson Biosciences, Franklin Lakes, USA
Tbet	Q4-46	BV650	Becton Dickinson Biosciences, Franklin Lakes, USA
TCRγδ	GL3	BV421	Biolegend Inc., San Diego, USA
VEGF	VG1	AF647	Novus Biologicals, LLC, Centennial, USA
CD31	n.a.	none	R & D Biosystems, Inc., Minneapolis, USA
CHP	none	Cy3	3Helix Inc, Salt Lake City, USA
Col1	n.a.	biotin	Abcam plc., Cambridge, UK
biotin	n.a	SA-AF568	Thermo Scientific Fisher, Waltham, MA, USA
insulin	EPR17359	w/o	Abcam plc., Cambridge, UK
goat α-rabbit IgG	n.a.	biotin	Vector Laboratories, Inc., Newark, USA
rabbit α-goat IgG	n.a.	biotin	Vector Laboratories, Inc., Newark, USA

2.1.5 Cell isolation, insulin and cytokine assay

Product	Company
EasySep Mouse T Cell Isolation Kit	Stemcell Technologies, Vancouver, Canada
LegendPlex Mouse T Helper Cytokine Panel	Biolegend Inc., San Diego, USA
Mouse/Rat Insulin Kit	Mesoscale Diagnostics, LLC, Rockville, USA

2.1.6 Technical devices

Device	Application	Provider
BZ-X810	fluorescence microscope	Keyence Corporation, Ōsaka, Japan
Countess 3 automated cell counter	cell counting	Thermo Fisher Scientific Inc., Waltham, USA
CytoFlex LX	flow cytometer	BeckmanCoulter, Brea, USA
SkyScan 1172	microcomputed X-ray tomography (micro-CT)	Bruker Belgium S.A./N.V., Kontich, Belgium)
Fresco 17 centrifuge	centrifugation	Thermo Scientific Fisher, Waltham, MA, USA
heating block	heating of tubes	VWR International, LLC, Radnor, USA; Eppendorf SE, Hamburg, Germany
Leica CM3050 S	cryotome	Leica Biosystems, Nussloch, Germany
Leica TP1020	automatic tissue processor	Leica Biosystems, Nussloch, Germany
Leica THUNDER Imager Tissue	bright field microscope	Leica Biosystems, Nussloch, Germany
Megafuge 40	centrifugation	Thermo Fisher Scientific Inc., Waltham, USA
NanoPhotometer P360	RNA concentration	Implen GmbH, Munich, Germany
RM2235	paraffin microtome	Leica Biosystems, Nussloch, Germany
UV Quick Cryosection Mounter	mounting of crysections	Section-Lab Co. Ltd., Yokohama, Japan

2.1.7 Software and analyzing programs

Software	Application	Provider
LAS X THUNDER software	microscopic image processing	Leica Biosystems, Nussloch, Germany
BZ-X Analyzer software	microscopic image processing	Keyence Corporation, Ōsaka, Japan
FlowJo, version 10.8.1	evaluation of flow cytometry data	Tree Star, Ashland, USA

continued: ***Software and analyzing programs***		
ImageJ, version 1.53v	image processing/histo-morphometry	open source
CTan software, version 1.18.8.0	micro-CT evaluation	Bruker Belgium S.A./N.V., Kontich, Belgium
CTVox software	3D visualization of micro-CT scans	Bruker Belgium S.A./N.V., Kontich, Belgium
GraphPad Prism, version 9.1.1	graphics and statistics	GraphPad Software, Inc., San Diego, USA
NRecon, version 1.7.0.3	micro-CT reconstruction	Bruker Belgium S.A./N.V., Kontich, Belgium
R, version 4.1.2	graphics and statistics	The R Foundation for Statistical Computing, Vienna, Austria

2.2 Methods

2.2.1 Animals, housing and diet

2.2.1.1 Experimental design using DIO mice

The animal experiments were planned and conducted according to the instructions of the Federation of European Laboratory Animal Science Associations (FELASA) and communicated following the guidelines of Animal Research: Reporting of In Vivo Experiments (ARRIVE). The *in vivo* studies were in agreement with the German Animal Welfare Act, and ethical permission was approved by the local state authorities Landesamt für Gesundheit und Soziales Berlin (approval no. G0008/12; T0119/14; T0249/11; G 0160/17; G0141/19). In this work, two well-established models of high-fat diet (HFD)-induced obesity and bone injury in environmentally exposed mice were combined. C57BL/6 mice were chosen for this study due to strong fracture healing capacities and potent immune competence [142, 143]. The fracture was introduced after 12 weeks of age when peak adult bone mass is achieved and bone material properties also reach peak values [144]. Male C57BL/6J mice were selected for the diet-induced obesity (DIO) study due to their suitability as a standard strain for this this research purpose. Additionally, these mice exhibit increased susceptibility to DIO, which is attributed to a spontaneous deletion mutation in the gene encoding nicotinamide nucleotide transhydrogenase (NNT) [145]. NNT reduces levels of reactive oxygen species (ROS) through increasing the oxygen consumption. It has been postulated that this mutation is associated with increased fat mass and impaired glucose homeostasis.

The design of the study is based on DIO experiments conducted by Sbierski-Kind et al. (2018) [30]. In a similar manner, this work includes two DIO studies utilizing short-term and long-term

HFD protocols to induce the onset of obesity and persistent obesity (Fig. 4, A and B). The HFD (60 kJ% from fat, 19 kJ% from proteins, and 21 kJ% from carbohydrates, Sniff Spezialitäten GmbH, Soest, Germany) with 6 % (w/v) sucrose in drinking water started at 5 or 8 weeks of age and was continued for either 7 or 16 weeks. Age-matched animals were maintained on standard chow diet. Mice were housed under non-SPF conditions to stimulate the adaptive immunity though mild antigen exposure, which leads to the generation of effector/memory T cells. The rhythm of light-and-dark cycle was adjusted to 12 h and the temperature to 20 °C. Water and food was provided ad libitum. Body weight was measured weekly throughout the experiment. Metabolic alterations were assessed using the glucose (GTT) and insulin tolerance tests (ITT) one week before the introduction of the osteotomy (chapter 2.2.3, p. 30).

The metabolic tests conducted in this study revealed distinct responses to the HFD, with the differentiation primarily based on the results obtained from the glucose tolerance test (GTT) (Fig. 4, C). In addition to control mice fed a standard chow diet, the experimental groups consisted of obese mice categorized as either having high glucose tolerance (GT) or low GT. DIO mice with high GT demonstrated a more efficient regulation of glucose, indicating a healthier glucose metabolism and maintained glucose tolerance despite the HFD. In contrast, obese mice with low GT exhibited impaired glucose metabolism and difficulties in maintaining stable glucose levels, reflecting reduced glucose tolerance. By comparing these groups, the study aimed to identify the factors and mechanisms that differentiate obese mice with high GT from those with low GT.

To investigate whether targeting $CD8^+$ T cells improves bone healing and to determine if the mechanism is indeed related to T cells, several mice from the obese low GT group were administered an antibody for specific for the depletion of $CD8^+$ T cells directly prior to surgery. This intervention was conducted as part of the long-term HFD study.

After the categorization of mice fed a HFD, the animals underwent a femoral osteotomy (chapter 2.2.2, p. 29) and the analysis was performed 3d/7d and 21d post-surgery (Fig. 4, B and C). Flow cytometry was used to define the cellular immunoprofile. Single-cell ribonucleic acid (RNA) and bulk RNA sequencing were employed to identify molecular expression patterns related to vascularization, immunity, as well as the osteogenic and adipogenic potential. Histology and immunohistochemistry (IHC) were used to visualize and quantify various tissues involved in fracture healing. Additionally, these techniques assessed tissue alterations associated with obesity in the liver and pancreas. The bone healing outcome was analyzed through micro-computed X-ray tomography (micro-CT). Herein, the work also examined the intestinal microbiome that is known to be shaped by obesity and has a role in modulating immune responses.

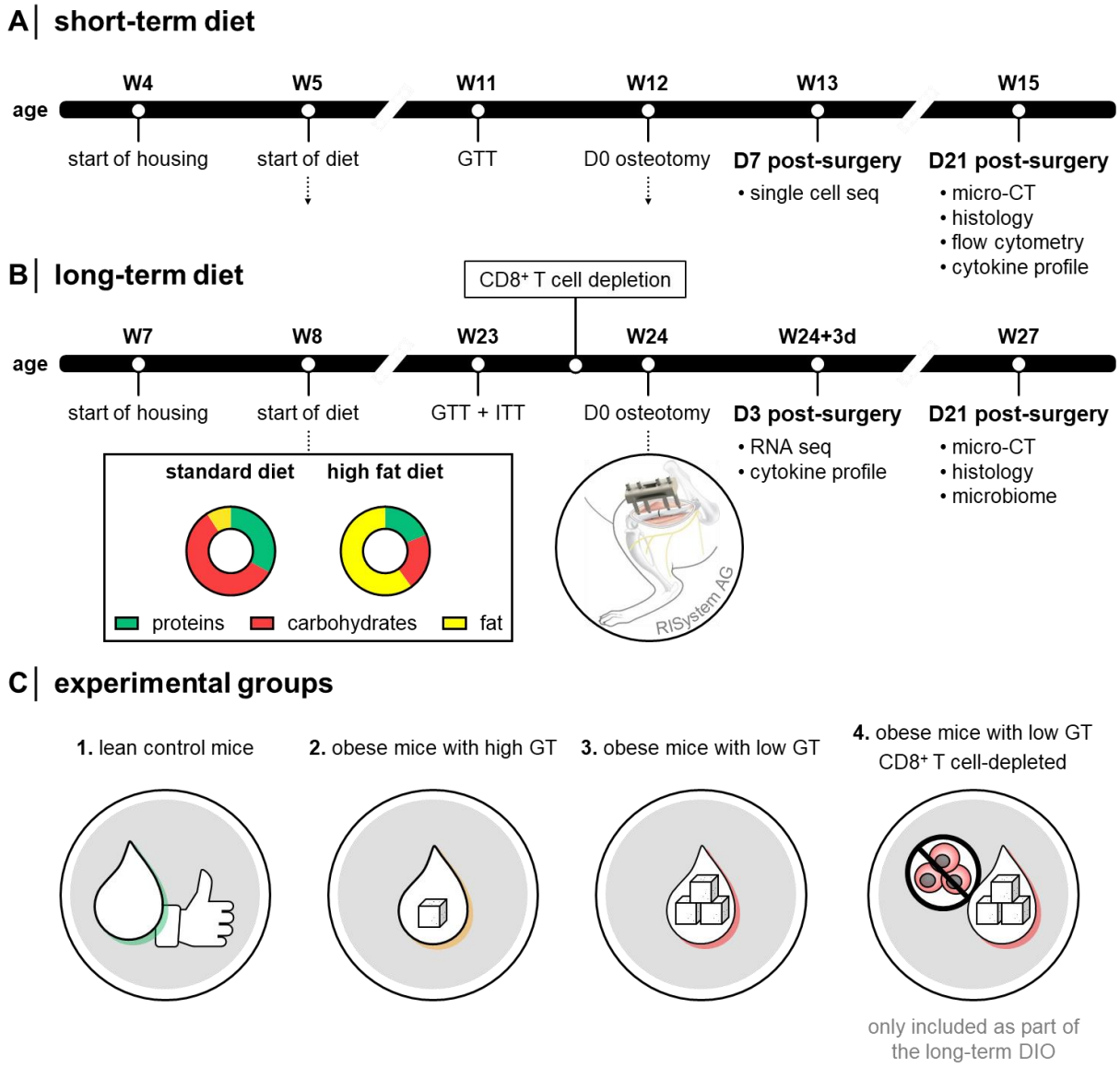

Fig. 4 | Experimental groups and timeline of the *in vivo* HFD-studies. A, B | Mice were transferred to the non-SPF animal facility after arrival and the feeding of the HFD started a week later for either 7 **(A)** or 16 weeks **(B)**, while the control groups simultaneously received standard chow diet. A week prior to surgery, the GTT and ITT were performed. Animals were sacrificed 3 or 7 and 21 days after surgery for in-depth analysis of the bone healing outcome (micro-CT and histology), immunoprofile and microbiota. **C |** The study compared lean control mice (1) with obese mice that either developed high (2) or low GT (3) after HFD. Selected animals of the obese low GT group additionally received a $CD8^+$ T cell-depleting antibody (4) to improve bone fracture healing in obesity. micro-CT: micro-computed X-ray tomography, seq: sequencing.

2.2.1.2 Experimental design using aged mice

The work also presents data from another *in vivo* osteotomy study investigating fracture healing complications associated with an increased experienced immune system in aged mice compared to undisturbed bone repair in mice with a more naïve immune phenotype [146]. The main objective was to examine whether the observed differences in the immune systems and healing outcome are attributed to variances in the gut microbiome.

For that, female C57BL/6N mice from the same litter were kept in SPF or non-SPF housing for over a year, starting from the age of 8-10 weeks. Mice in the SPF facility were housed in individually ventilated cages with air filtration. Conversely, the non-SPF cages were not equipped with a lid, facilitating the environmental antigen exchange, and purification of air was reduced in the husbandry. This approach enabled the generation of distinct immunological experiences, referred to as low immune experience in the SPF housing and high immune experience in the non-SPF facility. One group from each housing condition did not receive an osteotomy (0d) and served to characterize the native microbiome. Additionally, two more groups from the SPF and non-SPF cages underwent the surgical procedure (chapter 2.2.2, p. 29). The cecal microbiome was examined prior to surgery (0d) and from mice at 3d and 21d post-fracture.

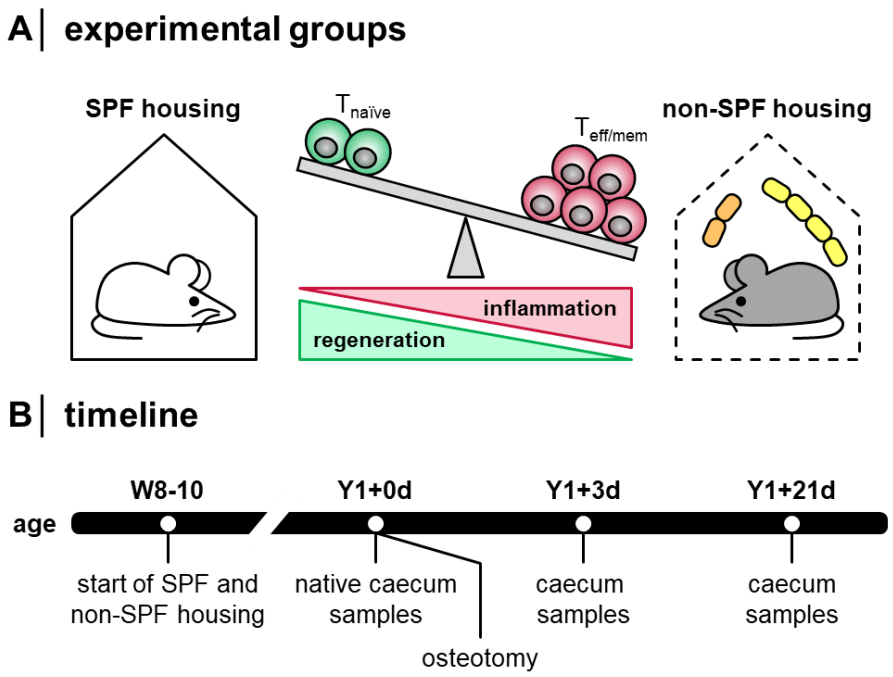

Fig. 5 | Experimental groups and timeline of the *in vivo* study using aged mice. Mice were either housed under SPF or non-SPF conditions starting from the age of 8-10 weeks. After one year, caecal samples were taken from one mouse group of each husbandry prior to surgery (0d) to investigate the native microbiome. Two additional groups from each facility received a femoral fracture and caecum samples were obtained from mice at 3d and 21d post-surgery.

2.2.2 Murine osteotomy and surgical procedure

In preparation for the surgery, mice were treated with an analgesic (buprenorphine) and antibiotic (clindamycin). The osteotomy was performed under isoflurane anesthesia and temperature of mice was maintained with a heating pad set to 37 °C. Eyes were hydrated by applying an ointment and the surgical incision site was disinfected after shaving. The incision was placed along the left femur axis and a blunt preparation of surrounding muscle tissue allowed preservation of ligament and muscle integrity. Therefore, bone healing could be investigated without interference from soft

tissue trauma. With the usage of forceps, the femur was bared by simultaneously protecting the sciatic nerve from injury. After drilling 0.4 mm holes orthogonally to the femur length, an external fixator (MouseExFix, RISystem AG, Landquart, Switzerland) was installed and stabilized with four pins. The femur was osteotomized between the inner pins with a Gigli wire saw of 0.66 mm in diameter to establish a non-critical size defect of 0.7 mm. After properly repositioning muscles and ligaments, the skin was closed using a non-resorbable surture material and treated with a wound spray adhesive. Directly after osteotomy, mice were supplemented with fluids to improve recovery and avoid dehydration caused by the surgical conditions. In the postoperative care, mice received analgesics (tramadol) through the drinking water and pellet for 3d. The fracture healing outcome was investigated 3d/7d and 21d post-surgery. For that, cervical dislocation was applied under deep anesthesia (ketamine and medetomidine) and organs were collected for further analysis.

Published data confirm that this osteotomy model has been thoroughly established and demonstrates high reproducibility [88, 90, 97].

2.2.3 Analysis of metabolic parameters

2.2.3.1 Glucose and insulin tolerance test

The glucose tolerance test (GTT) was utilized to evaluate the ability to regulate glucose metabolism. Herein, mice were fasted overnight, and the following morning, they received an injection (i.p.) of 5 µL 20 % (v/v) glucose/g body weight. One week prior to surgery, the blood glucose levels were monitored at 0/15/30/60/120 min post-glucose administration using a glucose meter (Accu-Chek Guide, Roche Holding AG, Basel, Switzerland). The blood drop was obtained by cutting off 1-2 mm of the tail tip using sharp scissors.

The insulin tolerance test (ITT) is a method used to assess insulin sensitivity and the body's response to insulin. For the determination of insulin action, 4 h-fasted mice received 5 µL of 0.150 U/mL insulin/g bodyweight (i.p.). Again, blood glucose levels were measured 0/15/30/60/120 min post-injection. To preserve the tail tip, a small incision was made in the lateral tail vein using a sharp scalpel blade to collect blood samples. The tolerance tests were carried out at an interval of five days to minimize stress for the mice.

2.2.3.2 Determination of non-fasting plasma insulin levels

The collection procedure is a terminal method performed under deep anesthesia. The animal was placed in dorsal recumbency and the puncture site was disinfected. A syringe with a 24 gauge needle was inserted until blood flash appeared in the needle hub. Sufficient amount of blood has been collected by aspiration and upon completion, mice were euthanized. Blood samples were

collected in heparin tubes and stored on ice until blood plasma was extracted by centrifugation at 2000x*g* for 10 min. The plasma was obtained from the supernatant and frozen at -80 °C until further processed.

To evaluate the ability of insulin secretion, plasma insulin was analyzed by a sandwich immunoassay on a Mesoscale Diagnostics, LLC (Rockville, USA) platform. The assay has been performed according to the manufacturer's specifications. Briefly, an insulin antibody was precoated on an electrode. After adding blood plasma and the sulfotag labeled detection antibody, a read buffer created a suitable chemical environment to analyze electrochemiluminescence on an Mesoscale Diagnostics SECTOR instrument (Mesoscale Diagnostics, LLC, Rockville, USA). Voltage was applied to the electrodes causing the bound and labeled antibody to emit light. The light intensities enabled the quantitative measurement of insulin present in blood plasma based on a standard curve.

2.2.4 Multiparameter flow cytometry

2.2.4.1 Sample collection and preparation

The study acknowledged the influence of obesity on the immune system. To investigate the phenotypic immune signatures throughout the regenerative process, flow cytometry was employed to analyze samples from peripheral blood, spleen and intact contralateral bone marrow at specific time points.

Blood collection during the running experiments did not require anesthesia and was achieved by puncture of the submandibular (facial) vein using a lancet. The sample was collected with a capillary tube and cooled on ice for subsequent processing.

Spleen and bone samples were stored in 1xPBS on ice until analysis. The bone marrow was extracted from the bone cavity by cutting the bone ends, and the bone cavities were subsequently rinsed with 1xPBS on ice through attachment of a syringe with a 24-gauge needle at one end. Spleens were cut into small pieces in 1xPBS on ice and, similar to bone marrow, processed to obtain a single-cell suspension through mincing the tissues through a 40 µm nylon mesh filter using a syringe plunger. The resulting cell suspension was collected in a tube kept on ice.

Blood samples were simply centrifugated (7 min, 400×*g*, 4 °C) and the supernatant was removed.

The cells from each tissue were resuspended in red blood cell (RBC) lysis buffer (Biolegend Inc., San Diego, USA) and incubated for 5 min. Cells were washed twice with 1xPBS between centrifugation steps (7 min, 400×*g*, 4 °C) and resuspended in 1xPBS. Cell counting was performed by mixing equivalent volumes of a trypan blue solution and the cell suspension. Cell counting occurred in a counting chamber of the Countess 3 automated cell counter (Thermo Fisher Scientific Inc., Wal-

tham, USA). The cell suspensions were adjusted to a cell concentration of 1×10^7 cells/mL in 1xPBS and 150 µL were transferred into a 5 mL polystyrene tube.

Live/dead discrimination was accomplished by using a Fixable Live/Dead staining kit (Thermo Fisher Scientific Inc., Waltham, USA), which incubated for 30 min on ice. After washing the cells with ice-cold flow cytometry (FC) buffer (1xPBS / 0.5 % (w/v) bone serum albumin (BSA) / 0.1 % (w/v) sodium acid), the cells were centrifuged (7 min, 400×*g*, 4 °C). To prevent non-specific binding of antibodies to Fc receptors, a FcX blocking solution (Biolegend Inc., San Diego, USA) was added to the resuspended cells.

2.2.4.2 Antibody staining for flow cytometry

Staining with antibodies was similarly performed on ice in FC buffer to restrict internalization of several surface molecules. For cell surface staining, 100 µL of the antibody solution (Tab. 1) was added to the cell pellet and incubated in the dark and on ice for 20 min. Cells were washed with FC buffer and after centrifugation (7 min, 400×*g*, 4 °C), cells were incubated in 1xTrueNuclear Fix Solution (Biolegend Inc., San Diego, USA) for 60 min at room temperature. Cells were washed twice with 1x permeabilization buffer (Biolegend Inc., San Diego, USA) and the centrifuged cells were resuspended with the mix of antibodies for intracellular staining (Tab. 1) for 30 min at room temperature. Washing was again performed with 1xpermeabilization buffer, cells were subsequently centrifuged (7 min, 400×*g*, 4 °C) and washed with FC buffer. After the final centrifugation step (7 min, 400×*g*, 4 °C), cells were resuspended in 1xPBS and filtered prior to analysis.

The stained cells were analyzed using a CytoFlex LX system (BeckmanCoulter, Brea, USA), and data analysis was performed using a bead-based compensation matrix. Gates were set using fluorescence minus one (FMO) controls, and the FlowJo software (FlowJo LLC, Ashland, USA) was used for data analysis. The gating strategy for Thelper cells is illustrated in Fig. 6, while Fig. 7 demonstrates the gating strategy for macrophages and dendritic cells (DCs).

Tab. 1 | Summary of extra- and intracellular (i) markers which identify Thelper cell and macrophage subsets. Information about marker, antibody clone, fluorochrome and dilution.

Marker	Clone	Fluorochrome	dilution
Thelper cell subset panel			
CD45	30-F11	V500	1:25
CD3e	145-2C11	BB700	1:50
CD4	GK1.5	APC/Fire750	1:100
CD8α	53-6-7	BV785	1:200
TCRγδ	GL3	BV421	1:50
CD62L	MEL-14	APC-R700	1:100
CD44	IM7	PE-Cy7	1:200
CD25	PC61	PE-Dazzle594	1:200
FoxP3 (i)	MF23	AF488	1:50
Tbet (i)	Q4-46	BV650	1:20
GATA3 (i)	L50-823	AF647	1:10
RORγt (i)	Q31-378	PE	1:200
Macrophage subset panel			
CD45	30-F11	AF488	1:200
CD3	145-2C11	PE-Cy7	1:50
CD19	6D5	PE-Cy7	1:100
CD335	29A1.4	PE-Cy7	1:33
CD11c	N418	PerCP/Cy5.5	1:50
CD11b/Mac-1	M1/70	BV510	1:50
Ly6-G	1A8	APC/Fire750	1:50
MHC class II	M5/114.15.2	BV785	1:400
CD80	16-10A1	BV650	1:50
CD86	GL-1	BV421	1:50
CD163	TNKUPJ	PE	1:200
VEGF (i)	VG1	AF647	1:100
CD206 (i)	C068C2	PE/Dazzle594	1:100

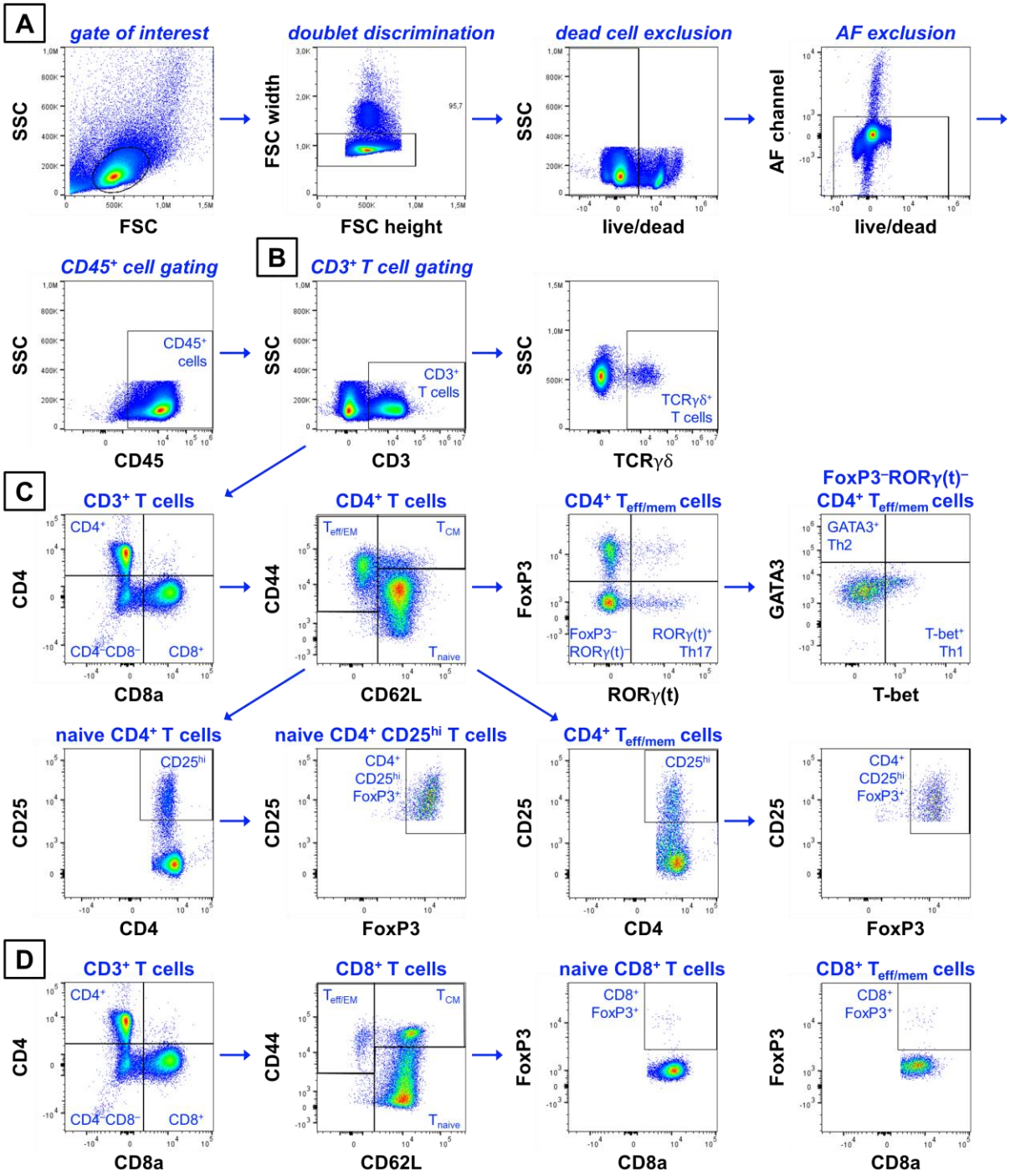

Fig. 6 | Gating strategy for analyzing the CD4⁺ T helper subsets Th1, Th2 and Th17 as well as CD4⁺CD25^hiFoxP3⁺ T cells and CD8⁺FoxP3⁺ cells. A | CD45⁺ lymphocytes were analyzed by gating on all splenocytes based on the forward (FSC) and sideward scatter (SSC). Doublet cells were discriminated and excluded, along with autofluorescent (AF) and dead cells. **B |** The focus on CD45⁺CD3⁺ T cells allowed for the identification of naïve (CD62L⁺CD44⁻), central memory (CM, CD44⁺CD62L⁺) and effector/effector memory (EM, CD44⁺CD62L⁻) cells within the CD4⁺ (C) and CD8⁺ T cell population (D). **C |** CD4⁺ T helper subsets were further characterized by the expression of specific transcription factors, such as Tbet for Th1, GATA3 for Th2 and RORγ(t) for Th17. The CD4⁺CD25^hiFoxP3⁺ staining should partially resemble the phenotype of Treg cells. **D |** CD8⁺FoxP3⁺ T cells are known to possess regulatory functions similar to those of Treg cells.

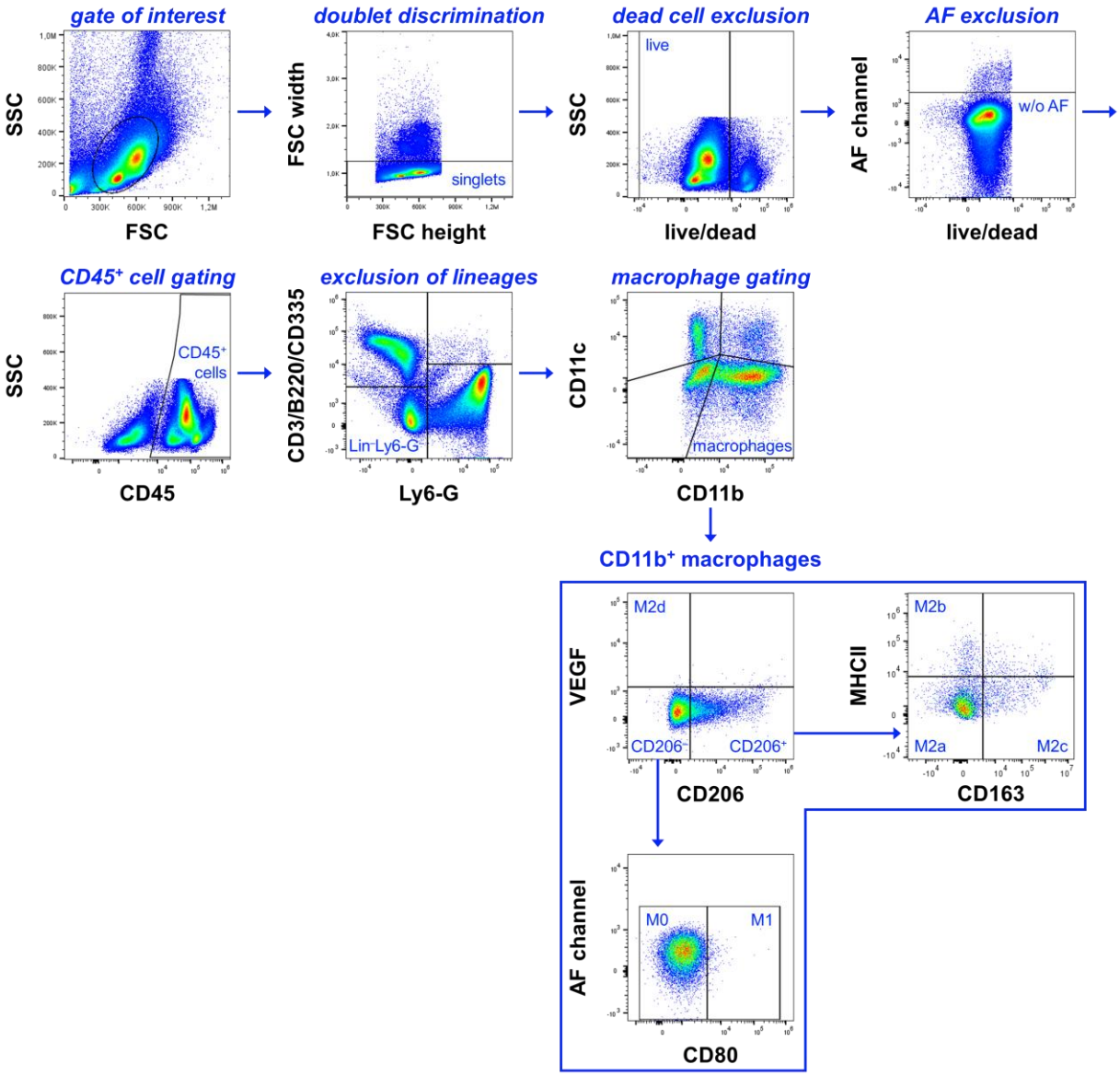

Fig. 7 | Gating strategy for the determination of macrophage subsets. To determine macrophage subsets, the cell population of interest was narrowed down within all bone marrow cells based on the scatter plot analysis. The next steps involved excluding doublets, autofluorescent (AF) cells, and dead cells to achieve a clean identification of $CD45^+$ lymphocytes. The subsequent gating steps excluded $CD3^+$ T cells, $B220^+$ B cells, $CD335^+$ NK cells, and $Ly6G^+$ neutrophils. Following these exclusions, further phenotyping of $CD11b^+$ macrophages enabled the detection of different macrophage subsets: $CD206^-VEGF^+$ M2d, $CD206^+CD163^-MHCII^-$ M2a, $CD206^+CD163^-MHCII^+$ M2b, $CD206^+CD163^+MHCII^-$ M2c as well as $CD206^-CD80^-$ M0 and $CD206^-CD80^+$ M1 macrophages.

2.2.5 Single cell RNA-sequencing of peripheral T cells

This study aimed to investigate the T cell composition and subset-specific gene signatures in peripheral blood of lean and obese mice on the basis of single cell RNA-sequencing.

2.2.5.1 Isolation of peripheral T cells

Pan-T cells were enriched using an untouched magnetic cell sorting approach (EasySep Mouse T Cell Isolation Kit, STEMCELL Technologies, Vancouver, Canada) according to the manufacturer's instructions. The isolation procedure was performed on ice and parameters for centrifugation were set to 400×*g* at 4 °C for 7 min. Briefly, after erythrocyte lysis of intracardiac blood samples, non-T cells were targeted with biotinylated antibodies and incubated with streptavidin-coated magnetic beads. Labeled cells were separated from T cells using a magnet and the enriched target cell suspension was transferred to another tube. Cells were stored at 4 °C until further processed.

2.2.5.2 Single cell RNA-sequencing

Single cell RNA-sequencing was performed externally in the laboratory of Mir-Farzin Mashraghi (Deutsches Rheuma-Forschungszentrum Berlin, Berlin, Germany). Briefly, the isolated cell suspensions were applied to the 10XGenomics workflow for single cell capturing and RNA gene expression (GEX) library preparation. For that, each sample within an experimental group was stained with a unique hashtag antibody to enable pooling of samples. The suspensions were loaded onto a microfluidic chip to catch single cells and to generate next generation sequencing complementary DNA (cDNA) libraries upon cell lysis [147]. Hereby, the oligonucleotides were specifically barcoded to generate cDNAs from a single cell with the same barcode, enabling the obtained sequences to be traced back to their original cell. The GEX library was ultimately sequenced on a NextSeq500 device (Illumina, Inc., San Diego, USA).

2.2.5.3 Analysis of single cell RNA-sequencing data

Data analysis was accomplished by Stephan Schlickeiser (Berlin Institute of Health at Charité, Berlin, Germany). In brief, raw sequence reads were processed using cellranger 3.1.0, which includes a default detection of intact cells. Mkfastq and count served as format for default demultiplexing and quantification of gene expression. Refdatacellranger-mm10-1.2.0 was applied for mouse genome mapping. Raw unique molecular identifier (UMI) counts were further processed and analyzed using R 4.0.2, which included filtering of poor-quality cells, normalization, clustering, dimensionality reduction and differential abundance/expression analysis based on edgeR's quasi-likelihood methods.

2.2.6 Cytokine secretion

Cytokines as indicator for the inflammatory environment were characterized in plasma of intracardiac blood. The bead-based immunoassay LegendPlex Mouse T Helper Cytokine Panel (Biolegend Inc., San Diego, USA) helped to quantify multiple soluble analytes simultaneously with a flow cytometer. The assay follows the same essential principles of a sandwich immunoassay that captures an analyte with two antibodies. The kit contained bead sets in two sizes with different levels of allophycocyanin (APC) fluorescence to enable discrimination. Each bead population is coated with a specific antibody capturing a particular analyte. After washing, a biotinylated antibody detected a specific cytokine on the beads. A streptavidin (SA)-phycoerythrin (PE) complex bound the biotin-capture antibody, transmitting a fluorescence signal with intensities correspondent to the amount of bound analyte. The concentration of a particular cytokine was quantified based on a known standard curve. The assay was performed according to the manufacturer's protocol. However, the analysis has been optimized for a reduced reaction volume of capture beads, sample, detection antibody and SA-PE, using 10 µL instead of 25 µL. Therefore, the samples and beads were incubated over night at 4 °C under shaking. The other steps were performed as described by the manufacturer. The multiplex assay was measured on a CytoFlex LX system (BeckmanCoulter, Brea, USA) and analyzed with the LegendPlex Software (v8.0, BioLegend Inc., San Diego, USA).

2.2.7 Histological assessment

Histological analysis served to visualize and quantify structural components of the healing bone as well as changes of metabolically active organs, such as liver and pancreas. Harvested femora, liver and pancreas were fixed in paraformaldehyde (PFA) and either underwent cryopreservation (bone) or paraffin embedding (bone, liver and pancreas).

2.2.7.1 Cryopreservation and sectioning of bone specimens

Applying the Kawamoto's film method (Section-Lab Co. Ltd., Yokohama, Japan) allows tissue embedding without the need for decalcification [148]. In brief, fixated and still calcified tissue was transferred to super cryoembedding medium (SCEM) and frozen in ice-cold n-hexane. Sections of bone were processed in a cryotome and for that applied on an adhesive film.

Before tissue preservation, bones were incubated in 4 % (v/v) PFA for 4 h at 4 °C directly after removal. Subsequently, PFA was replaced by a 10 % (w/v) sucrose solution for 24 h at 4 °C to prevent crystal formation and tissue damage. Sucrose concentration increased gradually by exchanging with a 20 % (w/v) and final 30 % (w/v) sucrose solution, which were each added for

another 24 h at 4 °C. In preparation for embedding, a Dewar vacuum flask was filled with n-hexane and dry ice. The bone sample was inserted into a small metal form and submerged in SCEM medium without enclosing the external fixator. The embedding form was transferred to the cooling n-hexane until the media was frozen. Immediately afterwards, the external fixator and pins were quickly and carefully removed with the respective screwdriver. The frozen tissue block was further covered with SCEM medium, which was again completely frozen in n-hexane. After removal from the metal container, the blocks were stored at -80 °C until sectioning.

The final embedded tissue sample was further processed in a cryostat (Leica CM3050 S, Leica Biosystems, Deer Park, USA). After acclimatization of the tissue block in the cryostat at -23 °C, the specimen was sticked onto the cold sample holder using embedding medium (Tissue-Tak O.C.T. Compund, Sakura Finetek USA, Inc., Torrance, USA) and installed in the instrument together with the respective knife. Trimming off first tissue layers served to adjust the area of interest comprising the whole medullary cavity along the longitudinal axis. An adhesive cryofilm was placed onto the tissue which enabled cutting of hard, calcified bone and maintaining tissue integrity. Serial sections of 7 µm were placed onto cooled slides (SuperFrost Plus, Thermo Fisher Scientific Inc., Waltham, USA) and the cryofilm was secured using tape. Slides were stored at -80 °C until staining.

2.2.7.2 Paraffin embedding and sectioning of paraffin blocks

Samples (bone, liver and pancreas) were fixed in 4 % PFA (v/v) for 24 h. Before the embedding process, the bones underwent decalcification. This involved rinsing the bone samples under running water and incubating them in a solution of ethylenediaminetetraacetic acid (EDTA, Carl Roth GmbH + Co. KG, Karlsruhe, Germany). The EDTA solution served to remove minerals and aid in the processing of hard tissue. Decalcification asted for two weeks, with a biweekly change of the decalcifier solution. Prior to embedding using an automatic tissue processor (Leica TP1020, Leica Biosystems, Deer Park, USA), all tissue samples were washed under running water for 45 minutes. The dehydration process started with a series of increasing ethanol concentrations ranging from 70% (v/v) to 99.9% (v/v), followed by xylene at room temperature (Tab. 2). Subsequently, the tissue was placed into melted paraffin (Paraplast Plus, Leica Biosystems, Deer Park, USA). After one day, the liquid paraffin, along with the tissue, was poured into a metal mold. The resulting block was allowed to cool down and stored at room temperature until sectioning.

Tab. 2 | Preparation for paraffin embedding by an automated tissue processor for hard and soft tissue. Incubation of tissue started with increasing concentrations of ethanol (EtOH), followed by xylene and ended in liquid paraffin.

step	solution	incubation time in h for	
		bone	soft tissue
1	70 % EtOH	1	1
2-3	80 % EtOH	1	1
4-5	96 % EtOH	1	2
6-8	99.9 % EtOH	2	2
9-10	xylene	1	1
11-12	liquid paraffin	2	2

By using a microtome (RM2235, Leica Biosystems, Deer Park, USA), paraffin sections were cut with a thickness of 4 µm and collected on a water film. Sections were stretched on warmed water at around 42 °C until transfer onto slides. Slides with tissue sections were further dried at 37 °C overnight and stored until staining.

2.2.7.3 Movat's Pentachrome stain of bone tissue

Movat's Pentachrome is a classical histological staining technique used for the descriptive evaluation of the callus morphology, including calcified bone/collagen and mineralized cartilage (Safran du Gâtinais, yellow), hyaline cartilage (Alcian blue, green-blue), connective tissue (Alcian blue, translucent blue-grey), bone marrow (Brilliant Crocein-acid fuchsin, red) and cell nuclei (Weigert's iron hematoxylin, blue-black). In preparation for the staining procedure (Tab. 3), paraffin sections were deparaffinized with xylene in two steps for 10 min and rehydrated in ethanol of descending concentration (99,9 % (v/v), 99,9 % (v/v), 96 % (v/v), 80 % (v/v), 70 % (v/v)) à 2 min and washed in distilled water for 2 min. Cryopreserved sections were shortly thawed for 2 min and transferred to a 4 % PFA solution followed by distilled water for 5 min.

Tab. 3 | Protocol of Movat's Pentachrome stain.

1.	3 % (v/v) acetic acid, pH 2.5	3 min
2.	1 % (w/v) Alcian Blue in 3 % (v/v) actic acid, pH 2.5	30 min
3.	3 % (v/v) acetic acid, pH 2.5	3 min
4.	Distilled water	Rinse
5.	Alkaline ethanol (90 mL 96 % (v/v) EtOH in 10 mL 25 % NH_3)	20 min
6.	Tap water	10 min
7.	Distilled water	Rinse
8.	Weigert's iron hematoxylin (equal amounts of solution A and B)	15 min
9.	Tap water	10 min
10.	Distilled water	Rinse
11.	Brilliant Crocein-acid fuchsin	15 min
12.	0,5 % (v/v) acetic acid, pH 2.5	Rinse
13.	5 % (v/v) phosphotungstic acid	20 min
14.	0,5 % (v/v) acetic acid, pH 2.5	1 min
15.	99,9 % (v/v) ethanol	3x à 2 min
16.	6 % (w/v) Safran du Gatinais in 99.9 % EtOH	1 h
17.	99,9 % (v/v) ethanol	3x à 2 min
18.	Xylene	2x à 2 min
19.	Mounting with Vitro-Cloud for paraffin sections or with SCMM-R2 using a UV polymerizer for cryosections	

2.2.7.4 Hematoxylin-eosin stain of liver tissue

After dewaxing and rehydration of paraffin sections, liver was processed for routine hematoxylin-eosin (HE) staining to evaluate the development of hepatic fat in the course of the high-fat diet (Tab. 4). Hematoxylin stains the nuclei of cells blue-purple, while eosin stains the cytoplasm and extracellular matrix shades of pink. This staining method enables the examination of accumulative fat, which is represented as fat vacuoles.

Tab. 4 | Workflow of the hematoxylin-eosin stain.

1.	Harris' hematoxylin solution	7 min
2.	Distilled water	2x 2 min
3.	0.25 % HCl in 70 % ethanol	20 sec
4.	Tap water	10 min
5.	0.2 % (v/v) eosin	2 min
6.	96 % ethanol	20 sec
7.	96 % ethanol	Rinse
8.	99,9 % ethanol	2x 2 min
9.	Xylol	2x 2 min
10.	Mounting with Vitro-Cloud	

2.2.7.5 Immunohistochemistry based on alkaline phosphatase detection

Immunohistochemistry enabled the detection of specific proteins, which were targeted with a selective antibody on a tissue slide. Herein, visualization of the antigen-antibody complex was accomplished by an enzymatic alkaline phosphatase (AP) reaction on the basis of avidin-biotin binding. The AP staining procedure was applied to visualize vessels in the fractured bone by targeting CD31, a type I transmembrane glycoprotein, which is constitutively expressed in tube-forming endothelial cells [149]. Insulin staining was conducted to assess the functionality of β-cells in the pancreatic tissue (Tab. 5).

After deparaffinization and rehydration of paraffin sections, slides of bone and pancreas were placed in citrate buffer, pH 6.0, for 6 h at 60 °C and covered with foil. This pretreatment was performed to unmask proteins, as formalin fixation can lead to protein crosslinking that can obscure antigen sites in tissues. After antigen retrieval, samples were washed in 1xPBS, pH 7.4, and the area to be stained was encircled with a hydrophobic pen. All subsequent steps were performed in a humid chamber. To eliminate unspecific binding of the secondary antibody, tissue samples were incubated with a blocking solution containing normal serum for 30 min at room temperature. The primary antibody, which identifies the protein of interest, was applied over night at 4 °C. The next day, slides were rinsed twice with 1xPBS for 5 min each and addition of a biotinylated secondary antibody, diluted in blocking solution, aimed to detect the primary antibody species. During the incubation period of 30 min at room temperature, the avidin-biotin-alkaline phosphatase complex (Vectastain ABC-AP Kit Standard, Vector Laboratories, Inc., Newark, USA) was prepared according to the manufacturer's instructions. Residual secondary antibody was removed by two washes in 1xPBS for 5 min each. Afterwards, the complex, which binds to the biotinylated antibody, was applied to the tissue for 30 min at room temperature. The samples were washed twice in 1xPBS à 5 min and prepared for substrate administration by incubation in chromogen buffer twice for

5 min. The staining procedure was completed by adding the AP substrate (ImmPACT Vector Red Substrate Kit, Vector Laboratories, Inc., Newark, USA), which underwent catalysis to produce a magenta-colored product, allowing for the visualization of target structures. To stop the reaction, the sections were immersed in 1xPBS and subsequently washed with 1xPBS for 5 min.

Cell nuclei were counterstained with methyl green (Vector Laboratories, Inc., Newark, USA) for 25 min at room temperature. Afterwards, the slides were shortly placed in 96 % (v/v) ethanol followed by incubation in 99.9 % (v/v) ethanol twice for 2 min each. The samples were passed through a d-limonene containing clearing agent twice for 2 min. Following this step, the slides were mounted using Vectamount (Vector Laboratories, Inc., Newark, USA) and covered with a coverslip.

Mayer's hemalum (Merck KGaA, Darmstadt, Germany) diluted 1:2 in H_2O was used as an additional nuclear counterstain. Slides were dyed for 2 min at room temperature followed by incubation in tap water for 5 min. Finally, the sections were mounted with Aquatex (Merck KGaA, Darmstadt, Germany) covered with a coverslip. For all staining experiments, samples incubated without primary antibody served as negative controls. The stained tissue samples were ultimately imaged by brightfield microscopy.

Tab. 5 | Immunohistochemical staining of CD31⁺ blood vessels in fractured bones and insulin-producing islets on pancreas sections. Prior to staining, a blocking solution containing normal serum against the host species of the secondary antibody was added to the slides, followed by incubation with the primary antibody. Target structures were visualized by staining with a biotinylated antibody, which interacted with the avidin-biotin complex coupled to alkaline phosphatase. After substrate administration, the enzymatic reaction produced a magenta reaction product. Cell nuclei were either counterstained with methyl green or Mayer's hemalum, and slides were preserved using mounting medium and a coverslip.

	staining of	
	CD31 in the fracture gap	**insulin on pancreatic islets**
normal serum	anti-rabbit serum	anti-goat serum
primary antibody	goat anti-mouse CD31 (1:100)	rabbit anti-mouse insulin (1:200)
secondary antibody	rabbit anti-goat IgG, biotinylated (1:200)	goat anti-rabbit IgG, biotinylated (1:200)
counterstaining	methyl green	Mayer's hemalum
mounting medium	Vectamount	Aquatex

*2.2.7.6 **Fluorescent staining of bone: Visualization of Col1 and denaturated collagen fibers***

Paraffin-embedded fractured bones were stained for Col1, which served as an indicator for both healing progression and quality. The potential damage to collagen fibers was evaluated using a collagen hybridizing peptide (CHP) conjugate. After removing paraffin and rehydrating the samples, the slides were washed with 1xTBS. Enzymatic antigen retrieval was performed using pepsin

(Merck KGaA, Darmstadt, Germany) for 40 min at 37 °C, and hyaluronidase (Merck KGaA, Darmstadt, Germany) for 10 min at 37 °C in a humidity chamber, which was also used for the subsequent steps. The tissue was permeabilized using 0.03 % Triton X-100 in 1xTBS for 30 min at room temperature and sections were incubated in blocking solution with normal horse serum.

Immunofluorescent staining of Col1

After blocking, the primary biotinylated antibody targeting Col1 (Abcam plc., Cambridge, UK, 1:50 in antibody diluent) was added overnight and incubated at 4 °C. The following day, slides underwent three 5-min washes in 1xTBS at room temperature. For detection of the primary antibody, a streptavidin-AF568 conjugate (Thermo Fisher Scientific Inc., Waltham, USA, 1:400 in 1xTBS) covered the tissue samples for 1 h at room temperature. The slides were washed again three times with 1xTBS for 5 min each, followed by a change in 1xTBST for 5 min and a wash in 1xTBS for 5 min at room temperature. Nuclear staining was performed using 4′, 6-diamidino-2-phenylindole dihydrochloride (DAPI, Thermo Fisher Scientific Inc., Waltham, USA, 1:1500 in 1xTBS) for 20 min at room temperature. After three final changes in 1xTBS for 5 min at room temperature, slides were mounted using Fluoromount G (SouthernBiotech Associates, Inc., Birmingham, USA) and covered with a coverslip.

Staining with collagen hybridizing peptide

In preparation for staining, the stock solution of collagen hybridizing peptide (CHP)-Cy3 conjugate (3Helix Inc, Salt Lake City, USA) was diluted to 10 µm in 1xTBS prior to use. To avoid self-assembled monomers, the solution was heat-dissociated for 5 min at -80 °C and quenched promptly in an ice-water bath for 30 min. After blocking the tissue samples with normal serum, slides were immediately incubated with the prepared CHP conjugate overnight at 4 °C. The next day, slides were immersed three times in 1xTBS for 5 min each. After a wash in 1xTBST and 1xTBS for 5 min each, the cell nuclei were stained using DAPI (Thermo Fisher Scientific Inc., Waltham, USA, 1:1500 in 1xTBS) for 20 min at room temperature. The slides were washed with three changes of 1xTBS for 5 min each. Lastly, the sections were mounted using Fluoromount G (SouthernBiotech Associates, Inc., Birmingham, USA) and covered with a coverslip.

2.2.7.7 Imaging and analysis of stained tissue sections

Stained tissue slides were imaged using the light microscope Leica THUNDER Imager Tissue (Leica Biosystems, Nussloch, Germany) and the respective Leica LAS X THUNDER software (Leica Biosystems, Nussloch, Germany). White balance, shading correction and intensity as well as focus were adjusted for each sample, whereas magnification, image format, aperture and TL-Fld were kept constant. The software further processed the imaged tile scans to one microscopic image. Representative pictures of immunofluorescent stained tissue were acquired using the BZ-X810

microscope (Keyence Corporation, Ōsaka, Japan) and BZ-X Analyzer software (Keyence Corporation, Ōsaka, Japan) to produce a combined tile scan image. Filter settings, magnification and exposure time remained unchanged between samples. Overlay images were processed with BZ-X800LE Analyzer software (Keyence Corporation, Ōsaka, Japan).

Images were analyzed using ImageJ with a semi-automated and blinded approach. Tissue quantification for all stains was conducted using a custom macro (version *HM_Analysis_v0.99f.ijm*, Mario Thiele), which creates masks for different tissues by manually annotating the target tissue area and adjusting color thresholds. First, for each image, a region of interest (ROI) was defined, and the pixel size was converted to metric dimensions using the scale bar. To ensure consistent analysis of fractured bones, the width of the fracture gap was maintained at a constant size across the experimental groups. This was achieved by maintaining an equal distance from both the proximal and distal edges of the gap to the center. By selecting the void area along with the target tissues, including cortical and mineralized bone, cartilaginous tissue, bone marrow and AT in the bone, it was possible to calculate the specific tissue areas relative to the total ROI. Furthermore, this approach enabled the assessment of Col1- and CHP-positive areas within the fractured bone, as well as the evaluation of insulin-producing islets in the pancreas and fat within hepatic tissue.

2.2.8 Micro-computed X-ray tomography (micro-CT), reconstruction and analysis

Microcomputed X-ray tomography (micro-CT) is a non-invasive and non-destructive tool to visualize three-dimensional (3D) microstructures arranged by two-dimensional (2D) trans-axial slices [150]. For that, X-rays pass through a tissue and the initial radiation intensity decreases depending on the material and density of the tissue. Micro-CT is an indispensable method to assess bone callus properties, including callus size, geometry, bone architecture and mineralization, to interpret preclinical models in regenerative research.

2.2.8.1 Ex vivo micro-CT of murine femora

Fractured bones were collected and fixed in a 4 % (v/v) PFA in 1xPBS solution for 4 h at 4 °C. The samples were transferred to a serological pipette for stabilization, and the external fixator and pins were gently removed before scanning. Mechanically fixed bones were placed in a sample holder filled with 1xPBS to prevent dehydration and secured with cotton gauze fabric to avoid sample movement. The healing outcome was evaluated 21d post-surgery using a SkyScan 1172 micro-CT device (Bruker Belgium S.A./N.V., Kontich, Belgium) with specific settings (Tab. 6). Prior to the measurement, a scanner flat field correction was performed to eliminate image artifacts.

After the scan, the bone samples underwent an embedding procedure for histological assessment.

Tab. 6 | Parameters for the micro-CT to scan the 3D structure of osteotomized bones. Settings (voxel size, camera pixel binning, rotation step, source energy, exposure) are described for the DIO studies.

	experimental study	
	short-term HFD	**long-term HFD**
voxel size	8.01 µM	10.05 µm
camera pixel binning	2x2	2x2
rotation step	0.2 °	0.2 °
source energy	70 kV and 142 µA	80 kV and 124 µA
exposure	840 ms	1000 ms
beam filtering	0.5 mm aluminium filter	0.5 mm aluminium filter

2.2.8.2 Reconstruction and analysis of the micro-CT measurements

The scanned images required a 3D reconstruction by a modified algorithm of Feldkamp using the software NRecon (Bruker Belgium S.A./N.V., Kontich, Belgium) and applying Gaussian smoothing, ring artifact reduction, misalignment compensation, as well as beam hardening correction. The reconstructed, cross-sectional images were analyzed using the CTan software (Bruker Belgium S.A./N.V., Kontich, Belgium) within a defined volume of interest (VOI). This VOI encompassed a 2 mm callus, ensuring that the outer edges of the callus were equidistant from the center of the osteotomy gap.

To distinguish between non-mineralized and mineralized tissue, a global gray scale threshold was applied. For trabecular bone analysis, the images were binarized using adaptive thresholding, while cortical bone structures were excluded by implementing a morphological escalator technique. The bones were also calibrated for bone mineral density (BMD) measurement using an equivalent scan of validated phantoms (Bruker Belgium S.A./N.V., Kontich, Belgium) containing 0.25 and 0.75 g HA/cm^3. The CTan software was utilized to calibrate the BMD against the attenuation coefficient, which was calculated from the reconstruction. The CTVox software (Bruker Belgium S.A./N.V., Kontich, Belgium) was used to visualize representative micro-CT images.

2.2.9 Profiling of mRNA transcripts in bone: RNA isolation, sequencing and analysis

The transcriptomic analysis aimed to examine quantitative differences of bulk messenger RNA (mRNA) in fractured and intact contralateral bone samples obtained from lean and obese animals. The analysis focused on identifying variations in immune factors, osteogenesis and osteoclastogenesis markers, matrix components and vascularization-related genes.

2.2.9.1 Preparation of RNA from fractured and intact contralateral bone

RNA isolation based on the method of phenol-chloroform extraction to separate nucleic acid from proteins and lipids, followed by DNA digestion and ethanol precipitation of RNA [151].

After quickly harvesting the bone and removing soft tissue, including the fixator and pins, tissue was snap frozen in liquid nitrogen and stored at -80 °C until further use. To evaluate potential inherent alterations, the contralateral intact femur was collected and processed in the same manner. For the preparation of RNA transcripts, femora were pulverized with a stainless-steel mortar and pestle under permanent cooling with liquid nitrogen. The subsequent work was performed at room temperature when the tissue powder was homogenized in 1 mL TRIzol (Thermo Fisher Scientific Inc., Waltham, USA) containing phenol, guanidine isothiocyanate and ammonium thiocyanate. 0.2 mL chloroform (VWR International, LLC, Radnor, USA) was added and incubated for 10 min. After centrifugation for 10 min at 10 000×*g*, the lower phase and interphase contained organic components together with the phenol-chloroform mixture. The upper, less dense, aqueous phase contained the target RNA, which was transferred to another clean tube. The nucleic acid solution was mixed with 75 % (v/v) ethanol at a volume ratio of ethanol to DNA/RNA solution of 2:1 to accomplish precipitation of RNA transcripts. The extraction column (RNeasy Mini Kit, Qiagen, Venlo, Netherlands) was placed into a collection tube, loaded with a maximum volume of 0.7 mL and centrifugated for 30 sec at 10 000×*g*. The eluent was discarded and the step was repeated with the remaining sample solution. The column underwent a washing procedure using 0.35 mL of buffer RW1 and centrifugation for 30 sec at 10 000×*g*. The eluent was discarded and 0.08 mL of DNase was added to the column to remove contaminating DNA. After incubation for 15 min, the column was rinsed with 0.35 mL of buffer RW1 and centrifugated for 30 sec at 10 000×*g*. The eluent was discarded. The column was washed with 0.5 mL of RPE buffer and centrifuged for 2 min at 10 000×*g*. The membrane of the column was dried in a new clean collection tube at maximum rotational speed for 1 min. The first eluate of target RNA was obtained by transferring the column to a novel unused tube and adding 0.03 mL of nuclease-free H_2O which was pre-heated at 65 °C. After incubation for 5 min at room temperature, the sample was centrifugated for 2 min at 10 000×*g*. A second eluate was extracted by repeating the previous step with another clean tube. Before storage at -80 °C, RNA concentration and purity were assessed using a nanophotometer (Implen GmbH, Munich, Germany), which operates based on the principle of nucleic acid absorption at 260 nm. For the measurement, 1 µL of homogenized RNA extract covered the submicroliter unit. The lid (Lid 50, pathlength of 0.2 mm) was positioned on top, and the RNA concentration and purity were evaluated. Purity was assessed using the ratio of absorbance at 260 nm and 280 nm, with a ratio of 2.0 considered as an indicator of pure RNA.

2.2.9.2 Sequencing of RNA

Whole mRNA expression profiling was performed externally by the Core Unit Genomics located at the Berlin Institute of Health (BIH)/Max Delbrück Center for Molecular Medicine (MDC, Hannoversche Straße 28, 10115 Berlin, Germany) using the Illumina technology (Illumina, Inc., San Diego, USA). Briefly, RNA quality has been checked prior to sequencing by assessing RNA integrity number (RIN) to determine completeness of ribosomal (rRNA), which is an indicator for mRNA in a tissue sample [152]. The first step in the technique of RNA sequencing involved the conversion of fragmented RNA into complimentary DNA (cDNA). This conversion was carried out using reverse transcription [153]. Afterwards, sequencing adapters were ligated to the ends of cDNA fragments, followed by amplification. The generated cDNA library was analyzed by next generation sequencing to generate 50 million 100-nucleotide paired-end reads per sample.

2.2.9.3 Analysis of mRNA transcripts

Data analysis was accomplished by the Core Unit Bioinformatics (CUBI) (Berlin Institute of Health at Charité, Berlin, Germany). In brief, to run the analysis a pipeline called seasnap was used. STAR was applied for alignment of data and featureCounts to assign mapped sequencing reads to specified genomic features. Differential gene expression analysis of count data was conducted using DESeq2. The Wald test, available in DESeq2, was used for hypothesis testing when comparing the experimental groups.

2.2.10 Collection of caecum and feces for microbiome analysis

This study aimed to investigate the microbial composition, which is known to be influenced by obesity and aging. This analysis was conducted as part of both the long-term DIO study and another project involving immune-experienced mice in context of bone fracture healing.

Mice were sacrificed and the removed caeca and feces were immediately frozen in liquid nitrogen. Samples were stored at -80 °C until shipped on dry ice to the Institute for Food & Health (ZIEL) at the Technical University of Munich, Germany. The specimens were stored at -80 °C until further RNA processing. 16S rRNA gene tag sequencing (MiSeq, Illumina, Inc., San Diego, USA) of the conserved V3–V4 regions was performed at the ZIEL Core Facility Microbiome. Raw sequence reads were processed with IMNGS (www.imngs.org) based on the UPARSE approach, a de novo operational taxonomic unit (OTU)-picking strategy [154]. OTUs clustered at 97 % sequence similarity and only those OTUs with a relative abundance of ≥0.5 % total reads in at least one sample were further processed. Additional parameters were max. 2 barcode mismatches tolerated, 10 nucleotides trimmed at each the 5' and 3' end, trim quality score of 3, 3 expected errors and read length

between 300 and 600. The R-package Rhea was used for detailed downstream analysis to assess OTU normalization, relative abundances, alpha and beta diversity [155].

2.2.11 Statistical analysis and data visualization

Statistical evaluation and data visualization were conducted using the GraphPad Prism software (GraphPad Software, Inc., San Diego, USA) as well as R (The R Foundation for Statistical Computing, Vienna, Austria). Values were depicted as median ± ranges (truncated violin plot) or mean only (pie chart). Statistical difference between means was assessed by Welch's t-test, or unequal variances t-test, as the test assumes that both groups are sampled from Gaussian populations, but do not share equal variances. Statistical analysis for bulk and single cell RNA sequencing data based on multiple hypothesis testing. A p value or adjusted p value <0.05 was deemed statistically significant.

3 Results

3.1 Short-term obesity delayed bone fracture healing

3.1.1 Effects of high-fat diet on body weight, plasma glucose and circulating insulin

Diet-induced obesity (DIO) was assessed according to a standard protocol by feeding 5-week-old mice high-fat diet (HFD) (60 kcal% fat) for 7 weeks, whereas the age-matched control group obtained normal chow diet (10 kcal% fat) (Fig. 8, A). This murine model is well-established to induce obesity-associated hyperglycemia, glucose intolerance and insulin resistance, before T2DM manifests [14, 112]. Mice were housed under non-standard pathogen-free (non-SPF) conditions to facilitate a mild antigen exchange with the environment. This approach aimed to induce adaptive immune responses that partially mimic the physiological reactions observed in real-life situations. Mice were randomly assigned to either receive standard chow diet or HFD. The results obtained from the glucose tolerance test (GTT) conducted one week prior to the osteotomy indicated different responders to the HFD (Fig. 8, B). The GTT is a diagnostic test used to assess how the body processes an administered glucose load by monitoring blood glucose levels over time. Thus, obese mice were categorized into two groups based on their glucose tolerance (GT) status: DIO mice with high and low GT.

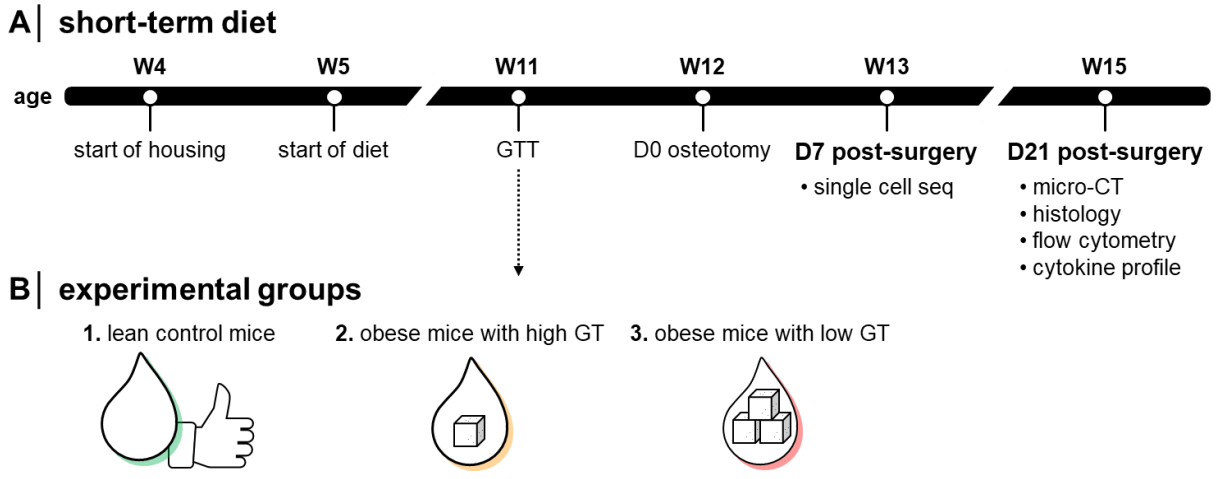

Fig. 8 | Timeline and experimental groups of the short-term *in vivo* HFD-study. A | Mice were transferred to the non-SPF animal facility after arrival and the feeding of the HFD started a week later for 7 weeks, while the control groups simultaneously received standard chow diet. A week prior to surgery, the glucose tolerance test (GTT) was performed. Animals were sacrificed 7 and 21d after surgery for in-depth analysis of the bone healing outcome (micro-CT and histology) and immunoprofile. **B |** Different responders to the HFD were identified based on the level of glucose tolerance (GT). The experimental groups compared lean control mice (1) with obese mice that either developed high (2) or low GT (3) after HFD. micro-CT: micro-computed X-ray tomography, seq: sequencing.

As indicated, despite similar final body weights (Fig. 9, A) and fasting glucose levels (Fig. 9, B, at 0 min) in both DIO groups, differences between HFD-fed mice were observed during the GTT (Fig. 9, B). In particular, obese mice with low GT showed a slower clearance of injected glucose compared to those with high GT, suggesting the development of glucose resistance and metabolic disturbances associated with progressed obesity. The calculation of the area under the curve (AUC) confirmed the distinct metabolic characteristics and allowed for the definition of a clear cutoff at 40000 (mg·min)/dL for categorizing the groups (Fig. 9, B). Notably, no difference was observed in non-fasting plasma insulin levels between the lean and both obese groups on the day of the section (21d post-fracture) (Fig. 9, C), suggesting the presence of functional pancreatic β-cells and a preserved insulin response [156].

Overall, the experimental setup enabled the generation of obese mice with distinct levels of glucose intolerance. These mice underwent a femoral osteotomy to investigate the impact of the different metabolic alterations on fracture healing and immune responses to injury.

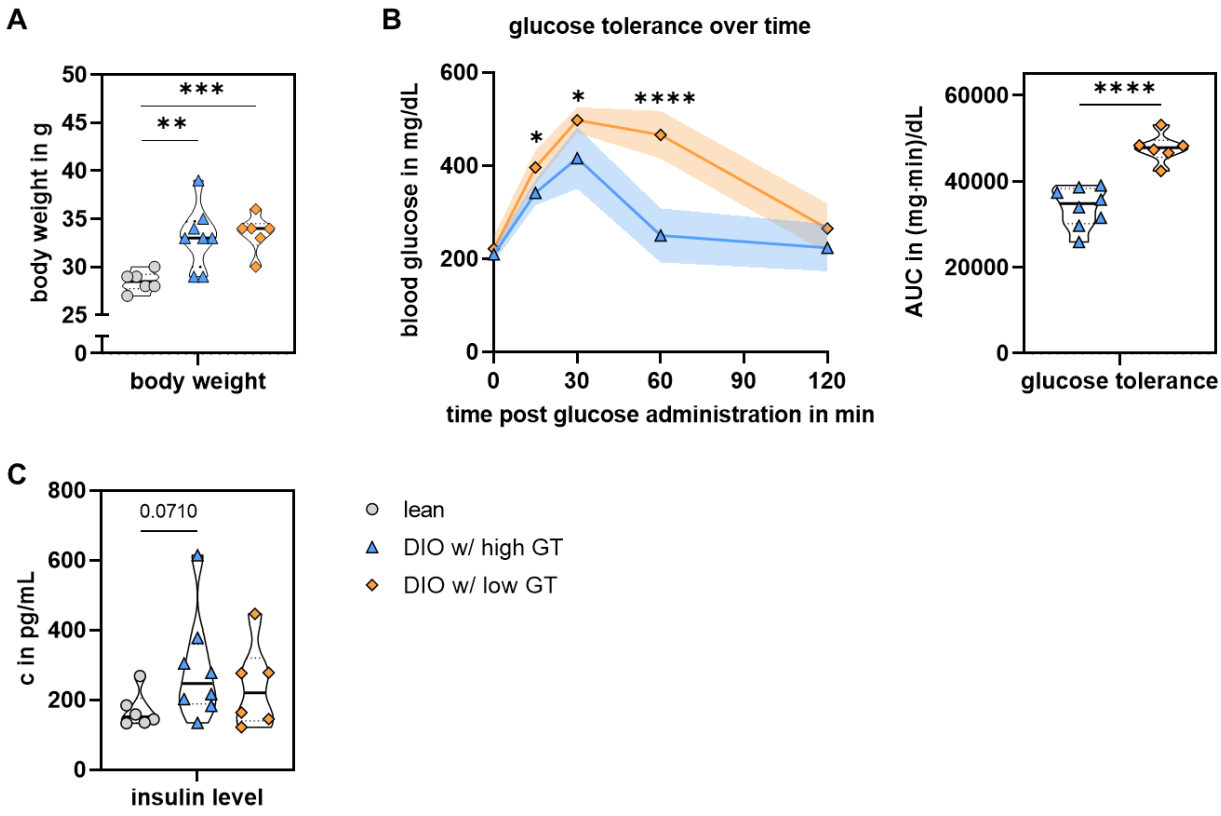

Fig. 9 | Mice exhibited obesity after 7 weeks of HFD. A | Body weight 21d post-surgery. 5-week-old mice were assigned to two groups: the lean control group received a standard diet, while the other group was fed a high-fat diet. Based on their response in the glucose tolerance test (GTT), the HFD group was further classified into obese mice with high or low glucose tolerance (GT). After a 7-week feeding period, all mice underwent a femoral osteotomy. **B |** GTT one week prior to femoral surgery. Mice were fasted for 4h and after injection (i.p) of 1 mg glucose/g body weight, blood glucose levels were monitored at specific time points post-glucose administration. The area under the curve (AUC) was calculated from the data obtained during the GTT. **C |** Determination of non-fasting plasma insulin levels 21d post-fracture. Median and interquartile range (IQR)/mean ± SD, *p<0.05, **p<0.01, ***p<0.001, ****p<0.0001. N=6-8 per group, Welch's t test

3.1.2 Macrophages from bone marrow were altered by obesity during bone remodeling

Obesity drives significant immune changes, particularly in macrophages, which play a major role in inflammation and constitute a significant cellular population in adipose tissue (AT) [157]. In parallel, macrophages take over an important part in the early stages of bone healing by invading the new lesion site and initiating immune reactions [158]. Dendritic cells (DCs) also participate in bone repair, especially by initiating and modifying the immune function of $CD8^+$ T cells [159]. However, in the context of obesity, DCs have been linked to disrupted immune responses and the progression of chronic low-grade inflammation [160]. In the present study, identification of macrophage and DC subsets of intact contralateral bone marrow (BM) by flow cytometry aimed to determine its impact on obese bone inflammation and the potential effect on fracture healing.

Herein, the bone fracture was introduced in the left femur by external fixation of 12-week-old mice after 7 weeks of diet. Analysis was performed using intact BM from the contralateral femur 21d after osteotomy, while the fractured bone was analyzed using micro-computed x-ray tomography and histology.

The investigation revealed comparable abundancies of $CD11b^+$ macrophages as well as $CD11c^+$ and $CD11b^+CD11c^+$ DCs in lean and obese mice (Fig. 10, A). DCs were less present and attracted to untreated BM (< 2,5%) in contrast to the macrophage compartment, mounting up to 13% of $CD45^+$ cells. Further phenotyping of macrophages enabled their classification into resting M0, pro-inflammatory M1 and alternatively activated M2 macrophages. Among the M2 subset, the different subtypes M2a, M2b, M2c and M2d can be identified, based on their specific cytokine secretion profiles and biological functions. The resting M0 subclass constituted the majority of the macrophage population in all experimental groups, without significant differences (Fig. 10, B). However, significant elevations of pro-inflammatory M1 macrophages were observed in DIO mice with high GT, and an increased tendency was revealed in the obese low GT group. Both obese groups additionally showed decreased frequencies of inactivated M2c macrophages, while the anti-inflammatory M2a and M2b subsets were not significantly altered by obesity. Moreover, obese mice with low GT were reduced in the proangiogenic M2d subset compared to lean mice.

Along with obesity-associates changes in the M2 subsets, the results indicate that the intact contralateral BM is slightly prone to pro-inflammation as consequence of obesity. Thus, this obesity-induced macrophage switch could be a considerable determinant for defective healing.

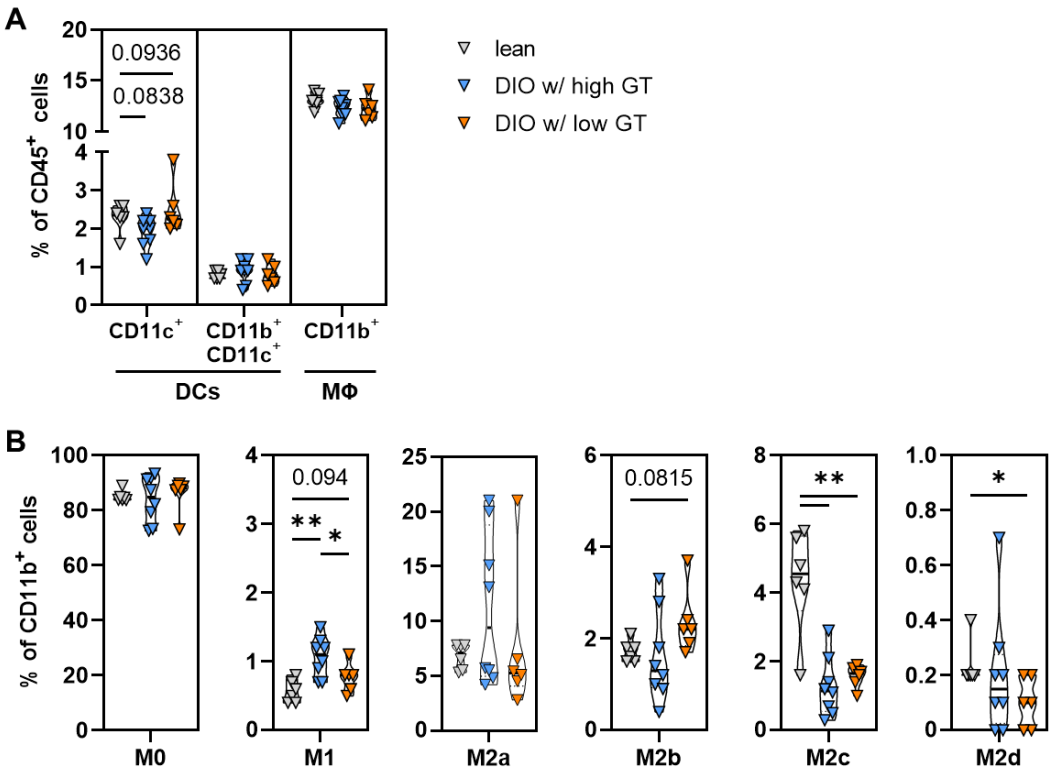

Fig. 10 | Analysis of dendritic cell and macrophage populations in intact bone marrow revealed minor changes due to obesity 21d post-surgery. A | Flow cytometric evaluation of dendritic cells (DCs) and macrophages (MΦs) did not reveal significant changes between lean and obese mice. **B |** Compared to lean mice, phenotyping of macrophages revealed increased frequencies of pro-inflammtory M1 cells, particularly in obese mice with high GT. Both obese groups showed a significant reduction in the inactivated M2c macrophage subset. In addition, obese mice with low GT exhibited a significant decrease in the numbers of the M2d subset. M2a and M2b macrophages were not affected by obesity. Median and IQR**,** *p<0.05, **p<0.01. N=6-8 per group, Welch's t test

3.1.3 Systemic obesity-associated alterations of T cells during bone remodeling

While previous research has focused on the contributions of innate immune cells like macrophages to metabolic diseases, adaptive immune cells, particularly T cells, have garnered significant attention. T cell functions and their interaction within the affected tissues are being recognized as important contributors to obesity development and progression. Therefore, the objective of this study was to investigate the effects of glucose intolerance associated with obesity on the development of T cell immunity. As described, the HFD group was divided into subgroups based on the responses to glucose tolerance testing, referred to as obese high GT and obese low GT mice. T cells from spleen and intact contralateral BM were investigated by flow cytometry 21d after the introduction of the fracture, while the fractured bone was analyzed using micro-computed x-ray tomography and histology.

The experimental groups in the study showed consistent levels of systemic $CD3^+$ T cells in the spleen (Fig. 11, A). Additionally, the $CD4^+$ and $CD8^+$ T cell compartments remained constant across

all the experimental groups (Fig. 11, B). Interestingly, the investigation revealed a significant increase in TCRγδ$^+$ T cells in obese mice compared to controls (Fig. 11, B).

Despite similar CD4$^+$ and CD8$^+$ T cell percentages, obesity caused notable changes in the systemic immunological memory. Specifically, it resulted in a shift of the naive CD8$^+$ T cell pool towards an experienced effector memory phenotype, with naive T cells being the predominant population. This observation was particularly evident in DIO mice with high GT, while DIO mice with low GT exhibited a trend towards increased CD8$^+$ memory T cells ($p=0.0601$). Similar alterations were observed in the CD4$^+$ T cell population of obese high GT mice, with a decreased proportion of naive CD4$^+$ T cells and a slight increase in the number of CD4$^+$ memory T cells compared to control mice (Fig. 11, C). Remarkably, the analysis revealed significant differences within the CD4$^+$ T cell compartment when comparing the DIO groups, while the frequencies were similar between lean and obese low GT mice. These observations suggest that the onset of glucose intolerance in obese mice with high GT may markedly influence the differentiation and phenotype of CD4$^+$ and CD8$^+$ T cells, leading to changes in the distribution of naïve and memory subsets.

Furthermore, the investigation revealed obesity-induced changes in the intact bone marrow of the contralateral femur, specifically in the abundance of CD3$^+$ T cells. The analysis found a significant accumulation of CD3$^+$ T cells in the obese groups, with more pronounced effects observed in obese high GT mice compared to controls (Fig. 11, E). However, the frequency of TCRγδ$^+$, CD4$^+$ and CD8$^+$ T cells remained unchanged despite the observed alterations in CD3$^+$ T cells (Fig. 11, F).

The distribution of naïve and memory T cells is reversed in the bone marrow compared to the spleen, with memory T cells being the dominant population. The evaluation of the CD4$^+$ T cell compartment did not reveal significant differences between the experimental groups. However, obese mice with high GT exhibited a significant reduction in the proportion of naive CD8$^+$ T cells, accompanied by a significant increase in the accumulation of CD8$^+$ memory T cells. In contrast, low GT mice displayed similar levels of naive and memory CD8$^+$ T cells as lean mice.

In summary, the study investigated the influence of glucose intolerance associated with obesity on T cell immune responses. The analysis revealed changes in the CD3$^+$ T cell population both systemically and locally in the bone marrow. Surprisingly, mild metabolic disturbances characterized by high GT showed an elevated experienced immunity that exceeds the memory development of progressed metabolic changes in obese low GT mice. This finding supports the initial hypothesis and importance to take different states of glucose intolerance into consideration. Notably, the early onset of glucose intolerance leads to significant cellular changes that potentially contribute to pro-inflammatory actions, which stabilize during disease progression.

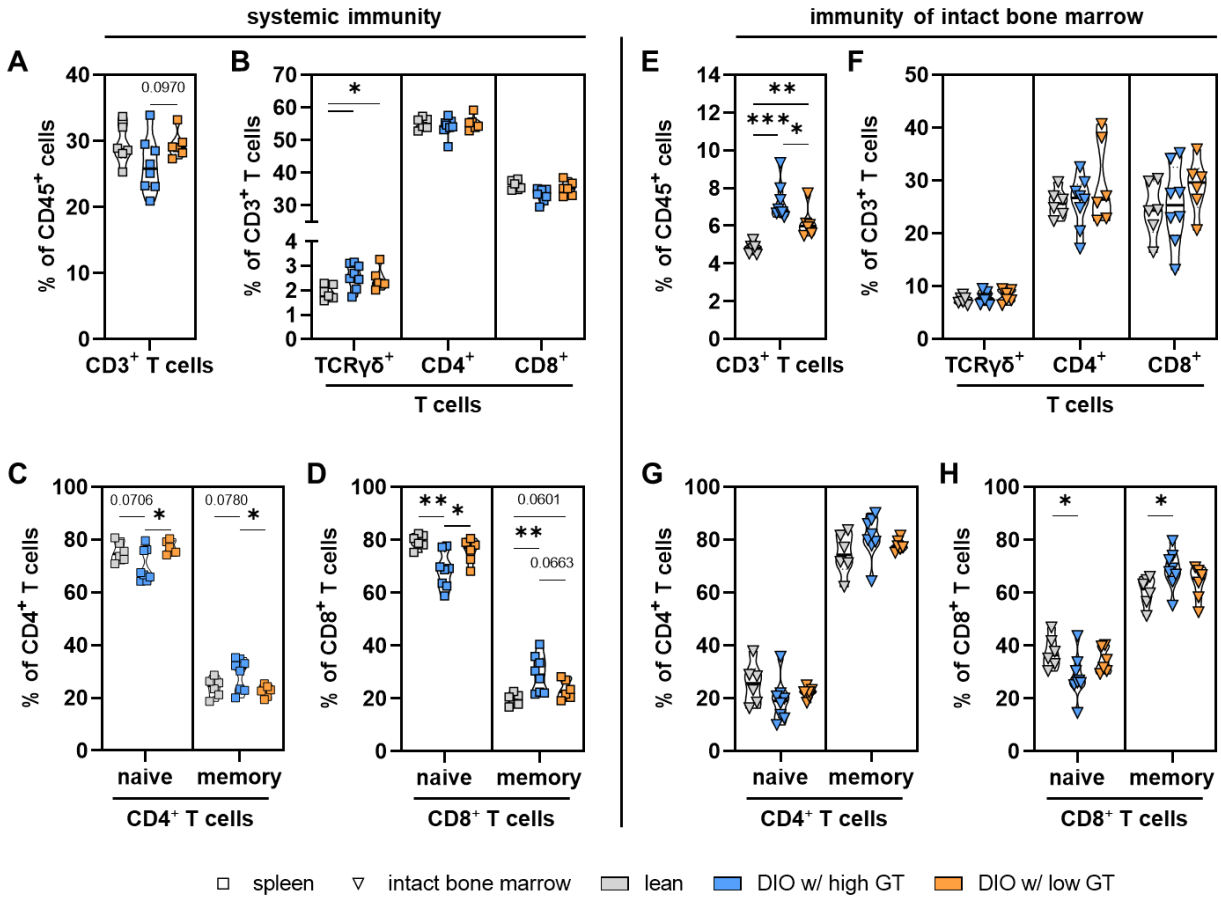

Fig. 11 | The adaptive T cell immunity significantly changed due to obesity. Flow cytometry analysis of the T cell phenotypes in the spleen (A-D) and bone marrow (E-H) 21d post-fracture. Significant increased abundances of systemic TCRγδ⁺ T cells were observed in obese groups compared to the control mice. Notably, CD3⁺ T cells accumulated in the contralateral bone marrow, indicating a strong immune reaction. Interestingly, the frequency of CD8⁺ effector/memory T cells was significantly increased in high GT mice in both the spleen and bone marrow, compared to the control group. Median and IQR, *p<0.05, **p<0.01, ***p<0.001. N=6-8 per group, Welch's t test

3.1.4 Obesity changed the abundance of CD4⁺ Thelper cells and induced a pro-inflammatory environment driven by Th17 cells

T cell immunity and obesity are strongly interlinked, with CD4⁺ T cells playing a crucial role in initiating and sustaining pro-inflammation [140, 161]. The investigation of Thelper cell subsets aimed to identify the immunological fingerprint shaped by obesity in these T cell populations. Flow cytometry was used to examine T cells present in the spleen and the intact contralateral bone marrow 21d after the osteotomy (Fig. 12), while the fractured bone was analyzed using micro-computed x-ray tomography and histology.

The pro-inflammatory (Tbet⁺) Th1 and anti-inflammatory (GATA3⁺) Th2 responses were significantly reduced in both obese groups compared to the control group at 21d post-fracture (Fig. 12, A). This suggests a shifted immune reaction due to obesity following a fracture.

Substantial alterations were observed in the systemic pro-inflammatory (RORγt$^+$) Th17 compartment. Both obese groups exhibited significantly increased frequencies of Th17 cells compared to lean mice (Fig. 12, B). This change coincided with elevated levels of memory CD4$^+$CD25^{hi}FoxP3$^+$ T cells, which are likely indicative of the Treg cell phenotype, in obese mice with high GT (Fig. 12, B). In contrast, obese low GT mice showed a trend towards higher levels of these cells (p=0.0545). Interestingly, the calculation of the ratio of CD4$^+$CD25^{hi}FoxP3$^+$ T cells to Th17 cells decreased by more than a factor of 2 in both DIO groups compared to lean mice (Fig. 12, B). In addition, CD4$^+$CD25^{hi}FoxP3$^+$ T cells can undergo reprogramming into another subtype that resembles Th17 cells in phenotype and function, termed as FoxP3$^+$ Th17 cells. Despite the observed disbalance in CD4$^+$CD25^{hi}FoxP3$^+$ T cells and Th17 cells, the presence of FoxP3$^+$ Th17 cells was consistent across all experimental groups and unaffected by obesity (Fig. 12, A).

Effects observed in CD4$^+$CD25^{hi}FoxP3$^+$ T cells were similarly shown in systemic regulatory CD8$^+$ FoxP3$^+$ T cells. Both obese groups exhibited significantly higher proportions of naive and memory CD8$^+$FoxP3$^+$ T cells compared to lean mice (Fig. 12, C). Thus, these findings suggest that the regulation of the adaptive immune system is enhanced in obese mice.

Analysis of the intact contralateral bone marrow showed fewer immunological alterations compared to the spleen. Significant increases were primarily observed in obese mice with high GT in terms of FoxP3$^+$ Th17 cells, Th17 cells and CD8$^+$FoxP3$^+$ T cells. In addition, the DIO group with low GT significantly accumulated CD4$^+$CD25^{hi}FoxP3$^+$ cells, which was similarly seen in the spleen. Unlike the systemic analysis, the evaluation of the CD4$^+$CD25^{hi}FoxP3$^+$/Th17 ratio did not reveal significant differences, suggesting that the imbalance observed was systemic rather than specific to the tissue.

Herein, significant changes in the adaptive Thelper phenotype were observed both systemically and partially in the intact bone marrow. Particularly, in obese mice with high GT a notable stimulation of pro-inflammatory Th17 cells was observed, similar to the effects seen in obese low GT mice. These findings emphasize the importance of considering glucose intolerance as a clinical risk factor that can influence cellular changes, including bone fracture healing, even in the early stages of obesity.

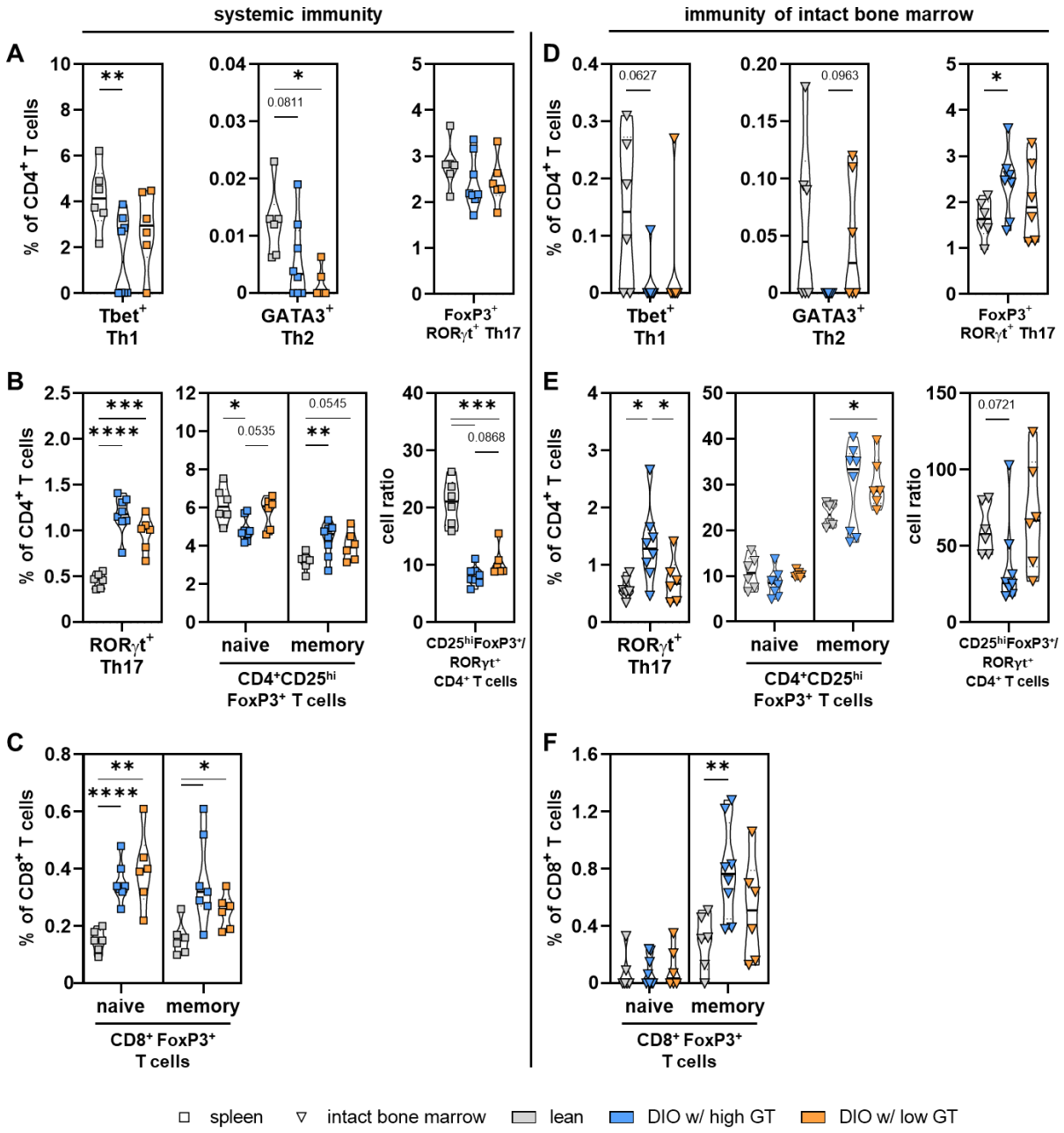

Fig. 12 | Obesity systemically changed the frequency of Thelper cells. A-C | Systemic analysis of Thelper subsets of spleen by flow cytometry 21d after surgery. **A |** The investigation revealed an attenuated and therefore shifted Th1 and Th2 response in obese mice compared to controls. **B |** Both obese groups significantly accumulated Th17 and $CD4^+CD25^{hi}FoxP3^+$ T cells, however resulting in a decreased $CD4^+CD25^{hi}FoxP3^+$/Th17 ratio in DIO mice compared to controls. **C |** Similarly to $CD4^+CD25^{hi}FoxP3^+$ T cells, the obese $CD8^+FoxP3^+$ T cell compartment significantly increased in comparison to lean mice, indicating a strong regulation of the adaptive immunity due to obesity. **D-F |** Analysis of contralateral intact bone marrow revealed less phenotypic Thelper changes 21d post-osteotomy. **D |** Th1 and Th2 responses were not altered in the bone marrow, while DIO mice with high GT significantly increased $FoxP3^+$Th17 cells compared to controls. **E |** In addition, the obese group with high GT exhibited an increased frequency of Th17 cells, while the $CD4^+CD25^{hi}FoxP3^+$ T cell compartment showed slight changes. In contrast, DIO mice with low GT revealed significantly increased proportions of $CD4^+CD25^{hi}FoxP3^+$ T cells. Unlike the systemic evaluation, the $CD4^+CD25^{hi}FoxP3^+$ T cell/Th17 cell ratio was not changed in the bone marrow. **F |** As observed in the spleen, obese mice with high GT exhibited significantly elevated levels of $CD8^+FoxP3^+$ T cells compared to the lean group. Median and IQR, *p<0.05, **p<0.01, ***p<0.001, ****p<0.0001. N=6-8 per group, Welch's t test

3.1.5 Th17-associated cytokines induced by obesity dominate the systemic secretion profile during late-stage bone healing

T cells express a broad spectrum of cytokines, forming a communication network that plays a crucial role in obese tissue inflammation and fracture healing. To study the changes regulated by T cells, blood plasma from lean and obese mice with high and low GT was analyzed using a multiplexed immunosorbent assay to detect T helper cell-related cytokines 21d after the surgery.

During the bone remodeling phase, circulating cytokines including tumor necrosis factor-α (TNF-α), interleukin-2 (IL-2), IL-6, IL-5, and IL-13 were induced in all experimental groups. However, no significant differences were observed related to obesity (Fig. 13).

But notably, the systemic secretion of IL-9, IL-17F, and IL-22 was significantly elevated in both obese groups compared to lean mice (Fig. 13). These cytokines are part of the secretion profile of Th17 cells and support the findings obtained from flow cytometry. Specifically, IL-17F and IL-22 are known to promote a pro-inflammatory environment in the tissue [159, 162]. IL-4, which is anti-inflammatory and primarily secreted by Th2 cells [163], additionally showed slightly higher concentrations in obese mice with high GT and significantly increased levels in DIO mice with low GT compared to the control group (Fig. 13).

In summary, the results support the hypothesis that obesity induces adaptive immune responses, particularly within the Th17 axis. Remarkably, these changes were equally or even more pronounced in obese mice with high GT, highlighting the significant detrimental effects during the early stages of glucose intolerance development. Furthermore, the findings suggest that pro-inflammation may not increase with progressing metabolic disturbances in obese mice with low GT, suggesting a potential adaptive response to mitigate metabolic inflammation.

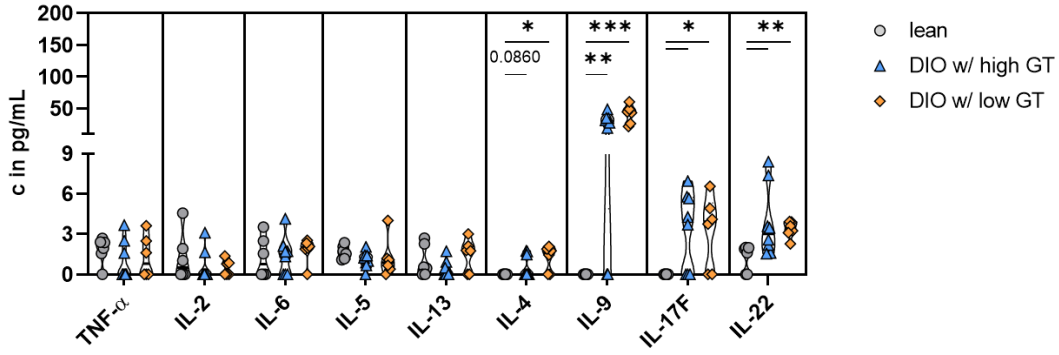

Fig. 13 | The analysis of T cell-related cytokines revealed significant changes induced by obesity. Systemic cytokines were measured 21d post-fracture from blood plasma of lean and obese mice. Compared to controls, obesity significantly stimulated the production of the pro-inflammatory cytokines IL-17F and IL-22, which belong to the cytokine secretion profile of Th17 cells. The analysis additionally revealed increased levels of IL-4 and, to the highest extent, IL-9, both of which are known to play a role in regulating inflammatory immunity. Median and IQR, *p<0.05, **p<0.01, ***p<0.001. N=6-8 per group, Welch's t test

3.1.6 Cellular indexing of transcriptome sequencing confirmed the expansion of likely CD4⁺ Treg cells associated with obesity

To complement the *ex vivo* findings, single-cell RNA sequencing (scRNAseq) was conducted on blood T cells from lean and obese mice. Due to sample size limitations, only obese mice with low GT were compared to controls 7d post-fracture. This earlier timepoint aimed to provide further insights into the systemic impact of obesity-induced glucose intolerance on the development of T cell immunity during initial bone repair. Another focus was to evaluate functional differences during the resolution of inflammation, as the previous analysis has shown an imbalance of pro- and anti-inflammatory T cell responses. In preparation for the analysis, T cells were isolated using untouched magnetic activated cell sorting. For the scRNAseq, the final T cell suspensions were labeled with unique oligo-tagged antibodies specific to ubiquitous surface proteins. This step enabled pooling and indexing of biological replicates per group. Subsequently, the generated transcripts of individual cells were sequenced.

The total number of cells that passed the quality control filter were 5687 from lean and 7115 from obese mice. Data were visualized using the t-distributed stochastic neighbor embedding (t-SNE) (Fig. 14, A). The clustering and marker gene annotation identified 8 distinct populations in conjunction with external data that provide well defined transcriptomic signatures of various murine immune cell populations [164]. Herein, two clusters divide at approximately 0 of the first t-SNE axis which separates $CD4^+$ from $CD8^+$ T cells. The $CD8^+$ T cell population was categorized into three subclusters, while the $CD4^+$ T cell population was divided into four subsets. These subclusters represented naïve, memory, and effector T cells, as well as likely $CD4^+$ Treg cells from top to bottom of the t-SNE map. The separation is warranted by the gradual expression of for example CD44, Nkg7, Itgb1 and Sell (CD62L). Likely $CD4^+$ Treg cells were identified as *Il7r* (CD127), high *Foxp3*, *Il2ra* and *Ctla4* expressing cluster, however activated $CD4^+$ non-Treg cells cannot be fully excluded as these cells may exhibit overlapping transcriptomic signatures. The $CD8^+$ T cell population additionally consisted of cells that were annotated as natural killer T (NKT) cells or γδ T cells due to transcriptional similarity.

Differential expression (DE) and abundance analysis (DA) using the scRNAseq data were performed to examine changes in gene expression within specific subpopulations (DE) between the groups and to identify compositional changes in cell types (DA). T cell subsets were well represented in all biological replicates (Fig. 14, B). The analysis revealed significant increased levels of likely $CD4^+$ Treg cells, $CD4^+$ memory and $CD4^+$ effector T cells in obese mice compared to lean controls (Fig. 14, B and C). Contrary, the frequencies within the $CD8^+$ T cell compartment were not significantly altered by obesity (Fig. 14, B). These findings recapitulate the results obtained from the flow cytometric analysis and indicate that obesity has a significant impact on $CD4^+$ T cells.

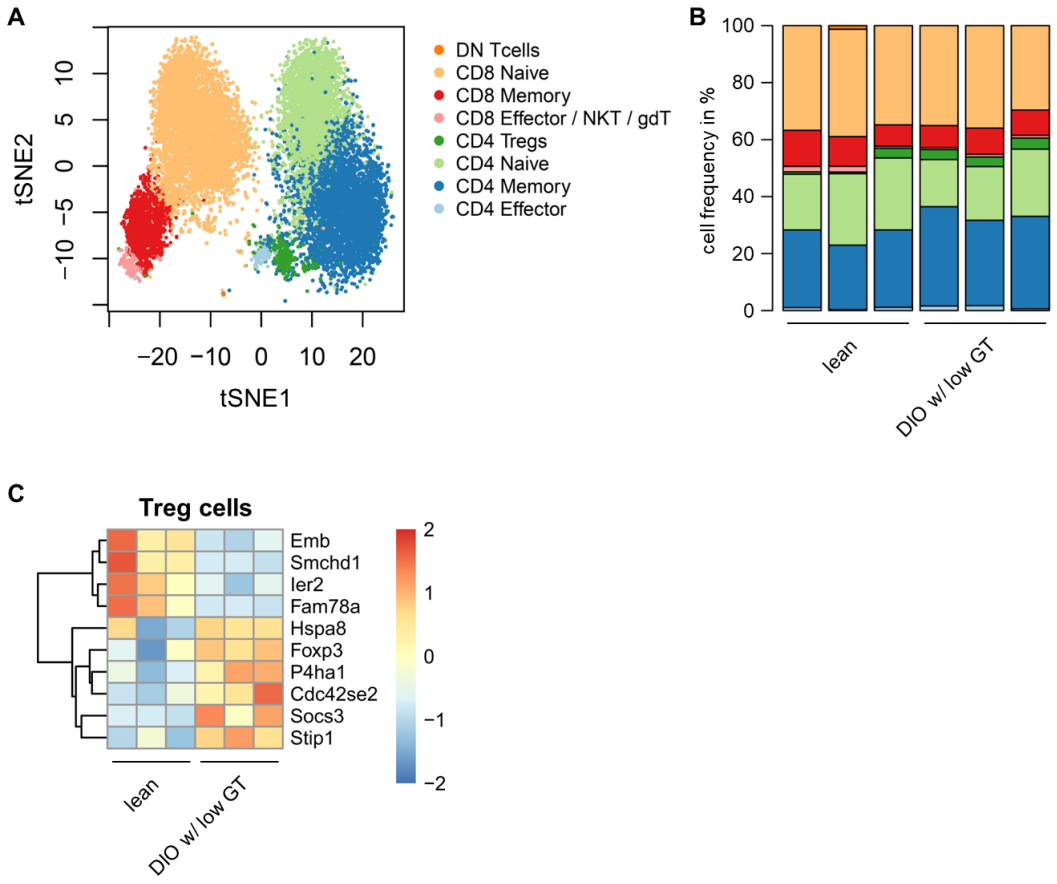

Fig. 14 | Single-cell transcriptomes of blood samples from lean and obese mice with low GT 7d post-fracture. A | UMAP representation of all T cells in peripheral blood of lean and obese mice with low GT. Colors indicate cluster membership identified by using shared nearest neighbor (SNN) modularity optimization. DN: double-negative. **B** | T cell subset abundancies with respective color coding are demonstrated for each sample from lean or DIO low GT mice. **C** | Heatmap of RNA expression of genes associated with likely CD4+ Treg cells were pronounced in DIO low GT mice compared to the lean counterparts. Blue to red color shading shows row Z-scores representing across-samples scaled average counts. N=3 per group

Furthermore, the scRNA seq data were tested for differently regulated pathways and enrichment is represented as log2-fold change when comparing lean over obese mice (Fig. 15). This means that for example a value of 1 represents a two-fold increase in controls, while a value of -1 explains that a pathway in lean mice has only half of the presence or activity as compared to the obese group. Thus, negative values simultaneously illustrate enriched pathways in obese mice. The analysis demonstrated that obesity induced functional differences in T cells. Chemokine (e.g. *Cxcr3*, *Cxcr5*, *Cxcr6* and *Ccr2*) and NOD (nucleotide-binding oligomerization domain)-like (e.g. *Myd88*, *Oas2* and *Ripk1*) receptor pathways were enriched in obese CD4+ T cells in comparison to lean mice (Fig. 15, A; Supp. 1). These pathways primarily control trafficking and inflammation [165-168], which suggests an increased immune activity due to obesity. Obese CD8+ T cells additionally exhibited a significantly stronger expression of type II interferon signaling (e.g. *Ifngr1*, *Irf1*, *Irf9*) that underlines an increased mediation of pro-inflammatory IFN-γ signaling due to obesity (Fig. 15, B). Moreover, CD4+ and CD8+ T cells contained significantly higher levels of genes

that are associated with infections (e.g. Herpes simplex virus 1, Epstein-Barr virus and Legionellosis) in comparison to lean controls, indicating an obesity-mediated T cell activation.

Overall, the scRNAseq data align with the flow cytometric analysis, supporting the observed immune alterations induced by obesity. The functional analysis additionally revealed an increased activity of $CD4^+$ and $CD8^+$ T cells in obese mice, suggesting that these immune cells may have an impact on fracture healing processes.

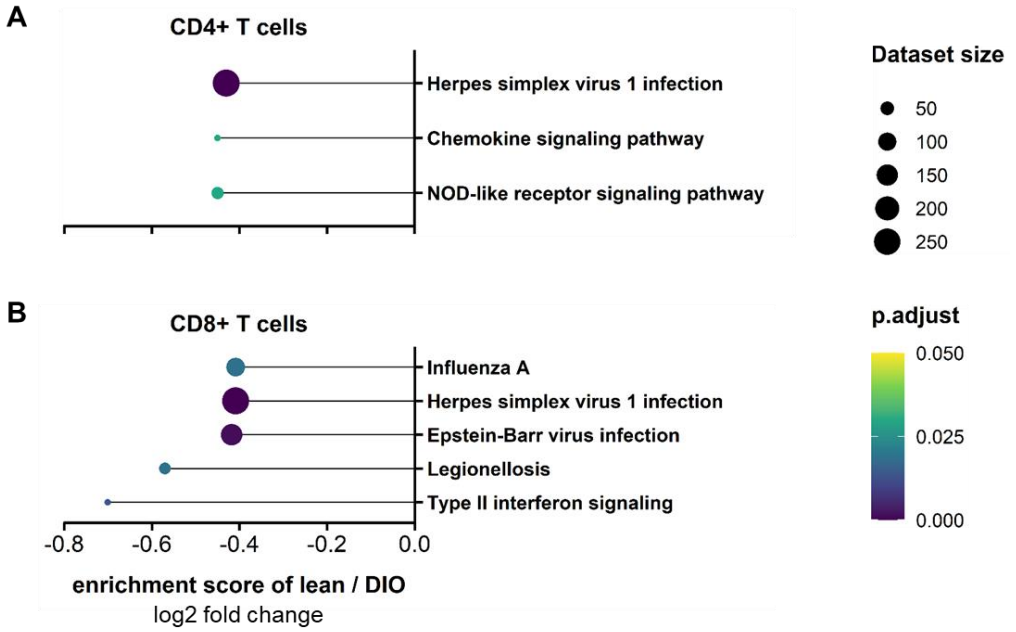

Fig. 15 | Significantly enriched pathways in obese $CD4^+$ (A) and $CD8^+$ T cells (B). Kyoto Encyclopedia of Genes and Genomes (KEGG) and WikiPathways enrichment analysis were conducted using the single cell RNA sequencing data. The vertical coordinates represent the enriched pathways, and the horizontal coordinates are the enrichment scores represented as log2 fold change. The size of each point corresponds to the number of genes included in the dataset, and the color of the point reflects the p-adjust value. The analysis revealed that obese $CD4^+$ and $CD8^+$ T cells are more active than the lean controls in terms of trafficking and inflammation. N=3 per group

3.1.7 Impaired fracture healing in mice with diet-induced obesity

As above mentioned, an osteotomy was administered in the left femur and healing was observed 21d after the surgery. The outcome of fracture healing was determined by micro-computed x-ray tomography (micro-CT) to compare bone repair of lean mice with the obese groups.

The results of the study indicate that obesity had deleterious effects on the process of fracture healing. The micro-CT analysis of fractures in obese mice, in comparison to the controls, revealed an incompletely bridged fracture gap (Fig. 16, A) and a significant reduction in bone volume (BV) relative to total callus volume (TV), described as BV/TV (Fig. 16, B). However, bone mineral density (BMD) and minimal polar moment of inertia (MMIp), which represents a computational calculation of torsional stability, were similar across all experimental groups (Fig. 16, C and D). The mi-

cro-CT analysis further identified differences in the trabecular structure, with a reduced tendency of the trabecular number (Tb.N) in obese high GT mice (Fig. 16, E) and significantly reduced values in obese mice with low GT. However, trabecular spacing and thickness were not significantly affected. Additionally, total porosity was significantly increased in fractures of obese mice compared to lean controls, regardless of the glucose intolerance status.

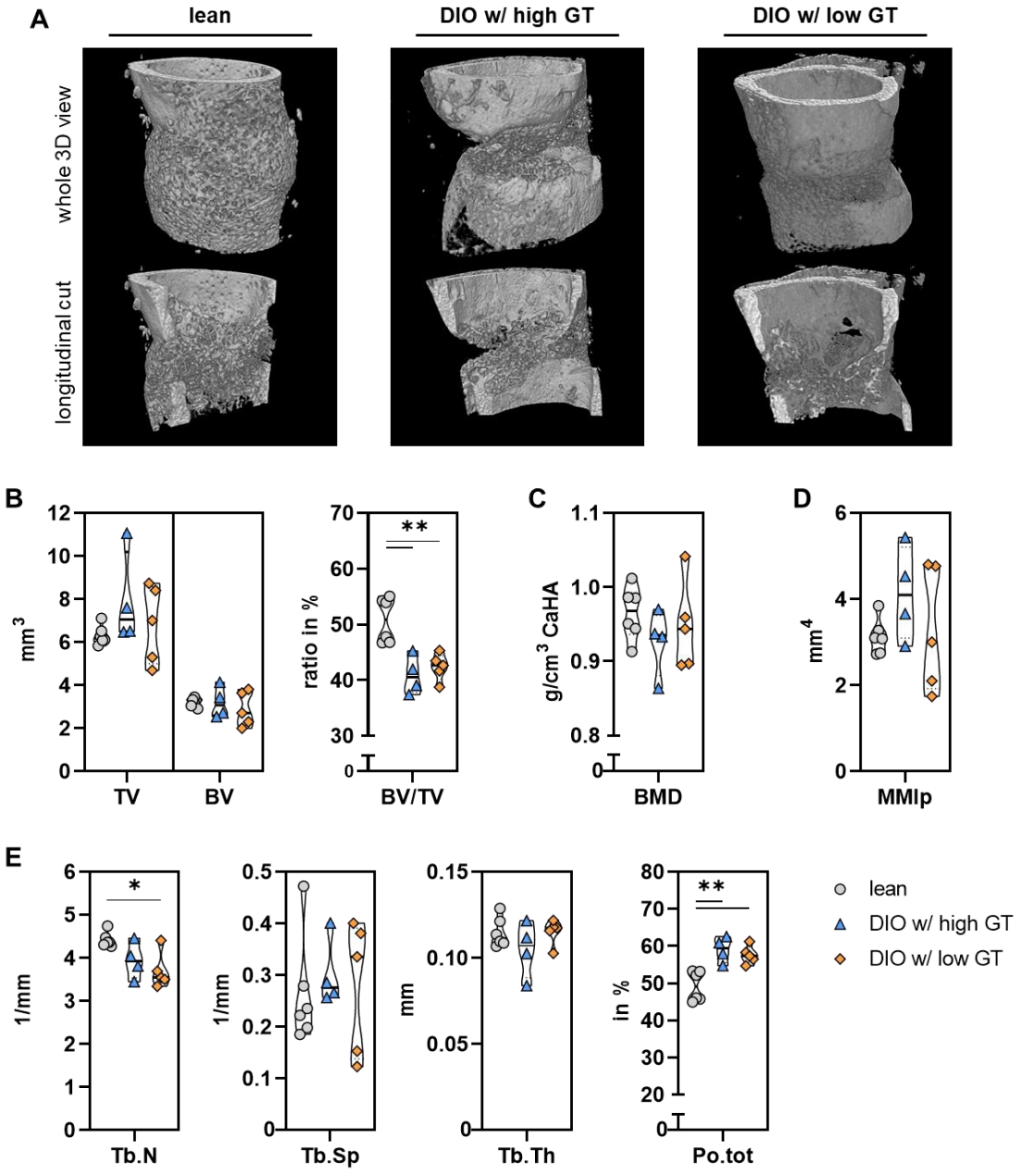

Fig. 16 | Analysis of the osteotomy gap unveiled impaired bone fracture healing in obese mice. **A** | Representative images of the fracture gap 21d post-surgery assessed by micro-computed x-ray tomography in a 2 mm frame. **B** | The callus volume (TV) and bone volume (BV) were comparable between all experimental groups, whereas the ratio of BV to TV (BV/TV) significantly decreased due to obesity. **C, D** | Calculation of bone mineral density (BMD) and minimal polar moment of inertia (MMIp) revealed similarities across all groups. **E** | In contrast, the trabecular architecture, including the trabecular number (Tb.N) and total porosity (Po.tot), was adversely impacted in obese compared to lean mice, with more pronounced effects seen in DIO mice with low GT. However, the spacing of trabeculae (Tb.Sp) and the thickness (Tb.Th) were not significantly altered. Median and IQR, *p<0.05, **p<0.01. N=4-6 per group, Welch's t test

Using the micro-CT data, the fracture gap was further divided into three segments to investigate the healing properties in relation to their location within the long bone. The site-specific analysis revealed that both obese groups showed a significant reduction in newly mineralized bone (BV/TV) compared to lean mice, starting from the center of the gap and progressing towards distal fracture ends (Fig. 17, C). At the proximal fracture site, obese mice with high GT additionally exhibited a significantly increased callus (Fig. 17, A) and bone volume (Fig. 17, B) compared to controls, which correlates with a higher callus stability determined by MMIp (Fig. 17, D).

The data revealed that impaired healing in obese mice occured at the knee suggesting decreased blood and nutrient supply as one potential underlying cause. The results also indicate that bone formation in obese high GT mice is pronounced proximally to compensate for the defect.

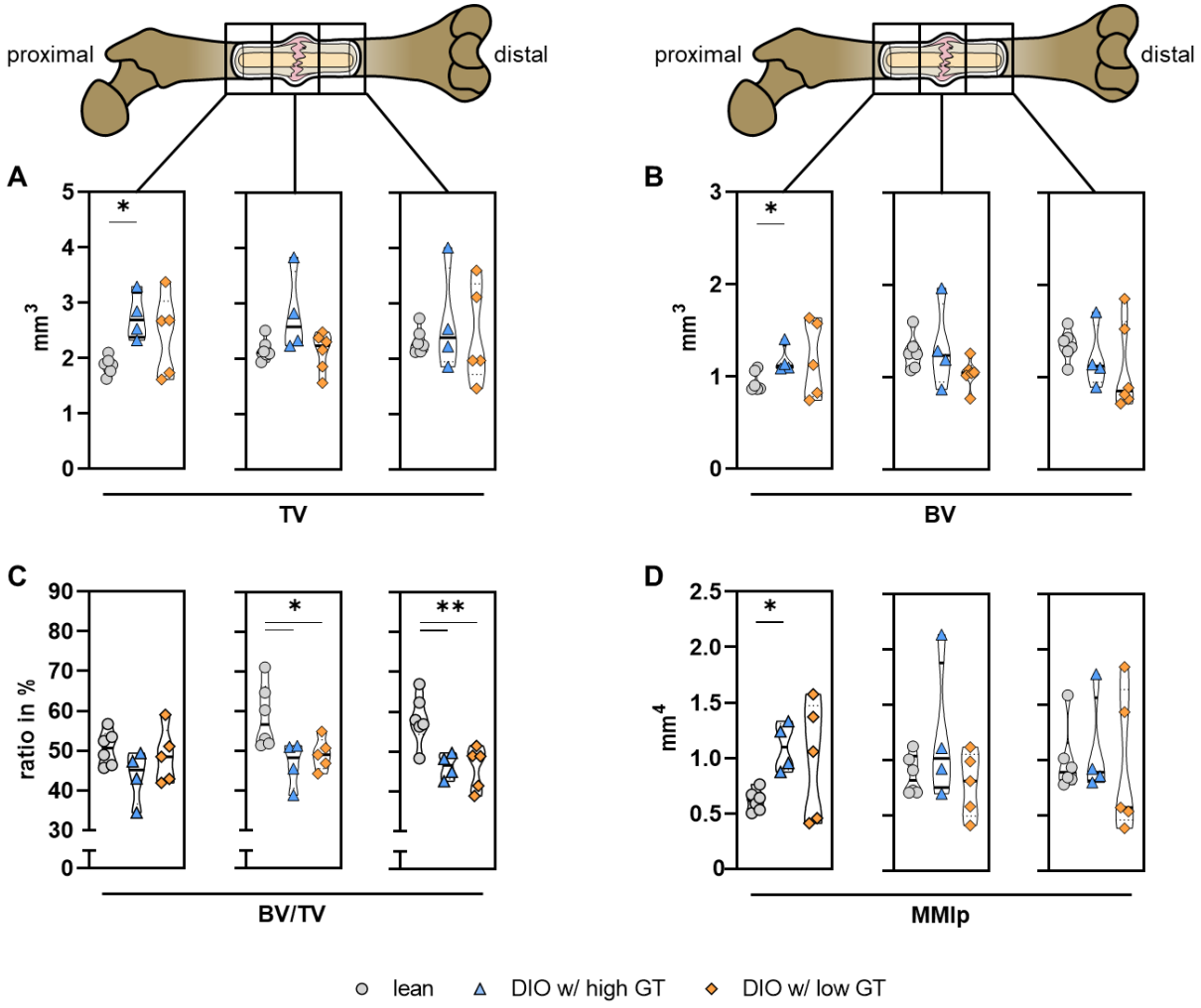

Fig. 17 | Site-specific analysis of bone repair highlights differences in healing progression at the distal fracture site in obese mice, as determined by micro-CT. Significant alterations were detected in terms of BV/TV in both obese groups, particularly at the gap center and distal end **(C).** Moreover, the analysis revealed alterations at the proximal end for obese mice with high GT, including TV **(A)**, BV **(B)** and MMIp **(D)**. Median and IQR, *p<0.05, **p<0.01. N=4-6 per group, Welch's t test

3.1.8 Bone repair in obesity showed accumulation of fibrocartilage tissue

Following the micro-CT evaluation, histomorphometric analysis was conducted using Movat's pentachrome staining to investigate the involved tissues 21d after the surgery. This staining method provides detailed information about different tissue types and their distribution in the fracture site.

The staining of control fractures unveiled a mineralized osteotomy gap, represented in yellow (Fig. 18, A). However, the fracture of obese mice predominantly contained green/blue tissue indicating a gap filled with cartilage and connective tissue, along with fat vacuoles. This finding suggests that in obese mice, the bone fracture healing process is delayed compared to lean controls. By 21d after the fracture introduction, the healing process has not reached the mineralization stage, which is typically observed in lean mice.

Indeed, in mice with high GT, the quantitative evaluation revealed a significant predominance of cartilage (Fig. 18, B). Moreover, obese low GT mice tended to generate connective tissue, assuming a defect in cartilage formation and/or an earlier resorption of the cartilagenous callus. Furthermore, it was observed that the fracture gap in both obese groups exhibited a slightly higher accumulation of fat compared to lean controls ($p<0.0850$). However, these alterations in tissue deposition resulted in a significant decrease in the proportion of bone marrow, with more pronounced effects seen in obese mice with a low GT.

The detected compositional changes associated with obesity in the microenvironment of the healing bone further support the results obtained from micro-CT. Bone repair in obese mice was dominated by a persistent fibrocartilage callus, indicating a delay in the healing process of the bone fracture. A potential determinant for the fracture healing defects in these mice could be an altered chondrocyte and/or osteoblast activity as well as the development of adipose tissue at the expense of osteogenic differentiation.

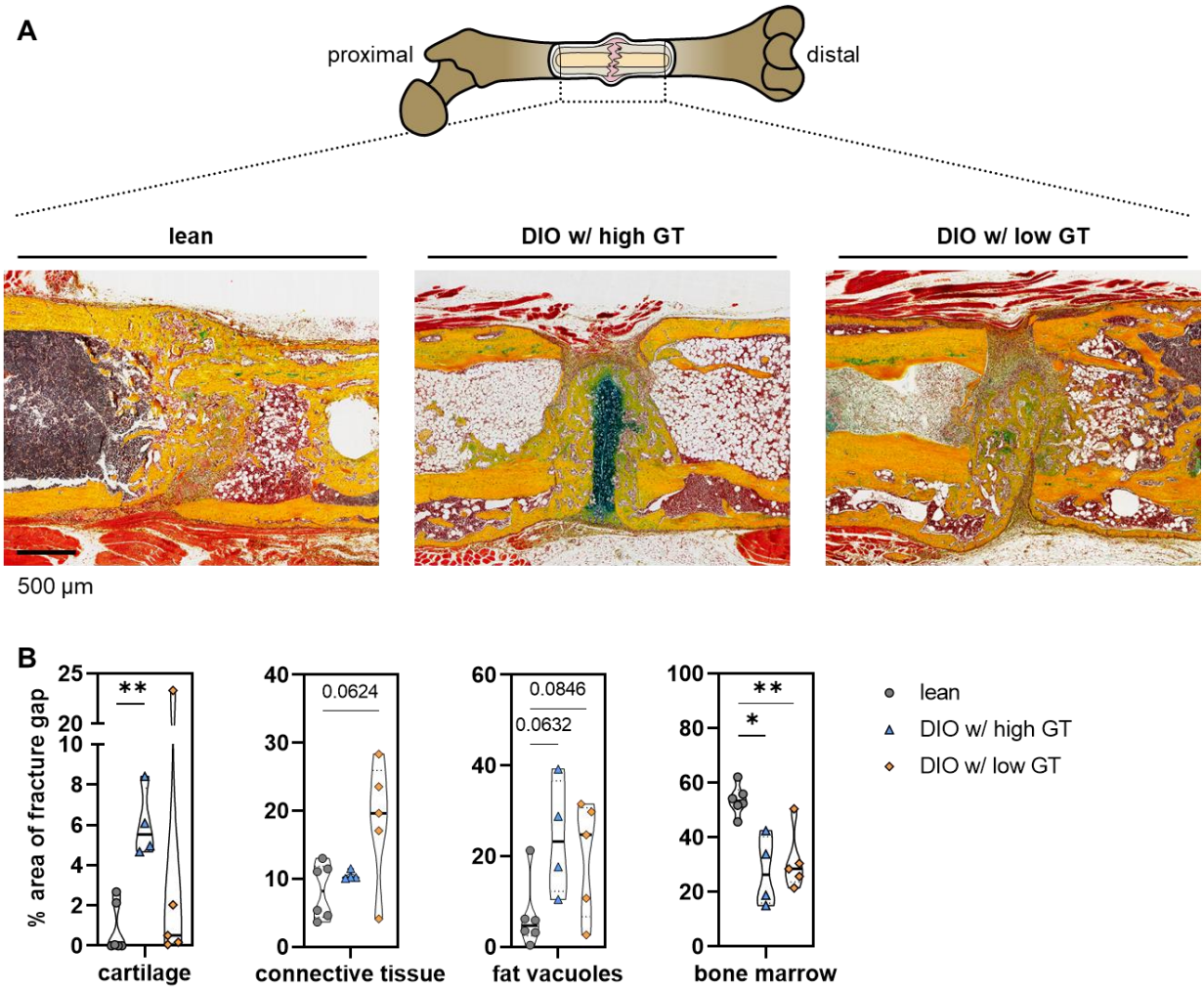

Fig. 18 | Differences in glucose tolerance related to obesity were associated with an altered tissue deposition during bone fracture healing. A | Representative images of fracture healing 3 weeks after osteotomy. Visualization of mineralized bone (yellow), cartilage (blue/green), bone marrow (red) and connective tissue (transluscent blue/green) by Movat's Pentachrome staining in a 3 mm frame. **B** | Evaluation of the relative tissue area to the total callus area. Median and IQR, *p<0.05, **p<0.01. N=4-6 per group, Welch's t test

3.1.9 Col1 deposition and collagen fiber formation in the woven bone were not altered by obesity

The observed differences associated with obesity in terms of cartilage and connective tissue deposition suggest that these alterations may be attributed, in part, to changes in the collagen structure. An immunofluorescent staining of collagen 1 (Col1), which is the most abundant fibrillar collagen in the remodeled callus, aimed to investigate its distribution and abundance within the callus tissue [169].

Col1 was present within the mineralized fracture, connective tissue and cortices, and its abundance was consistently detectable to the same extent in all experimental groups, regardless of the

glucose intolerance status (Fig. 19, A, B and D). These results indicate that the deposition of Col1 during bone remodeling may not be affected by obesity.

However, it should be emphasized that while obesity may not impair Col1 deposition, it can still lead to alterations in the quality of collagen formation. Obesity can potentially impact the structural and functional properties of collagen fibers, leading to alterations in its composition, organization and cross-linking. Collagen proteins are typically composed of three helical strands that undergo an unfolding process during tissue remodeling. Nonetheless, under certain conditions such as obesity-induced T2DM, the assembly and disassembly of collagen strands may be insufficient or altered, leading to pathological changes in the collagen structure [170]. Unfolded collagen can be detected using a synthetic collagen hybridizing peptide (CHP) that consists of the tripeptide sequence glycine-X-Y, which closely resembles the structure of native collagen and enables the hybridization with denatured, unfolded collagen molecules [171]. CHP is described to specifically bind to unfolded collagen strands with negligible binding to collagen helices [171, 172]. Contrary to the assumption that the amount of defective and unfolded collagen strands would increase with progressing glucose intolerance associated with obesity, the proportion of unfolded collagen was comparable between lean and obese groups (Fig. 19, C and D). Instead, the results revealed a process of dynamic bone remodeling that similarly occurred in all experimental groups (Fig. 19, C and D). Interestingly, the CHP signal was detected in areas of the mineralized callus and connective tissue, but not in sites where cartilage had accumulated, which is in contrast to the deposition of Col1. Surprisingly, the cortical areas exhibited a particular abundance of unfolded collagen.

Moreover, the mean fluorescence intensity and the relative area, representing the normalized signal-positive area to the total callus area, were determined to quantify the expression of Col1 and CHP within the fracture gap (Fig. 19, D). As observed by the microscopic images, the fluorescence signals for CHP and Col1, as well as the relative areas positive for CHP and Col1 were found to be comparable between the groups.

In summary, the deposition and arrangement of Col1 and unfolded collagen molecules in the fracture of lean and obese mice were similar. This suggests that diet-induced obesity does not pathologically alter collagen formation and organization in the context of bone fracture healing.

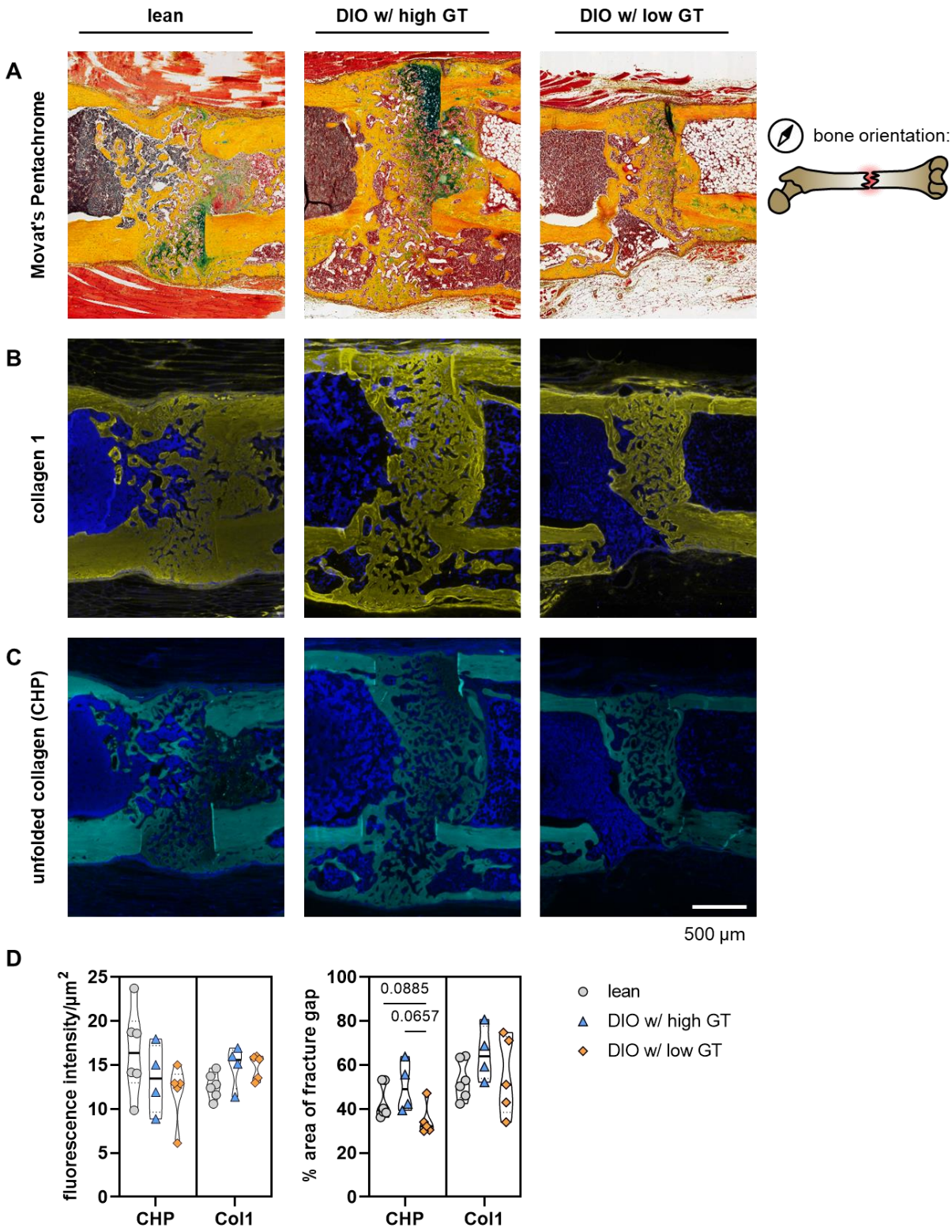

Fig. 19 | The formation of Col1 and unfolded collagen were comparable between lean and obese groups 21d post-fracture. A | Microscopy of corresponding Movat's Pentachrome stained fracture gaps (2mm) from either lean or obese mice with high or low GT. **B |** Representative images of fluorescent Col1 staining (yellow) and DAPI-stained nuclei (blue). **C |** Representative images of IF staining using collagen hybridizing probe (CHP) (cyan) which binds to unfolded collagen molecules. DAPI-stained nuclei in blue. **D |** Quantitation of the mean fluorescence intensities of detected Col1 and CHP signals and calculation of relative Col1- and CHP-stained areas normalized to the analyzed total callus area. Median and IQR. N=4-6 per group, Welch's t test

3.1.10 Blood vessel formation in fractures of obese mice was similar to controls

The findings obtained from the micro-CT analysis additionally raised the question of whether bone regeneration is impaired in obesity due to reduced blood supply, known as angiopathy. Endothelial dysfunction, disrupted neovascularization and the presence of senescent cells are commonly observed in individuals with T2DM [173]. These factors contribute to the development of chronic non-regenerating wounds and potentially impair the bone fracture healing process.

In particular, the micro-CT analysis revealed abnormalities in the callus morphology in obese mice 21d after introducing the fracture. The control mice developed a dense callus, while the defects in the obese groups occurred in the center of the fracture callus. Specifically, obese mice with high GT partially formed tube-like bridges along the cortex site, whereas obese mice with low GT partially exhibited sparse and hollow calli (Fig. 20, A).

Therefore, immunohistochemical staining of blood vessels aimed to investigate the potential impairment in vascularization. In this study, CD31 was used as a marker for tube formation, which is a type I transmembrane glycoprotein and constitutively expressed on angio-vasculogenic endothelial cells [149].

In all experimental groups, blood vessel formation was detectable in the newly mineralized bone, the bone marrow and fat tissue (Fig. 18, B). Moreover, the quantitation of the relative $CD31^+$-stained area in fractures of both lean and obese mice demonstrated similar results (Fig. 20, C). This suggests that the level of vascularization in the fractured bones was comparable between the experimental groups, despite their different metabolic states.

Furthermore, analysis of proximal and distal fracture ends aimed to determine side-specific modifications, as observed by micro-CT. However, the results of this analysis showed similar findings in both control and obese mice, indicating that the process of vascularization occurred uniformly along the fracture, without any local differences between the proximal and distal ends.

In summary, the findings suggest that obesity does not appear to have a significant effect on vascularization during bone fracture healing. Consequently, it is unlikely that angiopathy plays a major role in causing the partial malformations observed in the fracture callus of obese mice.

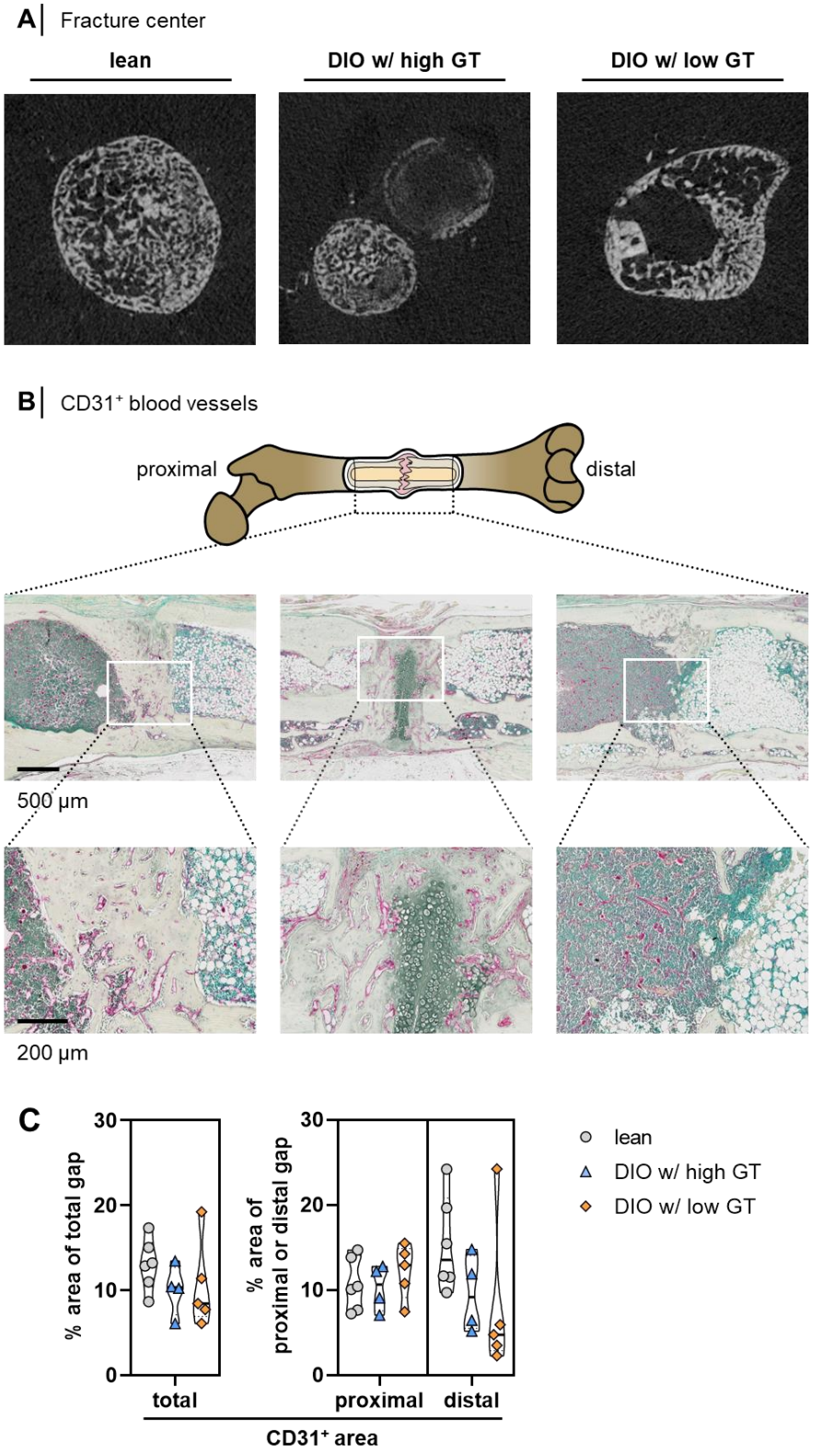

Fig. 20 | Neovascularization was comparable between the fractures of lean and obese mice 21d post-surgery. A | Representative micro-CT images showing differences in the callus center formation. View from top as vertical cut through the bone. **B |** Immunohistochemical staining of CD31⁺ blood vessels (red) within fracture gaps of lean and obese mice with either high or low GT. Methyl green staining was used to assess the background staining of bone marrow, cartilage and muscle tissue (green). **C |** Quantitation of the CD31⁺ area normalized to the total callus area in fractures of lean and obese mice. Median and IQR. N=4-6 per group, Welch's t test

3.2 Long-term obesity altered the bone mineral density and early matrix deposition in bone fractures without affecting the healing outcome

In a subsequent obesity study, the HFD was extended from previously described 7 to 16 weeks, which is further referred to as long-term DIO. This approach was in accordance with DIO experiments conducted by Sbierski-Kind et al. (2018) [30] on which the experimental setup is built upon. This project intended to provide further insights, when obesity is persistent and manifests along with immunological changes. The primary aims of the present study were threefold with respect to different degrees in metabolic changes associated with obesity: (I) to assess additional information about the metabolic differences of the obese groups in terms of insulin resistance, β-cell constitution and fatty liver development; (II) to comprehensively investigate the gut microbial ecosystem, which is acknowledged to be shaped by diet and immunity; (III) to uncover molecular players in fracture repair along with an immunomodulatory intervention to improve healing.

3.2.1 Multiparameter clustering of obese mice based on physiological tests

Obesity was induced by providing 8-week-old mice with high-fat diet (60 kcal% fat) for 16 weeks. Again, control mice received standard chow diet (10 kcal% fat) for the same duration (Fig. 21, A).

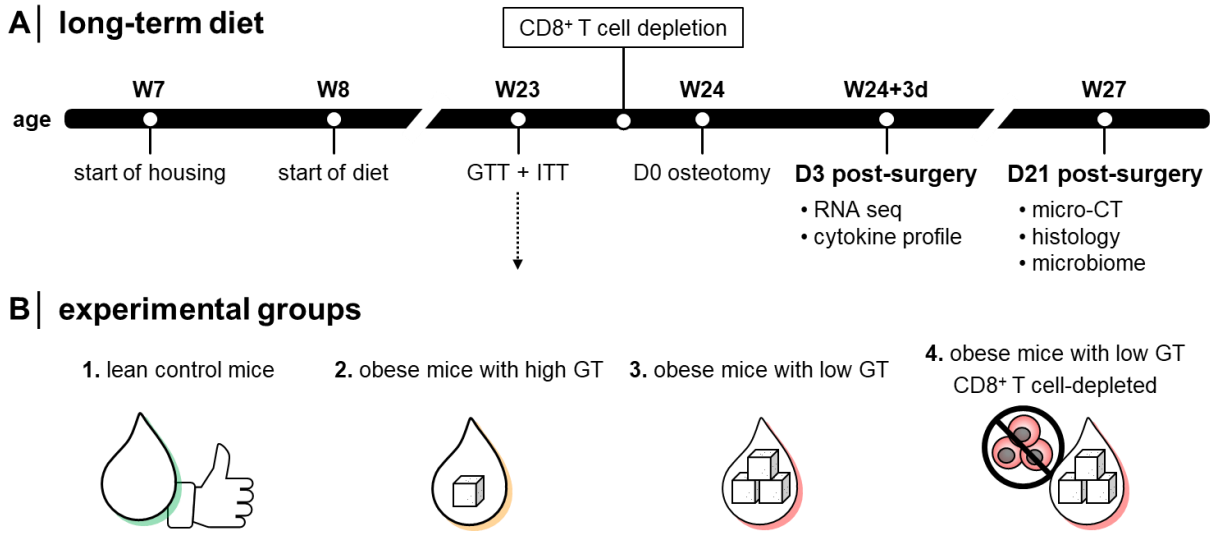

Fig. 21 | Timeline and experimental groups of the long-term *in vivo* HFD-study. A | Mice were transferred to the non-SPF animal facility after arrival and the feeding of the HFD started a week later for 16 weeks, while the control groups simultaneously received standard chow diet. A week prior to surgery, the GTT and ITT were performed to identify the degree of obesity. Animals were sacrificed 3 and 21d after surgery for in-depth analysis of the bone healing outcome (micro-CT and histology), immunoprofile and microbiota. **B |** The experimental groups compare lean control mice (1) with obese mice that either developed high (2) or low GT (3) after HFD. Selected animals of the obese low GT group additionally received a $CD8^+$ T cell-depleting antibody (4) to investigate the contribution of $CD8^+$ T cells to bone fracture healing in obesity. micro-CT: micro-computed X-ray tomography, seq: sequencing.

In the short-term study, categorization of obese mice to the respective HFD subgroup was accomplished by a determined AUC value obtained from the GTT. However, in the long-term study, the classification was achieved by using the kmeans algorithm for clustering and the PCA for visualization (Fig. 22, A). To the best of my knowledge, this is the first described approach that allows unbiased stratification of different HFD responders. This operation takes into account the complexity of data obtained from additional physiological measurements performed in the long-term study compared to the short-term project. Parameters such as weight one week prior to surgery, weight gain over time due to the extended diet, and results obtained from the glucose tolerance test as well as insulin tolerance test (ITT) were included in the computational clustering to achieve the stratification. It is important to note that in order to find the optimal approach, two other plausible combinations of data packages were investigated. The first combination involved using results from the GTT and ITT, while the second combination included either weight or weight gain over time along with data from the GTT and ITT. After comparing the clusters obtained from the different input datasets, inclusion of the mentioned four parameters provided the most suitable clustering concept. The previous designation of the experimental groups was retained in the long-term study, illustrating the two obese subtypes with either high or low GT.

The project also investigated the potential effects mediated by an increased $CD8^+$ T cell response during bone fracture healing in obese mice, drawing from the DIO study conducted by Sbierski-Kind, et al. (2018) [30], as a reference to explore the role of $CD8^+$ T cells in this context. For that, the group that received the HFD and developed severe glucose intolerance and insulin resistance (low GT) was further divided into two subgroups. One of these subgroups underwent a depletion of $CD8^+$ T cells. This technique has previously confirmed a beneficial effect on bone fracture healing in context of terminally differentiated $CD8^+$ T cells by systemic and local removal in the bone marrow [88]. Even though mice were treated after clustering, the $CD8^+$ T cell-depleted HFD group is already depicted in the following illustrations to ensure similarity between both DIO groups with low GT in regards to metabolic parameters.

When compared to the starting weight, obese mice with high GT exhibited 74,3 (± 16,9) % increase in body weight, the low GT DIO group reached a growth of 76,5 (±16,9) % and obese $CD8^+$ T cell-depleted mice with low GT accumulated 59,4 (± 14,2) % of weight, whereas lean mice only gained 27,9 (± 7,7) % body weight (Fig. 22, B). The final body weights one week prior to surgery, revealed a significant difference between both obese groups with low GT compared to obese mice with high GT (Fig. 22, B). This should be considered since possible differences in mechanical loading and acquisition of bone due to body weight gain can occur. Nonetheless, even when the clustering analysis was performed without including body weight data, significant differences in body weight between obese mice with high and low GT could not be eliminated. This observation suggests a correlation between body weight gain, glucose and insulin resistance.

In addition to weight monitoring, lean mice showed a proper glucose elimination in the GTT, rapidly reaching peak blood glucose concentrations post-administration and returning to basal concentrations shortly after (Fig. 22, C). In a striking contrast, all obese groups plateaued at significantly higher values. DIO high GT and control mice reached highest levels at a similar timepoint, whereas DIO groups with low GT exhibited a delayed response. Calculation of the AUC validated these observations, demonstrating significant differences between control and obese mice as well as obese mice with high GT compared to both DIO groups with low GT.

The ITT additionally aimed to investigate insulin sensitivity by measuring the degree to which blood glucose levels decrease after insulin administration. The control mice rapidly reduced their glucose levels as a result of insulin action, whereas the obese groups demonstrated a compromised response to the insulin load, which was indicated by only a slight decrease in glucose levels (Fig. 22, D). This suggests an impairment in insulin sensitivity with more pronounced effects observed in both obese groups with low GT. Calculation of the AUC confirmed a significant difference between lean and obese mice, as well as between the obese group with high GT and the obese low GT mice (Fig. 22, D).

Together these data collectively illustrate that the classification of DIO groups was successfully achieved in the long-term DIO study, and comparable to the conceptualization observed in the short-term diet project. Therefore, this model offers a reliable representation of different obesity subtypes represented by mild (DIO with high GT) and progressed (DIO with low GT) metabolic derangements prior to the onset of T2DM. These animals were subsequently used for a more comprehensive metabolic and microbial analysis.

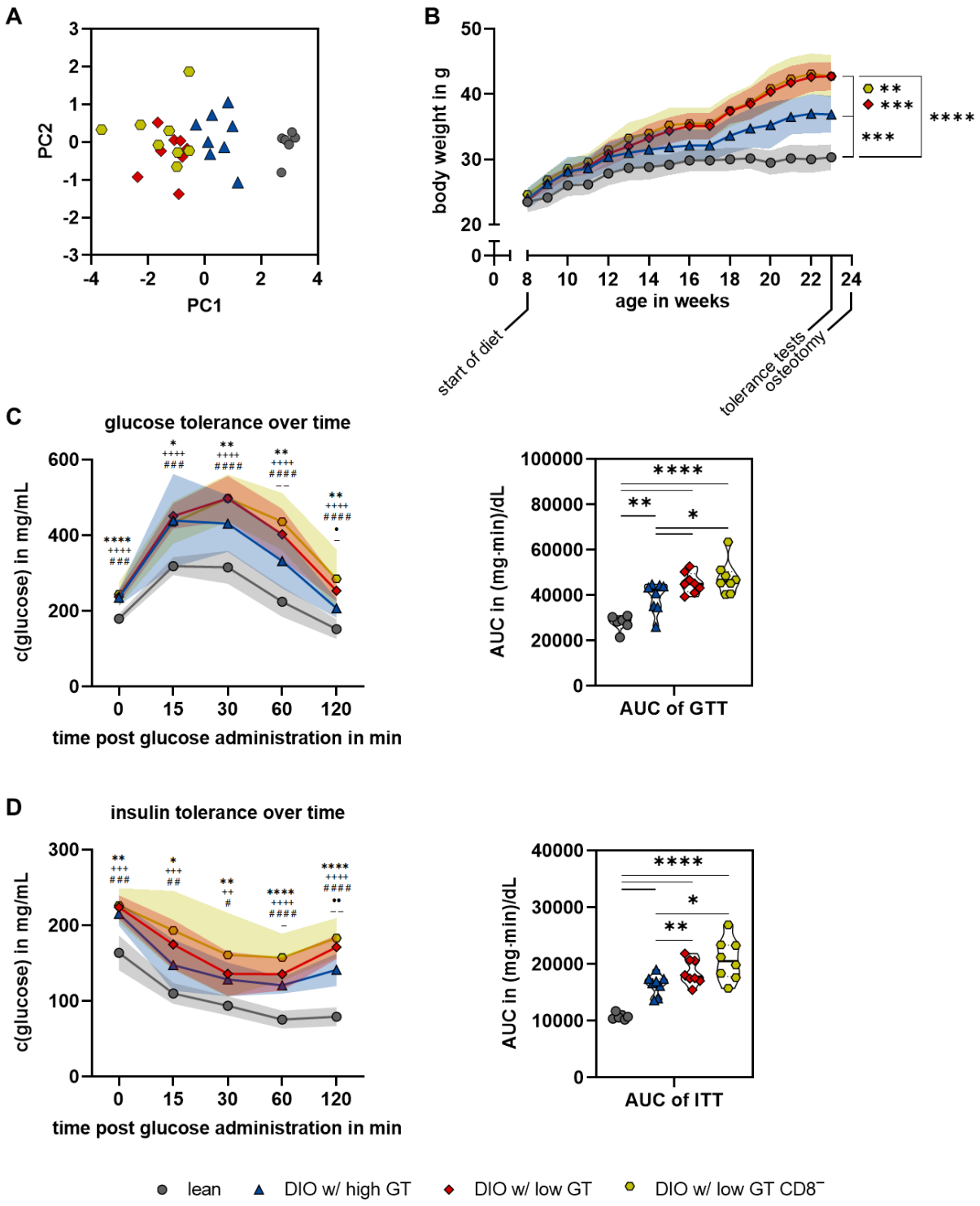

Fig. 22 | Clustering of HFD-fed mice facilitated the identification of distinct metabolic subtypes. **A** | Visualization of controls and different DIO clusters by PCA. Note that CD8⁺ T cell depletion was performed after clustering. **B** | Body weight gain over the period of 16 weeks demonstrated a modest increase in weight of control mice, whereas the obese groups gained weight to a significant higher degree. **C** | Determination of glucose tolerance showed a significant impaired response to process the defined glucose load in obese mice compared the lean group. **D** | Evaluation of insulin resistance by administering a specific insulin concentration underlined the metabolic differences observed in HFD-fed mice in comparison to lean mice. Mean ± SD/median and IQR (for AUC results), *p<0.05, **p<0.01, ***p<0.001, ****p<0.0001. Annotation to the statistical evaluation of the tolerance tests: [*] lean vs. DIO w/ high GT; [+] lean vs. DIO w/ low GT; [#] lean vs. DIO w/ low GT CD8⁻; [•] DIO w/ high GT vs. DIO w/ low GT; [–] DIO w/ high GT vs. DIO w/ low GT CD8⁻. N=6-8 per group, Welch's t test

3.2.2 Obesity induced β-cell compensation as a result of glucose intolerance

To profoundly study the diverse metabolic abnormalities that occur in the DIO subsets, pancreata were stained for insulin-producing β-cells. An increase in pancreatic islets would be characteristic for β-cell compensation, which is a physical counter-reaction to the constant fat and glucose exposure [174]. Pancreata were sampled together with the fractured bones 21d after the surgery (Fig. 23, A). As mentioned, several mice from the DIO group with low GT were treated with a $CD8^+$ T cell-depleting antibody during the initial inflammatory phase of bone repair. This treatment had a sustained neutralizing effect for several weeks (Fig. 29, p. 82) and may have potential effects on metabolic actions [175]. As previously stated, data from the GTT and ITT were obtained prior to the intervention.

The immunohistochemical staining of insulin-producing β-cells in the pancreas demonstrated that the total and relative area of the islets in the obese high GT mice were slightly higher compared to the control group (Fig. 23, B and C). However, these differences were not statistically significant. In contrast, the DIO groups with low GT exhibited a significantly increased total and relative islet area compared to lean mice.

The expanded islet surface area observed in the obese low GT groups is a consequence of the significantly increased islet formation, as evidenced by the greater number of islets/mm^2 compared to the control mice (Fig. 23, D). This observation clearly indicates a response to insulin resistance, suggesting a compensatory effect.

Interestingly, the mean islet area remained unaffected by obesity, indicating that the islet morphology was not altered (Fig. 23, E).

Moreover, analysis of non-fasting plasma insulin levels 21d after introducing the fracture revealed a significant increase in obese low GT mice compared to controls (Fig. 23, F). This indicates the development of hyperinsulinemia, which was not observed in obese mice with high GT, and slightly pronounced in the obese $CD8^-$ low GT group ($p=0.088$) when compared to the control group. Although metabolic changes in obese $CD8^-$ low GT mice were confirmed on cellular level, the intervention in obese $CD8^-$ low GT mice may have temporarily affected insulin metabolism. Evidence comes from a C57BL/6J DIO study which validates an increase in insulin sensitivity by antibody depletion of $CD8^+$ lymphocytes [50].

In summary, the data confirmed that the DIO model still exhibited functional insulin secretion and β-cell development, even though these processes were altered by obesity. Again, the analysis supports the classification of a mild (DIO with high GT) and progressed disease subtype (DIO with low GT), with a change now also demonstrated in the pancreas due to insulin resistance.

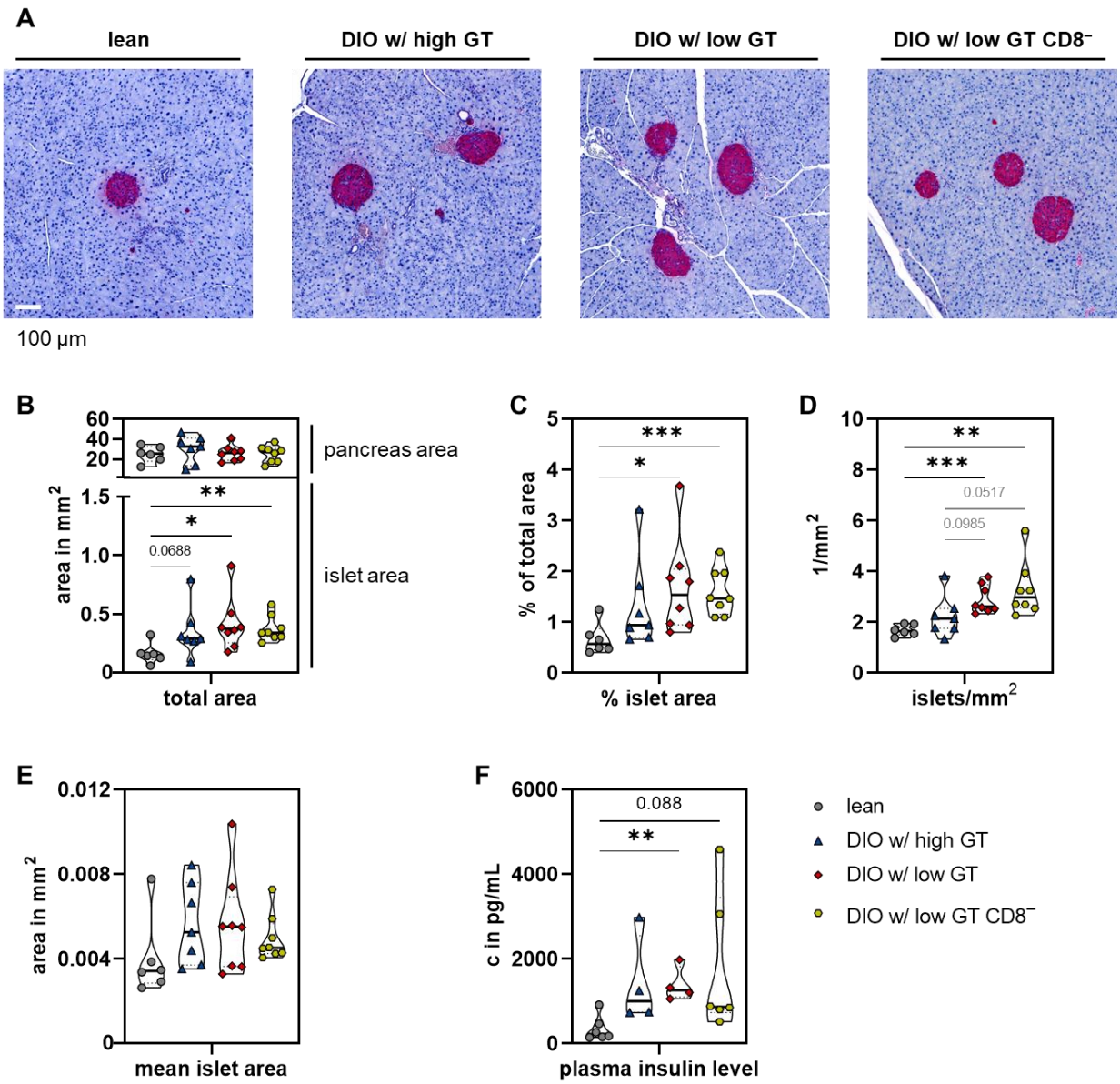

Fig. 23 | Effect of obesity on pancreatic β-cell parameters obtained 21d post-fracture. A | Immunohistochemical staining of insulin-producing islets (red) of control and obese mice with different glucose tolerances. **B, C |** Both obese low GT groups exhibited a significantly increased total and relative islet area in comparison to lean mice. **D |** Development of low GT correlated with a significantly higher islet number compared to lean mice. **E |** Evaluation of mean islet area unveiled that the β-cell morphology was not affected by obesity. **F |** As consequence of β-cell compensation, mice with low GT exhibited an increase in circulating non-fasting plasma insulin levels as compared to the control group. Median and IQR, *p<0.05, **p<0.01, ***p<0.001. N=3-4 per group, Welch's t test

3.2.3 Obesity progression promoted the development of fatty liver

Obesity is frequently associated with an accelerated risk for liver steatosis that may progress to nonalcoholic fatty liver disease [30, 176]. It results from an imbalance between the rate of fatty acid uptake and de novo synthesis as well as the rate of oxidation and export [177]. Therefore, analysis of liver addressed the question whether the obese groups also exhibit differences in the

hepatic pathophysiology. The livers were sampled together with the fractured bones and pancreata 21d after the surgery. The evaluation of hepatic fat deposition was performed through hematoxylin/eosin staining. The analysis revealed that DIO mice with high GT only exhibited a mild fat accumulation similar to the control group (Fig. 24, A). In sharp contrast, both obese groups with low GT significantly accumulated fat droplets, and thus the liver tissue appeared less dense and showed a fatty degeneration. Quantification of the fat mass evidenced the hepatic differences, demonstrating a significant increase in the total and relative fat area in the DIO groups with low GT compared to control and obese high GT mice (Fig. 24, B and C). The pathological alterations are likely to result from the obesity-associated glucose and insulin resistance as well as weight gain.

These observations verified the emergence of distinct obese subtypes, each exhibiting unique metabolic changes, and underscore the complex nature of metabolic disorders associated with obesity. The progression of metabolic disturbances in obese low GT mice particularly involved notable modifications in both the pancreas and other insulin-sensitive tissues, including the liver. These changes are likely to contribute to the systemic metabolic dysfunction linked to obesity, which can have repercussions on bone health as well.

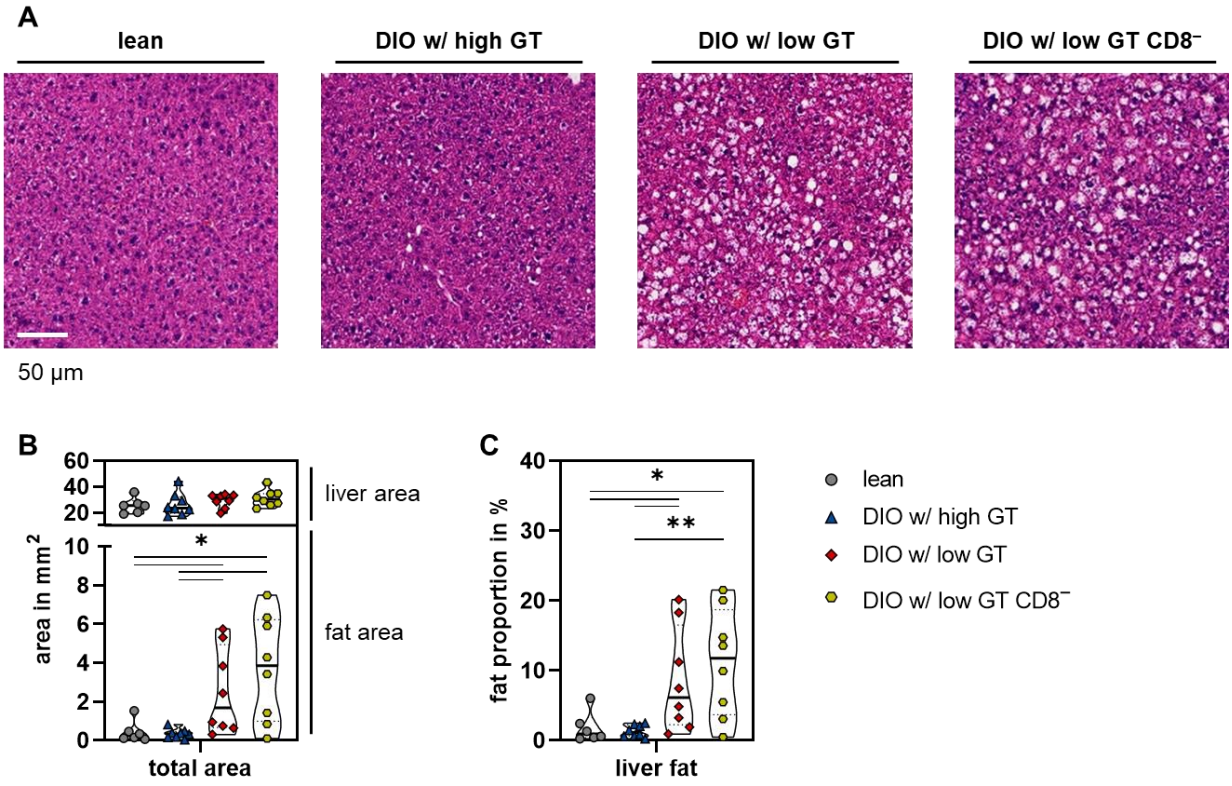

Fig. 24 | The DIO clusters revealed differences in the development of fatty liver after 16 weeks of high-fat diet. A | Representative images of the hematoxylin/eosin-stained liver sections. Fat droplets were significantly elevated in both DIO groups with low GT, whereas lean and high GT mice exhibited a minor accumulation. **B, C |** Calculation of the total (B) and relative (C) fat area evidenced significant pathological alterations of the liver in DIO mice with low GT compared to the control mice and obese group with high GT. Median and IQR, *p<0.05, **p<0.01. N=6-8 per group, Welch's t test

3.2.4 Microbiome signatures linked to glucose and insulin resistance in obesity

It is well established that the microbiome and its dysbiosis play a critical role in the development of obesity. In addition, the microbiome is closely associated with the modulation of the adaptive immunity and the occurrence of metabolic inflammation. Therefore, the investigation of murine caecum and feces samples sought to explore potential pathological bacteria in the context of obesity. As previously described, the study employed a 16-week long-term HFD to induce obesity. To assess the microbial diversity and composition, 16S ribosomal RNA (rRNA) gene sequencing was performed on samples collected 21d post-osteotomy. Samples from lean mice were compared to the identified DIO subtypes, exhibiting either mild (high GT) or progressed metabolic changes (low GT). Additionally, the analysis also included obese mice with low GT that were deficient in $CD8^+$ T cells. The study aimed to answer two main questions: (I) whether obesity with different metabolic characteristics leads to distinct bacterial communities, and (II) if the identified bacterial strains contribute to changes in metabolism, immunity and the microenvironment of bone tissue.

3.2.4.1 DIO is not associated with a decrease in the gut microbiome diversity

The microbiome study revealed that the quantification of microbial community members, represented as operational taxonomic units (OTUs), demonstrated a comparable number of taxa, indicating a similar bacterial richness between the microbiota of lean and obese mice (Fig. 25, A). In addition, comparison of caecum and feces samples did not reveal any significant alterations. Another evaluation of the microbial diversity, also known as alpha-diversity, is the determination of Shannon effective counts, an index capturing the community structure and placing more weight on the evenness of microbial abundancies. Again, the analysis revealed a comparable diversity between the experimental groups (Fig. 25, A). The results suggest that, despite differences in metabolic health and the absence of $CD8^+$ T cells in obese low GT mice, the microbial diversity remained relatively consistent across these groups.

Moreover, multidimensional scaling using PCA visualized differences in diversity between samples (beta-diversity) based on general UniFrac distances, an all-against-all distance matrix including shared taxonomic composition and genetic distances of the community members in each sample to the members in the other sample. The distance calculation features spots of a sample with a certain bacterial profile. The visualization revealed that the bacterial signatures of the cecal and fecal samples within each experimental group clustered closely together. This indicates a relatively high consistency within these gut compartments in each experimental group (Fig. 25, B). The PCA also illustrated that bacterial profiles of the lean group significantly differed from those of all DIO mice with a large distance between them ($p = 0.001$), while significant diversities between the obese groups were not detected.

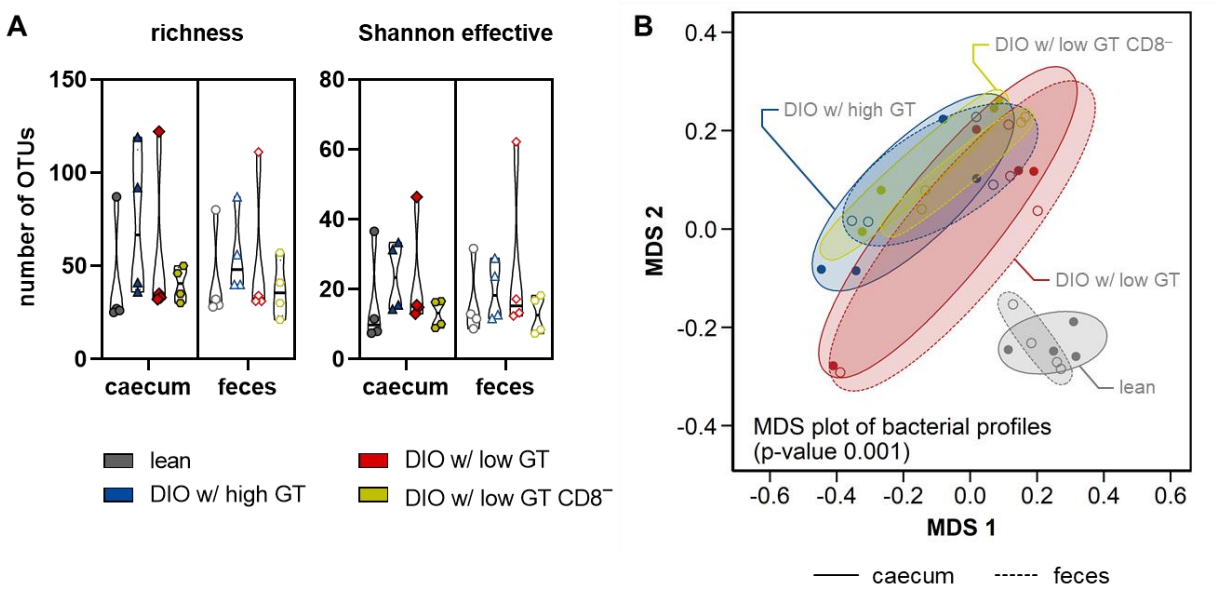

Fig. 25 | Diversity of cecal and fecal microbiota assessed by 16S rRNA gene amplicon sequencing. **A** | Diversity within samples (α-diversity) was assessed using richness and Shannon effective counts. The diversity was comparable across all groups, and among cecum and feces, regardless of the metabolic status. Median and IQR. N=4 per group. **B** | Multi-dimensional scaling (MDS) of Unifrac distances of the cecal and fecal microbiota for each group revealed a significant clustering pattern, with lean mice distinctly separated from the obese groups. N=4 per group. Permutational multivariate analysis of variance (PERMANOVA).

3.2.4.2 Obesity triggered an altered bacterial taxonomic signature on phylum level

The microbiome analysis further examined the taxonomic composition of abundant bacteria to identify potential shifts in the microbiome. The analysis aimed to provide insights into specific microbes that may contribute to the observed differences among the groups, as revealed by the assessment of β-diversity. Preponderant bacterial colonizers in the caecum and feces in all groups originated from the phyla Firmicutes, Bacteroidetes, Verrucomicrobia and, to a smaller extent, Proteobacteria (Fig. 26, A). Remarkably, Actinobacteria and Desulfobacteria were detected in obese mice, while these phyla were absent in the control group. Significant alterations on phylum level were primarily apparent in cecal samples, including a significantly reduced Bacteroidetes phylum in DIO high ($p = 0.0422$) and $CD8^-$ low GT mice ($p = 0.0259$). A significant decrease was also identified for Proteobacteria in the obese group with high GT ($p = 0.0424$).

Furthermore, a disturbed microbiome in obesity and T2DM is commonly described by an increased Firmicutes (F) to Bacteroidetes (B) ratio, a used marker for dysbiosis [178, 179]. In this study, a marginal elevation was observed in the obese groups with low GT, without a significant difference (Fig. 26, B). These results indicate comparability among all groups. In addition, lower proportions and loss of Verrucomicrobia are typically observed in obesity and overweight studies [180, 181]. However, in contrast to those findings, Verrucomicrobia were equally abundant in lean and obese mice (Fig. 26, A).

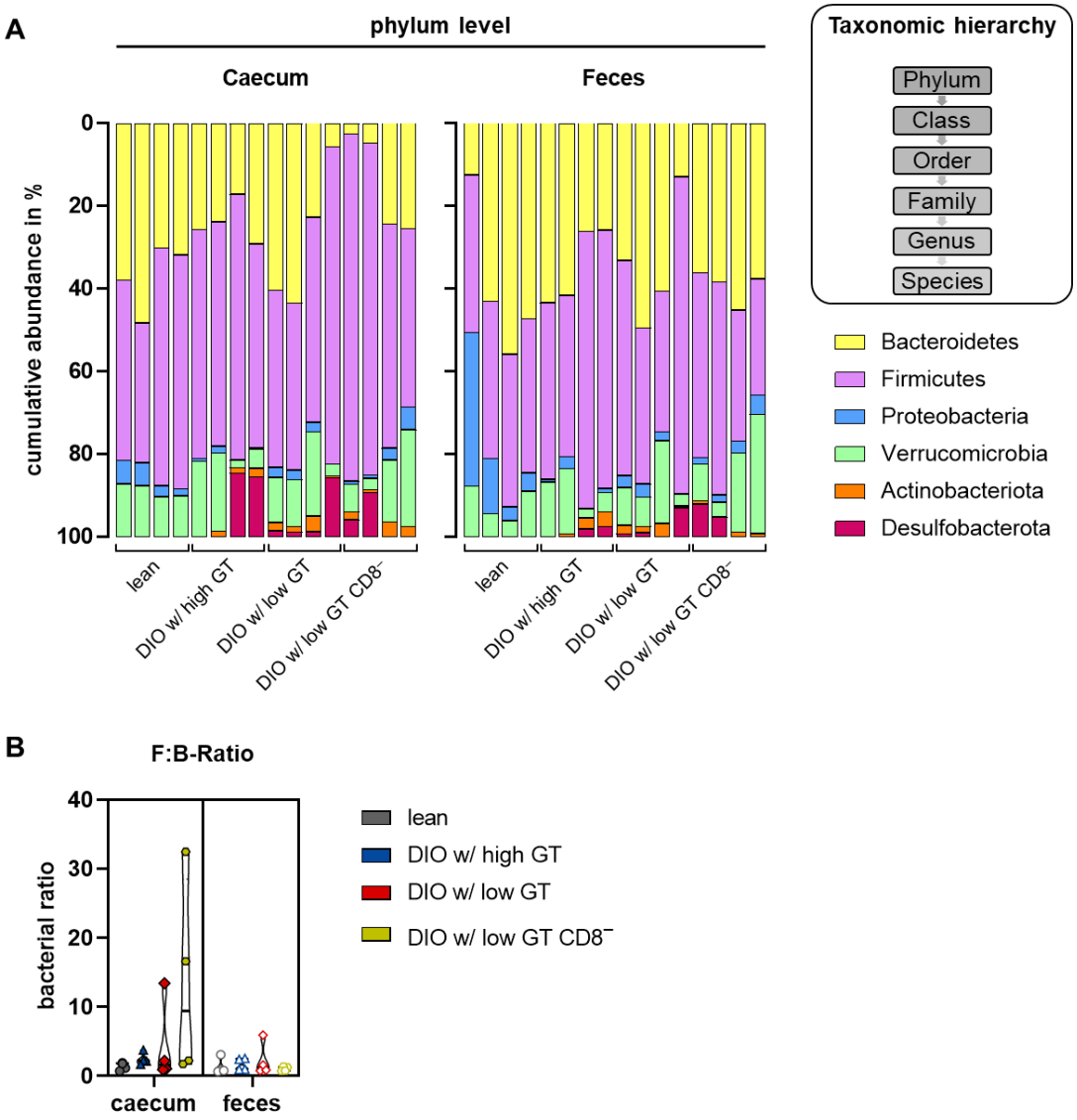

Fig. 26 | DIO induced alterations in the microbial composition on phylum level. A | Gut microbiota profiles are presented on phylum level. The HFD and the corresponding control diet were given for 16 weeks. Cecal and fecal samples were obtained 21d post-fracture from lean and obese mice with high and low GT as well as from obese CD8⁻ low GT mice. Obesity facilitated the colonization with the phyla Actinobacteriota and Desulfobacterota in all obese groups, while these phyla were not prevalent in lean mice. DIO mice with high GT and obese CD8⁻ mice with low GT demonstrated a significant decrease in Bacteroidetes, and the obese group with high GT additionally exhibited a significant reduction in Proteobacteria. **B |** Calculation of the Firmicutes (F) to Bacteriodetes (B) ratio revealed comparable results across all experimental groups. Mean/median and IQR. N=4 per group.

3.2.4.3 Bacterial indicators for obesity and disease progression

When comparing the microbiota of lean and obese mice, the phyla Actinobacteriota and Desulfobacteria were found to colonize the obese gut, whereas these phyla were not detected in the gut of the control group. Species from the order Coriobacteriales accounted for the only proportion within the Actinobacteria phylum in the gut of obese mice (Fig. 27). Similarly, the phylum Desulfobacterota only consisted of the order Desulfovibrionales within the obese microbiome. As above mentioned, the phylum Bacteroidetes slightly decreased, while the Firmicutes phylum minorly

accumulated and diversified upon obesity induction. Specifically, DIO mice exhibited an increase in the Firmicutes class Bacillus in both the caecum and feces. Under conditions of obesity, the Firmicutes class Clostridia underwent significant modifications, while lean mice predominantly harbored the order Lachnospirales within the Clostridia class. The microbiome of all DIO groups was significantly different from the lean counterparts in terms of the abundance of the Firmicutes orders Erysipetrichales (Bacilli), Lactobacillales (Bacilli) and Peptostreptococcales Tissierellales (Clostridia). These findings indicate distinct microbial compositions associated with DIO.

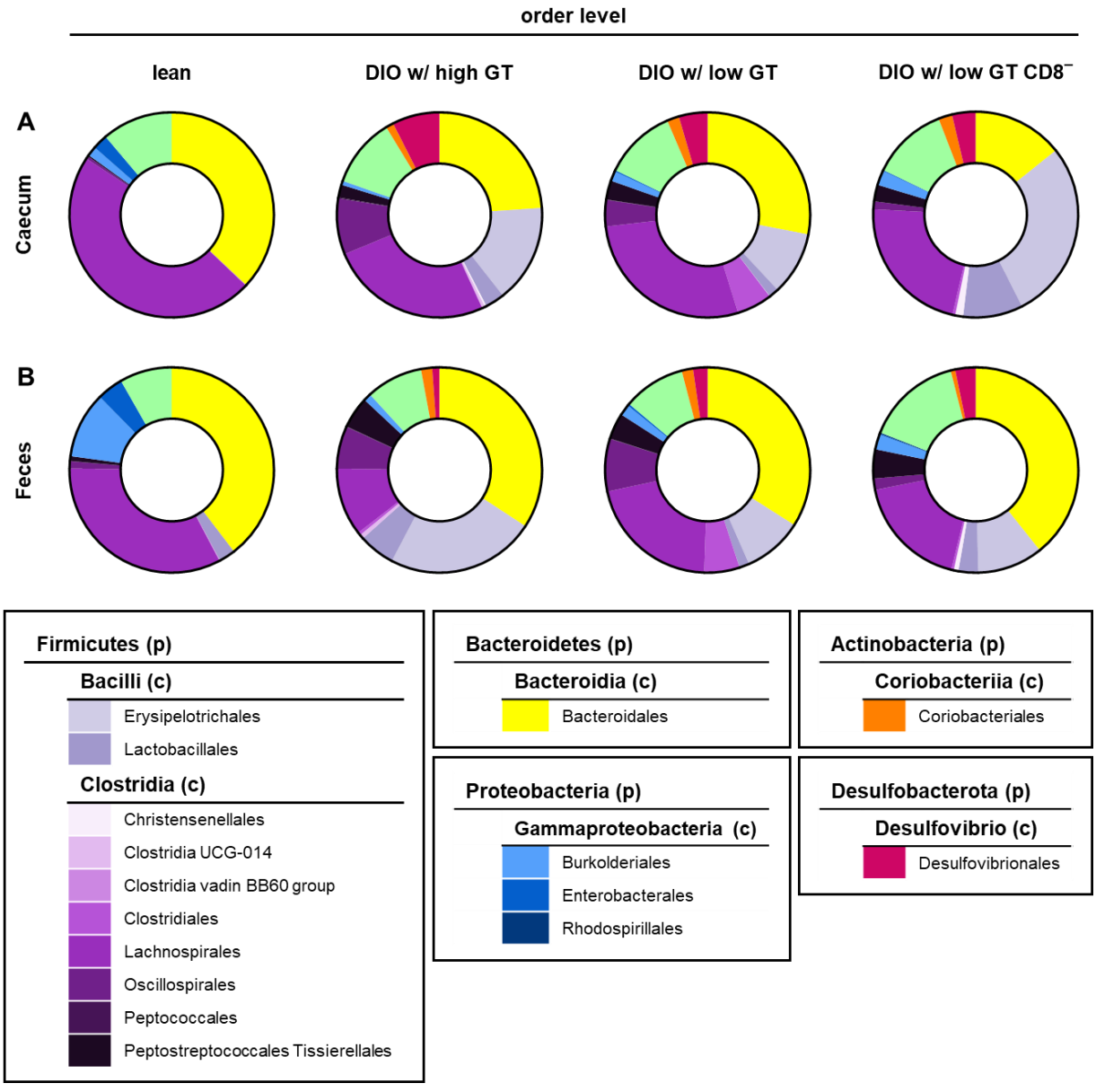

Fig. 27 | Obesity primarily changed the composition of the phylum Firmicutes, particularly at order level. The HFD facilitated the colonization with the Firmicutes classes Bacilli and Clostridia, which significantly increased in the abundance of the orders Erysipetrichales, Lactobacillales and Peptostreptococcales Tissierellales in comparison to caecal **(A)** and fecal samples **(B)** from lean controls. p: phylum, c: class. Mean. N=4 per group

Differences in microbiota between obese mice with high and low GT became even more heterogenous in terms of genera belonging to the phylum Firmicutes. Elevated proportions of genera belonging to Firmicutes (Blautia, Colidextribacter and Ligilactobacillus) and Bacteroidetes (OTU4) were exclusively detected in the obese groups, while these bacteria were not abundant in lean mice (Fig. 28, A). However, these alterations were only significant in obese high GT mice compared to controls. Similar observations were made for the genus Erysipelatoclostridium (Firmicutes), with a significant increase observed in the obese groups with low GT (Fig. 28, B). Moreover, the abundances of Clostridium sensu stricto13 and OTU8 (both Firmicutes), and OTU42 (Desulfobacteria) were highly and significantly detected in obese low GT mice (Fig. 28, B). These bacteria were either minor or absent in the control and other obese groups, indicating a specific association with low glucose tolerance and insulin sensitivity.

Interestingly, obesity resulted in a significant depletion of the genus OTU35, which belongs to the family Muribaculaceae within the Bacteroidetes phylum. This reduction was observed in both caecal and fecal samples among all the obese groups. This finding, along with the abundance of Actinobacteriota and Desulfobacterota in the obese gut microbiome, further distinguishes the microbial profile of the obese groups from that of control mice (Fig. 28, C).

Notably, genera belonging to the Bacteroidetes phylum, such as Bacteroides and Parabacteroides, as well as Anaerotroncus from the phylum Firmicutes showed either presence in both the lean and obese low GT group or in obese high and $CD8^-$ low GT mice (Fig. 28, D). This result suggests that the microbiome of the identified obese subtypes, characterized by high or low GT, is significantly different. It also indicates that these differences may change throughout the course of obesity development, disappearing or reappearing again in obese low GT mice. Interestingly, the depletion of $CD8^+$ T cells partially altered the microbial profile of the obese low GT group, resembling the bacterial signature of obese mice with high GT. These data demonstrate a potential interplay between specific bacteria and the adaptive immune system.

To summarize, the data indicate that obesity strongly affected the gut microbial composition already on phylum level, while the bacterial diversity remained unaffected. Notable differences between the obese groups were observed on genus level, particularly within the Firmicutes phylum, which diversified due to obesity. In addition, manipulation of the immune system in obese low GT mice using a $CD8^+$ T cell-depleting antibody resulted in significant changes in genera within the Firmicutes and Bacteroidetes phyla. This suggests a reciprocal relationship between the gut bacteria and the immune system.

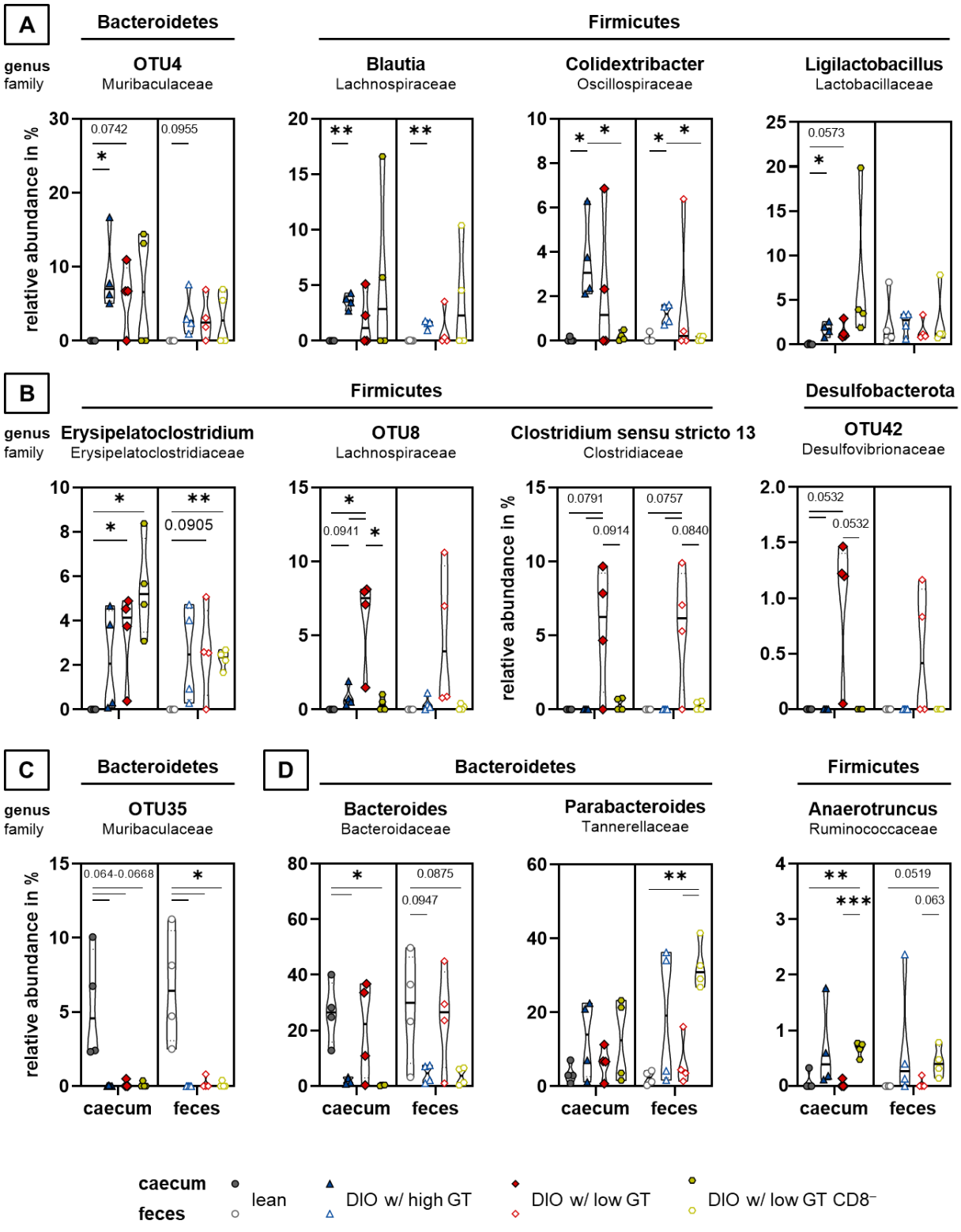

Fig. 28 | Obesity with different metabolic characteristics induced microbial shifts on genus level that were pronounced in cecal samples. Significant relative abundances of dominant bacterial genera (with indication of the phylum and family affiliation), which were only apparent in either obese high **(A)** or low **(B)** GT mice. The summary also demonstrates significant microbial changes present in all obese groups **(C)** and genera that were either shared by lean and obese mice with low GT or obese high and CD8⁻ low GT mice **(D)**. Median and IQR, *p<0.05, **p<0.01, ***p<0.001. N=4 per group, Welch's t test

3.2.5 Long-term obesity elevated bone mineral density in mice with low glucose tolerance

After monitoring the metabolic profile resulting from high-fat diet, the mice underwent a femoral osteotomy at the age of 24 weeks following a 16-week diet. Upon fracture introduction, the influence of obesity on bone fracture healing was assessed using micro-CT 3 weeks post-surgery. As previously described, obese mice were categorized into two groups based on their metabolic characteristics, namely obese mice with either high or low GT.

Additionally, within the obese low GT group, several mice received a $CD8^+$ T cell-depleting antibody during the initial inflammatory phase of fracture healing, leading to the formation of a subgroup referred to as obese $CD8^-$ low GT mice. The removal of $CD8^+$ T cell resulted in a significant decrease in their levels as evidenced by flow cytometry, reducing from 45,8 (± 2,6 %) % to under 0.1 % (± 0,02) % immediately after the intervention (Fig. 29). However, over a period of 3 weeks, the cells gradually recovered, with levels increasing to 6.1 (± 0,2) %.

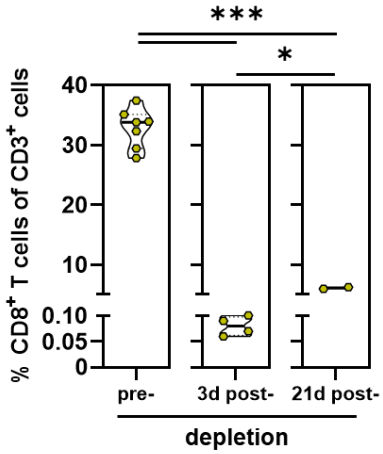

Fig. 29 | Removal of $CD8^+$ T cells persisted until 3 weeks post-intervention. The analysis of the $CD8^+$ T cell abundance was performed by flow cytometry. Levels of $CD8^+$ of $CD3^+$ T cells in peripheral blood of obese low GT mice pre-treatment, and in spleen 3d as well as 21d after $CD8^+$ T cell removal. Median and IQR, *p<0.05, ***p<0.001. N=2-7, Welch's t test

The micro-CT evaluation revealed that all experimental groups, regardless of obesity induction, developed a mineralized callus stabilizing the fracture gap within 21d after the surgery (Fig. 30). However, this observation contradicts the results obtained from the short-term obesity study, which demonstrated a noticeable defect in the bridging of the fracture. These contrasting results suggest that the impact of obesity on fracture healing may vary depending on the duration of obesity exposure. Additionally, in the obese high GT and $CD8^-$ low GT groups, the fracture imaging revealed that one out of four animals displayed incomplete bridging (Fig. 30).

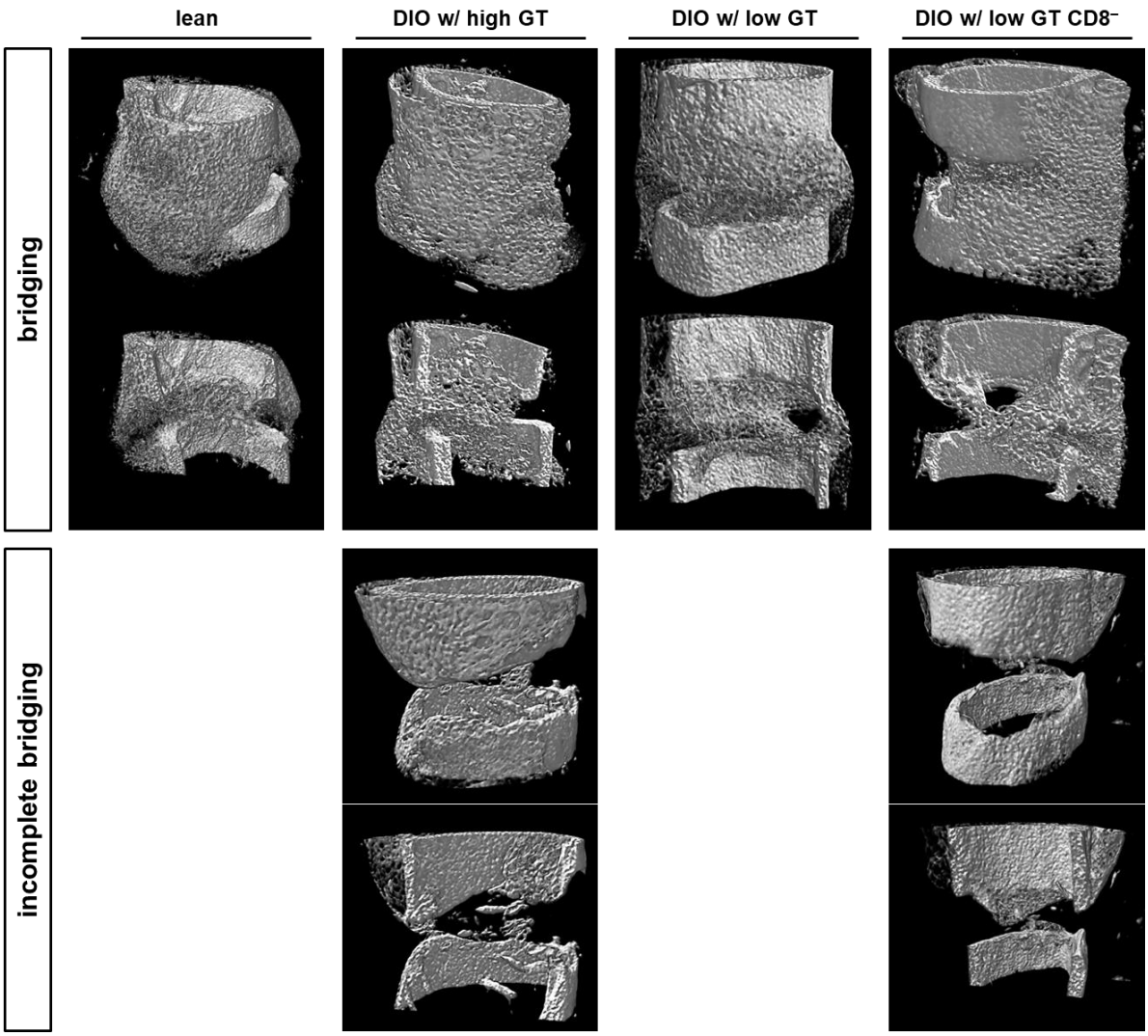

Fig. 30 | Micro-CT images displaying the complete 3D representation and longitudinal sections of fracture gaps from lean and obese mice 3 weeks post-surgery, following a 4-month diet intervention. Remarkably, the healing outcome was comparable among all experimental groups. However, DIO mice with high GT and obese CD8⁻ low GT mice partially exhibited incomplete bridging of fractures (1 out of 4).

The micro-CT evaluation further demonstrated that the obese groups tended towards a decreased total callus volume (TV) compared to lean mice (Fig. 31, A). Consistent with this, the relative proportion of newly mineralized bone within the fracture gap (BV/TV) increased gradually with progressing metabolic alterations, although this elevation was not statistically significant (Fig. 31, A). Moreover, the minimal polar moment of inertia (MMIp), which measures resistance to torsional forces, was not affected (Fig. 31, B). Most notably, the obese groups exhibited a more pronounced change in bone mineral density (BMD). However, the BMD tended to increase in obese high GT mice ($p=0.0579$) and reached a significant elevation in the obese low GT groups compared to lean mice, with values ranging between 1.22 (± 0.06) and 1.25 (± 0.08) g/cm^3 (Fig. 31, C). In contrast, lean mice displayed a significantly lower BMD of 0.99 (± 0.05) g/cm3 ($p<0.01$-0.05). The results indicate a more advanced mineralization process in obese low GT mice, which coincides with a smaller callus formation (TV). Furthermore, the results demonstrate a comparable trabecular

microstructure in terms of trabecular number (Tb.N), spacing (Tb.Sp) and thickness (Tb.Th) between the fractures of lean and obese mice (Fig. 31, D).

In summary, extending the HFD from 7 to 16 weeks resulted in a different, potentially more beneficial, healing progression and outcome under obesity conditions. The bone repair in obese mice was comparable to controls in almost all aspects, except for BMD that considerably increased due to obesity. Hence, depleting $CD8^+$ T cells did not further improve healing in obese low GT mice.

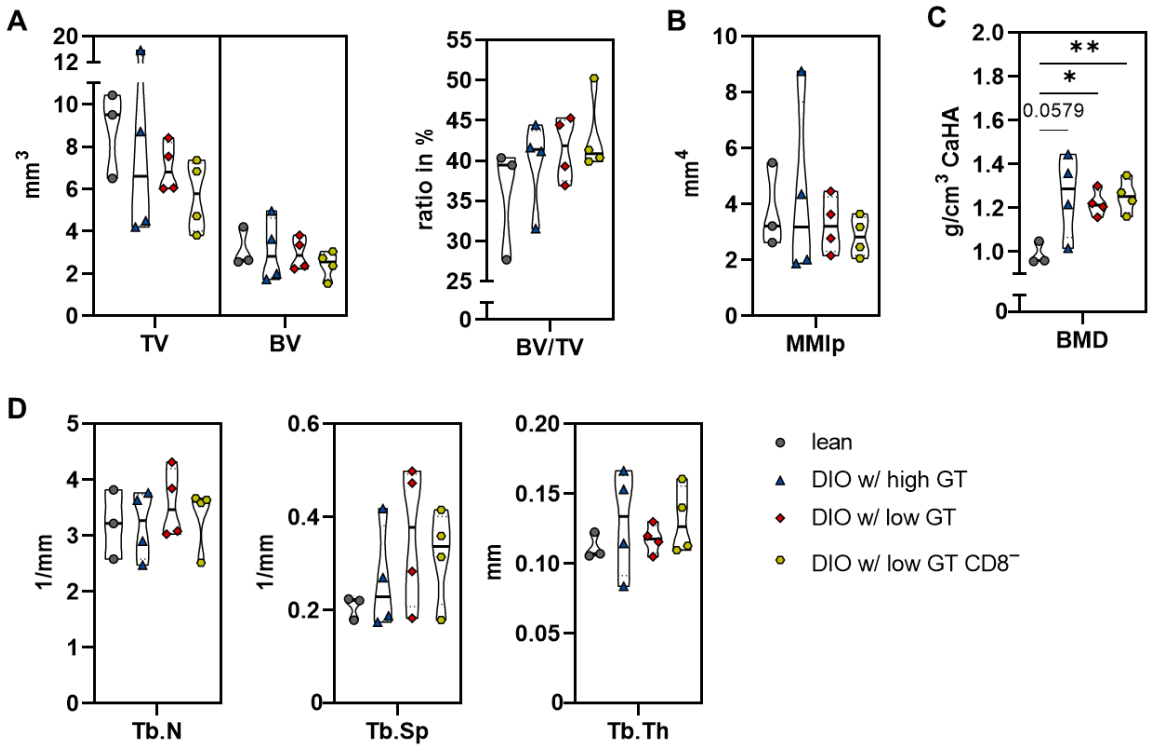

Fig. 31 | The micro-CT analysis revealed a similar healing outcome between lean and obese mice, 21d post-osteotomy. A, B | Total callus volume (TV), bone volume (BV), the ratio of BV to TV (BV/TV) and minimal polar moment of inertia (MMIp) were not altered by obesity. **C** | Evaluation of the BMD revealed significant differences between control and obese low GT mice. **D** | Obesity did not affect the microstructure in comparison to fractures of lean mice. Median and IQR, *p<0.05, **p<0.01. N=3-4 per group, Welch's t test

3.2.6 Fracture healing in obese mice exhibited an altered cartilage deposition

Bone sections additionally underwent the classical Movat's Pentachrome staining. As confirmed by micro-CT analysis 21d post-surgery, obese mice with high GT and $CD8^-$ mice with low GT partially displayed incompletely bridged fractures, whereas bridged gaps were revealed in control and obese low GT mice (Fig. 32, A).

The histomorphometric analysis further demonstrated significant differences in tissue deposition (Fig. 32, B). Control mice attained a large callus, predominantly containing cartilage, while the fracture in obese low GT mice is characterized by mineralized tissue and thereby the amount of cartilage significantly decreases. The healing pattern in obese high GT and $CD8^-$ low GT mice is

more inconsistent. The closing fracture gap in obese high GT mice mainly contained cartilage or connective tissue, while mineralized tissue dominated in obese CD8- low GT mice. Moreover, fractures in obese CD8- low GT mice were significantly reduced in cartilage and connective tissue due to either more mineralization or incomplete bridging in comparison to controls. The staining also revealed a significant accumulation of fat distally from the fracture gap in the obese low GT groups compared lean mice (Fig. 32, B). CD8- low GT mice additionally showed a significant increase in the total fat proportion. The relative amount of bone marrow displayed variations, influenced by factors such as callus size, newly mineralized bone, cartilage, connective tissue and fat, collectively contributing to its displacement (Fig. 32, B).

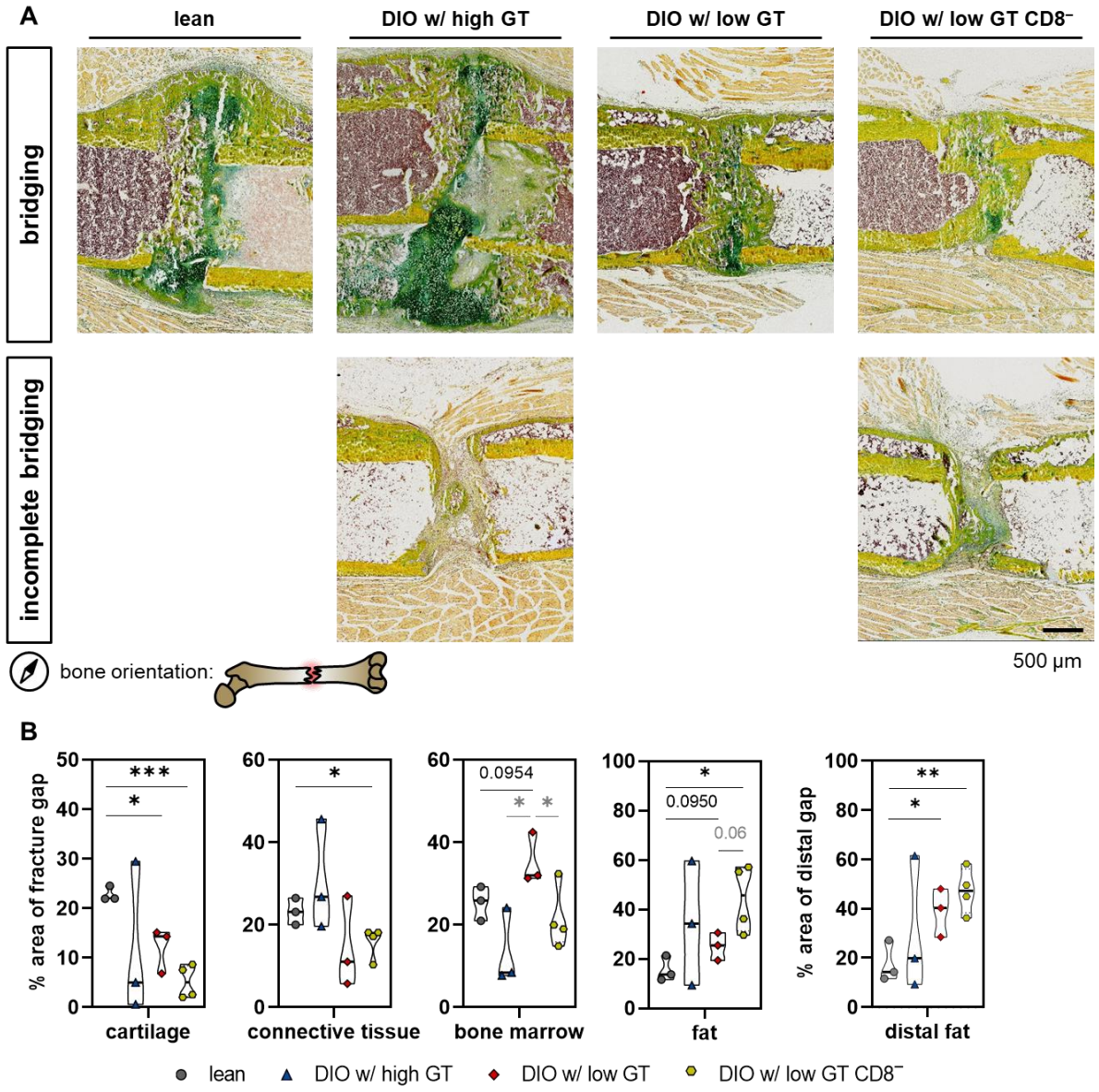

Fig. 32 | Progressed metabolic changes in obese low GT mice resulted in a reduction in cartilage within the fracture site, 21d post-osteotomy. A | Representative images of the fracture gaps (3 mm frame), distinguished in bridging and incompletely bridged fractures. The Movat's Pentachrome staining visualized mineralized bone (yellow), cartilage (blue/green), connective tissue (blue/green) and bone marrow (red). **B |** The histomorphometrical analysis assessed the relative area of cartilage, connective tissue, bone marrow and fat. Median and IQR, *p<0.05, ***p<0.001. N=3-4 per group, Welch's t test

3.2.7 The transcriptome of intact contralateral bones defined systemic obesity-associated changes

While the micro-CT evaluation demonstrated similar fracture healing outcomes between lean and obese mice, the histomorphometric analysis revealed distinct healing patterns, specifically in terms of cartilage deposition. To understand the underlying mechanisms, subsequent RNA sequencing was conducted to analyze gene expression levels and to determine potentially altered molecular pathways in response to obesity. For this purpose, intact contralateral and fractured bones were collected from mice after undergoing the 16-week long-term diet, and the samples were taken 3d post-fracture. The analysis during the early stage of bone repair intended to characterize the initial processes involved in cartilage formation and matrix deposition, with a particular focus on identifying molecular signatures specific to the DIO groups.

Bulk RNA sequencing of intact contralateral femora was performed to investigate the undisturbed bone microenvironment and to assess adipogenesis, osteoblast (OB) and osteoclast (OC) development, the ECM constitution and angiogenesis (Fig. 33, Supp. 2). Differential gene expression (DE) analysis compared the unfractured bone of lean over obese mice as well as the DIO group with either high or low GT over CD8$^-$ mice with low GT. Most notably, the results, expressed as log2-fold change, showed that the obese groups were closely related, as evidenced by high expression levels of markers that have been linked to adipogenesis (*Adipor1* [adiponectin receptor 1], *Lep* [leptin], Rnx1t1 [Runt-related transcription factor 1, translocated to 1]) and fatty acid metabolism (i.e. *Cd36*, *C1qtnf9* [C1q and TNF related 9], *Fabp3* [fatty acid binding protein 3], *Fabp4*, *Plin4* [perilipin 4], *Plin5*) when compared to lean mice (Fig. 33). These data suggests that in obese mice, adipocyte differentiation and accumulation play a dominant role in the bone microenvironment, leading to a modification of bone formation by favoring adipogenesis over osteogenesis. However, the relationship between excess fat and healing complications is controversial, and the net detrimental or positive effects have not been fully studied. Most notably, the data highlight the severe consequences of even mild metabolic changes on bone health, as bone adipogenesis precedes fatty liver development in obese high GT mice, resulting in a unique bone phenotype.

Interestingly, the analysis revealed differences in insulin-like growth factor (IGF) signaling. The expression of the insulin growth-factor-binding protein *Igfbp2* [insulin-like growth factor (IGF) binding protein 2] is commonly decreased in obesity [182]. Here, the analysis confirmed a significant *Igfbp2* deficiency in both DIO groups with low GT compared to lean bones. IGFBP2 is normally bound to IGF-1 or IGF-2, and thus regulates its bioavailability [183]. IGFBP2 knockout in a male C57BL/6J study demonstrated an effect on bone turnover and elevated fat mass. As a result, the observed alterations in IGF signaling could potentially contribute to skeletal acquisition. In line with that, all obese femora showed significantly increased levels of *Igfbp5* that is acknowledged as

central regulator of IGF signaling, and to stimulate bone formation [184, 185]. In bone, the complex of IGF-IGFBP5 is also described to bind to hydroxyapatite in large quantities [186], which correlates with elevated BMD values determined in this study.

Surprisingly, inflammatory cues were less pronounced in obese bones relative to the lean counterparts. However, chemokines and their cognate receptors become of interest regarding their role in modulating the immune landscape, particularly in adipose tissue homeostasis and inflammation. Significant deficiencies in *Ccr7*, *Cxcr5* and *Ccl2* were partly detected in obese low GT mice, however these effects are not extensively studied. Most notably, all DIO groups significantly upregulated *Ccrl2* [CCR-like 2], an atypical chemokine receptor for the non-chemokine chemotactic protein chimerin which is described to be induced by HFD, but without an exact function [187].

In addition, the expression of the Wnt (Wingless-related integration site) ligands *Wnt9a*, *Wnt11* and *Wnt16* was significantly induced in the obese groups. These signaling molecules either activate canonical β-catenin-dependent (*Wnt9a*, *Wnt16*) or -independent (*Wnt11*, *Wnt16*) non-canonical pathways and are critical positive regulators of chondrogenesis, OB lineage commitment of MSCs and bone mass [188-190]. The DIO groups with high and low GT also significantly enriched transcripts of the matrix metalloproteinase (MMP) *MMP27*, which degrades and remodels the ECM [191]. The increased remodeling activity may partly be associated with bone marrow AT, which substantially shaped the bone microenvironment and could affect the healing process.

Moreover, lean mice significantly differed from the obese groups in terms of increased levels of the disintegrin and metalloprotease *Adam12*, which stimulates chondrocyte proliferation and maturation [192]. Other classical osteogenic signals, such as of *Alpl* [alkaline phosphatase], *Sp7* [osterix] and *Col1a1*, were also significantly detected in lean samples over DIO mice with low GT. Concomitantly, expression levels were significantly increased for a variety of fibrillar (*Col1a1*, *Col1a*, *Col5a2*, *Col11a1*, *Col11a2)* and non-fibrillar collagens (*Col8a1, Col13a1* and *Col22a1*) as well as crosslinking enzymes (*Lox* [lysyloxidase], *Loxl4* [lysyl oxidase like 4]) in control femora relative to those of obese low GT mice. These data uncovered a change in the OB and chondrocytes lineage as well as in the formation of collagen, which is associated with progressed metabolic changes in obesity.

In this regard, the analysis revealed the pivotal role of $CD8^+$ T cells in collagen and ECM deposition. The $CD8^+$ T cell removal in obese low GT mice especially restored the homeostatic *Col1a1* and *Col1a2* expression, indicating an interdependence of bone mineralization and adaptive T cell immunity. Additionally, the significant alterations observed in the OB lineage in obese low GT mice disappeared upon neutralization of $CD8^+$ T cells, emphasizing the contribution of $CD8^+$ T cells to OB differentiation and function. Surprisingly, the $CD8^+$ T cell depletion shifted the ECM expression towards the pattern observed in obese mice with high GT, showing higher tran-

script levels of genes such as *Aspn* [asporin], *Fbln1* [fibulin 1], *Fbln2*, *Fbln7*, *Postn* [periostin], *Thbs2* [thrombospondin] and *Thbs4* in comparison to lean controls.

Overall, the analysis of intact bones from the different obese groups revealed a strong molecular similarity characterized by high expression levels of adipogenic markers. However, obese low GT mice exhibited alterations in the OB lineage along with changes in collagen formation that were reversed following the $CD8^+$ T cell removal.

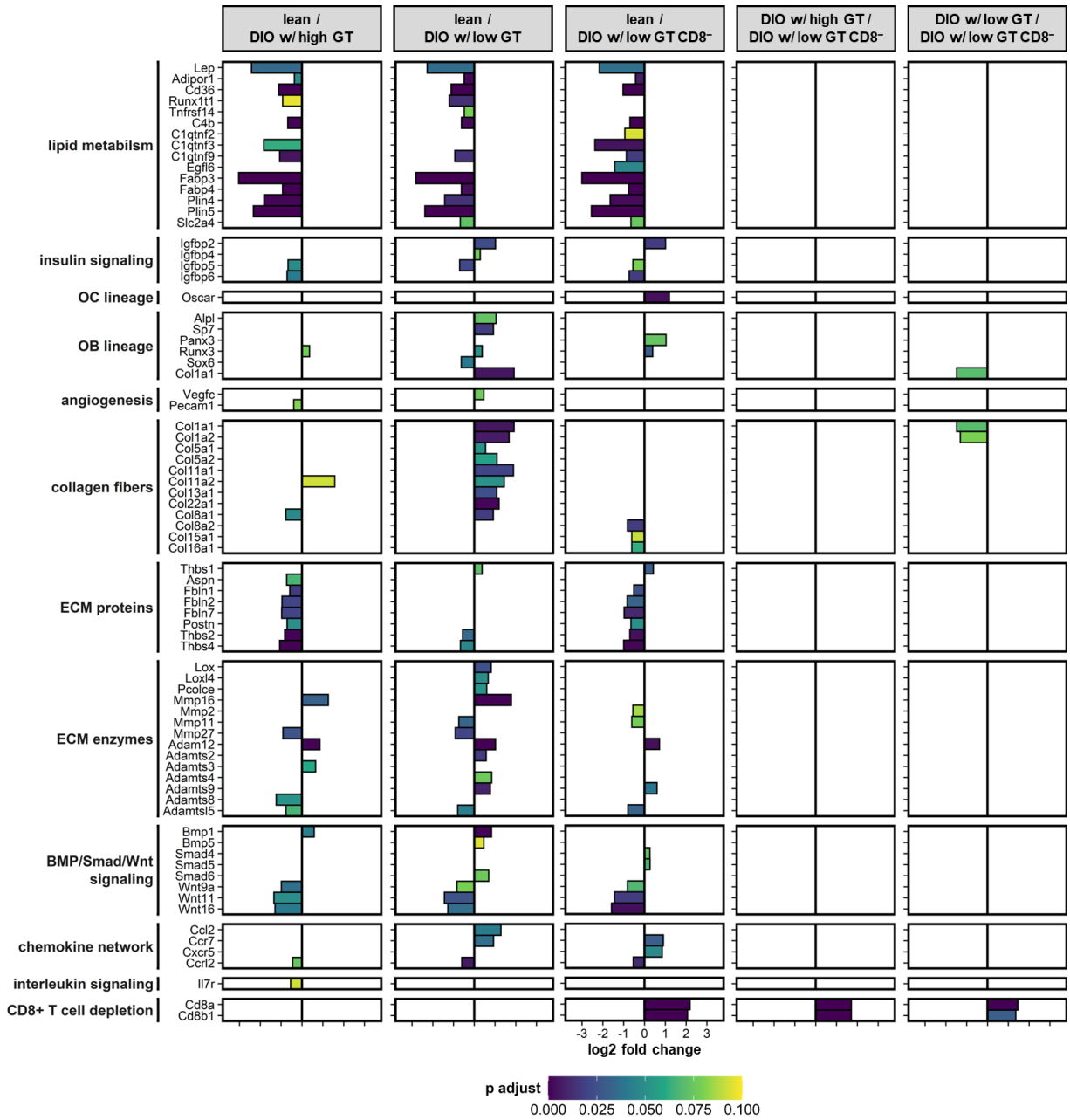

Fig. 33 | The transcriptomic analysis revealed an adipogenic microenvironment in intact contralateral bones as well as changes in osteoblasts, chondrocytes and collagen formation associated with obesity. Obesity was established through a long-term HFD and bones were obtained 3d after the surgery. Selected differentially expressed (DE) genes described as log2 fold change of lean over all DIO groups, and obese high or low GT mice over obese $CD8^+$ T cell-depleted mice with low GT. N=2-4 per group, Wild test

3.2.8 Transcriptional analysis of local cell contributions to early fracture healing

To gain molecular insights into the cellular contributions to early bone repair, the osteotomized femora were compared to the intact counterparts. The analysis provided evidence that cells from the osteogenic (*Pth1r* [parathyroid hormone receptor 1], *Alpl*, *Sp7*, *Col1a1*, *Spp1* [osteopontin], *Stab2* [stabilin 2], *Ctgf* [connective tissue growth factor], *Tnfsf11* [RANKL]) and osteoclastogenic lineage (*Tnfrsf11a* [RANK], *Mmp14*, *Ctsk* [cathepsin K]) were involved in the initial healing phase across all experimental groups (Fig. 34). Chondrocytes identified by RNA transcripts of *Sox9*, *Acan* [aggrecan] and C*ol10a1* as well as fibroblasts (*Fn11* [fibronectin 1], *S100a4* [S100 Calcium Binding Protein A4], *Dcn* [decorin]) were additionally detected at the lesion site, along with osteocytes (*Dmp1* [Dentin matrix acidic phosphoprotein 1], *Dmpk* [dystrophia myotonica-protein kinase], *Sfrp1* [secreted frizzled-related protein 1]) and endothelial cells (EC) (*Pecam1* [Platelet endothelial cell adhesion molecule], *Emcn* [endomucin]). As described in the literature, monocytes (*Cd14*) and macrophages (*Cd68*) accounted for the primary immune cell populations present at the fracture site, whereas as T (*Cd3*) and B cells (*Ptprc* [protein tyrosine phosphatase receptor type C, B200]) were not found to be enriched in the fracture. Remarkably, the data showed that the fractured bones were more deficient in T and B cells when compared to the intact counterparts. This effect was demonstrated in another osteotomy study showing that lymphocytes were withdrawn from the lesion site initially but reoccurred during the mineralization phase [84].

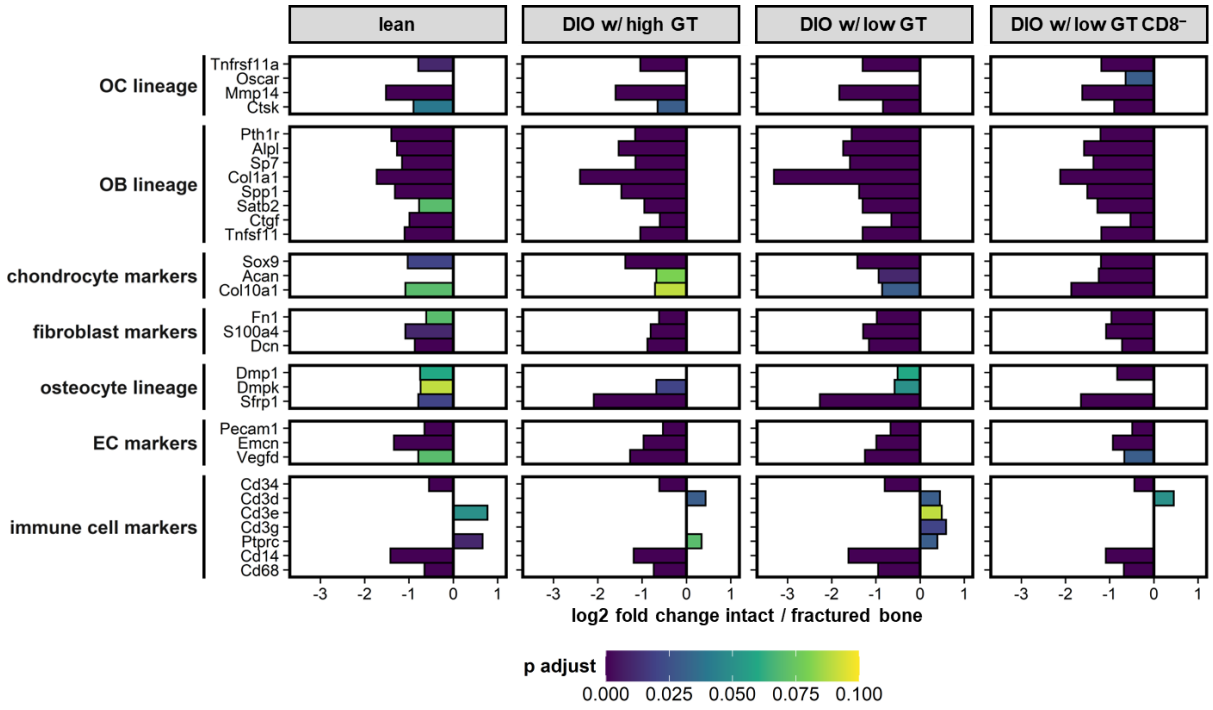

Fig. 34 | Fractures of obese mice displayed similar levels of active cell types during healing compared to lean controls. Analysis of DE genes of intact contralateral bones and fractured femora within an experimental group, expressed as log2 fold change, aimed to illustrate cell lineages involved in the initial bone healing phase. OC: osteoclast, OB: osteoblast, EC: endothelial cell. N=2-4 per group, Wild test

3.2.9 Transcriptomic profiling of early bone repair unveiled aberrant collagen and ECM deposition in obese mice

As revealed by the transcriptomic analysis, levels of immune cell markers were comparable among all experimental groups. Concomitantly, investigation of secreted cytokines in the blood indicated that long-term obesity did not further induce pro-inflammatory actions (Fig. 35). These findings align with the short-term study, implying that persistent obesity and progressed metabolic changes do not exacerbate adaptive immune responses, but rather provoke an immunological adaptation to the constant metabolic imbalance. The results are consistent with findings by Porsche et al. (2021) showing that AT T cells can become exhausted as a mechanism to mitigate metabolic inflammation [193]. T cell exhaustion refers to a state of functional impairment observed in chronic inflammatory conditions, where T cells gradually lose their effector functions and exhibit increased expression of inhibitory receptors. This reaction potentially represents one of the underlying mechanisms observed in the long-term study.

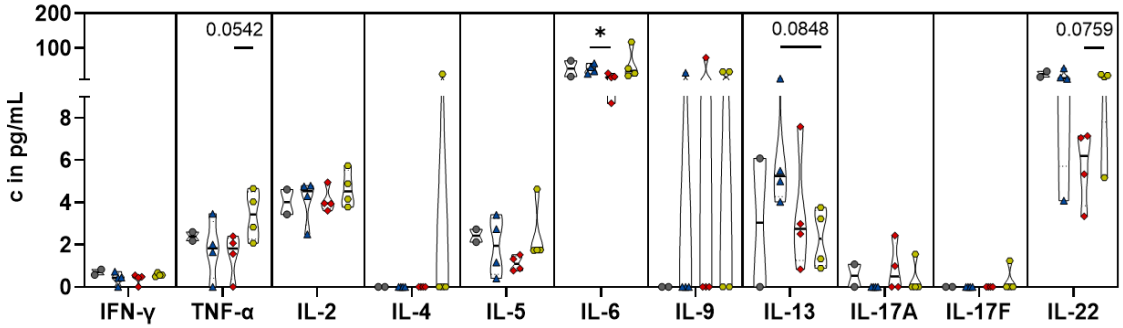

Fig. 35 | Profiling of T cell-related cytokines revealed similar levels between DIO mice and controls. Systemic cytokines were measured 3d post-fracture from blood plasma of lean and obese mice. Compared to controls, obesity did not enhance inflammatory responses. Median and IQR, *p<0.05, N=2-4 per group, Welch's t test

As described, analysis of intact contralateral bone on molecular level revealed a strong similarity between the obese groups in terms of adipogenic transcripts. Alterations in the ECM deposition and formation of OB and chondrocytes were related to progressed metabolic alterations in obese low GT mice. Results obtained from the analysis of fractured bones underline a clear distinctive molecular pattern of bone repair in lean and obese mice. As evident from the illustration of variances in gene expression profiles in the PCA plot, the osteotomized bones from obese high GT, low GT and CD8$^-$ low GT mice demonstrated proximal clustering, whereas the control group segregated separately (Fig. 36). The data also demonstrate that fracture healing in DIO mice with low GT is more consistent across samples, while a greater variation in the distribution of biological samples is seen in obese high GT and CD8$^-$ low GT mice. This observation is in conjunction with results obtained from micro-CT and the histological analysis. This suggests that obese mice

with high GT may be in a transitional disease state with a mild metabolic imbalance, contributing to multifaceted repair mechanisms. Additionally, the immunomodulatory intervention may have driven compensatory immune responses that adapt to the lack of $CD8^+$ T cells and lead to diverse healing patterns in the absence of $CD8^+$ T cells.

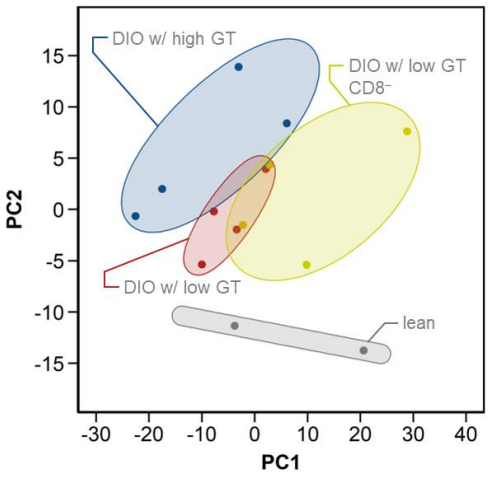

Fig. 36 | Fracture healing in obese mice separated from bone repair in controls on transcriptomic level. The principal component analysis illustrates the variance of gene expression profiles of fractured bones from obese mice and control samples where each point indicates a sample. N=2-4 per group

Investigation of bone fractures in obese mice confirmed excess lipids and adipocytes, as observed in intact contralateral bones (Fig. 37). In addition to an increased AT, fractured bones of DIO mice with high and low GT exhibited elevated levels of the mRNA transcripts *Ccl7*, *Ccl12* and *Cxcl15* compared to lean controls. These chemokines are acknowledged to produce inflammatory effects by attracting monocytes, macrophages [194, 195] and neutrophils [196] to an injury site. Moreover, the expression of *Ccr5* and *Il7r* was significantly increased in obese high and low GT mice compared to lean mice. Both receptors are known for their critical role in adipose tissue inflammation [197, 198]. Fractures in lean mice, on the other hand, showed increased *Il11* transcripts, which act as a blocking agent of adipogenesis in bone marrow stromal cells [199].

During initial fracture healing, the formation of cartilage and connective tissue is crucial for the proper development of a hard callus. The alterations in bone mineral density and cartilage deposition observed in obese fractures through micro-CT and histological staining, may be attributed to changes in collagen and ECM turnover, as indicated by the RNA transcript analysis of early bone fractures. Obesity development, regardless of the metabolic status, increased cartilage breakdown through the upregulation of mRNA transcripts of ECM modulators (*Mmp27*, *Adam23*, *Adamts6* [Adam with thrombospondin motifs 6], *Adamts12*, *Adamtsl1* [ADAMTS-like protein 1]) in comparison to lean controls. In conjunction with the enhanced ECM rearrangement observed in both obese high and low GT mice compared to the control group, the analysis revealed high expression levels of anabolic enzymes (*Itih5*, *Lox*, *Loxl*, *P4ha3* [prolyl 4-hydroxylase subunit alpha 3]) and

ECM components (*Lama4* [laminin subunit alpha 4], *Eln* [elastin], *Fbln2* [fibulin 2], *Kera* [keratocan], *Postn* [periostin], *Thbs2* [thrombospondin 2], *Thbs4*, *Gdf5* [growth differentiation factor 5]) as well as fibrillar (*Col3a1*) and non-fibrillar collagens (*Col14a1*, *Col15a1*). Besides, the study provides evidence that obesity progression, meaning the transition from mild to progressed metabolic changes, distinctly altered the deposition of fibrillar (*Col5a3*) and non-fibrillar collagens (*Col4a5*, *Col8a2*, *Col18a1*) when comparing lean with the low GT DIO group. Intriguingly, several detected ECM components such as collagens (III, IV, V) and laminin (LAMA4) [200] are known characteristics of AT remodeling, causing AT fibrosis [201] and potentially interfering with bone repair by promoting fibrotic scarring.

In context of dysregulated collagen and ECM development, bone fracture healing in obese mice may potentially involve disturbances in the osteoblastic and osteoclastic lineages. Bone repair in the obese groups with high and low GT exhibited decreased levels of osteoblast (*Alpl* and *Runx3*) and osteoclast (*Oscar*) markers compared to control fractures.

In addition, lean fractures displayed elevated RNA levels of *Smad6* ["small" worm phenotype (SMA), mothers against decapentaplegic (MAD) homolog 6], a critical regulator of BMP signaling, indicating a stronger control of BMP activity compared to fractures in DIO mice. BMPs play a role in stimulating both osteoblast and chondrocyte differentiation. Smad6 acts as a modulator of BMPs by providing feedback inhibition, thus attenuating cartilage formation [202]. Unlike fractures in obese mice, *Wnt4* transcripts were additionally enriched in fractured bones of controls. Wnt4 is described to promote osteogenic differentiation [203] and to limit skeletal inflammation during aging [204]. Moreover, factures of lean mice displayed increased levels of vascularization stimulators, such as *Vegfa* and *Vegfc*, indicating a defective or delayed process due to obesity.

Lastly, the analysis demonstrated that $CD8^+$ T cells contribute to ECM formation during healing, as evidenced by the absence of accumulative ECM deposition in obese $CD8^-$ low GT mice compared to controls. Strikingly, obese $CD8^-$ low GT mice exhibited increased mRNA levels of *Col10a1* compared to DIO high and low GT mice, highlighting the crucial role of $CD8^+$ T cells in regulating collagen formation and chondrocytes. Furthermore, removal of $CD8^+$ T cells in obese low GT mice resulted in a reduction of chemokine and receptor transcripts (*Cxcl5*, *Ccl7*, *Ccl12*, *Ccr5*), indicating a decrease in inflammatory actions.

In conclusion, the initial repair process in fractures of obese mice is characterized by an amplified synthesis of fibrillar and non-fibrillar collagen family members, as well as ECM components and their modulators. This observation is further emphasized during the progression of metabolic changes associated with obesity and is likely the joint outcome of bone marrow adiposity and MSC lineage commitment, contributing to an enhanced callus formation through active and early extracellular matrix (ECM) remodeling. This transcriptome-based catalogue, including a wide range of

ECM components, osteocellular, adipogenic and immune markers, expands the fundamental knowledge of initial bone fracture healing in the context of obesity.

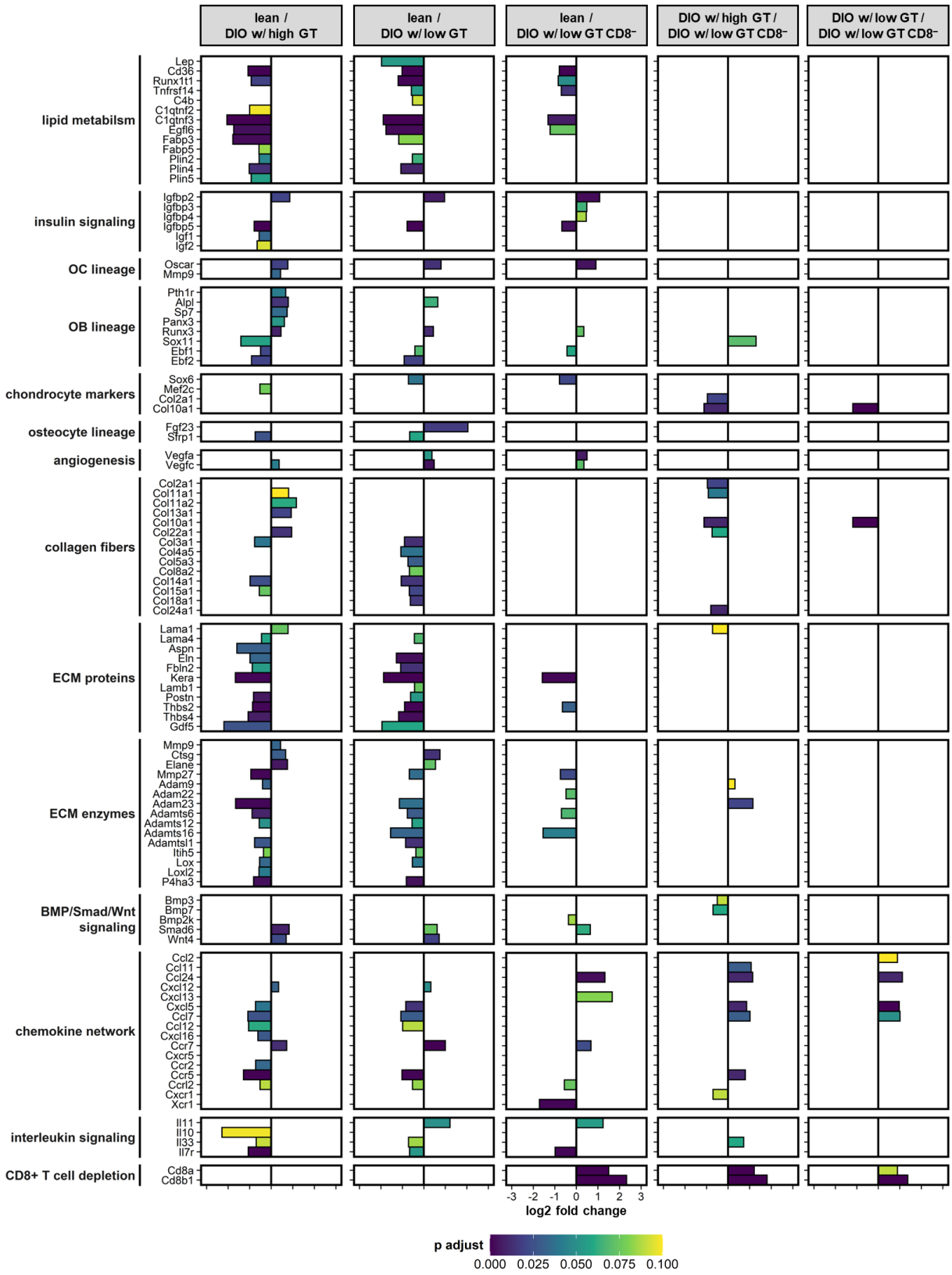

Fig. 37 | Obesity promoted the formation of collagen and ECM during initial bone repair. Results of DE genes in fractured bones are given as log2 fold change of either lean over obese groups, or obese mice with high/low GT over obese CD8⁺ T cell-deficient mice. N=2-4 per group, Wild test

3.3 The effect of the immune experience and bone fracture healing on the gut microbiome in aged mice

Microbial dysbiosis is increasingly recognized as a factor contributing to metabolic disturbances, as demonstrated in the previous DIO study. Changes in immunity display another determinant for an altered bacterial profile. The microbiome co-evolves and changes along with the adaptive immune system, which increases with age. However, so far disregarded were effects of the microbial composition on shaping the aged immunity – and vice versa. This is a considerable aspect as the experienced adaptive immune system plays a crucial role in delayed and failed fracture healing, especially in the elderly population [205]. Therefore, the etiology of immunity-associated healing complications can potentially be attributed to the gut microbiota.

The following study aimed to characterize the aged microbiome in context of bone repair as part of the project 'Local immune cell contribution during fracture healing in the aged – novel role for interleukin 22' (Bucher et al., 2022) [146]. The decreased regenerative potential related to aging is attributed to immunological memory changes, which were achieved by altering the housing conditions of an *in vivo* mouse model. For twelve months, one experimental group was housed in an SPF environment, resulting in a naïve immunophenotype due to minimal antigen exchange and referred to as "low immunoaged". In contrast "high immunoaged" mice developed experienced memory T cells due to permanent contact with environmental antigens.

Both differently immune-experienced groups originated from the same litter, and the cecal microbiome was sampled from a group of mice prior to osteotomy (0d), as well as from additional mouse groups 3d and 21d post-fracture for endpoint analysis. The cecum, along with the colon and feces, harbors a substantial portion of the body's microbiota. It serves as a reservoir of recycled microbes that can help to restore the microbial balance and provides valuable information about the gut constitution [5]. Bacterial 16S rRNA gene sequencing of cecal samples delivered first insights into the relationship between the gut microbiota, aged immunity and bone regeneration.

3.3.1 The bacterial diversity was affected by an advanced immunoage

The flow cytometric analysis prior to surgery showed that both naïve immune cell compartments of $CD4^+$ and $CD8^+$ T cells were significantly diminished in the immuno-experienced group. With enhanced immunoaging, the proportion of naïve $CD4^+$ T cells from spleen significantly decreased from 29.6 % (± 6.0) in low immunoaged mice to 17.8 % (± 4.3) in the high immunoaged group ($p=0.03$) (data from Bucher et al., 2022 [146], not shown). The major memory population in the $CD4^+$ T cell pool were effector memory (EM) T cells increasing from 37.3 % (± 5.6) in low immunoaged mice to 54.3 % (± 4.6) in the high immunoaged group (p-value <0.01). Similarly, naïve

$CD8^+$ T cells were significantly less abundant in mice with a high immunoage compared to low immunoaged mice ($p<0.01$). The prominent $CD8^+$ memory population in high immunoaged mice consisted of central memory (CM) T cells, which accounted for 61.1 % (± 1.3) of the population. In contrast, low immunoaged mice had a lower proportion of $CD8^+$ CM T cells, with only 36.6 % (± 2.4) ($p<0.01$). These age-related effects were also observed in the bone marrow. Overall, the flow cytometric evaluation revealed the development of differently experienced immune systems associated with the housing conditions. In addition, bone repair was delayed in high immunoaged mice 21d post-surgery, which could be associated with the increased memory development and significant changes in cytokine levels (data from Bucher et al., 2022 [146], not shown).

Regarding the microbiome, the enumeration of bacterial community members present in the cecal sample revealed a comparable alpha-diversity, represented as bacterial richness, between low and high immunoaged mice before the fracture was introduced (Fig. 38, A). Surprisingly, this suggests that the overall diversity of bacteria in the native microbiome was similar in both groups at the age of 12 month. Mice from both groups further underwent an osteotomy in the left femur by external fixation. To prevent surgical site infections, both experimental groups were treated with the bone-penetrating antibiotic clindamycin during surgery. This treatment resulted in a significant elimination of bacteria, as determined 3d after the osteotomy (Fig. 38, A). However, 21d post-surgery, mice with a more advanced adaptive immunity (high immunoage) showed a slower reconstitution of their microbiome compared to mice with a low immunoage, as evidenced by a decreased microbial richness (Fig. 38, A). In addition, the determination of Shannon effective counts provides a measure of both richness and evenness of microbial abundances. Similarly to the richness analysis 21d post-fracture, the calculation of the Shannon index revealed a decreased microbial diversity in high immunoaged compared low immunoaged mice (Fig. 38, A).

Moreover, the distance calculation evaluates the beta-diversity between samples based on general UniFrac distances, an all-against-all distance matrix including shared taxonomic composition and genetic distances of the community members in each sample to the members in the other sample. The MDS plot illustrates a close clustering and relationship of both experimental groups prior to surgery (0d) (Fig. 38, B). However, the administration of antibiotics (Abx) significantly separated both groups from their native microbiome shortly after the introduction of the fracture and Abx treatment on day 3. Remarkably, the analysis 21d after the surgery identified a distinctive shift of bacterial profiles in high immunoaged mice compared to their undisturbed microbiota pre-surgically (0d), while the low immunoaged group returned to its initial state of bacterial diversity.

Overall, the reduced microbial diversity in high immunoaged mice after Abx administration is likely attributed to the stronger pressure exerted by the adaptive immunity.

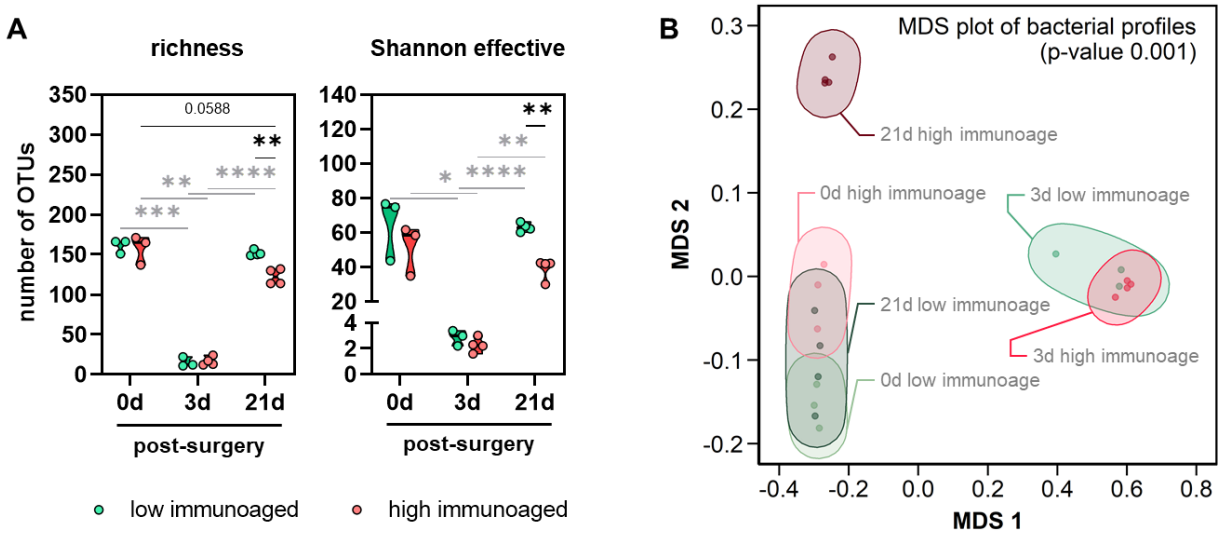

Fig. 38 | Diversity of cecal microbiota analysis assessed by 16S rRNA gene amplicon sequencing. **A |** Diversity within samples (α-diversity) was estimated by richness and Shannon index. Diversity 3d post-surgery is significantly reduced due to clindamycin administration. The high immune experience significantly hindered the microbial reconstitution 3 weeks after treatment. Median and IQR, *p<0.05, **p<0.01, ***p<0.001, ****p<0.0001. N=3-4 per group, Welch's t test **B |** The MDS plot shows alterations in diversity between samples (β-diversity) based on general UniFrac distances and revealed a distinct clustering of mice with a high immunoage 21d after fracture. p=0.001. N=3-4 per group, PERMANOVA

3.3.2 The experienced immunity disturbed the reconstitution of the phylum Bacteroidetes after antibiotics treatment

Both pre-surgery and 21d post-fracture, a majority of the community members belonged to the Bacteroidetes and Firmicutes phyla (Fig. 39, A), which are common components of the human and murine intestinal microbiota [206]. Other phyla such as Candidatus Saccharibacteria, Deferribacteres, Proteobacteria and Verrucomicrobia comprised a smaller proportion in the cecal microbiota among both experimental groups. Notably, the high immunoaged mice exhibited a significantly higher abundance of the phylum Verrucomicrobia compared to the low immunoaged group.

The administration of clindamycin had a detectable effect 3d after the fracture, leading to a significant proteobacterial blooming in both groups, while diminishing the presence of other phyla. 21d after the osteotomy and Abx administration, the clindamycin effect notably reduced and the microbial composition on phylum level returned to its pre-antibiotic state in both low and high immunoaged mice.

Upon analyzing operational taxonomic units (OTUs) that provide strain-level information [207], it was observed that the immunological experience had a significant impact on the recolonization of OTUs from the phylum Bacteroidetes (Fig. 39, B). The reestablishment of the class Bacteroidia, belonging to Bacteroidetes, was partially suppressed 21d post-surgery in high immunoaged mice, even though they were originally present in the microbiota in both groups and reconstituted in

the low immunoaged group (Fig. 39, B). Similar to the class Bacteroidia, the classes Deltaproteobacteria and Deferribacteres also exhibited a partial suppression in their recolonization, although to a lesser extent compared to Bacteroidetes.

Altogether, these data indicate that the advanced experienced immune system significantly delayed the cecal reconstitution, adversely affecting the composition of the phylum Bacteroidetes.

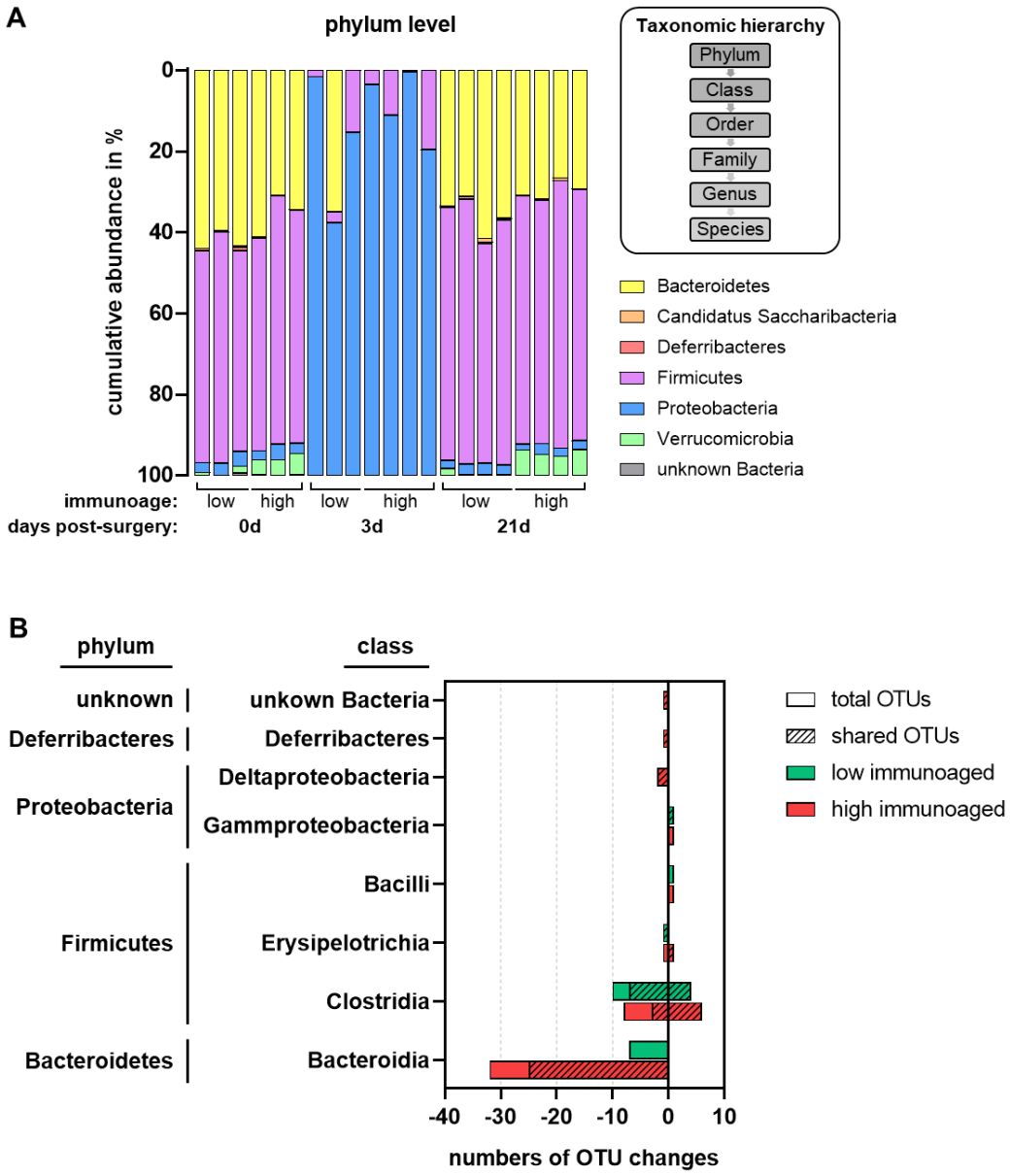

Fig. 39 | Taxonomic gut microbiota composition. A | Cumulative abundance chart showing phyla level composition of cecal samples before osteotomy (0d), 3d and 21d post-fracture in low and high immunoaged mice. The proteobacterial blooming 3d after fracture resulted from clindamycin treatment during surgery. **B |** Description of overall changes in operational taxonomic units (OTUs) comparing bacterial enumerations prior to surgery (0d) with the reconstituted microbiome 21d after fracture in low (green) and high (red) immunoaged mice. The illustration depicts OTUs (dashed fill) that were present before Abx treatment in both low and high immunoaged groups in relation to total OTU changes. In particular, shared bacteria from the class Bacteroidia (Bacteroidetes phylum) recolinized the caecum in low immunoaged mice 21d after treatment. However, high immunoaged mice exhibited a bacterial loss as these shared microbes did not reoccur after 21d, even though they were originally present. Mean. N=3-4 per group

3.3.3 Immunoage-associated alterations in the gut microbiome on genus level

Among the predominant Bacteroidetes family that reduced due to Abx treatment were members of the important short chain fatty acid producers Porphyromonadaceae [208] (Fig. 40, A). Significant differences were observed in the genus Barnesiella and other unidentified Porphyromonadaceae strains, which were absent in high immunoaged mice 21d post-fracture (Fig. 40, A). Moreover, it was observed that in both experimental groups, the genera Odoribacter (a member of the Porphyromonadaceae family) and Prevotella (belonging to the Prevotellaceae family) were also eliminated as a result of the clindamycin treatment. These microbes are associated with the host's immunity and play a role in the induction of intestinal Th17 cells [209, 210].

In high immunoaged mice, significant decreased abundances of the butyrate-producing bacterium Clostridium IV [211], as well as other unknown genera within the Firmicutes phylum were identified 21d after the surgery (Fig. 40, A). Additionally, a similar trend was observed in the commensal genus Mucispirillum [212], which belongs to the Deferribacteres phylum. Its abundance also decreased in high immunoaged mice following the surgery and Abx treatment.

In addition, the Abx administration resulted in a balanced abundance of the genus Parasutterella 21d post-fracture in both low and high immunoaged mice. Prior to surgery, mice with a more naïve immune experience displayed a higher abundance of Parasutterella (Fig. 40, B).

Furthermore, the analysis revealed significant elevated abundances of genera belonging to the Bacteroidetes phylum, including the facultative pathogen Bacteroides and unknown symbiotic Bacteroidales strains particularly in mice with a high immunoage (Fig. 40, C) [213, 214]. The mutualist Ruminococcus, a member of the Firmicutes phylum, additionally enriched in both low and high immunoaged groups 21d after surgery and Abx administration [215].

Interestingly, high immunoaged mice significantly harbored the genus Akkermansia compared to low immunoaged mice prior to facture introduction and 21d after surgery (Fig. 40, D). This finding suggests a robust colonization with species from Akkermansia that are associated with a healthy gut lining and reduced metabolic disorders in humans [216].

In summary, the advanced immune system in high immunoaged mice along with the Abx treatment had a significant and persistent effect on the reconstitution of the microbiome, impacting the microbial diversity and composition. Notable changes were detected in the Bacteroidetes phylum, which includes important bacteria involved in the production of short chain fatty acids.

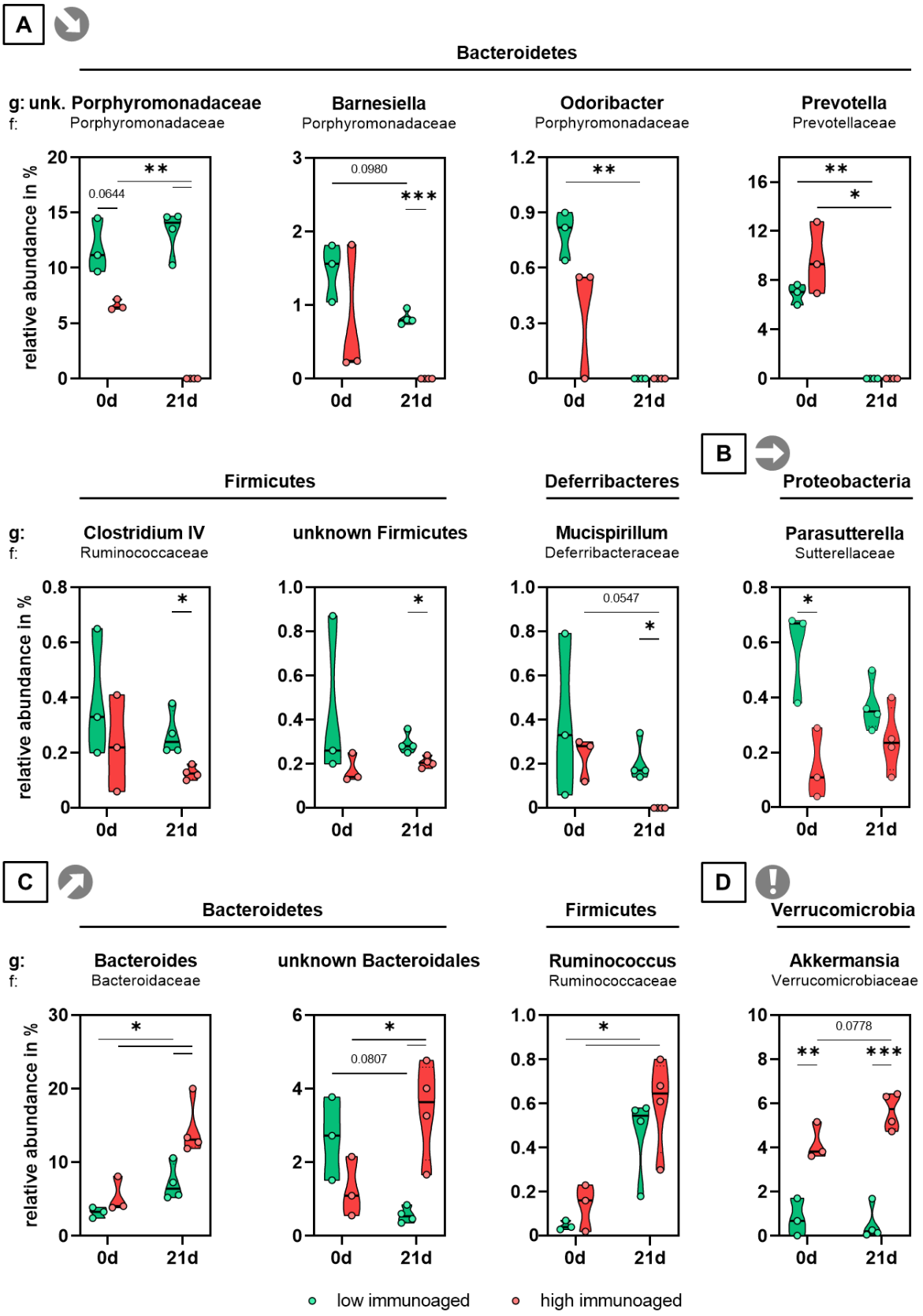

Fig. 40 | Relative abundance of taxonomic groups on genus level that were significantly different between low and high immunoaged mice before and 21d after Abx treatment. Illustration of decreased **(A)**, equalized **(B)**, increased **(C)** and striking **(D)** differences between both groups. Data obtained 3d post-surgery were excluded from the analysis due to the vast Abx-induced elimination of bacteria. g: genus, f: family. Median and IQR, *p<0.05, **p<0.01, ***p<0.001. N=3-4 per group, Welch's t test

4 Discussion

The course of bone fracture healing is a complex interplay of cellular and molecular events, coordinated to regenerate a completely functional and resilient bone. However compromised conditions, such as those observed in obesity-associated type 2 diabetes mellitus (T2DM) deteriorate the event cascade, leading to impaired healing or non-unions. Additionally, already obesity itself poses early dangers that are increasingly gaining attention in preventative healthcare. Heightened inflammation, specifically regulated by the adaptive immunity, plays a pivotal role in the pathophysiology of obesity and contributes to healing defects. Despite the high obesity prevalence only limited clinical data provide information about this relationship.

Thus, the present study postulated that the increased pro-inflammatory state associated with obesity might contribute to delayed bone repair. To address this hypothesis, the study had two primary objectives. Firstly, it aimed to investigate how different degrees of obesity, as encountered in the clinic, influence adaptive immune responses and their impact on bone fracture healing. This investigation encompassed both short-term and long-term obesity effects to examine the onset and persistent impacts of the condition. Secondly, the study aimed to evaluate the potential of immunomodulation to enhance bone repair. Furthermore, considering the well-established role of the microbiome in the development of obesity, as well as its close link to adaptive immunity and metabolic inflammation, the study explored potential pathological changes in the composition of gut bacteria within the context of immunity-regulated fracture healing. To achieve this, a model of high-fat diet (HFD)-induced obesity was used along with femoral osteotomy. Two obese subtypes were identified based on their body and metabolic parameters, representing mild (with high glucose tolerance, GT) or progressed metabolic changes (with low GT).

The findings demonstrated that the onset of obesity, induced by a short-term HFD, stimulated pro-inflammatory responses associated with the adaptive immunity. These changes resulted in impaired healing and an altered microarchitecture of femoral fractures in both obese groups. However, differences between the obese subtypes were observed in the formation of cartilage and connective tissue. Interestingly, in obese mice with low GT, the progressive metabolic changes were found to sustain the altered immune signature without exacerbating pro-inflammation, indicating a body's adaption to metabolic disturbances as the disease aggravates.

Consistent with these observations, long-term persistent obesity resulted in reduced pro-inflammation in the obese groups, reaching levels comparable to those seen in lean control mice. Surprisingly, along with increased weight gain, callus adiposity and bone mineralization, the pre-

viously observed healing defects associated with short-term obesity were reversed. However, increased remodeling and formation of extracellular matrix (ECM) were observed during initial bone repair, with more pronounced effects in obese mice with low GT. This finding suggests a potential risk for fibrotic scarring. However, the disturbance in the ECM formation in the obese group with low GT was restored by neutralizing potentially detrimental $CD8^+$ T cells during the early healing phase. This observation underlines the pivotal role of $CD8^+$ T cells during bone fracture healing and provides a promising therapeutic avenue for enhancing bone formation in certain patients. Strikingly, obese mice with high GT demonstrated callus adiposity prior to the onset of fatty liver. This finding indicates that bone marrow adiposity is an early event preceding systemic changes, resulting in a unique bone phenotype that can impact bone repair.

In addition, the study investigated the role of the gut microbiome, which is known to be involved in obesity development and closely linked to adaptive immunity and metabolic inflammation. Analysis of murine caecum and feces samples revealed that the long-term HFD altered the structure of the microbiome, while bacterial diversity remained unaffected. Moreover, obese mice with low GT exhibited a distinct microbial signature primarily associated with metabolic rather than immunological changes. Interestingly, the neutralization of $CD8^+$ T cells partially reversed this microbial signature, indicating that specific bacteria underlie immune regulation.

Furthermore, a previous osteotomy study conducted on aged mice also revealed an immunity-mediated colonization process in the gut microbiome. It was demonstrated that the restoration of a beneficial and fermentative microflora after antibiotics administration was impeded by the experienced adaptive immunity, which developed in aged mice. This finding carries critical implications during the recovery process.

Overall, this study has presented compelling evidence that abnormal bone formation takes place prior to the development of T2DM, particularly during the progression of obesity. The adaptive immune system becomes more activated during the onset of obesity, resulting in impaired bone formation. Although the skeletal system adapts to the immunological and metabolic imbalances associated with persistent obesity, these adaptations are still accompanied by alterations in the ECM. These findings have clinical relevance regarding the impact of obesity on immunity, bone and gut health. Addressing obesity becomes crucial for making appropriate and timely decisions for vulnerable patients. Thus, this study opens up new avenues to explore fundamental mechanisms related to immune-regulated bone repair in the context of obesity, as well as potential treatment approaches.

4.1 The role of adaptive immunity in impaired bone fracture healing in obese mice after a short-term high-fat diet

In the short-term study, I revealed that the impairment of the metabolism-immune function axis is associated with defective fracture healing. Here, the work is based on an established diet-induced obesity (DIO) model, which served to imitate the clinical metabolic disbalance seen in obese and prediabetic individuals. When providing high-fat diet, mice develop obesity, hyperglycemia and hyperinsulinemia. But the animals responded differently to the diet intervention and either represent mild (with high GT) or progressed metabolic changes (with low GT). This categorization offers a valuable framework for understanding the mechanisms related to distinct metabolic characteristics, akin to the conceptualization of prediabetic and T2DM subtypes observed in humans.

In particular, the obese groups demonstrated a dysregulated adaptive immunity in the $CD3^+$ T cell compartment, characterized by increased levels of systemic $TCR\gamma\delta^+$ and Th17 cells, resulting in an imbalance of the $CD4^+CD25^{hi}FoxP3^+$ T cell/Th17 cell axis. Remarkably, obese mice with high GT had additional changes in the immunological makeup displayed by enriched systemic $CD8^+$ memory T cells and pro-inflammatory M1 macrophages in the bone marrow. Concomitantly, I report an association of the Thelper cell-derived pro-inflammatory cytokines IL-17F, IL-22 and IL-9 to impaired fracture healing in both obese groups. Thus, my findings highlight the impact of short-term obesity on immune and skeletal processes, emphasizing their severity. It represents a major clinical challenge because of the high obesity prevalence and large number of undiagnosed cases. To gain a better knowledge about obesity and prediabetes is a relevant aim that could considerably reduce the number of diabetics and associated disorders.

During obesity and T2DM, innate immune cells and most notably macrophages gain a pro-inflammatory phenotype that aggravates the disease pathophysiology and comorbidities [217]. Macrophages especially accumulate in adipose tissue (AT), and growing evidence suggests that metabolic reprogramming alters the macrophage function, leading to impaired wound healing in diabetics [217-220]. In bone fracture healing, macrophages have the capability to steer fortunate endochondral ossification in all phases of bone regeneration [221, 222], whereas depletion of macrophages deteriorates bone formation [221, 223]. Macrophages can form specialized active subsets and are discriminated into classically activated, pro-inflammatory M1 and alternatively activated M2 macrophages with the subtypes M2a, M2b, M2c and M2d. In the present study, identification of macrophage subsets of intact contralateral bone marrow aimed to investigate the bone microenvironment and the potential impact on fracture healing in the context of obesity. Remarkably, polarization of macrophages towards the pro-inflammatory M1 phenotype was pronounced in obese mice with high GT and mice with low GT displayed an increased tendency. In

contrast, the inactivated M2c macrophages were reduced in both obese subtypes, while anti-inflammatory M2a and M2b as well as proangiogenic M2d macrophages were less affected by obesity. In this context, a DIO study from Kang at al. (2021) showed that transferring macrophages with an inflamed phenotype from obese into lean mice impaired bone repair [224]. In addition, findings by Dai et al. (2022) discovered that osteopontin-secreting macrophages present in AT contribute to selective osteoclast activation and modulation of bone marrow resident macrophages. These mechanisms were responsible for obesity-induced bone loss *in vivo* [225]. However, specific M2 macrophage subtypes and their behavior *in vivo* are still not fully understood [42]. In summary, my experimental set-up revealed that already obesity with mild glucose intolerance (high GT) contributed to shaping the pro-inflammatory macrophage microenvironment of intact bone marrow underlining the importance to focus on early disease development.

Similarly to macrophages, dendritic cells are a prerequisite in successful bone fracture healing through their interaction with T cells. However, in the context of obesity, dendritic cells are also associated with disturbed immune responses and the progression of chronic low-grade inflammation [160]. Nonetheless, abundances of dendritic cells in intact contralateral bone marrow were comparable between all experimental groups. Certainly, a local analysis and temporal resolution over the fracture healing period may provide more information about bridging the innate with the adaptive immunity in fractures under compromised conditions.

Contrary to the innate immune system, obesity induced drastic changes of the systemic adaptive immunity. This work revealed a substantial elevation of $CD3^+$ T cells in bone marrow implicating an increased $CD3^+$ T cell-driven immune response. The investigation further unveiled augmented systemic levels of $CD8^+$ memory T cells in obese mice. Most strikingly, the DIO group with high GT revealed a significant accumulation, while obese low GT mice showed a trending increase. Several studies have demonstrated that an experienced adaptive immunity profoundly affects bone homeostasis and repair [88, 90, 205]. Additional work shows that obesity increases memory T cell numbers in AT and spleen, causing severe pathology [30, 226, 227]. Particularly in the present study, I detected peripheral $CD4^+$ and $CD8^+$ T cells in obese mice with low GT that displayed the features of functional effector cells. Enrichment analysis of the single cell sequencing data illustrated differentially expressed genes that were mainly associated with signaling of chemokine and NOD-like receptors in $CD4^+$ T cells in obesity. The pathways primarily control trafficking and inflammation [165-168] implicating an increased immune activity in obese mice. Especially, the enhanced type II interferon pathway in obese $CD8^+$ T cells, underlines an increased mediation of IFN-γ signaling. Moreover, gene programs associated with T cell function during chronic infections were likewise enriched in obese $CD4^+$ and $CD8^+$ T cells. Thus, obese T cells gain transcriptional and functional properties of activated effector/memory T cell states. The findings highlight-

ed the probable importance of key genes and the biological behavior of obese T cells, which provide increased immunity and potentially deteriorate regenerative processes.

Moreover, this work demonstrated a considerable systemic accumulation of γδ T cells in obese mice with high and low GT (Fig. 41). During diet-induced obesity, γδ T cells are described to be resident in AT contributing to pro-inflammatory responses through the stimulation of macrophage TNF-α expression [59, 60, 228]. Whereas in a DIO study using TCRγδ$^{-/-}$ mice, significant improvements were observed in terms of insulin resistance, liver and muscle inflammation, along with reduced abundances of AT macrophages. This was accompanied by reductions in CC-chemokine ligand 2 (CCL2) and interleukin (IL) 6 [228]. γδ T cells are additionally attributed a substantial role in bone fracture healing and their absence has been associated with improved biomechanical strength and stability [229]. The findings indicate that the "obesity-γδ T cell axis" may profoundly contribute to chronic low-grade inflammation and thereby impairs fracture healing.

Furthermore, in my experimental setup, obesity induced a significant phenotype change in systemic CD4^{+} T cells in both DIO groups, as observed 21d post-fracture. The flow cytometric results confirmed a systemic increase in the abundance of Th17 cells, indicating a preserved pro-inflammatory state. Activated Th17 cells play a pivotal role in regulating bone fracture healing. Studies have shown that these cells promote bone resorption through the secretion of IL-17 at the fracture site, thereby enhancing osteoclast activity, while suppressing the development and activity of osteoblasts involved in bone formation [230-232]. However, long-lasting and excessive Th17 signaling, as observed in my research, leads to amplified inflammation. This exaggerated inflammation has been shown to contribute to bone loss, particularly in the context of diabetes-associated periodontitis [233]. Consequently, targeting Th17 cells could restore cellular homeostasis by restricting cytokine secretion and modulating the interaction between the immune and skeletal systems.

While Th17 cells promote pro-inflammatory signals, anti-inflammatory CD4^{+} Treg cells play a role in maintaining immune homeostasis, suppressing excessive immune activation and regulating osteoclast activity [234]. Even though both T cell subsets originate from the same precursor, they fulfill different functions in immunity and bone remodeling. Treg cells, unlike Th17 cells, are capable of blocking osteoclasts by inhibiting RANKL and macrophage colony-stimulating factor (M-CSF), which leads to increased bone mass [235]. Therefore, understanding the balance of Th17 and Treg cells under healthy and compromised conditions is crucial for gaining novel insights and developing treatment strategies. Interestingly, my data demonstrated increased proportions of CD4^{+}CD25^{hi}FoxP3^{+} T cells, which likely represent the phenotype of Treg cells, during obesity development, with a more pronounced effect seen in obese high GT mice. Notably, these findings

contradict the prevailing understanding of decreased Treg levels in the context of obesity, as commonly observed in both murine models and individuals in the peripheral blood and AT [236-240]. However, other studies reported unaltered [241] or even increased Treg proportions in humans [242]. This controversy underlines the complexity of the obesity pathophysiology and its effects on shaping immunity. Certainly, the effects of obesity on Treg cells can vary depending on factors such as mouse strain, antigen environment, feeding duration and interventions. But currently, the mechanism by which Treg cells regulate metabolism and AT inflammation in metabolic disorders remains largely unexplored [236, 243]. Hence, defining this work as highly necessary is justified. In addition, the single cell sequencing analysis corroborated these findings in peripheral blood of obese low GT mice, indicating a stronger regulation of the adaptive immune system. Relating thereto, increased $CD4^+CD25^{hi}FoxP3^+$ T cell numbers potentially counteract the Th17 expansion stimulated by obesity. However, despite the increase in $CD4^+CD25^{hi}FoxP3^+$ T cells due to obesity, the data revealed significantly decreased $CD4^+CD25^{hi}FoxP3^+$ T cell/Th17 cell ratios in both obese groups. This imbalance has also been reported in obese individuals and is associated with chronic inflammation [244-246]. Consequently, my results demonstrate the importance of translating these findings to patients. In line with this, obesity not only affected the $CD4^+CD25^{hi}FoxP3^+$ T cell compartment after obesity induction and injury, but also induced $CD8^+Foxp3^+$ T cells in both obese groups. This immune subtype holds immunoregulatory functions and inhibits excessive immune reactions in obesity to maintain immune homeostasis [247]. Nonetheless, only a relatively limited number of studies has addressed the role of $CD8^+FoxP3^+$ T cells in the context of obesity or fracture healing *in vivo*, as the concept of $CD8^+FoxP3^+$ has not been unanimously agreed upon [248, 249].

Moreover, the cytokine expression data strengthen the evidence of an imbalance between pro- and anti-inflammation as underlying mechanism, which delays fracture healing. In this study, IL-17F was highly induced due to obesity, which was associated with defective bone repair. Th17 cells and γδ T cells are the primary sources of IL-17F production, both sharing a similar secretion profile [250]. IL-17F, known for its pro-inflammatory properties, can induce the expression of inflammatory cytokines and chemokines, such as IL-6 and IL-8, in non-hematopoietic cells [251-254]. The IL-17F protein sequence shares homology with IL-17A, and both cytokines are considered critical elements and potential biomarkers for amplified chronic low-grade inflammation in obese individuals [255, 256]. However, the role of IL-17F in bone reconstitution is still relatively understudied and controversial. A study has shown that IL-17F promotes osteoblast maturation *in vitro* [257], while another report suggests that IL-17 can induce osteoclast formation [258]. Overall, IL-17F is proposed to be a key regulator that connects T cell and bone biology [257]. The stimulating effects on these types of bone cells may vary depending on specific conditions and concentrations. Interestingly, IL-17F is well-known for its involvement in the pathogenesis of pso-

riasis [259-261], and a dual inhibition of IL-17A and IL-17F has shown efficacy in controlling the disease in clinical studies [262, 263]. However, limited research is available exploring the specific role of IL-17F in bone regeneration in regards to obesity. IL-17A has gained significant recognition as a key contributor to bone resorption in osteoporosis [264] and a promising target for therapeutic interventions in conditions such as psoriasis [265, 266], arthritis [267, 268], hepatic diseases [269, 270] and obesity [271]. Thus, my data opens the window for further investigation to explore the regulatory activity of IL-17F in context of fracture repair in health and disease.

In addition, the pro-inflammatory cytokine IL-22 has been significantly detected in obese high and low GT mice compared to lean controls. IL-22 is the signature molecule of activated Th22 cells, as well as Th17, Th1 cells and type 3 innate lymphoid cells (ILC3) during inflammation in non-hematopoietic tissues [272, 273]. It induces antimicrobial peptides [272, 273], chemokines and acute-phase proteins [274]. IL-22 plays a complex dual-natured role in inflammation and obesity. On the one hand, it provides therapeutic and metabolic benefits by protecting against endoplasmic reticulum/oxidative stress, preserving the mucosal barrier integrity, and restoring glucose tolerance [275, 276]. On the other hand, IL-22 has been found to be elevated in T2DM [277] and to intensify AT inflammation in diabetic patients [162]. Similar to IL-17F, the role of IL-22 in bone fracture healing is controversial, and its activity in regeneration in obese individuals is less explored [278-280]. A recent study, however, has identified IL-22 as a central signal pathway impairing bone formation in an identical pre-clinical model using immunoaged mice [146]. Blocking of IL-22 has shown to reverse the delayed healing outcome mediated by inflammation, which is more prevalent in the elderly. This suggests that obesity, which often develops in the elderly, may amplify immune responses that disrupt fracture repair and increase with age.

In addition to IL-17F and IL-22, obesity led to elevated circulating levels of IL-4 and IL-9 in this study, which were more pronounced in obese low GT mice. Both cytokines play important roles in immune regulation, but their functions in obese fracture healing are less understood. IL-4, an anti-inflammatory cytokine, promotes Th2 differentiation and initiates alternative macrophage activation when secreted by Th2 cells, mast cells, eosinophils and basophils [281]. It can also resolve Th17-mediated inflammation [282], which highlights IL-4 as potential regulator of Th17 cell responses. Studies have reported increased IL-4 levels in obesity [283, 284] and linked IL-4 to lipid metabolism by inhibiting adipogenesis and promoting lipolysis [163, 285]. Interestingly, IL-4 has dose-dependent effects on osteogenic differentiation of human adipose stem cells, promoting ALP activity for bone formation, but negatively regulating early RUNX2 expression, a key transcription factor for osteoblast differentiation [286]. My findings suggest that increased IL-4 levels likely counteract the Th17 cell response, but excessive secretion can contribute to alterations in bone formation.

IL-4 and IL-9 are possibly interconnected, as IL-4 can induce IL-9 secretion [287] and was found to be highly expressed by obese low GT mice in this work. IL-9 is a pleiotropic inflammatory factor that promotes immune tolerance when secreted by Th9 and Th2 cells [288, 289]. Moreover, the demonstrated expansion of Th17 and $CD4^{+}CD25^{hi}FoxP3^{+}$ T cells observed in obese mice is potentially influenced by IL-9, which has been shown to induce the differentiation of these T cell subtypes [290-292]. Obesity studies have also reported increased levels of IL-9 in adipose-rich environments [293], while weight loss in overweight and obese individuals leads to decreased IL-9 concentrations [294]. In addition, the increase in IL-9 in the context of obesity may negatively affect bone repair. IL-9 has been associated with the induction of pathogenic osteonecrosis in femoral head patients and has been linked to increased osteoclastogenesis in rheumatoid arthritis, with cartilage degradation and amplified inflammation being seen as the underlying mechanisms [295, 296]. Although the correlation between IL-9 production in obesity and impaired fracture healing is unclear, my work demonstrated another therapeutic approach that may be relevant *in vivo* and for clinical translation.

Conclusion and outlook

The study has provided valuable insights into the role of obesity on the modulation of adaptive immunity and its detrimental effects on bone fracture healing. Analysis of the immune cell composition and cytokine profiles revealed significant pro-inflammatory cues (Fig. 41), opening up new opportunities for investigating essential immunological mechanisms and potential therapeutic interventions to improve bone repair.

The work emphasizes the importance of carefully considering cytokine concentrations and exposure duration to shape their effects on bone regeneration in obese individuals. In addition, the data highlight the crucial role of T cells as key regulators connecting immune and skeletal responses in terms of metabolic deterioration. Therefore, the work underlines a clear need to investigate how distinct metabolic characteristics affect T cell metabolism, function or even exhaustion. It is warranted to explore potential mechanisms associated with metabolic reprogramming, including T cell oxidative metabolism and the capacity for fat and glucose uptake. Such investigations can provide valuable information into the interplay between metabolic dysregulation and immune function, contributing to a better understanding of bone regeneration in the context of obesity.

The findings emphasize that the onset of obesity already establishes a distinct inflammatory state. Consequently, early management of glycemic control and body weight is crucial to mitigate the detrimental effects of obesity, including complications like fracture healing defects. By targeting and modulating the immune response, it may be possible to reduce inflammation and enhance bone repair in obese individuals.

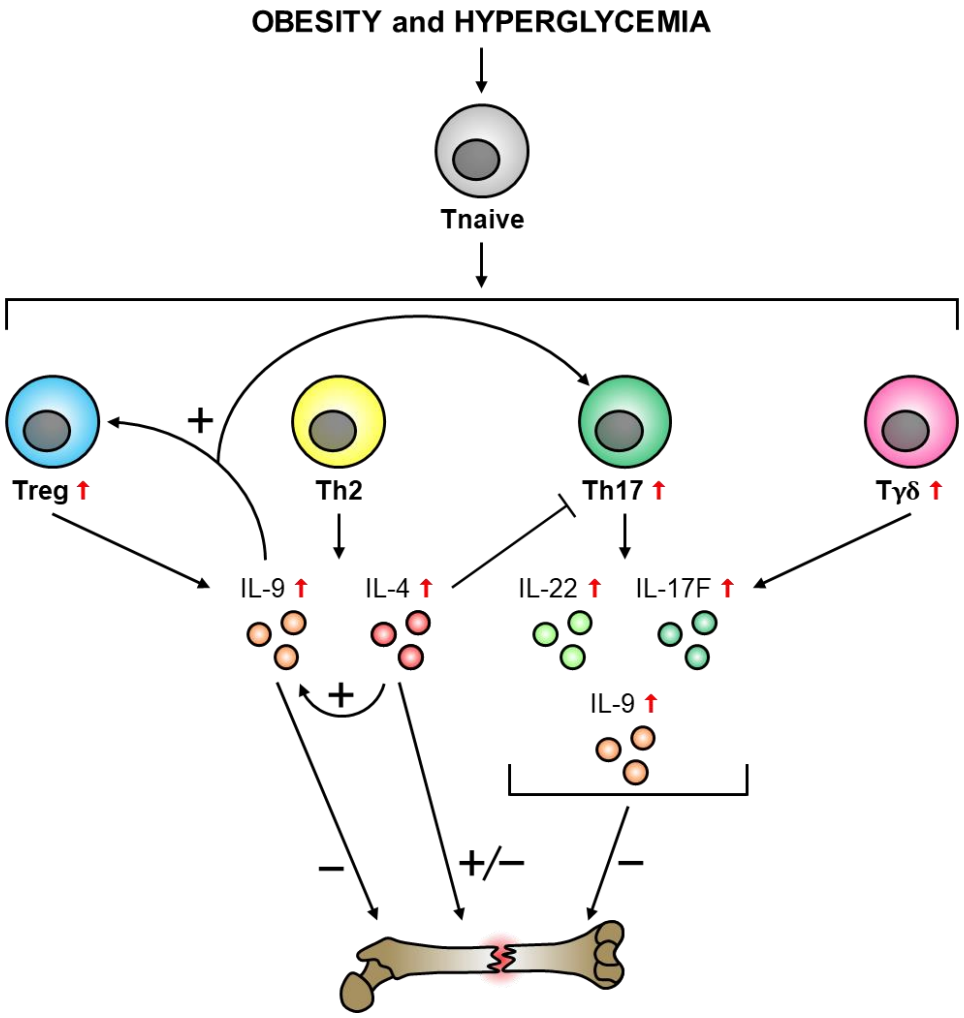

Fig. 41 | Schematic illustration of the immunological changes associated with obesity and their potential impact on bone fracture healing. Obesity promotes the differentiation/polarization into Th17 cells, which secrete IL-17F along with TCRγδ+ T cells. In addition to IL-17F, IL-22 and IL-9 contribute to delayed bone repair. On the contrary, the increased presence of CD4+CD25hiFoxP3+ T cells and elevated levels of IL-4, primarily released by Th2 cells, counteract the pro-inflammatory Th17 responses.

4.2 Comparison of bone repair after short- and long-term obesity

The study aimed to test the hypothesis whether distinct metabolic characteristics associated with obesity exert different effects on the adaptive immunity and bone fracture healing, leading to delayed and impaired bone repair. In this work, mice exposed to short-term high-fat diet for 7 weeks exhibited a significantly reduced bone formation 21d post-fracture and a delay in fracture healing compared to lean mice (Fig. 44, p. 123). The callus in obese mice showed abnormalities in the woven bone microstructure, including increased porosity and reduced trabecular numbers. These findings align with other studies conducted on male C57BL/6J DIO models, which reported impaired fracture healing due to defects in cartilage and Col1 deposition, as well as in the formation

of an adipose callus [14, 107, 112]. A report also associated defective repair with reduced levels in bone mineral density [14] that were not detected in this work.

Obesity may affect fracture healing during the stage of cartilage formation, which is a required step in the sequential process of bone repair. In the initial stage, chondrocytes infiltrate the fracture site and surrounding area to build a soft callus, which undergoes hypertrophy, soft-callus mineralization, vascularization and remodeling [297]. Notably, in this study, it was observed that while the callus of lean mice had already mineralized, the callus of obese high GT mice exhibited a dominance of cartilage, indicating a delayed callus formation. Furthermore, obese mice with low GT experienced an accelerated resorption of the cartilaginous callus, which was replaced by connective tissue. These results demonstrate that the varying degrees of glucose intolerance induce aberrant molecular mechanisms of soft and hard callus formation, leading to detrimental consequences for the healing outcome. The data are in accordance with reports using DIO models characterized by hyperglycemia and glucose intolerance [14, 112]. However, the underlying mechanism contributing to the distinct healing processes observed in this study remains poorly understood due to limited research data. The healing defects may be attributed to the differential commitment of mesenchymal stromal cells (MSCs) towards adipogenesis at the expense of osteogenesis, which could contribute to decreased bone formation in the obese groups [112].

Khajuria et al. (2020) [14] additionally revealed an association between DIO and collagen-fiber defects, which deteriorate callus mineralization and strength. Col1, the most abundant fibrillar collagen in the remodeled callus, consists of three helical strands [169]. Under pathological conditions, such as obesity-induced T2DM, these fibers may disassemble, incompletely assemble, or unfold [170]. However, the present data illustrated an unaffected Col1 deposition and similar levels of unfolded collagen. These contrasting results may be attributed to differences in the duration of the high-fat diet and the used fracture model. Specifically, Khajuria et al. (2020) employed an open mid-diaphysis tibial fracture using a spinal needle that is inserted in the intramedullary canal, with the fracture created by 3-point bending. This procedure damages the integrity of the endosteum and bone marrow, and disrupts the healing zone with the implant [298]. The healing progression of unstable fixed osteotomies is partially distinct from stable fixations, making direct comparisons difficult. Therefore, utilizing a stable external fixator potentially offers the advantage of undisturbed collagen deposition and enables monitoring of bone remodeling, not only in the adjacent callus but also within the fracture gap.

In addition to investigating collagen content, future work may focus on examining the collagen microstructure, including factors such as fiber orientation and thickness, throughout various stages of healing to explore the connection between the metabolic status and the healing process. Given that obesity can impact chondrocyte activity [14], upcoming studies should consider the as-

sessment of chondrocyte hypertrophy markers, such as Col10 and matrix metallopeptidase 13 (MMP13), to investigate the formation of soft callus in obese mice with distinct metabolic characteristic. Advanced glycation end products (AGEs) may also contribute to the decreased bone content in obese fractures. In this context, AGEs mitigate the differentiation of MSCs and osteoblast activity [299] as well as alter the collagen structure and elasticity of fibers through non-enzymatic crosslinking [300]. The pathological accumulation in obesity and T2DM is known to result in compromised bone quality [14, 301, 302].

Moreover, patients with T2DM suffer from diabetic comorbidities, such as microvascular complications, that negatively affect bone architecture and regeneration [303, 304]. The data presented in this report demonstrate that neovascularization is not impaired in obese mice during the later stages of fracture repair. These findings align with the results obtained in the DIO fracture model established by Brown et al. in 2014 [112], while studies conducted with leptin receptor-deficient (db/db) T2DM mice have shown a decreased microvascular invasion [305, 306]. These findings suggest that angiopathy may be more commonly diagnosed in individuals with manifest T2DM and less frequently associated with obesity. Impaired vascularization seen in T2DM is attributed to the diminished proliferation and activity of MSCs [307]. This is accompanied by a decrease in the expression of angiogenic genes and proteins, including vascular endothelial growth factor A (VEGF-A), VEGF-C, angiopoietin 1, and angiopoietin 2 [308, 309]. Therefore, validating vascular gene expression can offer valuable insights into vascularization processes.

Since vascularization and collagen deposition were not affected by obesity, the healing defects can be associated with increased pro-inflammation, primarily mediated by $CD3^+$ T cells, as previously described. Most notably, this observation was not further enhanced by progressed glucose intolerance in obese low GT mice, suggesting a body's compensatory response to metabolic disturbances.

This compensatory effect was evident in the extended obesity study, in which the HFD was prolonged from 7 to 16 weeks. This part of the work aimed to investigate the metabolic changes and molecular pathways during early callus formation, specifically focusing on the differences observed in the identified obese groups in the context of persistent obesity. Additionally, an immunomodulatory treatment approach was explored to improve fracture repair. Furthermore, the investigation of the microbiome sought to assess potential microbial indicators that could be associated with metabolism, adaptive immune immunity and tissue regeneration.

A significant finding of the follow-up study was that the prolonged HFD did not exacerbate early pro-inflammatory cytokines, which is consistent with the observations from the short-term study. These findings are in accordance with Histing et al. (2016), who demonstrated a low inflammatory response in C57BL/6J mice after a comparable feeding period and a similar healing outcome

after applying a stabilized femur fracture [310]. In this work, I identified elevated levels of bone mineral density in the obese groups, with the effect being more pronounced in obese mice with low GT. This observation is associated with a positive stimulation of bone formation that was comparable to the outcome seen in age-matched standard-fed mice. These data implicate that skeletal acquisition outweighs immunological changes when obesity manifests, resulting in a more mature bone and slightly more rapid fracture healing in obese mice. Similar to the findings of the short-term study, long-term obesity significantly altered tissue deposition. Particularly, cartilage deposition was attenuated in obese mice with low GT compared to the control group. This observation is likely linked to elevated bone mineral density resulting from body weight gain and increased mechanical load [101, 311, 312], even though the physical activity might decrease with rising weight [313, 314]. The extended HFD evidently enhanced a stronger weight gain and BMD. Additionally, it is described that BMD is normal or higher in T2DM patients [315], who commonly suffer fracture at higher BMD values than non-diabetics [100]. However, other studies showed a beneficial impact of increased BMD levels [316, 317]. These studies underline the complex and debated relationship between BMD and obesity/T2DM, emphasizing the need for further investigations.

Moreover, literature has demonstrated a correlation of BMD and leptin levels [310]. Leptin, as an adipocyte-derived hormone, has been shown to play a role in facilitating osteoblast proliferation and mineralization [318]. Data from RNA sequencing in this work confirmed significantly enhanced levels of leptin transcripts in all obese groups, further supporting this identified correlation.

In comparison to the short-term HFD, an increased number of non-union fractures were observed in obese high GT and $CD8^-$ low GT mice, whereas the fractures in mice with low GT bridged. The varying healing patterns were confirmed by RNA sequencing, suggesting that mild metabolic changes in obese high GT mice were less manifested and induced transient multifaceted repair mechanisms. Similarly, the $CD8^+$ T cell removal potentially contributed to several, yet unknown, compensatory side effects, as the immunological responses adapt to the $CD8^+$ T cell deficiency. As a result, this process could lead to the diversification of bone fracture healing.

Another obesity-associated tissue defect observed through histology was the elevated distal callus adiposity in the long-term obesity study. Most notably, RNA sequencing discovered increased mRNA levels indicative for adipocytes and adipogenesis in the obese groups. Strikingly, obese mice with high GT displayed these obesity-associated changes in the bone microenvironment prior to the occurrence of systemic metabolic changes, such as liver steatosis. In contrast, obese mice with low GT developed a fatty liver, insulin resistance and compensatory pancreatic β-cells. These findings highlight the severity of even mild glucose intolerance (high GT) on bone health, particu-

larly affecting the bone marrow as a source of MSCs in the early stages the disease. This can potentially disrupt bone regenerative processes.

Given the excessive caloric intake surpassing energy expenditure, it is recognized that lipid expansion is accompanied by ECM deposition and remodeling [319], as evidenced by the bulk transcriptomic analysis in this work. The results revealed the molecular program of early-stage fracture healing in obesity, characterized by increased breakdown and synthesis of ECM compared to lean mice. Obesity, characterized by an excess of lipids and adipocytes, contributed to the accumulative deposition of fibrillar (*Col3* and *Col5*) and non-fibrillar (*Col4*) collagens, as well as ECM proteins such as *Lama4.* This observation could be associated with fibrotic scarring, which leads to a decrease in the extracellular matrix flexibility [200], as seen in conditions such as non-alcoholic steatohepatitis, inflammation and insulin resistance [320-322]. The expression levels of chondrocyte markers were comparable in both the obese groups and controls. However, the data revealed reduced *Alpl* transcripts, indicating a decreased osteoblast formation and activity alongside an increased commitment to adipogenesis.

Even though inflammatory cues were less pronounced due to obesity, the elimination of $CD8^+$ T cells in obese low GT mice partially reversed the aberrant cartilage deposition and remodeling mechanisms, emphasizing the strong interplay between immunity and early callus formation. In support of this, a study implementing weekly depletion of $CD8^+$ T cells demonstrated improvement in the pathophysiology of DIO, as the treatment reduced AT macrophage recruitment, inflammation and insulin resistance [175]. Overall, these findings reinforce the importance of adaptive immunity as a relevant factor in the process of tissue regeneration.

Summary and conclusion

To the best of my knowledge, this study presents the first investigation into the impact of different metabolic characteristics associated with obesity on adaptive immunity and fracture healing. The findings demonstrated that the pro-inflammatory state related to short-term obesity impaired bone fracture healing. The results also indicated that a comprehensive understanding of healing alterations in the context of obesity emerged during long-term obesity, highlighting the skeletal system's ability to adapt to ongoing metabolic and immunological imbalances [193, 323]. Although persistent obesity can reverse previously observed healing defects, it still leads to modifications in the ECM.

These findings have important clinical implications, shedding light on the influence of obesity on immune function and bone health. As a result, this study paves the way for further research into the fundamental mechanisms governing immune-regulated bone repair in obesity and potential treatment strategies.

4.3 Gut microbiota associated with obesity and the progression of metabolic changes

The purpose of this side project was to explore obesity-related microbial signatures and their association with dysbiosis, which is known to contribute to metabolic inflammation and potentially impact bone repair. The work also sought to identify specific key bacteria that are characteristic for the different obese groups. These findings could have important implications for adjusting therapeutic strategies in disease management, such as targeting pathogenic bacteria or supplementing beneficial commensals in cases of microbial loss [324]. The importance of microbiota in obesity has been shown in studies involving germ-free mice, which remain lean and glucose tolerant on HFD [325, 326].

As previously described, obesity was induced in mice by subjecting them to a long-term high-fat diet for 16 weeks, starting at the age of 8 weeks. Following the diet, mice underwent a femoral osteotomy. Prior to surgery, the obese mice were divided into two groups based on the progression of metabolic alterations: obese mice with high and low GT. A subgroup of low GT mice additionally received treatment with an antibody that depletes $CD8^+$ T cells during the initial phase of bone healing with the aim to boost bone formation.

16S rRNA sequencing was performed on cecal and fecal samples taken three weeks post-surgery. Surprisingly, the results revealed that the microbial alpha-diversity in obese mice was identical to that of lean mice. Adiposity and T2DM are commonly associated with a reduction in bacterial richness [327-329]. However, other DIO studies reported conflicting results [330, 331]. A study conducted by Wu, et al. (2010) [332] found a comparable bacterial diversity between diabetic and non-diabetic individuals, but the researchers detected considerable alterations in the abundance of several phyla, genera and species. When calculating beta-diversity, which takes into account the ecological (dis)similarities in taxonomic composition, I revealed clear microbial differences that significantly distinguished the healthy gut microbiome in lean mice from the obese gut microbiome.

Upon analyzing the microbial structure on phylum level, I observed that microbes belonging to Bacteroidetes, Firmicutes, Virrucomicrobia and Proteobacteria were dominant in the gut of lean and obese mice, while Actinobacteria and Desulfobacteria were only abundant in the obese groups. These alterations were already present in DIO mice with high GT, but became more pronounced and highly associated with progressed metabolic changes in obese mice with low GT.

Specifically, the phylum Actinobacteria, which is associated with obesity and T2DM, has been suggested to play a role in the pathology, inflammation and dysbiosis observed in these conditions [333-335]. Interestingly, McCabe (2019) [336] provided evidence supporting a link between the composition of the microbiota and the bone microenvironment. Their study revealed a positive

association between the abundance of Actinobacteria and increased bone mineral density in obese mice. This finding aligns with my data obtained from the long-term study, which showed increased BMD values due to obesity, indicating a possible existence of a gut-bone axis. Furthermore, previous studies have reported an enrichment of the phylum Desulfobacteria [337, 338], which is known to upregulate the CD36 expression in the intestine, resulting in enhanced lipid uptake [337]. This mechanism may have detrimental effects on bone health by promoting lipid accumulation in the bone marrow, as evidenced by increased *CD36* transcripts in both fractured and unfractured bones of obese mice.

In addition, the Firmicutes/Bacteroidetes ratios, often implicated in the dysbiosis in the context of obesity, were comparable across all experimental groups [178, 179]. However, this correlation is subject to controversial discussions due to inconsistent data obtained in various obesity studies [339-342].

Most notably, significant differences between the obese groups predominantly became obvious in caecal samples. This highlights the importance of including the entire gastrointestinal tract in future studies rather than relying solely on fecal samples, to obtain a more comprehensive understanding of the microbial profile. Despite the similarities observed in diversity and on phylum level, the investigation of bacteria on genus level revealed significant alterations influenced by the different metabolic status and immunomodulatory approach. Particularly, I observed notable changes in the Firmicutes phylum, which is known to be modulated by obesity. Within this phylum, bacteria from the class Bacilli were enriched in samples from obese mice but only marginally present in control samples from the control group. The relative abundance of specific genera such as Blautia, Colidextribacter and Ligilactobacillus (belonging to Firmicutes) as well as OTU4 (belonging to Bacteroidetes) was significantly elevated in the gut microbiota of DIO mice with high GT and showed an increasing trend in obese low GT mice, while these microbes were absent in lean mice. The prevalence of Blautia (Firmicutes) in my research work is consistent with a rat study on T2DM [343], and has been identified in prediabetes and T2DM patients [344, 345]. Species from Blautia are known to play a dominant role in intestinal glucose metabolism by transforming the sugar to acetate, lactate, hydrogen, ethanol and succinate [346]. Moreover, the abundance of Blautia has been positively correlated with the diagnosis of osteoporosis [347], indicating a strong link to metabolism and bone health. Furthermore, my study established a connection between the presence of Colidextribacter (Firmicutes) and obesity, which is in accordance with other DIO studies [348, 349]. This genus is involved in maintaining the antioxidant activity of the colon in mice [350] but is positively associated with increased hyperglycemia and inflammatory cytokines, contributing to disease progression [351]. Moreover, I observed an increased abundance of the genus Ligilactobacillus (Firmicutes) in response to obesity. However, the specific behavior of Ligilactobacillus in obesity, inflammation or bone health is not sufficiently described

in the literature. Therefore, my work shows that further research is necessary to understand the complex links between microbiota and obesity. In addition, I identified bacteria (OTU4) from the family Muribaculaceae (Bacteroidetes) that were prevalent in the obese gut. Muribaculaceae are known to play a pivotal role in degrading complex polysaccharides and are thus involved in energy metabolism. This finding aligns with other literature reports [330]. However, the family Muribaculaceae remains poorly characterized in terms of specific species, host affinity, and potential functions [352]. Interestingly, I also found a high proportion of microbes (OTU35) belonging to the Muribaculaceae family in the gut of lean mice, while this genus was eradicated upon obesity induction. Overall, the abundance of bacteria from the Muribaculaceae family is positively and negatively affected by obesity, clearly influenced by the host metabolism.

Consistent with my results, longitudinal and cross-sectional studies have noticed a close relationship between insulin resistance and microbiota [353-355]. Zhou and co-workers (2019) [354] identified particular host-microbiome interactions that differed between insulin-sensitive and insulin-resistant participants. In line with these findings, my study highlighted the significant expansion of the key genera Erysipelatoclostridium, OTU8 (belonging to the Lachnospiraceae family) and Clostridium sensu stricto 13, all within the Firmicutes phylum, as well as OTU42 classified to the Desulfobacteria phylum, which were associated with obesity and progressive glucose intolerance in obese low GT mice. The colonization of the genus Erysipelatoclostridium, as observed in my study, has also been detected in other DIO studies [356, 357]. Species belonging to the genus Erysipelatoclostridium might be profound gut microbes, which are positively associated with the regulation of the host lipid metabolism [358] and modification of the CD36 expression, contributing to liver steatosis [359]. Similarly, OTU8, belonging to the family Lachnospiraceae (Firmicutes), is involved in the degradation of complex carbohydrates, leading to the production of short-chain fatty acids. The correlation between Lachnospiraceae and T2DM risk has been reported in several studies [343, 360, 361]. Kim et al. (2022) [361] suggested that the abundance of unclassified Lachnospiraceae is related to disease risk through the stimulation of insulin production. Interestingly, Li et al. (2020) [362] discovered a positive connection between abundant Lachnospiraceae and BMD in fecal samples, supporting the findings of my study. Furthermore, species from the genus Clostridium sensu stricto have been positively associated with increased body weight and serum lipids [363]. However, the contribution of Clostridium sensu stricto 13 to intestinal and bone health is poorly investigated, although my data suggests that it is an indicative bacterium for obesity with an advanced deteriorated metabolism (in obese low GT mice). Moreover, OTU42, a member of the phylum Desulfobacterota and the family Desulfovibrionaceae, exhbited increased presence in obese mice with low GT. Bacteria from the Desulfovibrionaceae family are known to play a role in sulfate reduction and contribute to inflammation in obesity, potentially through the

H_2S pathway [364] and the production of lipopolysaccharides [365]. Nevertheless, the extent to which this genus impacts skeletal acquisition is still uncertain.

Additionally, I observed a temporal relationship between gut microbiota, adiposity, glucose and insulin resistance, which was partially reversed on the genus level through the neutralization of $CD8^+$ T cells. This finding suggests that specific genera within the microbiome are sensitive to immune changes. The immunomodulatory intervention significantly shifted the obese microbiome in obese $CD8^-$ low GT mice towards a microbial signature similar to that of obese high GT mice. This means for example in case of the genus Bacteroides: Species from this genus are present under healthy conditions, experience depletion during obesity progression in obese high GT mice, and return after the manifestation of obesity in obese low GT. However, studies are lacking that explore the link between obesity progression and changes in the composition of the microbial community.

Summary and conclusion

To the best of my knowledge, the present study is the first to uncover the causal relationship between the microbiome, obesity-associated metabolic characteristics and bone health (Fig. 42). The findings of my work suggest that the increased abundance of specific obesity-related microbes contributes to (bone) adiposity and metabolic alterations, particularly affecting the glucose and lipid metabolism, with a minor impact on the immune system. Furthermore, I identified gut microbiota markers that were present even in obese mice with high GT and highlighted three genera as indicators of progressive metabolic changes in obese mice with low GT, as well as fatty liver disease. These results emphasize the potential of intestinal microbiota as auxiliary diagnostic tool for individualized therapy targeting the imbalanced microbiome.

However, our understanding of the link between the microbial composition and bone health in the context of obesity is still in its early stages. Current research is just beginning to explore the intricate connections with fecal microbiota transplantation as a potential approach that could investigate this relationship.

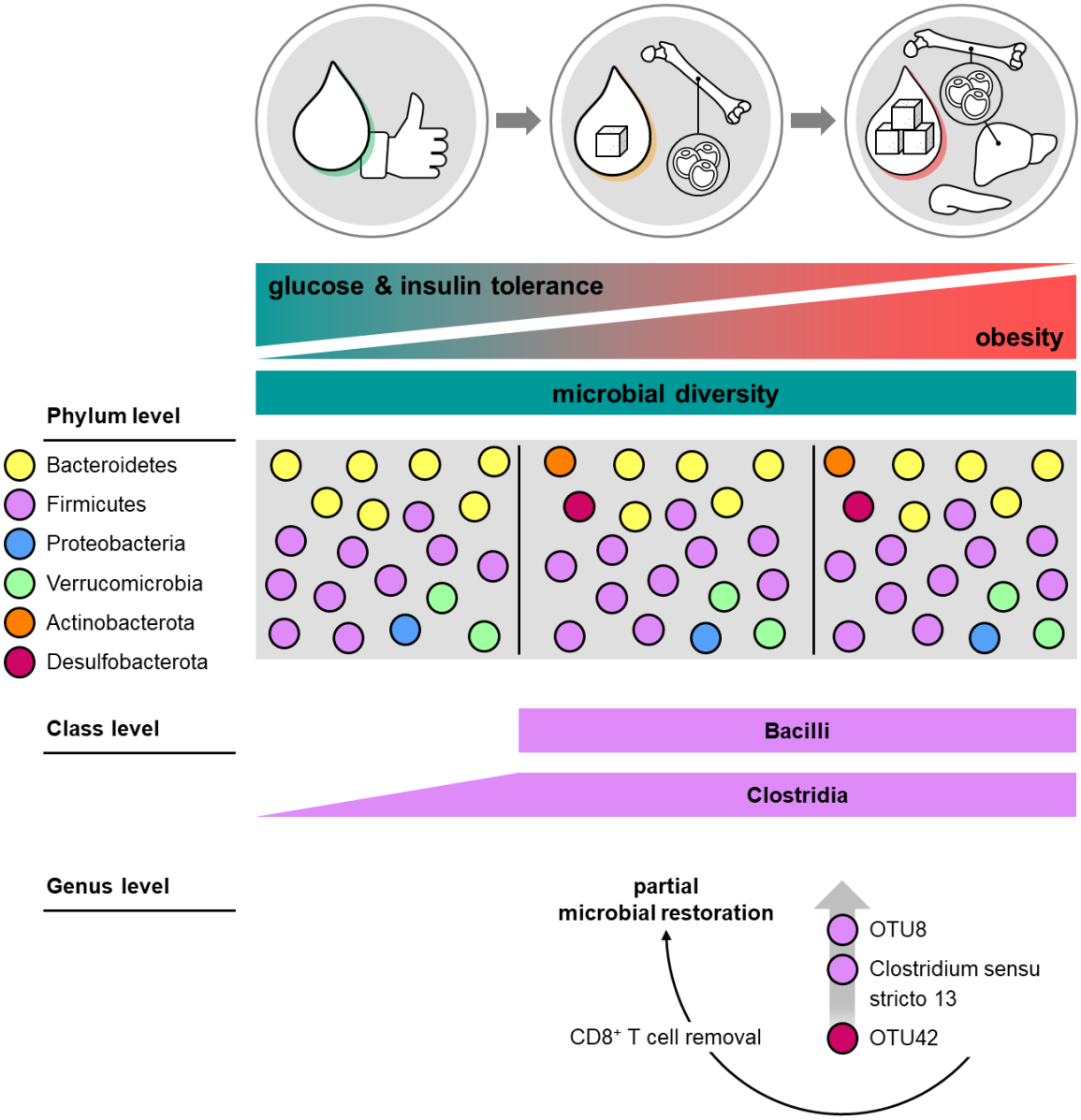

Fig. 42 | Association of gut microbial indicators for progressed metabolic changes in the context of obesity. Upon comparing the fecal and cecal microbiome of lean mice, obese mice with mild (high GT) and progressed glucose intolerance (low GT), my study revealed that obesity did not lead to decreased diversity. Instead, obesity triggered the colonization with the phyla Actinobacteria and Desulfobacterota and diversified the Firmicutes classes. Furthermore, the microbial signature of progressed obesity (low GT) was notably different from that seen in the mild disease state (high GT), characterized by an accumulation of the genera OTU8, Clostridium sensu stricto 13 and Desulfovibrionaceae. However, the removal of $CD8^+$ T cells in obese mice with low GT resulted in a partial restoration of the microbial community composition, leading to a shift towards the gut flora observed in obese mice with high GT.

4.4 Effects of the experienced adaptive immunity on the gut microbiome during bone regeneration

The side project also covered the emerging field of the microbiome in the context of regenerative medicine, specifically investigating its implications in the elderly population. Growing evidence suggests that the outcome of bone fracture healing is affected by an increased ratio of effector to naïve T cells, which can amplify inflammation and disrupt the balance between bone resorption and formation. So far disregarded were alterations in the microbiota influenced by age-related changes in the immune system in the context bone fracture healing. To the best of my knowledge, this work is the first investigation into this relationship, and although the complexity of these parameters presents challenges, valuable results have been obtained.

For this investigation, one-year-old mice were used to study varying levels of immune experience, also known as immunoage. To induce different immunological memories, mice were housed under distinct conditions that influenced their interaction with surrounding antigens. One group was kept in a specific pathogen-free (SPF) environment, ensuring minimal exposure to antigens, while the other group was housed in a non-SPF environment with access to a broader range of antigens. After one year of housing, a significant development of $CD4^+$ and $CD8^+$ memory T cells was observed in mice from the non-SPF husbandry, indicating a higher level of immune experience (high immunoage). In contrast, mice housed in the SPF facility showed a predominance of the naïve immune phenotype, suggesting a lower level of immune experience (low immunoage). The mice further underwent a femoral osteotomy. Caecal samples were collected from mice prior to surgery (0d), as well as at 3d and 21d post-osteotomy, and subjected to high-throughput sequencing to analyze the composition of the gut microbiota.

My data showed a comparable microbial richness before surgery between the low and high immunoaged mice. However, at 21d after the surgery and antibiotics administration, helping to prevent surgical infections, mice with an experienced immunity showed a significant delay in the reconstitution of gut bacterial communities. This difference was evident in the decreased gut microbiota richness and Shannon diversity index. Hence, the results suggest that an experienced immune system exerts a stronger regulatory effect on the composition and diversity of the microbiota, particularly following antibiotics treatment.

Clindamycin, a lincosamide antibiotic used during surgery, is intended for the treatment of bone or joint infections [366]. It is most effective against infections caused by susceptible anaerobic, such as Bacteroides and Prevotella, as well as aerobic microbes, including Staphylococcus and Streptococcus. However, the use of antibiotics as prophylaxis can potentially disrupt the beneficial microbiome, which plays a crucial role in the process of recovery [367]. These necessary bacteria

are involved in orchestrating immune, metabolic and neuroendocrine signals received from the stress of injury and during recovery [368]. In this study, clindamycin was found to have limited activity against Proteobacteria and Enterococci, resulting in their accumulation shortly after administration. The temporary treatment with clindamycin led to a suppression of the majority of the microbiota, but this effect was not observed to have a lasting impact in low immunoaged mice.

However, mice with a developed adaptive immune system showed significant disturbances in the gut microbiota after a single dose of clindamycin, leading to long-lasting depletion of species from the Bacteroidetes phylum. These findings align with previous studies demonstrating the potent activity of clindamycin against anaerobic species [369-371]. Notably, the presence of a mature adaptive immune system impeded the restoration of important short-chain fatty acid (SCFA) producers, specifically within the family Porphyromonadaceae, which includes the genus Barnesiella. SCFAs, such as acetate, propionate, and butyrate, are derived from the fermentation of non-digestible polysaccharides and play a role in maintaining the gut and immune homeostasis [372]. SCFAs also impact bone health by promoting the induction of Tregs and protecting against inflammatory bone loss [373]. Direct supplementation of butyrate has been shown to improve bone formation by enhancing the expression of the osteogenic Wnt ligand Wnt10b in Tregs within the bone marrow [374]. Therefore, the loss of SCFA-producing microbes in high immunoaged mice could contribute to bone healing defects observed in these animals.

In contrast to antibiotic-induced eliminations, mice with a high immunoage exhibited an enrichment of the genus Bacteroides following antibiotic challenge. Bacteroides species can protect against intestinal pathogens, but they can also cause severe pathology outside of their natural habitat [375]. Thus, the combination of clindamycin treatment and a high immunoage resulted in imbalanced abundances of mutualistic bacteria. Previous research has observed long-lasting susceptibility to Clostridium difficile infection after a single dose of clindamycin. This susceptibility is a result of the temporary disturbance of microbial communities caused by clindamycin, which creates a favorable niche for pathogens like Clostridium difficile to colonize, ultimately affecting the process of post-operative recovery [376].

Strikingly, high immunoaged mice demonstrated an elevated abundance of the genus Akkermansia pre-surgically and after antibiotic treatment during late-stage fracture healing, in comparison to low immunoaged mice. Among the Akkermansia species, Akkermansia muciniphila is of particular relevance as it resides in the mucus layer and closely interacts with host cells [377]. In both humans and mice, higher levels of A. muciniphila have been associated with a healthy gut lining and a decreased risk of metabolic disorders [378-380]. In the context of bone fracture healing, a study identified a correlation between the formation of type H vessels and accelerated bone fracture healing after the administration of A. muciniphila [381]. This positive effect was associated

with a reduction in gut permeability and inflammation. Similarly, supplementation with prebiotics such as Lactobacillus reuteri, Lactobacillus rhamnosus and Lactobacillus acidophilus has been shown to have bone-protective effects by increasing bone density. The improvements are associated with various mechanisms, including the decrease of $CD4^+$ T cells in the bone marrow that are known to promote osteoclastogenesis, an increase in Treg cell population, or the regulation of the Treg-Th17 axis to inhibit Th17 cells [374, 382-384]. Increasing evidence supports the notion that the bidirectional crosstalk between intestinal microbes and the immune system plays a role in modulating the bone environment [385].

Summary and outlook

In summary, mice with a higher level of immune experience showed significant changes in the richness and composition of their gut microbiome. These changes had both negative and positive effects. On one hand, the immune experience led to a depletion of important microbes that produce short-chain fatty acids (SCFA), which had a detrimental influence on the gut microbiome. On the other hand, it fostered an environment conducive to the colonization of beneficial microbes from the Akkermansia genus under more physiological conditions, as established in the non-SPF facility (Fig. 43). These results highlight the need for further research to investigate the functional consequences of the microbial imbalance caused by antibiotics and intensified by the immune experience. Additionally, the disruption of symbiosis and co-dependencies among different microbes, the potential impact on uniquely abundant microbes, the transfer of antibiotic-resistance genes, perturbations in gut immune cells, and the disturbed differentiation and stimulation of antigen-presenting cells and T cells are important areas for future investigations [386].

As demonstrated, the data revealed the destructive impact of antibiotics on the microbiome, and its restoration was found to be dependent on the level of immune experience, which highlights a previously neglected aspect in surgical care. The effects of antibiotics can persist long after their administration discontinued [367], and it may take years for the microbiome to fully recover in patients [368]. Further analysis with a longer follow-up period after antibiotic use would provide valuable insights into the duration of the microbiome reconstitution and its clinical implications.

Additionally, it is necessary to investigate the impact of a prolonged antibiotic treatment, higher concentrations or multiple doses on the microbial composition, to guide a reasonable and diligent use of antibiotics based on the patient's immune status in a clinical setting. Exploring the influence of the virome and fungome on the host's metabolome and immunity is another crucial aspect to consider. Finally, to validate the role of the microbiome in shaping memory immunity and bone regeneration, conducting microbial fecal transplantation from immune-experienced to germ-free mice would offer unique and novel insights into fracture healing.

By exploring the interplay between aging, adaptive immunity and bone fracture healing in context of the gut microbiome, this research aimed to address the critical medical need of considering the patient's immune and microbial profile in the realm of surgical recovery and healing outcome.

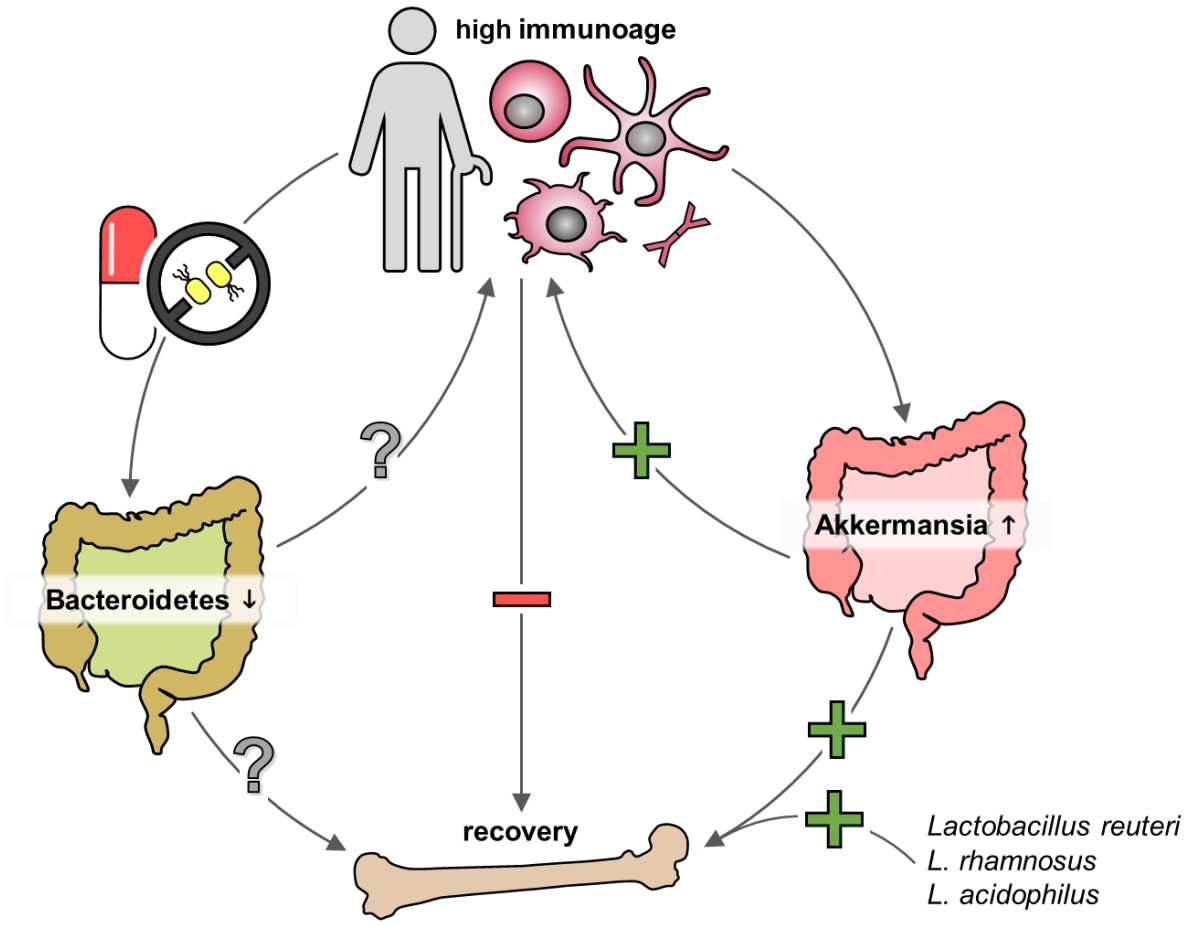

Fig. 43 | An experienced immunity affects the restoration of the gut microbiome following antibiotics administration and during recovery from bone fracture healing. Mechanisms of interaction demonstrating an incomplete reconstitution of the Bacteroidetes phylum, particularly in cases of an inhibitory high immunoage after clindamycin treatment. This effect impacts both intestinal and systemic immune stimulation, as well as the overall recovery from surgery. In contrast, the development of a stronger immunological experience is associated with the colonization of the Akkermansia phylum, which is linked to the induction of adaptive immune responses and improvement in bone fracture healing. Additionally, species belonging to the Lactobacillus genus contribute to shaping the bone microenvironment by increasing bone mineral density through modulation of the adaptive immune system.

5 Outlook

The findings of this work support the hypothesis that obesity-related pro-inflammation impairs bone fracture healing (Fig. 44). However, the skeletal system can adapt to metabolic disturbances associated with obesity, potentially overcoming the immunological changes and reversing the observed healing defects. Overall, based on this work, four main conclusions can be drawn:

1. The high-fat diet model demonstrates its ability to induce different phenotypes associated with obesity, showcasing the multifactorial nature of T2DM precursor conditions.
2. The identified obese subtypes hold clinical significance and offer valuable insights into the progression of the disease linked to altered immunity and bone fracture healing.
3. The observation of a bone phenotype preceding the systemic metabolic effects indicates the early influence of metabolic disturbances on bone health and fracture healing.
4. Obesity induced a pro-inflammatory state, leading to impaired bone repair. However, the body has the capacity to adapt to metabolic changes, although this adaptation may affect and potentially compromise regenerative processes of the skeletal system.

Ultimately, the question arises whether obesity delays bone healing and why? The data obtained from this work provides evidence that the effects of obesity on bone repair are multifaceted, involving various factors such as immunity, cytokines and an altered osteogenic response, which collectively influence callus development and mineralization. Additionally, the role of adipogenesis and the accumulation of adipose tissue within the bone marrow may be more relevant than previously recognized, potentially impacting the process of bone fracture healing.

Considering the complexity of the systemic disorder, the bone tissue microenvironment and the plasticity of immune cells, especially T cells and macrophages, the work provided evidence that a static vision of one obesity phenotype, as commonly established in obesity research, not fully captures the diverse effects on bone repair. Especially, the role of T cells and their altered function in systemic and local inflammation during fracture healing, as well as their relationship with matrix deposition, is only now starting to be investigated.

In addition, it poses a challenge for future studies to discriminate the consequences of obesity from the numerous comorbidities that affect bone metabolism much larger than obesity itself. In light of these considerations, the work presented here has identified new and promising targets for the development of novel personalized treatment strategies. These approaches should take into account the metabolic state of the patient and have the potential to mitigate the increasing number of obese fracture patients who are at high risk for healing complications.

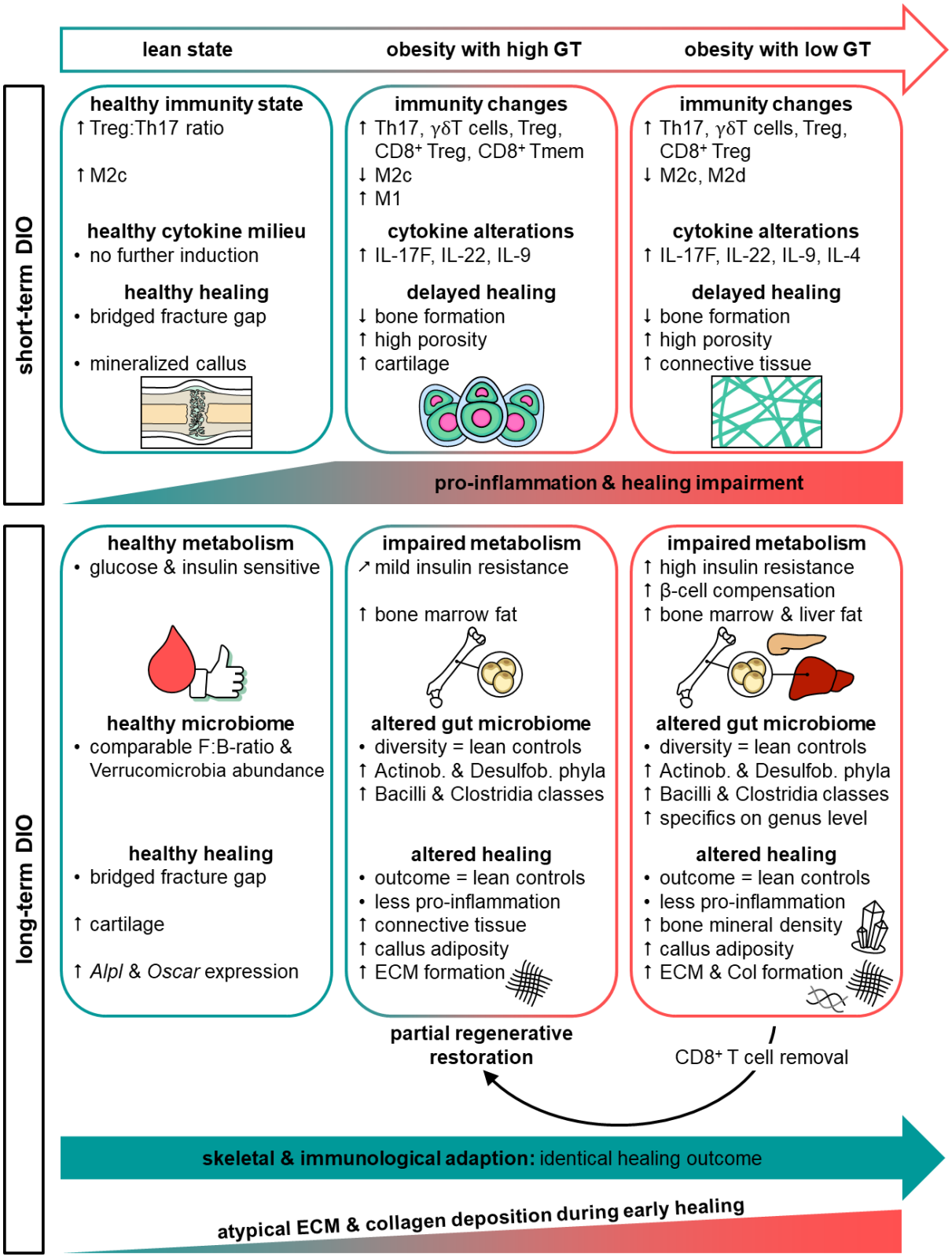

Fig. 44 | Metabolic, microbial and fracture healing alterations associated with obesity. Two obese subtypes with high and low glucose tolerance (GT) were identified. Short-term obesity induced an early pro-inflammatory state that impaired femoral fracture healing, and affected the deposition of cartilage and connective tissue. However, long-term obesity resulted in increased weight gain, callus adiposity and bone mineralization, along with reduced inflammation, which corrected the previous healing defects. But during early bone repair, excessive deposition of ECM and collagen was observed and pronounced in obese mice with low GT. This finding poses a potential risk for fibrotic scarring, which was reversed by removal of $CD8^+$ T cells. The Treg cell phenotype is herein defined as $CD4^+CD25^{hi}FoxP3^+$ and $CD8^+FoxP3^+$ T cells.

6 References

1. World Heath Organization. *Ageing and health*. 2018 20 Nov 2018]; Available from: http://www.who.int/news-room/fact-sheets/detail/ageing-and-health.
2. Haustein, T., et al. *Ältere Menschen in Deutschland und der EU*. 2016 20 Nov 2018]; Available from: https://www.bmfsfj.de/blob/93214/95d5fc19e3791f90f8d582d61b13a95e/aeltere-menschen-deutschland-eu-data.pdf.
3. Lobstein, T., et al., *Word Obesity Atlas 2022*. 2022, World Obesity Federation.
4. Schienkiewitz, A., et al., *Overweight and obesity among adults in Germany - Results from GEDA 2019/2020-EHIS.* J Health Monit, 2022. **7**(3): p. 21-28.
5. Bray, G.A., et al., *Obesity: a chronic relapsing progressive disease process. A position statement of the World Obesity Federation.* Obes Rev, 2017. **18**(7): p. 715-723.
6. Gutin, I., *In BMI We Trust: Reframing the Body Mass Index as a Measure of Health.* Soc Theory Health, 2018. **16**(3): p. 256-271.
7. de Mutsert, R., et al., *Associations of Abdominal Subcutaneous and Visceral Fat with Insulin Resistance and Secretion Differ Between Men and Women: The Netherlands Epidemiology of Obesity Study.* Metab Syndr Relat Disord, 2018. **16**(1): p. 54-63.
8. Heidemann, C., et al., *Temporal changes in the prevalence of diagnosed diabetes, undiagnosed diabetes and prediabetes: findings from the German Health Interview and Examination Surveys in 1997-1999 and 2008-2011.* Diabet Med, 2016. **33**(10): p. 1406-14.
9. Rathmann, W., et al., *Type 2 diabetes: prevalence and relevance of genetic and acquired factors for its prediction.* Dtsch Arztebl Int, 2013. **110**(19): p. 331-7.
10. Ryl, L., A.C. Saß, and T. Ziese *Gesundheit in Deutschland – die wichtigsten Entwicklungen*. 2016. DOI: 10.17886/rki-gbe-2016-021.2.
11. Rupp, M., et al., *The Incidence of Fractures Among the Adult Population of Germany-an Analysis From 2009 through 2019.* Dtsch Arztebl Int, 2021. **118**(40): p. 665-669.
12. Holmes, D., *Closing the gap.* Nature, 2017. **550**(7677): p. S194-S195.
13. Zura, R., et al., *Biological Risk Factors for Nonunion of Bone Fracture.* JBJS Rev, 2016. **4**(1).
14. Khajuria, D.K., et al., *Aberrant structure of fibrillar collagen and elevated levels of advanced glycation end products typify delayed fracture healing in the diet-induced obesity mouse model.* Bone, 2020. **137**: p. 115436.
15. Reaven, G.M., *Banting lecture 1988. Role of insulin resistance in human disease.* Diabetes, 1988. **37**(12): p. 1595-607.
16. Wilcox, G., *Insulin and insulin resistance.* Clin Biochem Rev, 2005. **26**(2): p. 19-39.
17. Czech, M.P., *Insulin action and resistance in obesity and type 2 diabetes.* Nat Med, 2017. **23**(7): p. 804-814.
18. Petersen, M.C. and G.I. Shulman, *Mechanisms of Insulin Action and Insulin Resistance.* Physiol Rev, 2018. **98**(4): p. 2133-2223.
19. Kahn, B.B. and J.S. Flier, *Obesity and insulin resistance.* J Clin Invest, 2000. **106**(4): p. 473-81.
20. Ginsberg, H.N., *Insulin resistance and cardiovascular disease.* J Clin Invest, 2000. **106**(4): p. 453-8.
21. Taniguchi, C.M., B. Emanuelli, and C.R. Kahn, *Critical nodes in signalling pathways: insights into insulin action.* Nat Rev Mol Cell Biol, 2006. **7**(2): p. 85-96.
22. Hardy, O.T., M.P. Czech, and S. Corvera, *What causes the insulin resistance underlying obesity?* Curr Opin Endocrinol Diabetes Obes, 2012. **19**(2): p. 81-7.
23. Wondmkun, Y.T., *Obesity, Insulin Resistance, and Type 2 Diabetes: Associations and Therapeutic Implications.* Diabetes Metab Syndr Obes, 2020. **13**: p. 3611-3616.

24. Muoio, D.M. and C.B. Newgard, *Mechanisms of disease:Molecular and metabolic mechanisms of insulin resistance and beta-cell failure in type 2 diabetes.* Nat Rev Mol Cell Biol, 2008. **9**(3): p. 193-205.
25. Bansal, N., *Prediabetes diagnosis and treatment: A review.* World J Diabetes, 2015. **6**(2): p. 296-303.
26. Wagner, R., et al., *Pathophysiology-based subphenotyping of individuals at elevated risk for type 2 diabetes.* Nat Med, 2021. **27**(1): p. 49-57.
27. (DZD), I.f.D.R.a.M.D.I.a.G.C.f.D.R. *Prediabetes subtypes identified*. 2021 11.01.2023]; Available from: https://www.dzd-ev.de/en/press/press-releases/press-releases-archive/press-releases-2021/prediabetes-subtypes-identified/index.html.
28. Romano, M., *Inflammation resolution: does the bone marrow have a say?* Am J Hematol, 2008. **83**(6): p. 435-6.
29. Kokkas, B., *1st international congress on neurobiology and clinical psychopharmacology and European psychiatric association conference on treatment guidance.* Ann Gen Psychiatry, 2010. **9**(Suppl 1): p. S1-S237.
30. Sbierski-Kind, J., et al., *Distinct Housing Conditions Reveal a Major Impact of Adaptive Immunity on the Course of Obesity-Induced Type 2 Diabetes.* Front Immunol, 2018. **9**: p. 1069.
31. de Luca, C. and J.M. Olefsky, *Inflammation and insulin resistance.* FEBS Lett, 2008. **582**(1): p. 97-105.
32. Liu, R. and B.S. Nikolajczyk, *Tissue Immune Cells Fuel Obesity-Associated Inflammation in Adipose Tissue and Beyond.* Front Immunol, 2019. **10**: p. 1587.
33. Kotzbeck, P., et al., *Brown adipose tissue whitening leads to brown adipocyte death and adipose tissue inflammation.* J Lipid Res, 2018. **59**(5): p. 784-794.
34. Schlecht, I., et al., *Visceral adipose tissue but not subcutaneous adipose tissue is associated with urine and serum metabolites.* PLoS One, 2017. **12**(4): p. e0175133.
35. Philipsen, A., et al., *Associations between ultrasound measures of abdominal fat distribution and indices of glucose metabolism in a population at high risk of type 2 diabetes: the ADDITION-PRO study.* PLoS One, 2015. **10**(4): p. e0123062.
36. Rytka, J.M., et al., *The portal theory supported by venous drainage-selective fat transplantation.* Diabetes, 2011. **60**(1): p. 56-63.
37. Makki, K., P. Froguel, and I. Wolowczuk, *Adipose tissue in obesity-related inflammation and insulin resistance: cells, cytokines, and chemokines.* ISRN Inflamm, 2013. **2013**: p. 139239.
38. Van Gaal, L.F., I.L. Mertens, and C.E. De Block, *Mechanisms linking obesity with cardiovascular disease.* Nature, 2006. **444**(7121): p. 875-80.
39. Zhao, Y., et al., *CD4(+) T cells in obesity and obesity-associated diseases.* Cell Immunol, 2018. **332**: p. 1-6.
40. Janeway, C.A.J., et al., *Immunobiology: The Immune System in Health and Disease. 5th edition.* 2001, New York: Garland Science.
41. Correa, L.H., et al., *Adipocytes and Macrophages Interplay in the Orchestration of Tumor Microenvironment: New Implications in Cancer Progression.* Front Immunol, 2017. **8**: p. 1129.
42. Castoldi, A., et al., *The Macrophage Switch in Obesity Development.* Front Immunol, 2015. **6**: p. 637.
43. Mantovani, A., et al., *Macrophage plasticity and polarization in tissue repair and remodelling.* J Pathol, 2013. **229**(2): p. 176-85.
44. Vieira-Potter, V.J., *Inflammation and macrophage modulation in adipose tissues.* Cell Microbiol, 2014. **16**(10): p. 1484-92.
45. Kohlgruber, A. and L. Lynch, *Adipose tissue inflammation in the pathogenesis of type 2 diabetes.* Curr Diab Rep, 2015. **15**(11): p. 92.
46. Donath, M.Y. and S.E. Shoelson, *Type 2 diabetes as an inflammatory disease.* Nat Rev Immunol, 2011. **11**(2): p. 98-107.
47. Marshall, J.S., et al., *An introduction to immunology and immunopathology.* Allergy Asthma Clin Immunol, 2018. **14**(Suppl 2): p. 49.

48. Wu, H., et al., *T-cell accumulation and regulated on activation, normal T cell expressed and secreted upregulation in adipose tissue in obesity.* Circulation, 2007. **115**(8): p. 1029-38.
49. Sauls, R.S., C. McCausland, and B.N. Taylor, *Histology, T-Cell Lymphocyte*, in *StatPearls*. 2022: Treasure Island (FL).
50. Nishimura, S., et al., *CD8+ effector T cells contribute to macrophage recruitment and adipose tissue inflammation in obesity.* Nat Med, 2009. **15**(8): p. 914-20.
51. Jagannathan-Bogdan, M., et al., *Elevated proinflammatory cytokine production by a skewed T cell compartment requires monocytes and promotes inflammation in type 2 diabetes.* J Immunol, 2011. **186**(2): p. 1162-72.
52. Ip, B., et al., *Th17 cytokines differentiate obesity from obesity-associated type 2 diabetes and promote TNFalpha production.* Obesity (Silver Spring), 2016. **24**(1): p. 102-12.
53. Nylander, A. and D.A. Hafler, *Multiple sclerosis.* J Clin Invest, 2012. **122**(4): p. 1180-8.
54. Leonardi, C., et al., *Anti-interleukin-17 monoclonal antibody ixekizumab in chronic plaque psoriasis.* N Engl J Med, 2012. **366**(13): p. 1190-9.
55. Wang, Q. and H. Wu, *T Cells in Adipose Tissue: Critical Players in Immunometabolism.* Front Immunol, 2018. **9**: p. 2509.
56. Sun, K., C.M. Kusminski, and P.E. Scherer, *Adipose tissue remodeling and obesity.* J Clin Invest, 2011. **121**(6): p. 2094-101.
57. Kiran, S., et al., *High Fat Diet-Induced CD8(+) T Cells in Adipose Tissue Mediate Macrophages to Sustain Low-Grade Chronic Inflammation.* Front Immunol, 2021. **12**: p. 680944.
58. Vantourout, P. and A. Hayday, *Six-of-the-best: unique contributions of gammadelta T cells to immunology.* Nat Rev Immunol, 2013. **13**(2): p. 88-100.
59. Caspar-Bauguil, S., et al., *Adipose tissues as an ancestral immune organ: site-specific change in obesity.* FEBS Lett, 2005. **579**(17): p. 3487-92.
60. Zuniga, L.A., et al., *IL-17 regulates adipogenesis, glucose homeostasis, and obesity.* J Immunol, 2010. **185**(11): p. 6947-59.
61. Stevens, M.M., *Biomaterials for bone tissue engineering.* Mater Today, 2008. **11**(5): p. 18-25.
62. DiGirolamo, D.J., T.L. Clemens, and S. Kousteni, *The skeleton as an endocrine organ.* Nat Rev Rheumatol, 2012. **8**(11): p. 674-83.
63. Loebel, C. and J.A. Burdick, *Engineering Stem and Stromal Cell Therapies for Musculoskeletal Tissue Repair.* Cell Stem Cell, 2018. **22**(3): p. 325-339.
64. Lopes, D., et al., *Bone physiology as inspiration for tissue regenerative therapies.* Biomaterials, 2018. **185**: p. 240-275.
65. Datta, H.K., et al., *The cell biology of bone metabolism.* J Clin Pathol, 2008. **61**(5): p. 577-87.
66. Zhu, G., et al., *Bone physiological microenvironment and healing mechanism: Basis for future bone-tissue engineering scaffolds.* Bioact Mater, 2021. **6**(11): p. 4110-4140.
67. Yin, T. and L. Li, *The stem cell niches in bone.* J Clin Invest, 2006. **116**(5): p. 1195-201.
68. Gori, J.L., et al., *Vascular niche promotes hematopoietic multipotent progenitor formation from pluripotent stem cells.* J Clin Invest, 2015. **125**(3): p. 1243-54.
69. Capulli, M., R. Paone, and N. Rucci, *Osteoblast and osteocyte: games without frontiers.* Arch Biochem Biophys, 2014. **561**: p. 3-12.
70. Pathak, J.L., N. Bravenboer, and J. Klein-Nulend, *The Osteocyte as the New Discovery of Therapeutic Options in Rare Bone Diseases.* Front Endocrinol (Lausanne), 2020. **11**: p. 405.
71. Asagiri, M. and H. Takayanagi, *The molecular understanding of osteoclast differentiation.* Bone, 2007. **40**(2): p. 251-64.
72. Saftig, P., et al., *Functions of cathepsin K in bone resorption. Lessons from cathepsin K deficient mice.* Adv Exp Med Biol, 2000. **477**: p. 293-303.
73. Boyce, B.F. and L. Xing, *The RANKL/RANK/OPG pathway.* Curr Osteoporos Rep, 2007. **5**(3): p. 98-104.
74. Sharma, U., D. Pal, and R. Prasad, *Alkaline phosphatase: an overview.* Indian J Clin Biochem, 2014. **29**(3): p. 269-78.
75. Karsenty, G., *The complexities of skeletal biology.* Nature, 2003. **423**(6937): p. 316-8.
76. Phillips, A.M., *Overview of the fracture healing cascade.* Injury, 2005. **36 Suppl 3**: p. S5-7.

77. Einhorn, T.A. and L.C. Gerstenfeld, *Fracture healing: mechanisms and interventions.* Nat Rev Rheumatol, 2015. **11**(1): p. 45-54.
78. Baht, G.S., L. Vi, and B.A. Alman, *The Role of the Immune Cells in Fracture Healing.* Curr Osteoporos Rep, 2018. **16**(2): p. 138-145.
79. Knighton, D.R., et al., *Oxygen tension regulates the expression of angiogenesis factor by macrophages.* Science, 1983. **221**(4617): p. 1283-5.
80. Bahney, C.S., et al., *Cellular biology of fracture healing.* J Orthop Res, 2019. **37**(1): p. 35-50.
81. Schindeler, A., et al., *Bone remodeling during fracture repair: The cellular picture.* Semin Cell Dev Biol, 2008. **19**(5): p. 459-66.
82. Arron, J.R. and Y. Choi, *Bone versus immune system.* Nature, 2000. **408**(6812): p. 535-6.
83. Mueller, C.G. and E. Hess, *Emerging Functions of RANKL in Lymphoid Tissues.* Front Immunol, 2012. **3**: p. 261.
84. Konnecke, I., et al., *T and B cells participate in bone repair by infiltrating the fracture callus in a two-wave fashion.* Bone, 2014. **64**: p. 155-65.
85. Gibon, E., L. Lu, and S.B. Goodman, *Aging, inflammation, stem cells, and bone healing.* Stem Cell Res Ther, 2016. **7**: p. 44.
86. Beura, L.K., et al., *Normalizing the environment recapitulates adult human immune traits in laboratory mice.* Nature, 2016. **532**(7600): p. 512-6.
87. Japp, A.S., et al., *Wild immunology assessed by multidimensional mass cytometry.* Cytometry A, 2017. **91**(1): p. 85-95.
88. Reinke, S., et al., *Terminally differentiated CD8(+) T cells negatively affect bone regeneration in humans.* Sci Transl Med, 2013. **5**(177): p. 177ra36.
89. Schmidt-Bleek, K., et al., *Inflammatory phase of bone healing initiates the regenerative healing cascade.* Cell Tissue Res, 2012. **347**(3): p. 567-73.
90. Bucher, C.H., et al., *Local immune cell contribution during fracture healing in the aged – novel role for interleukin 22.* Experimental & Molecular Medicine, 2022.
91. Di Rosa, F. and T. Gebhardt, *Bone Marrow T Cells and the Integrated Functions of Recirculating and Tissue-Resident Memory T Cells.* Front Immunol, 2016. **7**: p. 51.
92. Kverneland, A.H., et al., *Age and gender leucocytes variances and references values generated using the standardized ONE-Study protocol.* Cytometry A, 2016. **89**(6): p. 543-64.
93. Gilbert, L., et al., *Inhibition of osteoblast differentiation by tumor necrosis factor-alpha.* Endocrinology, 2000. **141**(11): p. 3956-64.
94. Kohara, H., et al., *IFN-gamma directly inhibits TNF-alpha-induced osteoclastogenesis in vitro and in vivo and induces apoptosis mediated by Fas/Fas ligand interactions.* Immunol Lett, 2011. **137**(1-2): p. 53-61.
95. Karnes, J.M., S.D. Daffner, and C.M. Watkins, *Multiple roles of tumor necrosis factor-alpha in fracture healing.* Bone, 2015. **78**: p. 87-93.
96. Okhrimenko, A., et al., *Human memory T cells from the bone marrow are resting and maintain long-lasting systemic memory.* Proc Natl Acad Sci U S A, 2014. **111**(25): p. 9229-34.
97. El Khassawna, T., et al., *T Lymphocytes Influence the Mineralization Process of Bone.* Front Immunol, 2017. **8**: p. 562.
98. Loder, R.T., *The influence of diabetes mellitus on the healing of closed fractures.* Clin Orthop Relat Res, 1988(232): p. 210-6.
99. Retzepi, M. and N. Donos, *The effect of diabetes mellitus on osseous healing.* Clin Oral Implants Res, 2010. **21**(7): p. 673-81.
100. Kanis, J.A., et al., *FRAX and the assessment of fracture probability in men and women from the UK.* Osteoporos Int, 2008. **19**(4): p. 385-97.
101. De Laet, C., et al., *Body mass index as a predictor of fracture risk: a meta-analysis.* Osteoporos Int, 2005. **16**(11): p. 1330-8.
102. Compston, J.E., et al., *Obesity is not protective against fracture in postmenopausal women: GLOW.* Am J Med, 2011. **124**(11): p. 1043-50.

103. Tanaka, S., et al., *Overweight/obesity and underweight are both risk factors for osteoporotic fractures at different sites in Japanese postmenopausal women.* Osteoporos Int, 2013. **24**(1): p. 69-76.
104. Sukumar, D., et al., *Obesity alters cortical and trabecular bone density and geometry in women.* Osteoporos Int, 2011. **22**(2): p. 635-45.
105. Lecka-Czernik, B., *Diabetes, bone and glucose-lowering agents: basic biology.* Diabetologia, 2017. **60**(7): p. 1163-1169.
106. Turki Jalil, A., et al., *Circulating and dietary advanced glycation end products and obesity in an adult population: A paradox of their detrimental effects in obesity.* Front Endocrinol (Lausanne), 2022. **13**: p. 966590.
107. Marin, C., et al., *Impaired soft and hard callus formation during fracture healing in diet-induced obese mice as revealed by 3D contrast-enhanced computed tomography imaging.* Bone, 2021. **150**: p. 116008.
108. Schwartz, A.V., et al., *Effects of TZD Use and Discontinuation on Fracture Rates in ACCORD Bone Study.* J Clin Endocrinol Metab, 2015. **100**(11): p. 4059-66.
109. Gimble, J.M., et al., *Peroxisome proliferator-activated receptor-gamma activation by thiazolidinediones induces adipogenesis in bone marrow stromal cells.* Mol Pharmacol, 1996. **50**(5): p. 1087-94.
110. Benova, A. and M. Tencerova, *Obesity-Induced Changes in Bone Marrow Homeostasis.* Front Endocrinol (Lausanne), 2020. **11**: p. 294.
111. Ambrosi, T.H., et al., *Adipocyte Accumulation in the Bone Marrow during Obesity and Aging Impairs Stem Cell-Based Hematopoietic and Bone Regeneration.* Cell Stem Cell, 2017. **20**(6): p. 771-784 e6.
112. Brown, M.L., et al., *Delayed fracture healing and increased callus adiposity in a C57BL/6J murine model of obesity-associated type 2 diabetes mellitus.* PLoS One, 2014. **9**(6): p. e99656.
113. Veldhuis-Vlug, A.G. and C.J. Rosen, *Clinical implications of bone marrow adiposity.* J Intern Med, 2018. **283**(2): p. 121-139.
114. Kershaw, E.E. and J.S. Flier, *Adipose tissue as an endocrine organ.* J Clin Endocrinol Metab, 2004. **89**(6): p. 2548-56.
115. Pepe, J., et al., *Adipokines and bone metabolism: an interplay to untangle.* J Endocrinol Invest, 2016. **39**(11): p. 1359-1361.
116. Carnevale, V., et al., *Relationship between bone metabolism and adipogenesis.* J Endocrinol Invest, 2010. **33**(7 Suppl): p. 4-8.
117. Zhang, Y., et al., *Irisin exerts dual effects on browning and adipogenesis of human white adipocytes.* Am J Physiol Endocrinol Metab, 2016. **311**(2): p. E530-41.
118. Andriankaja, O.M., et al., *Gene expression dynamics during diabetic periodontitis.* J Dent Res, 2012. **91**(12): p. 1160-5.
119. Sarkar, P.D. and A.B. Choudhury, *Relationships between serum osteocalcin levels versus blood glucose, insulin resistance and markers of systemic inflammation in central Indian type 2 diabetic patients.* Eur Rev Med Pharmacol Sci, 2013. **17**(12): p. 1631-5.
120. Faienza, M.F., et al., *Skeleton and glucose metabolism: a bone-pancreas loop.* Int J Endocrinol, 2015. **2015**: p. 758148.
121. Pacios, S., et al., *Diabetes aggravates periodontitis by limiting repair through enhanced inflammation.* FASEB J, 2012. **26**(4): p. 1423-30.
122. Santos, V.R., et al., *Receptor activator of nuclear factor-kappa B ligand/osteoprotegerin ratio in sites of chronic periodontitis of subjects with poorly and well-controlled type 2 diabetes.* J Periodontol, 2010. **81**(10): p. 1455-65.
123. Drosatos-Tampakaki, Z., et al., *Palmitic acid and DGAT1 deficiency enhance osteoclastogenesis, while oleic acid-induced triglyceride formation prevents it.* J Bone Miner Res, 2014. **29**(5): p. 1183-95.
124. Almeida, M. and C.A. O'Brien, *Basic biology of skeletal aging: role of stress response pathways.* J Gerontol A Biol Sci Med Sci, 2013. **68**(10): p. 1197-208.

125. Turnbaugh, P.J., et al., *The effect of diet on the human gut microbiome: a metagenomic analysis in humanized gnotobiotic mice.* Sci Transl Med, 2009. **1**(6): p. 6ra14.
126. Lee, N. and W.U. Kim, *Microbiota in T-cell homeostasis and inflammatory diseases.* Exp Mol Med, 2017. **49**(5): p. e340.
127. Ley, R.E., et al., *Obesity alters gut microbial ecology.* Proc Natl Acad Sci U S A, 2005. **102**(31): p. 11070-5.
128. Serino, M., et al., *Metabolic adaptation to a high-fat diet is associated with a change in the gut microbiota.* Gut, 2012. **61**(4): p. 543-53.
129. Kootte, R.S., et al., *Improvement of Insulin Sensitivity after Lean Donor Feces in Metabolic Syndrome Is Driven by Baseline Intestinal Microbiota Composition.* Cell Metab, 2017. **26**(4): p. 611-619 e6.
130. Zhang, J., et al., *The impact of the intestinal microbiome on bone health.* Intractable Rare Dis Res, 2018. **7**(3): p. 148-155.
131. Sjogren, K., et al., *The gut microbiota regulates bone mass in mice.* J Bone Miner Res, 2012. **27**(6): p. 1357-67.
132. Luo, Y., et al., *Microbiota from Obese Mice Regulate Hematopoietic Stem Cell Differentiation by Altering the Bone Niche.* Cell Metab, 2015. **22**(5): p. 886-94.
133. Schmidt-Bleek, K., R. Marcucio, and G. Duda, *Future Treatment Strategies for Delayed Bone Healing: An Osteoimmunologic Approach.* J Am Acad Orthop Surg, 2016. **24**(10): p. e134-5.
134. Schlundt, C., *Impact of the adaptive immune system in bone fracture healing*. 2017, Humboldt-Universität zu Berlin.
135. Mountziaris, P.M. and A.G. Mikos, *Modulation of the inflammatory response for enhanced bone tissue regeneration.* Tissue Eng Part B Rev, 2008. **14**(2): p. 179-86.
136. Zhao, Y., Z. Jiang, and C. Guo, *New hope for type 2 diabetics: targeting insulin resistance through the immune modulation of stem cells.* Autoimmun Rev, 2011. **11**(2): p. 137-42.
137. Brooks-Worrell, B., R. Narla, and J.P. Palmer, *Biomarkers and immune-modulating therapies for type 2 diabetes.* Trends Immunol, 2012. **33**(11): p. 546-53.
138. Kaufman, A. and K.C. Herold, *Anti-CD3 mAbs for treatment of type 1 diabetes.* Diabetes Metab Res Rev, 2009. **25**(4): p. 302-6.
139. Pescovitz, M.D., et al., *Rituximab, B-lymphocyte depletion, and preservation of beta-cell function.* N Engl J Med, 2009. **361**(22): p. 2143-52.
140. Winer, S., et al., *Normalization of obesity-associated insulin resistance through immunotherapy.* Nat Med, 2009. **15**(8): p. 921-9.
141. Larsen, C.M., et al., *Sustained effects of interleukin-1 receptor antagonist treatment in type 2 diabetes.* Diabetes Care, 2009. **32**(9): p. 1663-8.
142. Manigrasso, M.B. and J.P. O'Connor, *Comparison of fracture healing among different inbred mouse strains.* Calcif Tissue Int, 2008. **82**(6): p. 465-74.
143. Roch, F. and M.A. Bach, *Strain differences in mouse cellular responses to Mycobacterium lepraemurium and BCG subcutaneous infections. II. Production of interleukins 2, 4, and 6 and of interferon-gamma by draining lymph node cells.* Clin Immunol Immunopathol, 1991. **60**(3): p. 443-54.
144. Brodt, M.D., C.B. Ellis, and M.J. Silva, *Growing C57Bl/6 mice increase whole bone mechanical properties by increasing geometric and material properties.* J Bone Miner Res, 1999. **14**(12): p. 2159-66.
145. Toye, A.A., et al., *A genetic and physiological study of impaired glucose homeostasis control in C57BL/6J mice.* Diabetologia, 2005. **48**(4): p. 675-86.
146. Bucher, C.H., et al., *Local immune cell contributions to fracture healing in aged individuals - A novel role for interleukin 22.* Exp Mol Med, 2022. **54**(8): p. 1262-1276.
147. See, P., et al., *A Single-Cell Sequencing Guide for Immunologists.* Front Immunol, 2018. **9**: p. 2425.
148. Kawamoto, T. and K. Kawamoto, *Preparation of thin frozen sections from nonfixed and undecalcified hard tissues using Kawamot's film method (2012).* Methods Mol Biol, 2014. **1130**: p. 149-164.

149. Woodfin, A., M.B. Voisin, and S. Nourshargh, *PECAM-1: a multi-functional molecule in inflammation and vascular biology.* Arterioscler Thromb Vasc Biol, 2007. **27**(12): p. 2514-23.
150. Boerckel, J.D., et al., *Microcomputed tomography: approaches and applications in bioengineering.* Stem Cell Res Ther, 2014. **5**(6): p. 144.
151. Peirson, S.N. and J.N. Butler, *RNA extraction from mammalian tissues.* Methods Mol Biol, 2007. **362**: p. 315-27.
152. Kvastad, L., et al., *The spatial RNA integrity number assay for in situ evaluation of transcriptome quality.* Commun Biol, 2021. **4**(1): p. 57.
153. Kukurba, K.R. and S.B. Montgomery, *RNA Sequencing and Analysis.* Cold Spring Harb Protoc, 2015. **2015**(11): p. 951-69.
154. Edgar, R.C., *UPARSE: highly accurate OTU sequences from microbial amplicon reads.* Nat Methods, 2013. **10**(10): p. 996-8.
155. Lagkouvardos, I., et al., *Rhea: a transparent and modular R pipeline for microbial profiling based on 16S rRNA gene amplicons.* PeerJ, 2017. **5**: p. e2836.
156. Eckhardt, B.A., et al., *Accelerated osteocyte senescence and skeletal fragility in mice with type 2 diabetes.* JCI Insight, 2020. **5**(9).
157. Lee, J. and J.H. Choi, *Deciphering Macrophage Phenotypes upon Lipid Uptake and Atherosclerosis.* Immune Netw, 2020. **20**(3): p. e22.
158. Schlundt, C., et al., *The multifaceted roles of macrophages in bone regeneration: A story of polarization, activation and time.* Acta Biomater, 2021. **133**: p. 46-57.
159. Collin, M. and V. Bigley, *Human dendritic cell subsets: an update.* Immunology, 2018. **154**(1): p. 3-20.
160. Bertola, A., et al., *Identification of adipose tissue dendritic cells correlated with obesity-associated insulin-resistance and inducing Th17 responses in mice and patients.* Diabetes, 2012. **61**(9): p. 2238-47.
161. Rocha, V.Z., et al., *Interferon-gamma, a Th1 cytokine, regulates fat inflammation: a role for adaptive immunity in obesity.* Circ Res, 2008. **103**(5): p. 467-76.
162. Dalmas, E., et al., *T cell-derived IL-22 amplifies IL-1beta-driven inflammation in human adipose tissue: relevance to obesity and type 2 diabetes.* Diabetes, 2014. **63**(6): p. 1966-77.
163. Shiau, M.Y., et al., *Mechanism of Interleukin-4 Reducing Lipid Deposit by Regulating Hormone-Sensitive Lipase.* Sci Rep, 2019. **9**(1): p. 11974.
164. Heng, T.S., M.W. Painter, and C. Immunological Genome Project, *The Immunological Genome Project: networks of gene expression in immune cells.* Nat Immunol, 2008. **9**(10): p. 1091-4.
165. Lukens, J.R., et al., *The NLRP12 Sensor Negatively Regulates Autoinflammatory Disease by Modulating Interleukin-4 Production in T Cells.* Immunity, 2015. **42**(4): p. 654-64.
166. Qin, S., et al., *The chemokine receptors CXCR3 and CCR5 mark subsets of T cells associated with certain inflammatory reactions.* J Clin Invest, 1998. **101**(4): p. 746-54.
167. Morita, R., et al., *Human blood CXCR5(+)CD4(+) T cells are counterparts of T follicular cells and contain specific subsets that differentially support antibody secretion.* Immunity, 2011. **34**(1): p. 108-21.
168. Bakos, E., et al., *CCR2 Regulates the Immune Response by Modulating the Interconversion and Function of Effector and Regulatory T Cells.* J Immunol, 2017. **198**(12): p. 4659-4671.
169. Miedel, E.L., et al., *Type III collagen modulates fracture callus bone formation and early remodeling.* J Orthop Res, 2015. **33**(5): p. 675-84.
170. Fidler, A.L., et al., *The triple helix of collagens - an ancient protein structure that enabled animal multicellularity and tissue evolution.* J Cell Sci, 2018. **131**(7).
171. Zitnay, J.L., et al., *Molecular level detection and localization of mechanical damage in collagen enabled by collagen hybridizing peptides.* Nat Commun, 2017. **8**: p. 14913.
172. Hwang, J., et al., *Molecular assessment of collagen denaturation in decellularized tissues using a collagen hybridizing peptide.* Acta Biomater, 2017. **53**: p. 268-278.
173. Bitar, M.S., *Diabetes Impairs Angiogenesis and Induces Endothelial Cell Senescence by Up-Regulating Thrombospondin-CD47-Dependent Signaling.* Int J Mol Sci, 2019. **20**(3).

174. Cerf, M.E., *Beta cell dysfunction and insulin resistance.* Front Endocrinol (Lausanne), 2013. **4**: p. 37.
175. Breuer, D.A., et al., *CD8(+) T cells regulate liver injury in obesity-related nonalcoholic fatty liver disease.* Am J Physiol Gastrointest Liver Physiol, 2020. **318**(2): p. G211-G224.
176. Yang, K.C., et al., *Association of Non-alcoholic Fatty Liver Disease with Metabolic Syndrome Independently of Central Obesity and Insulin Resistance.* Sci Rep, 2016. **6**: p. 27034.
177. Fabbrini, E., S. Sullivan, and S. Klein, *Obesity and nonalcoholic fatty liver disease: biochemical, metabolic, and clinical implications.* Hepatology, 2010. **51**(2): p. 679-89.
178. Palmas, V., et al., *Gut microbiota markers associated with obesity and overweight in Italian adults.* Sci Rep, 2021. **11**(1): p. 5532.
179. Orbe-Orihuela, Y.C., et al., *High relative abundance of firmicutes and increased TNF-alpha levels correlate with obesity in children.* Salud Publica Mex, 2018. **60**(1): p. 5-11.
180. Pesoa, S.A., et al., *Comparison of Argentinean microbiota with other geographical populations reveals different taxonomic and functional signatures associated with obesity.* Sci Rep, 2021. **11**(1): p. 7762.
181. Ahmad, A., et al., *Analysis of gut microbiota of obese individuals with type 2 diabetes and healthy individuals.* PLoS One, 2019. **14**(12): p. e0226372.
182. Boughanem, H., et al., *Potential Role of Insulin Growth-Factor-Binding Protein 2 as Therapeutic Target for Obesity-Related Insulin Resistance.* Int J Mol Sci, 2021. **22**(3).
183. DeMambro, V.E., et al., *Gender-specific changes in bone turnover and skeletal architecture in igfbp-2-null mice.* Endocrinology, 2008. **149**(5): p. 2051-61.
184. Miyakoshi, N., et al., *Evidence that IGF-binding protein-5 functions as a growth factor.* J Clin Invest, 2001. **107**(1): p. 73-81.
185. Andress, D.L., *IGF-binding protein-5 stimulates osteoblast activity and bone accretion in ovariectomized mice.* Am J Physiol Endocrinol Metab, 2001. **281**(2): p. E283-8.
186. Campbell, P.G. and D.L. Andress, *Insulin-like growth factor (IGF)-binding protein-5-(201-218) region regulates hydroxyapatite and IGF-I binding.* Am J Physiol, 1997. **273**(5): p. E1005-13.
187. Xu, M., et al., *Ccrl2 deficiency deteriorates obesity and insulin resistance through increasing adipose tissue macrophages infiltration.* Genes Dis, 2022. **9**(2): p. 429-442.
188. Spater, D., et al., *Wnt9a signaling is required for joint integrity and regulation of Ihh during chondrogenesis.* Development, 2006. **133**(15): p. 3039-49.
189. Boyan, B.D., et al., *Role of Wnt11 during Osteogenic Differentiation of Human Mesenchymal Stem Cells on Microstructured Titanium Surfaces.* Sci Rep, 2018. **8**(1): p. 8588.
190. Moverare-Skrtic, S., et al., *Osteoblast-derived WNT16 represses osteoclastogenesis and prevents cortical bone fragility fractures.* Nat Med, 2014. **20**(11): p. 1279-88.
191. Eichberger, J., et al., *Loss of MMP-27 Predicts Mandibular Bone Invasion in Oral Squamous Cell Carcinoma.* Cancers (Basel), 2022. **14**(16).
192. Kveiborg, M., et al., *ADAM12-S stimulates bone growth in transgenic mice by modulating chondrocyte proliferation and maturation.* J Bone Miner Res, 2006. **21**(8): p. 1288-96.
193. Porsche, C.E., et al., *Obesity results in adipose tissue T cell exhaustion.* JCI Insight, 2021. **6**(8).
194. Chang, T.T., C. Chen, and J.W. Chen, *CCL7 as a novel inflammatory mediator in cardiovascular disease, diabetes mellitus, and kidney disease.* Cardiovasc Diabetol, 2022. **21**(1): p. 185.
195. DeLeon-Pennell, K.Y., et al., *Periodontal-induced chronic inflammation triggers macrophage secretion of Ccl12 to inhibit fibroblast-mediated cardiac wound healing.* JCI Insight, 2017. **2**(18).
196. Schmitz, J.M., et al., *Expression of CXCL15 (Lungkine) in murine gastrointestinal, urogenital, and endocrine organs.* J Histochem Cytochem, 2007. **55**(5): p. 515-24.
197. Kitade, H., et al., *CCR5 plays a critical role in obesity-induced adipose tissue inflammation and insulin resistance by regulating both macrophage recruitment and M1/M2 status.* Diabetes, 2012. **61**(7): p. 1680-90.
198. Lee, M., et al., *IL-7 receptor deletion ameliorates diet-induced obesity and insulin resistance in mice.* Diabetologia, 2015. **58**(10): p. 2361-70.

199. Takeuchi, Y., et al., *Interleukin-11 as a stimulatory factor for bone formation prevents bone loss with advancing age in mice.* J Biol Chem, 2002. **277**(50): p. 49011-8.
200. Mori, S., et al., *Characteristic expression of extracellular matrix in subcutaneous adipose tissue development and adipogenesis; comparison with visceral adipose tissue.* Int J Biol Sci, 2014. **10**(8): p. 825-33.
201. Buechler, C., S. Krautbauer, and K. Eisinger, *Adipose tissue fibrosis.* World J Diabetes, 2015. **6**(4): p. 548-53.
202. Li, X., et al., *Smad6 is induced by BMP-2 and modulates chondrocyte differentiation.* J Orthop Res, 2003. **21**(5): p. 908-13.
203. Chang, J., et al., *Noncanonical Wnt-4 signaling enhances bone regeneration of mesenchymal stem cells in craniofacial defects through activation of p38 MAPK.* J Biol Chem, 2007. **282**(42): p. 30938-48.
204. Yu, B., et al., *Wnt4 signaling prevents skeletal aging and inflammation by inhibiting nuclear factor-kappaB.* Nat Med, 2014. **20**(9): p. 1009-17.
205. Bucher, C.H., et al., *Experience in the Adaptive Immunity Impacts Bone Homeostasis, Remodeling, and Healing.* Front Immunol, 2019. **10**: p. 797.
206. Nguyen, T.L., et al., *How informative is the mouse for human gut microbiota research?* Dis Model Mech, 2015. **8**(1): p. 1-16.
207. Nguyen, N.P., et al., *A perspective on 16S rRNA operational taxonomic unit clustering using sequence similarity.* NPJ Biofilms Microbiomes, 2016. **2**: p. 16004.
208. Sakamoto, M., et al., *Butyricimonas synergistica gen. nov., sp. nov. and Butyricimonas virosa sp. nov., butyric acid-producing bacteria in the family 'Porphyromonadaceae' isolated from rat faeces.* Int J Syst Evol Microbiol, 2009. **59**(Pt 7): p. 1748-53.
209. Xing, C., et al., *Microbiota regulate innate immune signaling and protective immunity against cancer.* Cell Host Microbe, 2021. **29**(6): p. 959-974 e7.
210. Larsen, J.M., *The immune response to Prevotella bacteria in chronic inflammatory disease.* Immunology, 2017. **151**(4): p. 363-374.
211. Hold, G.L., et al., *Assessment of microbial diversity in human colonic samples by 16S rDNA sequence analysis.* FEMS Microbiol Ecol, 2002. **39**(1): p. 33-9.
212. Bunker, J.J., et al., *Innate and Adaptive Humoral Responses Coat Distinct Commensal Bacteria with Immunoglobulin A.* Immunity, 2015. **43**(3): p. 541-53.
213. Nakano, V., et al., *Adherence and invasion of Bacteroidales isolated from the human intestinal tract.* Clin Microbiol Infect, 2008. **14**(10): p. 955-63.
214. Kulagina, E.V., et al., *Species composition of Bacteroidales order bacteria in the feces of healthy people of various ages.* Biosci Biotechnol Biochem, 2012. **76**(1): p. 169-71.
215. La Reau, A.J. and G. Suen, *The Ruminococci: key symbionts of the gut ecosystem.* J Microbiol, 2018. **56**(3): p. 199-208.
216. Zhou, Q., et al., *Gut bacteria Akkermansia is associated with reduced risk of obesity: evidence from the American Gut Project.* Nutr Metab (Lond), 2020. **17**: p. 90.
217. Pavlou, S., et al., *Sustained high glucose exposure sensitizes macrophage responses to cytokine stimuli but reduces their phagocytic activity.* BMC Immunol, 2018. **19**(1): p. 24.
218. Boutens, L., et al., *Unique metabolic activation of adipose tissue macrophages in obesity promotes inflammatory responses.* Diabetologia, 2018. **61**(4): p. 942-953.
219. Freemerman, A.J., et al., *Metabolic reprogramming of macrophages: glucose transporter 1 (GLUT1)-mediated glucose metabolism drives a proinflammatory phenotype.* J Biol Chem, 2014. **289**(11): p. 7884-96.
220. Torres-Castro, I., et al., *Human monocytes and macrophages undergo M1-type inflammatory polarization in response to high levels of glucose.* Immunol Lett, 2016. **176**: p. 81-9.
221. Alexander, K.A., et al., *Osteal macrophages promote in vivo intramembranous bone healing in a mouse tibial injury model.* J Bone Miner Res, 2011. **26**(7): p. 1517-32.
222. Chang, M.K., et al., *Osteal tissue macrophages are intercalated throughout human and mouse bone lining tissues and regulate osteoblast function in vitro and in vivo.* J Immunol, 2008. **181**(2): p. 1232-44.

223. Schlundt, C., et al., *Macrophages in bone fracture healing: Their essential role in endochondral ossification.* Bone, 2018. **106**: p. 78-89.
224. Kang, M., et al., *Macrophage Control of Incipient Bone Formation in Diabetic Mice.* Front Cell Dev Biol, 2020. **8**: p. 596622.
225. Dai, B., et al., *Macrophages in epididymal adipose tissue secrete osteopontin to regulate bone homeostasis.* Nat Commun, 2022. **13**(1): p. 427.
226. Misumi, I., et al., *Obesity Expands a Distinct Population of T Cells in Adipose Tissue and Increases Vulnerability to Infection.* Cell Rep, 2019. **27**(2): p. 514-524 e5.
227. Yang, H., et al., *Obesity accelerates thymic aging.* Blood, 2009. **114**(18): p. 3803-12.
228. Mehta, P., A.M. Nuotio-Antar, and C.W. Smith, *gammadelta T cells promote inflammation and insulin resistance during high fat diet-induced obesity in mice.* J Leukoc Biol, 2015. **97**(1): p. 121-34.
229. Colburn, N.T., et al., *A role for gamma/delta T cells in a mouse model of fracture healing.* Arthritis Rheum, 2009. **60**(6): p. 1694-703.
230. Wang, L., et al., *Critical roles of adenosine A2A receptor in regulating the balance of Treg/Th17 cells in allergic asthma.* Clin Respir J, 2018. **12**(1): p. 149-157.
231. Wang, M., et al., *Th17 and Treg cells in bone related diseases.* Clin Dev Immunol, 2013. **2013**: p. 203705.
232. Liang, D., et al., *Anti-inflammatory or proinflammatory effect of an adenosine receptor agonist on the Th17 autoimmune response is inflammatory environment-dependent.* J Immunol, 2014. **193**(11): p. 5498-505.
233. Huang, Z., X. Pei, and D.T. Graves, *The Interrelationship Between Diabetes, IL-17 and Bone Loss.* Curr Osteoporos Rep, 2020. **18**(1): p. 23-31.
234. Fischer, L., et al., *Foxp3(+) Regulatory T Cells in Bone and Hematopoietic Homeostasis.* Front Endocrinol (Lausanne), 2019. **10**: p. 578.
235. Okamoto, K., et al., *Osteoimmunology: The Conceptual Framework Unifying the Immune and Skeletal Systems.* Physiol Rev, 2017. **97**(4): p. 1295-1349.
236. Priceman, S.J., et al., *Regulation of adipose tissue T cell subsets by Stat3 is crucial for diet-induced obesity and insulin resistance.* Proc Natl Acad Sci U S A, 2013. **110**(32): p. 13079-84.
237. Cottam, M.A., et al., *Multiomics reveals persistence of obesity-associated immune cell phenotypes in adipose tissue during weight loss and weight regain in mice.* Nat Commun, 2022. **13**(1): p. 2950.
238. Feuerer, M., et al., *Lean, but not obese, fat is enriched for a unique population of regulatory T cells that affect metabolic parameters.* Nat Med, 2009. **15**(8): p. 930-9.
239. Wagner, N.M., et al., *Circulating regulatory T cells are reduced in obesity and may identify subjects at increased metabolic and cardiovascular risk.* Obesity (Silver Spring), 2013. **21**(3): p. 461-8.
240. Agabiti-Rosei, C., et al., *Decreased circulating T regulatory lymphocytes in obese patients undergoing bariatric surgery.* PLoS One, 2018. **13**(5): p. e0197178.
241. Svec, P., et al., *Do regulatory T cells contribute to Th1 skewness in obesity?* Exp Clin Endocrinol Diabetes, 2007. **115**(7): p. 439-43.
242. van der Weerd, K., et al., *Morbidly obese human subjects have increased peripheral blood CD4+ T cells with skewing toward a Treg- and Th2-dominated phenotype.* Diabetes, 2012. **61**(2): p. 401-8.
243. Bradley, D., et al., *Adipose Tissue T Regulatory Cells: Implications for Health and Disease.* Adv Exp Med Biol, 2021. **1278**: p. 125-139.
244. Calcaterra, V., et al., *Th17 and Treg Balance in Children With Obesity and Metabolically Altered Status.* Front Pediatr, 2020. **8**: p. 591012.
245. Croce, S., et al., *Adipose Tissue Immunomodulation and Treg/Th17 Imbalance in the Impaired Glucose Metabolism of Children with Obesity.* Children (Basel), 2021. **8**(7).
246. Wen, J., et al., *Increasing Imbalance of Treg/Th17 Indicates More Severe Glucose Metabolism Dysfunction in Overweight/obese Patients.* Arch Med Res, 2021. **52**(3): p. 339-347.

247. Yu, Y., et al., *Recent advances in CD8(+) regulatory T cell research.* Oncol Lett, 2018. **15**(6): p. 8187-8194.
248. Nunez Ruiz, A., et al., *Diminished levels of regulatory T cell subsets (CD8+Foxp3, CD4+Foxp3 and CD4+CD39+Foxp3) but increased Foxp3 expression in adipose tissue from overweight subjects.* Nutrition, 2016. **32**(9): p. 943-54.
249. Niederlova, V., et al., *CD8(+) Tregs revisited: A heterogeneous population with different phenotypes and properties.* Eur J Immunol, 2021. **51**(3): p. 512-530.
250. Ferretti, S., et al., *IL-17, produced by lymphocytes and neutrophils, is necessary for lipopolysaccharide-induced airway neutrophilia: IL-15 as a possible trigger.* J Immunol, 2003. **170**(4): p. 2106-12.
251. Ishigame, H., et al., *Differential roles of interleukin-17A and -17F in host defense against mucoepithelial bacterial infection and allergic responses.* Immunity, 2009. **30**(1): p. 108-19.
252. Bastian, O., et al., *Systemic inflammation and fracture healing.* J Leukoc Biol, 2011. **89**(5): p. 669-73.
253. Kimura, A. and T. Kishimoto, *IL-6: regulator of Treg/Th17 balance.* Eur J Immunol, 2010. **40**(7): p. 1830-5.
254. Pappu, R., V. Ramirez-Carrozzi, and A. Sambandam, *The interleukin-17 cytokine family: critical players in host defence and inflammatory diseases.* Immunology, 2011. **134**(1): p. 8-16.
255. Polak-Szczybylo, E. and J. Tabarkiewicz, *IL-17A, IL-17E and IL-17F as Potential Biomarkers for the Intensity of Low-Grade Inflammation and the Risk of Cardiovascular Diseases in Obese People.* Nutrients, 2022. **14**(3).
256. Giles, D.A., et al., *Regulation of Inflammation by IL-17A and IL-17F Modulates Non-Alcoholic Fatty Liver Disease Pathogenesis.* PLoS One, 2016. **11**(2): p. e0149783.
257. Nam, D., et al., *T-lymphocytes enable osteoblast maturation via IL-17F during the early phase of fracture repair.* PLoS One, 2012. **7**(6): p. e40044.
258. Yago, T., et al., *IL-17 induces osteoclastogenesis from human monocytes alone in the absence of osteoblasts, which is potently inhibited by anti-TNF-alpha antibody: a novel mechanism of osteoclastogenesis by IL-17.* J Cell Biochem, 2009. **108**(4): p. 947-55.
259. Johansen, C., et al., *Characterization of the interleukin-17 isoforms and receptors in lesional psoriatic skin.* Br J Dermatol, 2009. **160**(2): p. 319-24.
260. Martin, D.A., et al., *The emerging role of IL-17 in the pathogenesis of psoriasis: preclinical and clinical findings.* J Invest Dermatol, 2013. **133**(1): p. 17-26.
261. Iznardo, H. and L. Puig, *Dual inhibition of IL-17A and IL-17F in psoriatic disease.* Ther Adv Chronic Dis, 2021. **12**: p. 20406223211037846.
262. Chiricozzi, A., et al., *Emerging treatment options for the treatment of moderate to severe plaque psoriasis and psoriatic arthritis: evaluating bimekizumab and its therapeutic potential.* Psoriasis (Auckl), 2019. **9**: p. 29-35.
263. Glatt, S., et al., *Dual IL-17A and IL-17F neutralisation by bimekizumab in psoriatic arthritis: evidence from preclinical experiments and a randomised placebo-controlled clinical trial that IL-17F contributes to human chronic tissue inflammation.* Ann Rheum Dis, 2018. **77**(4): p. 523-532.
264. Scheffler, J.M., et al., *Interleukin 17A: a Janus-faced regulator of osteoporosis.* Sci Rep, 2020. **10**(1): p. 5692.
265. Bartlett, H.S. and R.P. Million, *Targeting the IL-17-T(H)17 pathway.* Nat Rev Drug Discov, 2015. **14**(1): p. 11-2.
266. Nestle, F.O., D.H. Kaplan, and J. Barker, *Psoriasis.* N Engl J Med, 2009. **361**(5): p. 496-509.
267. Yeremenko, N., J.E. Paramarta, and D. Baeten, *The interleukin-23/interleukin-17 immune axis as a promising new target in the treatment of spondyloarthritis.* Curr Opin Rheumatol, 2014. **26**(4): p. 361-70.
268. Song, I.H., et al., *Relationship between active inflammatory lesions in the spine and sacroiliac joints and new development of chronic lesions on whole-body MRI in early axial spondyloarthritis: results of the ESTHER trial at week 48.* Ann Rheum Dis, 2011. **70**(7): p. 1257-63.

269. Yan, S., et al., *Critical role of interleukin-17/interleukin-17 receptor axis in mediating Con A-induced hepatitis.* Immunol Cell Biol, 2012. **90**(4): p. 421-8.
270. Nagata, T., et al., *Requirement of IL-17RA in Con A induced hepatitis and negative regulation of IL-17 production in mouse T cells.* J Immunol, 2008. **181**(11): p. 7473-9.
271. Teijeiro, A., et al., *Inhibition of the IL-17A axis in adipocytes suppresses diet-induced obesity and metabolic disorders in mice.* Nat Metab, 2021. **3**(4): p. 496-512.
272. Sugimoto, K., et al., *IL-22 ameliorates intestinal inflammation in a mouse model of ulcerative colitis.* J Clin Invest, 2008. **118**(2): p. 534-44.
273. Wolk, K., et al., *IL-22 increases the innate immunity of tissues.* Immunity, 2004. **21**(2): p. 241-54.
274. Sabat, R., W. Ouyang, and K. Wolk, *Therapeutic opportunities of the IL-22-IL-22R1 system.* Nat Rev Drug Discov, 2014. **13**(1): p. 21-38.
275. Gulhane, M., et al., *High Fat Diets Induce Colonic Epithelial Cell Stress and Inflammation that is Reversed by IL-22.* Sci Rep, 2016. **6**: p. 28990.
276. Wang, X., et al., *Interleukin-22 alleviates metabolic disorders and restores mucosal immunity in diabetes.* Nature, 2014. **514**(7521): p. 237-41.
277. Gong, F., et al., *Interleukin-22 Might Act as a Double-Edged Sword in Type 2 Diabetes and Coronary Artery Disease.* Mediators Inflamm, 2016. **2016**: p. 8254797.
278. Monasterio, G., et al., *IL-22-expressing CD4(+) AhR(+) T lymphocytes are associated with RANKL-mediated alveolar bone resorption during experimental periodontitis.* J Periodontal Res, 2019. **54**(5): p. 513-524.
279. Diaz-Zuniga, J., et al., *Increased levels of the T-helper 22-associated cytokine (interleukin-22) and transcription factor (aryl hydrocarbon receptor) in patients with periodontitis are associated with osteoclast resorptive activity and severity of the disease.* J Periodontal Res, 2017. **52**(5): p. 893-902.
280. El-Zayadi, A.A., et al., *Interleukin-22 drives the proliferation, migration and osteogenic differentiation of mesenchymal stem cells: a novel cytokine that could contribute to new bone formation in spondyloarthropathies.* Rheumatology (Oxford), 2017. **56**(3): p. 488-493.
281. Gadani, S.P., et al., *IL-4: a cytokine to remember.* J Immunol, 2012. **189**(9): p. 4213-9.
282. Guenova, E., et al., *IL-4 abrogates T(H)17 cell-mediated inflammation by selective silencing of IL-23 in antigen-presenting cells.* Proc Natl Acad Sci U S A, 2015. **112**(7): p. 2163-8.
283. El-Wakkad, A., et al., *Proinflammatory, anti-inflammatory cytokines and adiponkines in students with central obesity.* Cytokine, 2013. **61**(2): p. 682-7.
284. Schmidt, F.M., et al., *Inflammatory cytokines in general and central obesity and modulating effects of physical activity.* PLoS One, 2015. **10**(3): p. e0121971.
285. Tsao, C.H., et al., *Interleukin-4 regulates lipid metabolism by inhibiting adipogenesis and promoting lipolysis.* J Lipid Res, 2014. **55**(3): p. 385-97.
286. Bastidas-Coral, A.P., et al., *Cytokines TNF-alpha, IL-6, IL-17F, and IL-4 Differentially Affect Osteogenic Differentiation of Human Adipose Stem Cells.* Stem Cells Int, 2016. **2016**: p. 1318256.
287. Sarhangi, N., et al., *PPARG (Pro12Ala) genetic variant and risk of T2DM: a systematic review and meta-analysis.* Sci Rep, 2020. **10**(1): p. 12764.
288. Li, J., et al., *IL-9 and Th9 cells in health and diseases-From tolerance to immunopathology.* Cytokine Growth Factor Rev, 2017. **37**: p. 47-55.
289. Noelle, R.J. and E.C. Nowak, *Cellular sources and immune functions of interleukin-9.* Nat Rev Immunol, 2010. **10**(10): p. 683-7.
290. Elyaman, W., et al., *IL-9 induces differentiation of TH17 cells and enhances function of FoxP3+ natural regulatory T cells.* Proc Natl Acad Sci U S A, 2009. **106**(31): p. 12885-90.
291. Nowak, E.C., et al., *IL-9 as a mediator of Th17-driven inflammatory disease.* J Exp Med, 2009. **206**(8): p. 1653-60.
292. Singh, T.P., et al., *Involvement of IL-9 in Th17-associated inflammation and angiogenesis of psoriasis.* PLoS One, 2013. **8**(1): p. e51752.

293. Hamilton, J.A.G., et al., *Elevated Levels of Interleukin-9 in Obese Microenvironments Promote Leukemia Progression and Chemoresistance in B-Cell Acute Lymphoblastic Leukemia Cells.* Blood, 2019. **134**: p. 1468.
294. Kumagai, H., et al., *Which cytokine is the most related to weight loss-induced decrease in arterial stiffness in overweight and obese men?* Endocr J, 2018. **65**(1): p. 53-61.
295. Geng, W., W. Zhang, and J. Ma, *IL-9 exhibits elevated expression in osteonecrosis of femoral head patients and promotes cartilage degradation through activation of JAK-STAT signaling in vitro.* Int Immunopharmacol, 2018. **60**: p. 228-234.
296. Kar, S., et al., *Interleukin-9 Facilitates Osteoclastogenesis in Rheumatoid Arthritis.* Int J Mol Sci, 2021. **22**(19).
297. Hu, D.P., et al., *Cartilage to bone transformation during fracture healing is coordinated by the invading vasculature and induction of the core pluripotency genes.* Development, 2017. **144**(2): p. 221-234.
298. Haffner-Luntzer, M., et al., *Mouse Models in Bone Fracture Healing Research.* Current Molecular Biology Reports, 2016. **2**(2): p. 101-111.
299. Meng, H.Z., et al., *Advanced Glycation End Products Affect Osteoblast Proliferation and Function by Modulating Autophagy Via the Receptor of Advanced Glycation End Products/Raf Protein/Mitogen-activated Protein Kinase/Extracellular Signal-regulated Kinase Kinase/Extracellular Signal-regulated Kinase (RAGE/Raf/MEK/ERK) Pathway.* J Biol Chem, 2015. **290**(47): p. 28189-28199.
300. Krishnamoorthy, D., et al., *Dietary advanced glycation end-product consumption leads to mechanical stiffening of murine intervertebral discs.* Dis Model Mech, 2018. **11**(12).
301. Vashishth, D., et al., *Influence of nonenzymatic glycation on biomechanical properties of cortical bone.* Bone, 2001. **28**(2): p. 195-201.
302. Indyk, D., et al., *Advanced glycation end products and their receptors in serum of patients with type 2 diabetes.* Sci Rep, 2021. **11**(1): p. 13264.
303. Megas, P., *Classification of non-union.* Injury, 2005. **36 Suppl 4**: p. S30-7.
304. Mangialardi, G., et al., *Bone marrow pericyte dysfunction in individuals with type 2 diabetes.* Diabetologia, 2019. **62**(7): p. 1275-1290.
305. Roszer, T., et al., *Leptin receptor deficient diabetic (db/db) mice are compromised in postnatal bone regeneration.* Cell Tissue Res, 2014. **356**(1): p. 195-206.
306. Wallner, C., et al., *Application of VEGFA and FGF-9 enhances angiogenesis, osteogenesis and bone remodeling in type 2 diabetic long bone regeneration.* PLoS One, 2015. **10**(3): p. e0118823.
307. Pill, K., et al., *Vascularization mediated by mesenchymal stem cells from bone marrow and adipose tissue: a comparison.* Cell Regen, 2015. **4**: p. 8.
308. Vizoso, F.J., et al., *Mesenchymal Stem Cells in Homeostasis and Systemic Diseases: Hypothesis, Evidences, and Therapeutic Opportunities.* Int J Mol Sci, 2019. **20**(15).
309. Rezabakhsh, A., et al., *Type 2 Diabetes Inhibited Human Mesenchymal Stem Cells Angiogenic Response by Over-Activity of the Autophagic Pathway.* J Cell Biochem, 2017. **118**(6): p. 1518-1530.
310. Histing, T., et al., *Obesity does not affect the healing of femur fractures in mice.* Injury, 2016. **47**(7): p. 1435-44.
311. Tang, X., et al., *Obesity and risk of hip fracture in adults: a meta-analysis of prospective cohort studies.* PLoS One, 2013. **8**(4): p. e55077.
312. Lloyd, J.T., et al., *Body mass index is positively associated with bone mineral density in US older adults.* Arch Osteoporos, 2014. **9**: p. 175.
313. Tou, J.C. and C.E. Wade, *Determinants affecting physical activity levels in animal models.* Exp Biol Med (Maywood), 2002. **227**(8): p. 587-600.
314. Novak, C.M., C.M. Kotz, and J.A. Levine, *Central orexin sensitivity, physical activity, and obesity in diet-induced obese and diet-resistant rats.* Am J Physiol Endocrinol Metab, 2006. **290**(2): p. E396-403.

315. Ebrahimpur, M., et al., *Effect of diabetes on BMD and TBS values as determinants of bone health in the elderly: Bushehr Elderly Health program.* J Diabetes Metab Disord, 2019. **18**(1): p. 99-106.
316. Zura, R., et al., *Epidemiology of Fracture Nonunion in 18 Human Bones.* JAMA Surg, 2016. **151**(11): p. e162775.
317. Ishii, S., et al., *Pleiotropic effects of obesity on fracture risk: the Study of Women's Health Across the Nation.* J Bone Miner Res, 2014. **29**(12): p. 2561-70.
318. Gordeladze, J.O., et al., *Leptin stimulates human osteoblastic cell proliferation, de novo collagen synthesis, and mineralization: Impact on differentiation markers, apoptosis, and osteoclastic signaling.* J Cell Biochem, 2002. **85**(4): p. 825-36.
319. de Sousa Neto, I.V., et al., *Adipose Tissue Extracellular Matrix Remodeling in Response to Dietary Patterns and Exercise: Molecular Landscape, Mechanistic Insights, and Therapeutic Approaches.* Biology (Basel), 2022. **11**(5).
320. Marcelin, G., et al., *Deciphering the cellular interplays underlying obesity-induced adipose tissue fibrosis.* J Clin Invest, 2019. **129**(10): p. 4032-4040.
321. Henninger, A.M., et al., *Adipocyte hypertrophy, inflammation and fibrosis characterize subcutaneous adipose tissue of healthy, non-obese subjects predisposed to type 2 diabetes.* PLoS One, 2014. **9**(8): p. e105262.
322. Lawler, H.M., et al., *Adipose Tissue Hypoxia, Inflammation, and Fibrosis in Obese Insulin-Sensitive and Obese Insulin-Resistant Subjects.* J Clin Endocrinol Metab, 2016. **101**(4): p. 1422-8.
323. Wang, C.Y. and J.K. Liao, *A mouse model of diet-induced obesity and insulin resistance.* Methods Mol Biol, 2012. **821**: p. 421-33.
324. Magne, F., et al., *The Firmicutes/Bacteroidetes Ratio: A Relevant Marker of Gut Dysbiosis in Obese Patients?* Nutrients, 2020. **12**(5).
325. Backhed, F., et al., *Mechanisms underlying the resistance to diet-induced obesity in germ-free mice.* Proc Natl Acad Sci U S A, 2007. **104**(3): p. 979-84.
326. Rabot, S., et al., *Germ-free C57BL/6J mice are resistant to high-fat-diet-induced insulin resistance and have altered cholesterol metabolism.* FASEB J, 2010. **24**(12): p. 4948-59.
327. Turnbaugh, P.J., et al., *Diet-induced obesity is linked to marked but reversible alterations in the mouse distal gut microbiome.* Cell Host Microbe, 2008. **3**(4): p. 213-23.
328. Le Chatelier, E., et al., *Richness of human gut microbiome correlates with metabolic markers.* Nature, 2013. **500**(7464): p. 541-6.
329. Cotillard, A., et al., *Dietary intervention impact on gut microbial gene richness.* Nature, 2013. **500**(7464): p. 585-8.
330. Wang, B., et al., *A High-Fat Diet Increases Gut Microbiota Biodiversity and Energy Expenditure Due to Nutrient Difference.* Nutrients, 2020. **12**(10).
331. Guirro, M., et al., *Effects from diet-induced gut microbiota dysbiosis and obesity can be ameliorated by fecal microbiota transplantation: A multiomics approach.* PLoS One, 2019. **14**(9): p. e0218143.
332. Wu, X., et al., *Molecular characterisation of the faecal microbiota in patients with type II diabetes.* Curr Microbiol, 2010. **61**(1): p. 69-78.
333. Turnbaugh, P.J., et al., *A core gut microbiome in obese and lean twins.* Nature, 2009. **457**(7228): p. 480-4.
334. Kim, S.J., et al., *Dietary fat intake and age modulate the composition of the gut microbiota and colonic inflammation in C57BL/6J mice.* BMC Microbiol, 2019. **19**(1): p. 193.
335. Liu, F., et al., *Dysbiosis of urinary microbiota is positively correlated with type 2 diabetes mellitus.* Oncotarget, 2017. **8**(3): p. 3798-3810.
336. McCabe, L.R., et al., *Exercise prevents high fat diet-induced bone loss, marrow adiposity and dysbiosis in male mice.* Bone, 2019. **118**: p. 20-31.
337. Petersen, C., et al., *T cell-mediated regulation of the microbiota protects against obesity.* Science, 2019. **365**(6451).
338. Qin, J., et al., *A metagenome-wide association study of gut microbiota in type 2 diabetes.* Nature, 2012. **490**(7418): p. 55-60.

339. Rabot, S., et al., *High fat diet drives obesity regardless the composition of gut microbiota in mice.* Sci Rep, 2016. **6**: p. 32484.
340. Duncan, S.H., et al., *Human colonic microbiota associated with diet, obesity and weight loss.* Int J Obes (Lond), 2008. **32**(11): p. 1720-4.
341. Million, M., et al., *Correlation between body mass index and gut concentrations of Lactobacillus reuteri, Bifidobacterium animalis, Methanobrevibacter smithii and Escherichia coli.* Int J Obes (Lond), 2013. **37**(11): p. 1460-6.
342. Sze, M.A. and P.D. Schloss, *Looking for a Signal in the Noise: Revisiting Obesity and the Microbiome.* mBio, 2016. **7**(4).
343. Ibrahim, K.S., et al., *Characterisation of gut microbiota of obesity and type 2 diabetes in a rodent model.* Biosci Microbiota Food Health, 2021. **40**(1): p. 65-74.
344. Egshatyan, L., et al., *Gut microbiota and diet in patients with different glucose tolerance.* Endocr Connect, 2016. **5**(1): p. 1-9.
345. Kashtanova, D.A., et al., *Gut Microbiota in Patients with Different Metabolic Statuses: Moscow Study.* Microorganisms, 2018. **6**(4).
346. Liu, C., et al., *Reclassification of Clostridium coccoides, Ruminococcus hansenii, Ruminococcus hydrogenotrophicus, Ruminococcus luti, Ruminococcus productus and Ruminococcus schinkii as Blautia coccoides gen. nov., comb. nov., Blautia hansenii comb. nov., Blautia hydrogenotrophica comb. nov., Blautia luti comb. nov., Blautia producta comb. nov., Blautia schinkii comb. nov. and description of Blautia wexlerae sp. nov., isolated from human faeces.* Int J Syst Evol Microbiol, 2008. **58**(Pt 8): p. 1896-902.
347. Ling, C.W., et al., *The Association of Gut Microbiota With Osteoporosis Is Mediated by Amino Acid Metabolism: Multiomics in a Large Cohort.* J Clin Endocrinol Metab, 2021. **106**(10): p. e3852-e3864.
348. Cai, W., et al., *Ethanol extract of propolis prevents high-fat diet-induced insulin resistance and obesity in association with modulation of gut microbiota in mice.* Food Res Int, 2020. **130**: p. 108939.
349. Ke, X., et al., *Synbiotic-driven improvement of metabolic disturbances is associated with changes in the gut microbiome in diet-induced obese mice.* Mol Metab, 2019. **22**: p. 96-109.
350. Wang, M., et al., *Olive Fruit Extracts Supplement Improve Antioxidant Capacity via Altering Colonic Microbiota Composition in Mice.* Front Nutr, 2021. **8**: p. 645099.
351. Wang, H., et al., *Nanoparticles Isolated From Porcine Bone Soup Ameliorated Dextran Sulfate Sodium-Induced Colitis and Regulated Gut Microbiota in Mice.* Front Nutr, 2022. **9**: p. 821404.
352. Lagkouvardos, I., et al., *Sequence and cultivation study of Muribaculaceae reveals novel species, host preference, and functional potential of this yet undescribed family.* Microbiome, 2019. **7**(1): p. 28.
353. Schussler-Fiorenza Rose, S.M., et al., *A longitudinal big data approach for precision health.* Nat Med, 2019. **25**(5): p. 792-804.
354. Zhou, W., et al., *Longitudinal multi-omics of host-microbe dynamics in prediabetes.* Nature, 2019. **569**(7758): p. 663-671.
355. Wu, H., et al., *The Gut Microbiota in Prediabetes and Diabetes: A Population-Based Cross-Sectional Study.* Cell Metab, 2020. **32**(3): p. 379-390 e3.
356. Wang, X., et al., *Effects of high fructose corn syrup on intestinal microbiota structure and obesity in mice.* NPJ Sci Food, 2022. **6**(1): p. 17.
357. Ye, J., et al., *Pu-erh tea ameliorates obesity and modulates gut microbiota in high fat diet fed mice.* Food Res Int, 2021. **144**: p. 110360.
358. Martinez, I., et al., *Diet-induced alterations of host cholesterol metabolism are likely to affect the gut microbiota composition in hamsters.* Appl Environ Microbiol, 2013. **79**(2): p. 516-24.
359. Zhang, Q., et al., *Gut microbiota-mitochondrial inter-talk in non-alcoholic fatty liver disease.* Front Nutr, 2022. **9**: p. 934113.
360. Vacca, M., et al., *The Controversial Role of Human Gut Lachnospiraceae.* Microorganisms, 2020. **8**(4).

361. Kim, K., et al., *Role of an unclassified Lachnospiraceae in the pathogenesis of type 2 diabetes: a longitudinal study of the urine microbiome and metabolites.* Exp Mol Med, 2022. **54**(8): p. 1125-1132.
362. Li, B., et al., *Puerarin improves the bone micro-environment to inhibit OVX-induced osteoporosis via modulating SCFAs released by the gut microbiota and repairing intestinal mucosal integrity.* Biomed Pharmacother, 2020. **132**: p. 110923.
363. Zeng, Q., et al., *Discrepant gut microbiota markers for the classification of obesity-related metabolic abnormalities.* Sci Rep, 2019. **9**(1): p. 13424.
364. Shahi, S.K., et al., *Obesity induced gut dysbiosis contributes to disease severity in an animal model of multiple sclerosis.* Front Immunol, 2022. **13**: p. 966417.
365. Gong, J., et al., *Gut Microbiota Characteristics of People with Obesity by Meta-Analysis of Existing Datasets.* Nutrients, 2022. **14**(14).
366. Zeller, V., et al., *Continuous clindamycin infusion, an innovative approach to treating bone and joint infections.* Antimicrob Agents Chemother, 2010. **54**(1): p. 88-92.
367. Krezalek, M.A. and J.C. Alverdy, *The role of the microbiota in surgical recovery.* Curr Opin Clin Nutr Metab Care, 2016. **19**(5): p. 347-352.
368. Rios-Arce, N.D., et al., *Post-antibiotic gut dysbiosis-induced trabecular bone loss is dependent on lymphocytes.* Bone, 2020. **134**: p. 115269.
369. Zimmermann, P. and N. Curtis, *The effect of antibiotics on the composition of the intestinal microbiota - a systematic review.* J Infect, 2019. **79**(6): p. 471-489.
370. Bartlett, J.G., V.L. Sutter, and S.M. Finegold, *Treatment of anaerobic infections with lincomycin and clindamycin.* N Engl J Med, 1972. **287**(20): p. 1006-10.
371. Gorbach, S.L. and H. Thadepalli, *Clindamycin in pure and mixed anaerobic infections.* Arch Intern Med, 1974. **134**(1): p. 87-92.
372. Tan, J., et al., *The role of short-chain fatty acids in health and disease.* Adv Immunol, 2014. **121**: p. 91-119.
373. Lucas, S., et al., *Short-chain fatty acids regulate systemic bone mass and protect from pathological bone loss.* Nat Commun, 2018. **9**(1): p. 55.
374. Tyagi, A.M., et al., *The Microbial Metabolite Butyrate Stimulates Bone Formation via T Regulatory Cell-Mediated Regulation of WNT10B Expression.* Immunity, 2018. **49**(6): p. 1116-1131 e7.
375. Wexler, H.M., *Bacteroides: the good, the bad, and the nitty-gritty.* Clin Microbiol Rev, 2007. **20**(4): p. 593-621.
376. Buffie, C.G., et al., *Profound alterations of intestinal microbiota following a single dose of clindamycin results in sustained susceptibility to Clostridium difficile-induced colitis.* Infect Immun, 2012. **80**(1): p. 62-73.
377. Cani, P.D. and W.M. de Vos, *Next-Generation Beneficial Microbes: The Case of Akkermansia muciniphila.* Front Microbiol, 2017. **8**: p. 1765.
378. Zhou, Q., et al., *Association Between Gut Akkermansia and Metabolic Syndrome is Dose-Dependent and Affected by Microbial Interactions: A Cross-Sectional Study.* Diabetes Metab Syndr Obes, 2021. **14**: p. 2177-2188.
379. Zhao, S., et al., *Akkermansia muciniphila improves metabolic profiles by reducing inflammation in chow diet-fed mice.* J Mol Endocrinol, 2017. **58**(1): p. 1-14.
380. Bian, X., et al., *Administration of Akkermansia muciniphila Ameliorates Dextran Sulfate Sodium-Induced Ulcerative Colitis in Mice.* Front Microbiol, 2019. **10**: p. 2259.
381. Liu, J.H., et al., *Akkermansia muciniphila promotes type H vessel formation and bone fracture healing by reducing gut permeability and inflammation.* Dis Model Mech, 2020. **13**(11).
382. Britton, R.A., et al., *Probiotic L. reuteri treatment prevents bone loss in a menopausal ovariectomized mouse model.* J Cell Physiol, 2014. **229**(11): p. 1822-30.
383. McCabe, L.R., et al., *Probiotic use decreases intestinal inflammation and increases bone density in healthy male but not female mice.* J Cell Physiol, 2013. **228**(8): p. 1793-8.
384. Dar, H.Y., et al., *Bacillus clausii inhibits bone loss by skewing Treg-Th17 cell equilibrium in postmenopausal osteoporotic mice model.* Nutrition, 2018. **54**: p. 118-128.

385. Yan, J. and J.F. Charles, *Gut Microbiome and Bone: to Build, Destroy, or Both?* Curr Osteoporos Rep, 2017. **15**(4): p. 376-384.
386. Zhang, S. and D.C. Chen, *Facing a new challenge: the adverse effects of antibiotics on gut microbiota and host immunity.* Chin Med J (Engl), 2019. **132**(10): p. 1135-1138.

Publication related to this work

Results derived from the dataset published in chapter 3.3 *The effect of the immune experience and bone fracture healing on the gut microbiome in aged mice* are partially incorporated in the following publication:

Bucher, C.H., Berkmann, J.C., Burkhardt, L.M., Paschke, C., Schlundt, C., Lang, A., Wolter, A., Damerau, A., Geissler, S., Volk, H.-D., Duda, G.N., Schmidt-Bleek, K., *Local immune cell contributions to fracture healing in aged individuals - A novel role for interleukin 22.* Exp Mol Med, 2022. **54**(8): p. 1262-1276. DOI: 10.1038/s12276-022-00834-9

The results presented and discussed in the current doctoral thesis build upon the previously published data regarding the Shannon diversity index and taxonomic composition at the phylum level. Additionally, they contribute insights into richness, MDS plots of bacterial profiles, comparisons of OTUs before and after surgery, and the relative abundance of taxonomic groups at the genus level.

Furthermore, the experimental groups were redefined for the manuscript as follows: "aged" was changed to "low immunoaged", and "immunoaged" was relabeled as "high immunoaged". Their visual representation was also updated, with the low immunoaged group now shown in green and the high immunoaged group in red, respectively, replacing the previous colors of light orange and dark red. Instead of a box-and-whisker plot with a line at the median, the data are herein depicted as truncated violin plots with median and IQR.

Supplement

Supp. 1 | Enriched pathways resulted from single cell RNA sequencing of peripheral blood Pan T cells 7d post-fracture as part of the short-term DIO study.

gene platform	ID	description	set size
CD4+ T cells			
kegg.pathways	mmu05168	Herpes simplex virus 1 infection	267
kegg.pathways	mmu04062	Chemokine signaling pathway	99
kegg.pathways	mmu04621	NOD-like receptor signaling pathway	112
CD8+ T cells			
kegg.pathways	mmu05164	Influenza A	107
kegg.pathways	mmu05168	Herpes simplex virus 1 infection	268
kegg.pathways	mmu05169	Epstein-Barr virus infection	152
kegg.pathways	mmu05134	Legionellosis	36
wiki.pathways	WP1253	Type II interferon signaling (IFNG)	20

Supp. 2 | Identified differently expressed (DE) genes from bulk RNA sequencing of intact contralateral and osteotomized bones 3d post-fracture as part of the long-term DIO study.

marker	Ensembl ID	gene	protein
lipid metabolism	ENSMUSG00000026457	Adipor1	adiponectin receptor 1
	ENSMUSG00000046491	C1qtnf2	C1q and tumor necrosis factor related protein (C1QTNF) 2
	ENSMUSG00000058914	C1qtnf3	C1QTNF3
	ENSMUSG00000071347	C1qtnf9	C1QTNF9
	ENSMUSG00000073418	C4b	complement component 4B
	ENSMUSG00000002944	Cd36	CD36
	ENSMUSG00000000402	Egfl6	epidermal growth factor (EGF)-like-domain, multiple 6
	ENSMUSG00000028773	Fabp3	fatty acid binding protein 3
	ENSMUSG00000062515	Fabp4	fatty acid binding protein 4
	ENSMUSG00000027533	Fabp5	fatty acid binding protein 5
	ENSMUSG00000059201	Lep	leptin
	ENSMUSG00000028494	Plin2	perilipin 2
	ENSMUSG00000002831	Plin4	perilipin 4

continued: ***Supplement 2***

	ENSMUSG00000011305	Plin5	perilipin 5
	ENSMUSG00000006586	Runx1t1	Runt-related transcription factor (RUNX) 1 translocation partner 1
	ENSMUSG00000018566	Slc2a4	solute carrier family 2 (facilitated glucose transporter), member 4
	ENSMUSG00000042333	Tnfrsf14	tumor necrosis factor receptor superfamily, member 14
insulin	ENSMUSG00000020053	Igf1	insulin-like growth factor (IGF) 1
signaling	ENSMUSG00000048583	Igf2	IGF 2
	ENSMUSG00000039323	Igfbp2	IGF binding protein 2
	ENSMUSG00000020427	Igfbp3	IGF binding protein 3
	ENSMUSG00000017493	Igfbp4	IGF binding protein 4
	ENSMUSG00000026185	Igfbp5	IGF binding protein 5
	ENSMUSG00000023046	Igfbp6	IGF binding protein 6
OB lineage	ENSMUSG00000028766	Alpl	alkaline phosphatase
	ENSMUSG00000001506	Col1a1	collagen, type I, alpha 1
	ENSMUSG00000019997	Ctgf	connective tissue growth factor
	ENSMUSG00000057098	Ebf1	early B cell factor (EBF) 1
	ENSMUSG00000022053	Ebf2	EBF2
	ENSMUSG00000011118	Panx3	pannexin 3
	ENSMUSG00000032492	Pth1r	parathyroid hormone 1 receptor
	ENSMUSG00000070691	Runx3	runt related transcription factor 3
	ENSMUSG00000038331	Satb2	special AT-rich sequence binding protein
	ENSMUSG00000051910	Sox6	SRY (sex determining region Y)-box 6
	ENSMUSG00000063632	Sox11	SOX11
	ENSMUSG00000060284	Sp7	Sp7 transcription factor 7
	ENSMUSG00000029304	Spp1	secreted phosphoprotein 1
	ENSMUSG00000022015	Tnfsf11	tumor necrosis factor (ligand) superfamily, member 11
OC lineage	ENSMUSG00000028111	Ctsk	cathepsin K
	ENSMUSG00000017737	Mmp9	matrix metallopeptidase (MMP) 9
	ENSMUSG00000000957	Mmp14	MMP14
	ENSMUSG00000054594	Oscar	osteoclast associated receptor
	ENSMUSG00000026321	Tnfrsf11a	tumor necrosis factor receptor superfamily, member 11a, NFKB activator
osteocyte	ENSMUSG00000029307	Dmp1	dentin matrix protein 1
lineage	ENSMUSG00000030409	Dmpk	dystrophia myotonica-protein kinase
	ENSMUSG00000000182	Fgf23	fibroblast growth factor 23

continued: ***Supplement 2***

	ENSMUSG00000031548	Sfrp1	secreted frizzled-related protein 1
chondrocyte lineage	ENSMUSG00000030607	Acan	aggrecan
	ENSMUSG00000022483	Col2a1	collagen, type II, alpha 1
	ENSMUSG00000005583	Mef2c	myocyte enhancer factor 2C
	ENSMUSG00000051910	Sox6	SRY (sex determining region Y)-box 6
	ENSMUSG00000000567	Sox9	SOX9
fibroblast markers	ENSMUSG00000019929	Dcn	decorin
	ENSMUSG00000026193	Fn1	fibronectin 1
	ENSMUSG00000001020	S100a4	S100 calcium binding protein A4
EC markers/ angiogenesis	ENSMUSG00000054690	Emcn	endomucin
	ENSMUSG00000020717	Pecam1	platelet/endothelial cell adhesion molecule 1
	ENSMUSG00000023951	Vegfa	vascular endothelial growth factor A
	ENSMUSG00000031520	Vegfc	vascular endothelial growth factor C
	ENSMUSG00000031380	Vegfd	vascular endothelial growth factor D
collagen fibers	ENSMUSG00000001506	Col1a1	collagen, type I, alpha 1
	ENSMUSG00000029661	Col1a2	collagen, type I, alpha 2
	ENSMUSG00000022483	Col2a1	collagen, type II, alpha 1
	ENSMUSG00000026043	Col3a1	collagen, type III, alpha 1
	ENSMUSG00000031274	Col4a5	collagen, type IV, alpha 5
	ENSMUSG00000026837	Col5a1	collagen, type V, alpha 1
	ENSMUSG00000026042	Col5a2	collagen, type V, alpha 2
	ENSMUSG00000004098	Col5a3	collagen, type V, alpha 3
	ENSMUSG00000068196	Col8a1	collagen, type VIII, alpha 1
	ENSMUSG00000056174	Col8a2	collagen, type VIII, alpha 2
	ENSMUSG00000039462	Col10a1	collagen, type X, alpha 1
	ENSMUSG00000027966	Col11a1	collagen, type XI, alpha 1
	ENSMUSG00000024330	Col11a2	collagen, type XI, alpha 2
	ENSMUSG00000058806	Col13a1	collagen, type XIII, alpha 1
	ENSMUSG00000022371	Col14a1	collagen, type XIV, alpha 1
	ENSMUSG00000028339	Col15a1	collagen, type XV, alpha 1
	ENSMUSG00000040690	Col16a1	collagen, type XVI, alpha 1
	ENSMUSG00000001435	Col18a1	collagen, type XVIII, alpha 1
	ENSMUSG00000079022	Col22a1	collagen, type XXII, alpha 1
	ENSMUSG00000028197	Col24a1	collagen, type XXIV, alpha 1
	ENSMUSG00000029718	Pcolce	procollagen C-endopeptidase enhancer protein
ECM proteins	ENSMUSG00000021388	Aspn	asporin
	ENSMUSG00000029675	Eln	elastin

continued: ***Supplement 2***

	ENSMUSG00000006369	Fbln1	fibulin 1
	ENSMUSG00000064080	Fbln2	fibulin 2
	ENSMUSG00000027386	Fbln7	fibulin 7
	ENSMUSG00000038259	Gdf5	growth differentiation factor 5
	ENSMUSG00000019932	Kera	keratocan
	ENSMUSG00000032796	Lama1	laminin, alpha 1
	ENSMUSG00000019846	Lama4	laminin, alpha 4
	ENSMUSG00000002900	Lamb1	laminin B1
	ENSMUSG00000027750	Postn	periostin
	ENSMUSG00000040152	Thbs1	thrombospondin 1
	ENSMUSG00000023885	Thbs2	thrombospondin 2
	ENSMUSG00000021702	Thbs4	thrombospondin 4
ECM enzymes	ENSMUSG00000031555	Adam9	a disintegrin and metallopeptidase domain (ADAM) 9
	ENSMUSG00000054555	Adam12	ADAM12
	ENSMUSG00000040537	Adam22	ADAM22
	ENSMUSG00000025964	Adam23	ADAM23
	ENSMUSG00000036545	Adamts2	a disintegrin-like and metallopeptidase (reprolysin type) with thrombospondin type 1 motif (ADAMTS), 2
	ENSMUSG00000043635	Adamts3	ADAMTS3
	ENSMUSG00000006403	Adamts4	ADAMTS4
	ENSMUSG00000046169	Adamts6	ADAMTS6
	ENSMUSG00000031994	Adamts8	ADAMTS8
	ENSMUSG00000030022	Adamts9	ADAMTS9
	ENSMUSG00000047497	Adamts12	ADAMTS12
	ENSMUSG00000049538	Adamts16	ADAMTS16
	ENSMUSG00000066113	Adamtsl1	ADAMTS-like 1
	ENSMUSG00000043822	Adamtsl5	ADAMTS-like 5
	ENSMUSG00000040314	Ctsg	cathepsin G
	ENSMUSG00000020125	Elane	elastase
	ENSMUSG00000025780	Itih5	inter-alpha-trypsin inhibitor, heavy chain 5
	ENSMUSG00000024529	Lox	lysyl oxidase
	ENSMUSG00000034205	Loxl2	LOX-like 2
	ENSMUSG00000025185	Loxl4	LOX-like 4
	ENSMUSG00000031740	Mmp2	matrix metallopeptidase (MMP)2
	ENSMUSG00000000901	Mmp11	MMP11
	ENSMUSG00000028226	Mmp16	MMP16

continued: ***Supplement 2***

	ENSMUSG00000070323	Mmp27	MMP27
	ENSMUSG00000051048	P4ha3	procollagen-proline, 2-oxoglutarate 4-dioxygenase (proline 4-hydroxylase), alpha polypeptide III
BMP/Smad/ Wnt signaling	ENSMUSG00000022098	Bmp1	bone morphogenetic protein 1
	ENSMUSG00000029335	Bmp3	bone morphogenetic protein 3
	ENSMUSG00000032179	Bmp5	bone morphogenetic protein 5
	ENSMUSG00000008999	Bmp7	bone morphogenetic protein 7
	ENSMUSG00000034663	Bmp2k	BMP2 inducible kinase
	ENSMUSG00000024515	Smad4	SMAD family member 4
	ENSMUSG00000021540	Smad5	SMAD family member 5
	ENSMUSG00000036867	Smad6	SMAD family member 6
	ENSMUSG00000036856	Wnt4	Wingless-type MMTV integration site family, member 4
	ENSMUSG00000000126	Wnt9a	Wingless-type MMTV integration site family, member 9a
	ENSMUSG00000015957	Wnt11	Wingless-type MMTV integration site family, member 11
	ENSMUSG00000029671	Wnt16	Wingless-type MMTV integration site family, member 16
$CD8^+$ T cell depletion	ENSMUSG00000053977	Cd8a	CD8 antigen, alpha chain
	ENSMUSG00000053044	Cd8b1	CD8 antigen, beta chain 1
immune cell marker	ENSMUSG00000016494	Cd34	CD34 antigen
	ENSMUSG00000032094	Cd3d	CD3 antigen, delta polypeptide
	ENSMUSG00000032093	Cd3e	CD3 antigen, epsilon polypeptide
	ENSMUSG00000002033	Cd3g	CD3 antigen, gamma polypeptide
	ENSMUSG00000026395	Ptprc	protein tyrosine phosphatase, receptor type, C
	ENSMUSG00000051439	Cd14	CD14 antigen
	ENSMUSG00000018774	Cd68	CD68 antigen
chemokine network	ENSMUSG00000035385	Ccl2	chemokine (C-C motif) ligand (CCL) 2
	ENSMUSG00000035373	Ccl7	CCL7
	ENSMUSG00000020676	Ccl11	CCL11
	ENSMUSG00000035352	Ccl12	CCL12
	ENSMUSG00000004814	Ccl24	CCL24
	ENSMUSG00000049103	Ccr2	chemokine (C-C motif) receptor (CCR) 2
	ENSMUSG00000079227	Ccr5	CCR5
	ENSMUSG00000037944	Ccr7	CCR7
	ENSMUSG00000043953	Ccrl2	CCR-like 2

continued: ***Supplement 2***

	ENSMUSG00000029371	Cxcl5	chemokine (C-X-C motif) ligand (CXCL) 5
	ENSMUSG00000061353	Cxcl12	CXCL12
	ENSMUSG00000023078	Cxcl13	CXCL13
	ENSMUSG00000018920	Cxcl16	CXCL16
	ENSMUSG00000048480	Cxcr1	chemokine (C-X-C motif) receptor (CXCR) 1
	ENSMUSG00000047880	Cxcr5	CXCR5
	ENSMUSG00000060509	Xcr1	chemokine (C motif) receptor (XCR) 1
interleukin	ENSMUSG00000016529	Il10	interleukin (IL)-10
signaling	ENSMUSG00000004371	Il11	IL-11
	ENSMUSG00000024810	Il33	IL-33
	ENSMUSG00000003882	Il7r	IL-7 receptor